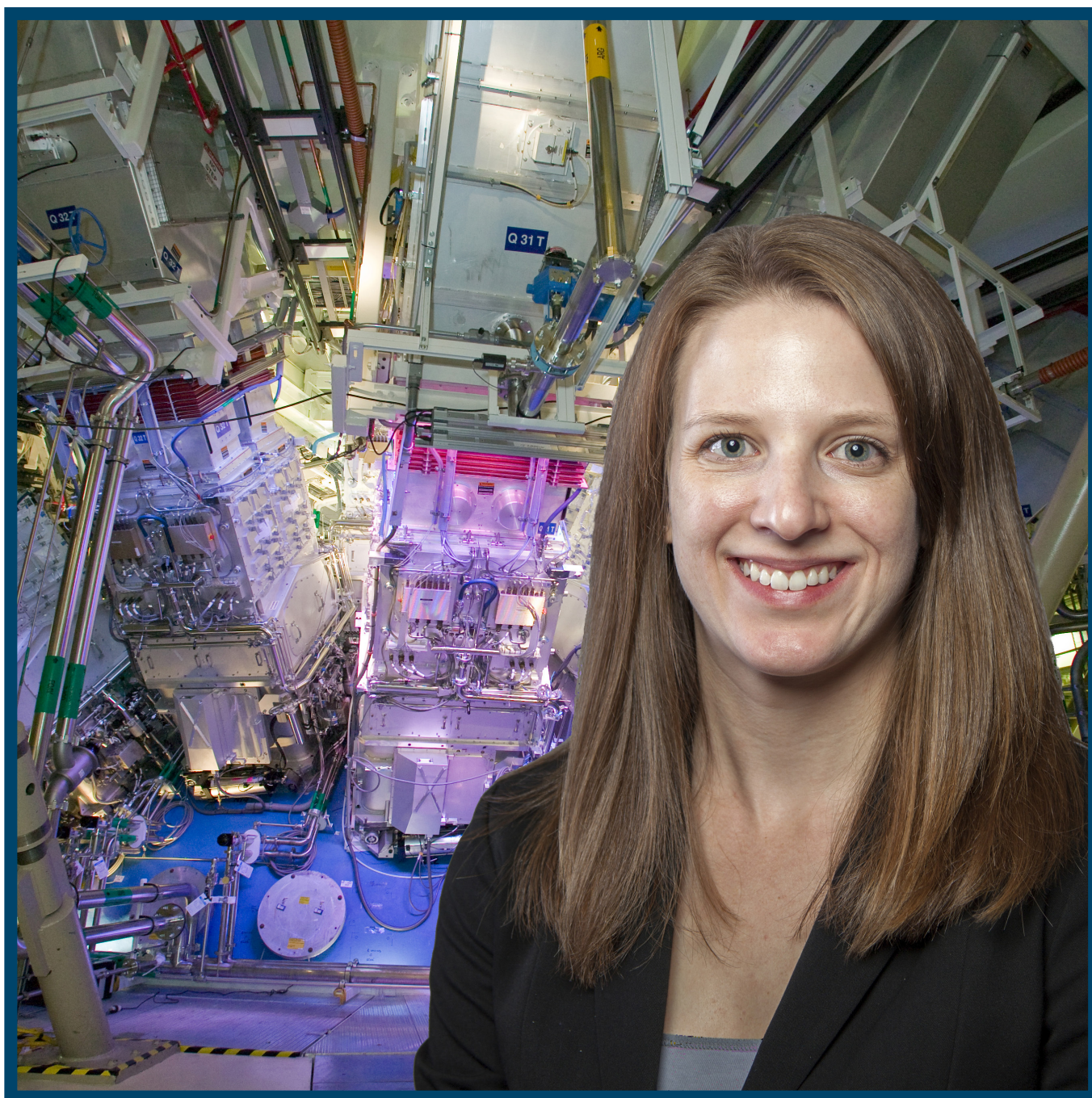# LLE Review

Quarterly Report

UR
LLE

About the Cover:

The cover photo (courtesy of Clayton Dahlen, LLNL) shows Michelle Gregor, graduate student in the Physics and Astronomy Department, at the target area of the National Ignition Facility (NIF). Her thesis work measured the shock and release behaviors of nanocrystalline diamond that is used as an ablator material on ignition targets on the NIF. Knowledge of the behavior of shocked material as it releases to lower pressures is important to inertial confinement fusion target design and the general behavior of high-energy-density material. Previous to Michelle's work, there were no shock data on nanocrystalline diamond, which has nanometer-scale grains and a density that is ~4% less than single-crystal diamond. Her experiments measured shocked diamond up to 25 Mbar and demonstrated that the nanocrystalline diamond has a stiffer response to shocks than predicted by models. She found that a porosity model accurately predicts this behavior.
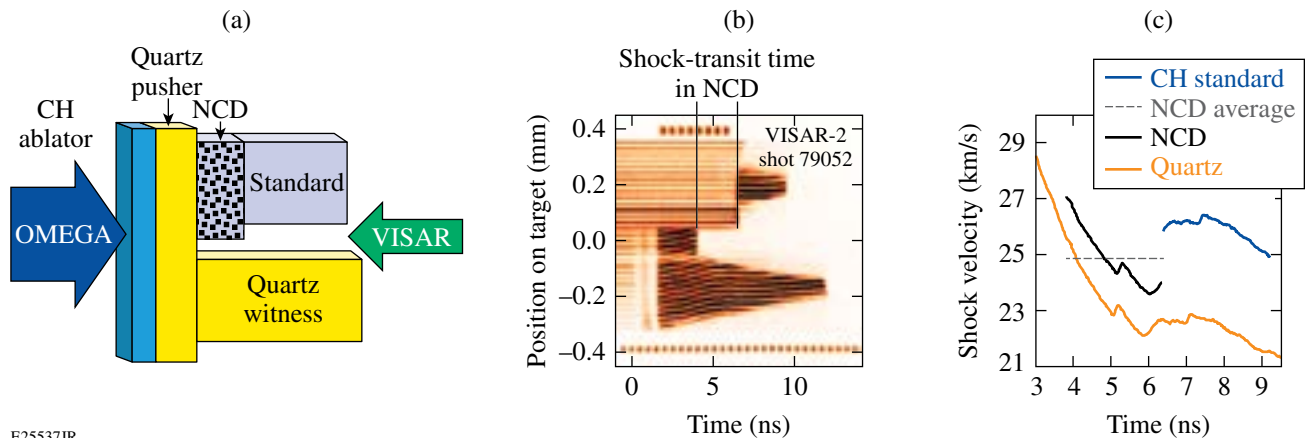
E25537JR

Michelle designed targets (a) comprising a CH ablator, a quartz pusher and witness, a nanocrystalline diamond (NCD) sample, and a standard positioned to facilitate measurements of transit times that allowed accurate shock-velocity measurements in the opaque NCD. Raw VISAR data are shown in (b) and extracted shock velocities in (c). The shock-velocity profile in NCD (solid black line) was inferred from the average shock velocity (dashed gray line) and the observed shock-velocity profile in the adjacent quartz witness (solid orange line) using the nonsteady waves correction. The shock-velocity profile in the CH standard (solid blue line) is observed once the shock breaks out of the NCD. Michelle's experiments measured nanocrystalline and single-crystal diamond that was shocked and then released into various standard materials whose properties are known. Using these data a Mie–Grüneisen equation of state was formulated that adequately modeled the release of both types of diamond.

For questions or comments, contact Wolfgang Theobald, Editor, Laboratory for Laser Energetics, 250 East River Road, Rochester, NY 14623-1299, (585) 273-2628.

www.lle.rochester.edu/

LLE Review

Quarterly Report

UR
LLE

Contents

In Brief

This volume of the LLE Review, covering July–September 2016, features "Hugoniot and Release Measurements in Diamond Shocked Up to 25 Mbar," by M. C. Gregor, D. N. Polsin, J. R. Rygg, G. W. Collins, and T. R. Boehly (LLE); D. E. Frantanduono, T. Braun, P. M. Celliers, and J. H. Eggert (LLNL); C. A. McCoy (SNL); and D. D. Meyerhofer (LANL). This article (p. 159) reports on measurements of the equation of state of carbon at extreme pressures. This is of interest to studies of planetary ice giants and white dwarfs and to inertial confinement fusion (ICF). Knowledge of the high-pressure shock-and-release responses of diamond is necessary to accurately model an ICF implosion and design ignition targets. The article presents Hugoniot and release data for both single-crystal diamond and high-density carbon (HDC), comprised of nanometer-scale grains, used as a National Ignition Facility ablator. Diamond was shock compressed to multimegabar pressures and then released into reference materials with known Hugoniots at the Omega Laser Facility. Hugoniot results indicate that HDC, which is ultrananocrystalline and ~4% less dense than single-crystal diamond, has a stiffer response than single-crystal diamond.

Additional research highlights presented in this issue include the following:

- V. N. Goncharov, S. P. Regan, E. M. Campbell, T. C. Sangster, P. B. Radha, J. F. Myatt, D. H. Froula, T. R. Boehly, J. A. Delettrez, D. H. Edgell, R. Epstein, C. J. Forrest, V. Yu. Glebov, D. R. Harding, S. X. Hu, I. V. Igumenshchev, F. J. Marshall, D. T. Michel, W. Seka, A. Shvydky, C. Stoeckl, W. Theobald, R. Betti, R. L. McCrory (LLE); and M. Gatu Johnson (MIT) point out that a major advantage of the laser direct-drive (DD) approach to ignition is the increased fraction of laser drive energy coupled to the hot spot and relaxed hot-spot requirements for the peak pressure and convergence ratios relative to the indirect-drive approach at equivalent laser energy (p. 172). With the goal of a successful ignition demonstration using direct drive, the recently established national strategy has several elements and involves multiple national and international institutions. These elements include the experimental demonstration on OMEGA cryogenic implosions of hot-spot conditions relevant for ignition at MJ-scale energies available at the National Ignition Facility (NIF) and developing an understanding of laser–plasma interactions and laser coupling using DD experiments on the NIF. DD designs require reaching central stagnation pressures in excess of 100 Gbar. The current experiments on OMEGA have achieved inferred peak pressures of 56 Gbar. Extensive analysis of the cryogenic target experiments and two- and three-dimensional simulations suggests that power balance, target offset, and target quality are the main limiting factors in target performance. In addition, cross-beam energy transfer (CBET) has been identified as the main mechanism for reducing laser coupling. Reaching the goal of demonstrating hydrodynamic equivalence on OMEGA includes improving laser power balance, target position, and target quality at shot time. CBET must also be significantly reduced and several strategies have been identified to address this issue.

- D. Turnbull, C. Goyon, G. E. Kemp, B. B. Pollock, D. Mariscal, L. Divol, J. S. Ross, S. Patankar, J. D. Moody, and P. Michel (LLNL) report the first complete set of measurements of a laser-plasma optical system's refractive index, as seen by an independent probe laser beam, as a function of the relative wavelength shift between the two laser beams (p. 181). Both the imaginary and real refractive index components are found to be in good agreement with linear theory using plasma parameters measured by optical Thomson scattering and interferometry; the former is in contrast to previous work and has

implications for cross-beam energy transfer in indirect-drive inertial confinement fusion, and the latter is measured for the first time. The data include the first demonstration of a laser-plasma polarizer with 85% to 87% extinction for the particular laser and plasma parameters used in this experiment, complementing the existing suite of high-power, tunable, and ultrafast plasma–based photonic devices.

- R. A. Hamilton, W. T. Shmayda, and F. J. Marshall describe an x-ray detection system (XDS) that has been developed and commissioned at the Laboratory for Laser Energetics with the intent of nondestructively extrapolating the pressure of tritium-filled targets from their measured activity (p. 186). The x-ray emissions from silica (SiO_2) and plastic (CH and CD) targets have been measured in the helium environment of the XDS with accurate repeatability prior to being imploded by the OMEGA Laser System in inertial confinement fusion experiments. The T_2 permeation half-lives were measured for three plastic targets, allowing for the actual initial-fill pressures of those targets to be calculated based on the slope of the pressure versus activity. The half-lives measured by the XDS are compared with values reported by the target manufacturer, differing with a range of up to 2.3×.

- R. Mancini reports on the Eighth Omega Laser Facility Users Group Workshop (p. 193).

- This volume concludes with a summary of LLE's Summer High School Research Program (p. 200), the FY16 Laser Facility Report (p. 202), and the National Laser Users' Facility and External Users' Programs (p. 205).

<div align="right">

Wolfgang Theobald
Editor

</div>

Hugoniot and Release Measurements in Diamond Shocked up to 26 Mbar

Introduction

The behavior of carbon at millions to billions of atmospheres of pressure is integral to evolution models for many solar and extrasolar planets (Uranus, Neptune, 55 Cancri E)[1,2] and white dwarf stars.[3,4] In Uranus and Neptune, carbon exists in the form of methane (CH_4) ice at the surface but may be in its elemental form near the core, where pressures and temperatures reach ~8 Mbar and ~8000 K, respectively.[5,6] Theoretical predictions suggest that the interiors of Uranus, Neptune, or Neptune-like exoplanets might contain diamond or even liquid oceans of carbon.[1,5] This strongly motivates studies of carbon's high-pressure response in both its solid and liquid phases.[7–9]

Carbon's equation of state (EOS) is also important to developing predictive models for inertial confinement fusion (ICF) experiments, where diamond shells are used to contain and compress the hydrogen fuel.[10] An ICF implosion uses a series of finely tuned shock waves to precompress the shell (ablator) and fuel. This initiates near isentropic compression while adding the desired amount of entropy needed to hydrodynamically stabilize the main implosion. An optimal target design is a delicate balance between these two effects. The diamond used in ICF targets is polycrystalline with grain sizes of ~10 nm (Refs. 11 and 12). The low surface roughness and isotropic character of this nanocrystalline diamond (NCD) compared to single-crystal diamond (SCD) makes NCD less susceptible to hydrodynamic instabilities seeded by crystal anisotropy at the ablator/fuel interface. Current implosion designs melt the NCD with the first shock to further limit instability growth. Modeling an ICF implosion requires accurate knowledge of NCD's response to multimegabar shocks and its behavior when it releases from these extreme pressures into the low-density fuel.

To date, data for carbon above the diamond melt boundary are limited to shock-compression measurements.[13–15] None of these data include NCD; high-precision measurements (relative density error < 1.5%) for SCD exist up to only 18 Mbar (Ref. 15). Shock Hugoniot data in solid diamond[16–18] and the solid–liquid coexistence region[7,8,15] are supplemented by ramp-compression measurements,[19,20] which are used to explore matter at temperatures significantly lower than temperatures on the Hugoniot. Ramp-compression data exist up to 8 Mbar in solid SCD[20] and 50 Mbar for solid NCD,[19] but theories describing liquid carbon above 18 Mbar are unconstrained by high-precision experiments. The experiments presented here provide high-pressure (up to 26 Mbar) shock-compression and release data for both full-density SCD ($\rho_0 = 3.515$ g/cm^3) and the lower-density NCD ($\rho_0 \sim 3.36$ g/cm^3) used in ICF capsules. The Hugoniot data provide a clear constraint on the pressure, density, and internal energy of liquid carbon, while the release data constrain the isentropes from these high-pressure, high-temperature shock states to a several-fold drop in pressure.[21,22]

Single-shock Hugoniot data for diamond (both SCD and NCD) were collected to 26 Mbar using impedance-matching (IM) techniques with quartz as a reference material. These new SCD data agree with density-functional theory molecular dynamics (DFT-MD) calculations for liquid carbon.[23] The data for NCD, which are expected to be at a slightly higher temperature, exhibit a compressibility that is even stiffer than shock-compressed SCD measurements and DFT-MD predictions. The NCD data suggest that, in addition to carbon's anomalously stiff fluid state, either its thermal properties are inadequately understood or the shock compression of NCD undergoes an additional (frictional) heating explained by its slightly lower density.

The release data were collected by releasing shock-compressed diamond into several lower-impedance materials with known shock Hugoniots including quartz,[24,25] CH,[26] silica foam,[25,27] and liquid D_2 (Refs. 28 and 29). This technique was previously used by Knudson, Desjarlais, and Pribram-Jones to benchmark the release of shocked quartz[25] and aluminum.[29] Data were acquired for diamond releasing from 8 to 20 Mbar, so release paths originated from both the coexistence region and liquid phase. The release data mostly agree with predictions using existing EOS models that do not include strength effects, indicating that strength does not largely affect the diamond release physics at these pressures. The release measurements into the low-density liquid D_2 are particularly valuable for

constraining ICF models since liquid D_2 is a good surrogate for the deuterium–tritium fuel in an ICF target.

The following sections describe the experimental design, targets, and diagnostics used in the laser-driven shock experiments; show the IM technique used to measure Hugoniot and release states; and present the NCD data analysis techniques followed by the results.

Experimental Technique

The experiments were performed at the Omega Laser Facility, a Nd:glass laser that is frequency tripled to a wavelength of 351 nm (Ref. 30). The experiments used 6 to 12 beams having temporally square pulses with durations of 2, 3, or 3.7 ns with total energies between 1.1 and 3.7 kJ. The beams with an 876-μm-diam laser focal spot were smoothed by spectral dispersion[31] and distributed phase plates.[32] On-target laser intensities of 0.66 to 3.3×10^{14} W/cm^2 were achieved, producing shock pressures up to 26 Mbar in the diamond targets.

The NCD targets were designed to provide both Hugoniot and release measurements on each shot. The targets [Fig. 148.1(a)] comprised a CH ablator, a Z-cut α-quartz standard (pusher), and an NCD sample glued to the pusher's rear surface. IM data were obtained at this interface for NCD Hugoniot measurements. A standard material [quartz, polystyrene (CH), SiO$_2$ foam, or liquid D_2] was in contact with the rear side of the NCD sample to determine its release behavior.

Adjacent to the NCD sample, a quartz witness provided a reference for the temporal history of the shock velocity. The witness was required because internal scattering attributed to the nanometer-sized diamond grains and their random orientations make NCD opaque to visible light.[12] For this reason, shock velocities in the NCD were measured from transit times. To facilitate these measurements, the NCD sample and rear standard were positioned to provide an unobstructed view of ~100 μm of the rear quartz pusher and NCD faces as shown in Figs. 148.1(a) and 148.1(b).

Examples of planar cryogenic and warm SCD target designs are shown in Fig. 148.2. SCD is transparent, obviating the need for the quartz witness, which allowed us to use one to three rear standards to obtain multiple release measurements on a single shot. Hugoniot measurements were made at the quartz/SCD interface and release measurements were made at the SCD/rear-standard interfaces. A thin (0.3- or 2-μm) gold layer was deposited on the rear of the CH ablator in some targets to help prevent preheat in the SCD and standards. A quartz baseplate (30 to 50 μm thick) was attached to the front side of the diamond whenever a gold layer was not used.

The NCD targets used nanocrystalline diamond (fabricated by Diamond Materials GmbH) identical to those used in ICF targets at the National Ignition Facility (NIF).[33] The density of the NCD samples was determined to be 3.360 ± 0.002 g/cm^3 using an Archimedes' measurement of a larger reference
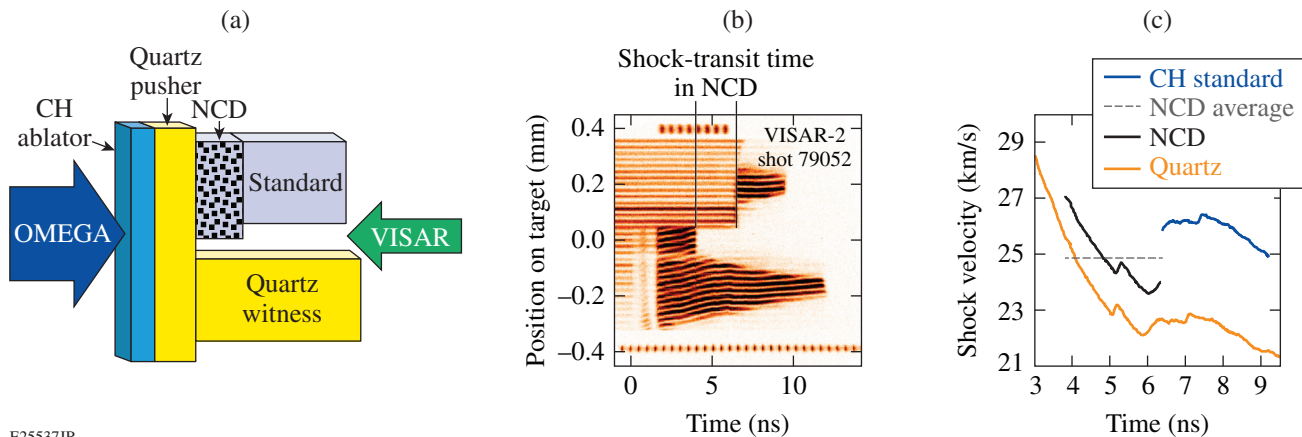
Figure 148.1
(a) The nanocrystalline diamond (NCD) target design comprising a CH ablator, a quartz pusher and witness, an NCD sample, and a standard positioned to facilitate measurements of transit times. (b) Raw VISAR (velocity interferometer system for any reflector) data from an experiment using the target design in (a). (c) Extracted shock velocities from (b). The shock-velocity profile in NCD (black line) was inferred from the average shock velocity (dashed line) and the observed shock-velocity profile in the adjacent quartz witness (orange line) using the nonsteady waves correction.[34] The shock-velocity profile in the CH standard (solid blue line) is observed once the shock breaks out of the NCD.

(a)

Quartz

CH ablator

OMEGA

SCD

Liquid D$_2$

VISAR

(b)

Gold

CH ablator

OMEGA

SCD

CH

Quartz VISAR
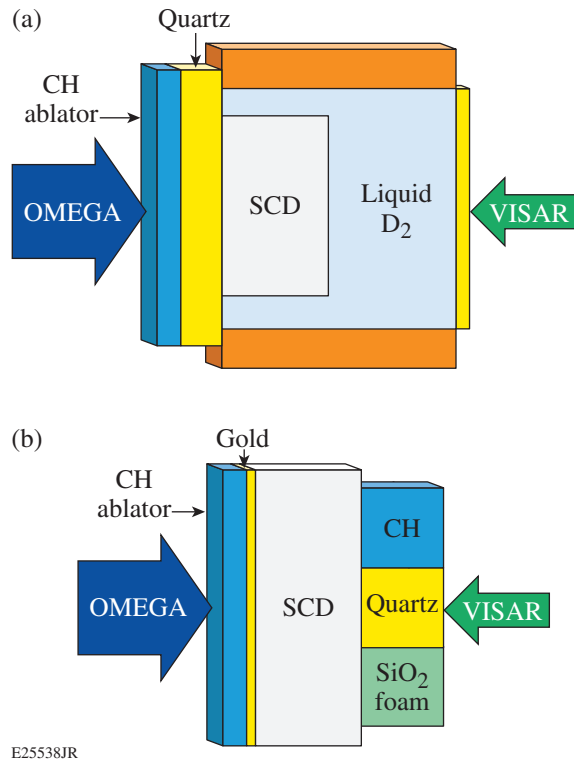
SiO$_2$ foam

E25538JR

Figure 148.2

Schematics of (a) planar cryogenic and (b) warm targets used in single-crystal diamond (SCD) Hugoniot and release experiments. Targets had a CH ablator and one to three standards (liquid D$_2$, CH, quartz, or SiO$_2$ foam) on the rear side of the SCD.

sample from the same batch.[12] The SCD foils obtained from Applied Diamond had a density of $\rho_0 = 3.515$ g/cm^3 and were natural with a $\langle 110 \rangle$ orientation or fabricated with chemical vapor deposition (CVD) with a $\langle 100 \rangle$ orientation. The quartz ($\rho_0 = 2.65$ g/cm^3), CH ($\rho_0 = 1.05$ g/cm^3), and SiO$_2$-foam ($\rho_0 \sim 0.2$g/cm^3) pieces (see Table 148.I for exact values) were obtained from Schafer Corporation. The planar cryogenic targets [Fig. 148.2(a)] comprised a liquid D$_2$–filled, cylindrical copper cell sealed with quartz on both faces. The initial D$_2$ density was determined from the temperature in the cryogenic cell and varied between 0.170 and 0.174 g/cm^3 on a shot-to-shot basis.[35] The uncertainty in the SiO$_2$ foam density was estimated to be ~2%, and uncertainties in the SCD, quartz, CH, and liquid D$_2$ densities were assumed to be negligible.

The shock velocities for impedance matching were measured using the line-imaging velocity interferometer system for any reflector (VISAR) described in Ref. 36. Opposite the drive beams, the VISAR probe beam is incident on the rear side of the target and the reflected signal is relayed to a pair of

interferometers. A delay etalon is inserted into one leg of each interferometer so that changes in Doppler shifts of the reflected probe beam, corresponding to moving reflective interfaces, are registered as fringe shifts in the interference pattern. The fringe shifts are proportional to the velocity of the moving interface through the velocity per fringe (VPF), which depends inversely on the etalon thickness and the index of refraction of the target medium at the 532-nm probe wavelength. The indices of refraction for the target materials at 532 nm were 2.42 (SCD), 1.55 (quartz), 1.59 (CH), 1.04 (0.2-g/cm^3 SiO$_2$ foam),[27] and 1.14 (0.174-g/cm^3 liquid D$_2$) (Ref. 28).

The two interferograms, which are recorded on separate streak cameras, provide time histories of the velocity of moving interfaces with ~10-ps resolution.[36] Fringe jumps or 2π phase ambiguities between the two records are resolved by using etalons of different thicknesses. The velocities presented here for the NCD Hugoniot and all release measurements are those measured using the more-sensitive VISAR leg. Measurements using the less-sensitive VISAR leg are presented for some SCD Hugoniot measurements because it provided better-resolved fringe shifts of the rapidly decaying shock at the quartz/SCD interface. Errors were estimated to be the larger of 5% of a fringe using the more-sensitive leg or the difference between the velocity from the more-sensitive leg and the weighted velocity average from both legs. An example of raw VISAR data and the extracted shock velocities from an NCD experiment using the target design in Fig. 148.1(a) are shown in Figs. 148.1(b) and 148.1(c). The VISAR diagnostic provides 1-D spatial resolution along the slit of the streak camera so that shock velocities are observed over an ~800-μm slice of the target.

The targets were shock compressed to a metallic fluid state producing a reflective shock front. VISAR recorded the shock velocity as a function of time in the transparent materials.[36] In opaque materials, the VISAR probe beam cannot reach the shock front within the target. Instead, VISAR registers the time that the shock breaks out of the opaque material. For example, the shock transit time in the NCD sample is given by the time between the two vertical lines in Fig. 148.1(b). The first time is registered by the arrival of the shock at the rear of the quartz pusher. The second time is registered from its arrival at the rear NCD interface. For transparent materials, higher-precision, *in-situ*, time-varying shock-velocity profiles were measured. A streaked optical pyrometer[37] (SOP) with an ~5-ps temporal resolution provided additional measurements of shock transit times. Average velocities in NCD were corrected using the nonsteady waves model discussed below.

Table 148.I: Diamond release data. All the single-crystal diamond (SCD) samples had a $\langle 110 \rangle$ orientation except for the SCD in shot 73733, which had a $\langle 100 \rangle$ orientation. U_s^C and U_s^{Stan} are the shock velocities at the interface between the diamond and the lower-impedance standard (quartz, CH, silica foam, or liquid D_2). U_s^{Stan} was corrected to account for the glue layer (when necessary) by linearly fitting to the measured shock velocity in the standard over a small time interval and extrapolating the fit backward across the glue layer. The initial densities of the liquid D_2 and foam samples are given in mg/cm^3 in column 3.

Shot	Diamond Type	Standard	U_s^C (km/s)	U_s^{Stan} (km/s)
77003	SCD	D_2 (174)	29.47±0.06	38.60±0.27
77848	SCD	D_2 (170)	28.56±0.06	36.86±0.12
77851	SCD	D_2 (170)	27.39±0.09	34.49±0.12
77856	SCD	D_2 (170)	29.10±0.06	37.83±0.13
79050	SCD	D_2 (174)	25.03±0.10	30.14±0.33
79053	SCD	D_2 (172)	24.62±0.10	29.29±0.22
73733	SCD	quartz	25.88±0.06	24.52±0.09
75397	SCD	quartz	23.67±0.07	21.63±0.15
75399	SCD	quartz	23.87±0.07	21.92±0.11
75400	SCD	quartz	23.20±0.11	21.05±0.16
75402	SCD	quartz	23.93±0.07	21.77±0.11
75404	SCD	quartz	29.05±0.7	27.61±0.11
77857	SCD	quartz	31.60±0.06	30.17±0.09
77859	SCD	quartz	31.57±0.06	30.05±0.09
77860	SCD	quartz	29.33±0.06	28.29±0.09
75397	SCD	CH	23.48±0.07	24.00±0.10
75399	SCD	CH	23.84±0.13	24.94±0.12
75400	SCD	CH	23.20±0.07	23.36±0.15
75404	SCD	CH	28.77±0.07	32.00±0.11
77857	SCD	CH	31.64±0.06	35.37±0.09
77859	SCD	CH	31.46±0.06	35.08±0.10
77860	SCD	CH	29.20±0.06	32.46±0.09
75397	SCD	foam (191)	23.63±0.07	25.01±0.16
75400	SCD	foam (191)	23.10±0.07	24.83±0.16
77004	NCD	D_2 (173)	26.68±0.82	33.29±0.12
77006	NCD	D_2 (172)	30.81±0.96	40.19±0.12
77002	NCD	quartz	31.21±0.45	30.11±0.09
77007	NCD	quartz	28.09±0.32	26.48±0.09
79048	NCD	quartz	22.16±0.18	20.44±0.16
77005	NCD	CH	28.09±0.33	31.90±0.09
77861	NCD	CH	25.76±0.31	27.92±0.10
77862	NCD	CH	24.48±0.26	26.25±0.09
79052	NCD	CH	23.94±0.16	25.87±0.16
79056	NCD	CH	26.57±0.28	28.93±0.16
79060	NCD	CH	22.93±0.20	24.87±0.25
79051	NCD	foam (198)	23.51±0.25	26.22±0.24

NCD: nanocrystalline diamond

Impedance-Matching Technique

Both Hugoniot and release states in diamond were measured using impedance matching (IM). The IM technique closes the Rankine–Hugoniot equations[22] to solve for pressure (P), density (ρ), and specific internal energy (E) in a shock-compressed material:

$$\rho_0 U_s = \rho \left(U_s - u_p\right), \tag{1}$$

$$P = P_0 + \rho_0 U_s u_p, \tag{2}$$

$$E = E_0 + \frac{1}{2}\left(P + P_0\right)\left(\frac{1}{\rho_0} - \frac{1}{\rho}\right). \tag{3}$$

These equations describe the jump conditions across a shock front, where U_s is the shock velocity, u_p is the particle velocity, and states upstream of the shock are characterized by the subscript 0 (Ref. 22). By measuring U_s and u_p, the kinematic EOS parameters P, ρ, and E can be determined. In these experiments, U_s is measured using VISAR and u_p is determined using the IM technique, which relies on the equilibration of P and u_p at the interface between the material of interest (diamond) and a material with a known EOS. This method for measuring the Hugoniot and release behavior is described in the following two sections.

1. Hugoniot Measurements

The Hugoniot of an uncharacterized sample is measured with knowledge of the standard's EOS and the shock velocities about the standard/sample interface. In this work, the diamond Hugoniot data were measured using a quartz standard.[24,25] The pressure and particle velocity in the shocked quartz at the quartz pusher/diamond interface are given by the intersection of the Rayleigh line [Eq. (2)] and the quartz Hugoniot (cubic form taken from Ref. 25). When the shock crosses into the diamond, the pressure and particle velocity are continuous at the contact interface to maintain equilibrium. Since diamond has higher impedance ($\rho_0 U_s$), the quartz is re-shocked to a higher pressure, off its principal Hugoniot, to reach this new (P, u_p) state. This state, given by the intersection in the P–u_p plane of the quartz re-shock and the diamond Rayleigh line, marks a state on the diamond's Hugoniot.

The quartz re-shock was modeled using a Mie–Grüneisen EOS of the form

$$P = P_H + \Gamma \rho (E - E_H) \tag{4}$$

with

$$E - E_H = \frac{1}{2}\left(P + P_H\right)\left(\frac{1}{\rho_1} - \frac{1}{\rho}\right), \tag{5}$$

where P_H and E_H are the pressure and specific internal energy, respectively, on the quartz principal Hugoniot, ρ_1 is the density in the singly shocked quartz upstream of the re-shock, and ρ, P, and E are the density, pressure, and specific internal energy, respectively, in the re-shocked quartz. This re-shock model used the same reference Hugoniot P_H and effective Grüneisen parameter $\Gamma = \Gamma_{eff}$ as the quartz release model described in Ref. 25. It should be noted that P_H and Γ_{eff} are not necessarily physical; they were optimized such that the quartz release model matched experimental data and first-principles molecular dynamics (FPMD) simulations. This same construct should be accurate for modeling the re-shock since the quartz compresses only 20% to 30%. Indeed, the diamond P–u_p data determined by this model are only 1% to 2% higher than those obtained using the simple reflected Hugoniot approximation.

2. Release Measurements

The release behavior of shocked diamond was measured by impedance matching between diamond and several lower-impedance standards. The initial and final states of the diamond release are determined using the known Hugoniots of the diamond materials (measured previously or in this study) and those of the standards. By using various lower-impedance standards, the diamond release is measured at incrementally lower end-state pressures, mapping the release path in P–u_p space.

The release standards used in these experiments have been suitably characterized: quartz,[24,25] CH,[26] silica foam,[25,27] and liquid D_2 (Refs. 28 and 29). The diamond–D_2 IM data are particularly valuable to ensuring that the initial stages of an ICF implosion set the fuel on the correct adiabat for an optimal implosion.

The CH and liquid-D_2 Hugoniot fits used in this work were re-analyzed using new data for the standards used in those IM studies. The CH Hugoniot data from Barrios,[26] which used a quartz standard, were re-analyzed using the updated quartz Hugoniot and release model from Knudson and Desjarlais.[25] Similarly the liquid-D_2 Hugoniot data from Hicks,[28] which used an aluminum standard, were re-analyzed by Knudson *et al.* and presented in Ref. 29. The liquid-D_2 Hugoniot from the Hicks experiments was used in this analysis because both works were performed on the OMEGA laser and had the same initial densities to within 2.5%. Because the Hicks Hugoniot fit was determined for $\rho_0 = 0.174$ g/cm^3, the $U_s^{D_2}$ data plotted

here were normalized to that initial density using the corrective term $2.29\left(1-\rho_0 \big/ \rho_0^{\mathrm{Hicks}}\right)$. This offset was determined in Ref. 28 by comparing the effect of ρ_0 on the Hugoniots that were modeled using the stiffest and softest D_2 EOS tables; it affected this data set by only <0.2%.

Shock velocities in diamond and the standards were measured at the IM interface and are presented in Table 148.I. The shock velocity in diamond at the point of breakout into the standard was measured directly from the VISAR data in SCD and inferred from the nonsteady wave correction in NCD. The shock velocity in the standard was extrapolated backward across the glue layer to this same point. The extrapolation was done by linearly fitting to the measured shock velocity over a 150- to 500-ps time interval when the shock first entered the standard. *HYDRA* simulations for a different shock experiment involving a quartz/LiH interface with a 0-, 2-, and 4-μm-thick oil layer between them showed that extrapolating the shock velocity backward across the entire oil (or glue) layer (as opposed to midway) most accurately represented shock behavior at the interface when the two materials were in direct contact.[38] Only data with steady or smoothly decaying shocks over 150 ps on both sides of the interface were used in the release analysis.

NCD Data Analysis

EOS data obtained from impedance matching require accurate measurements of shock velocities and error propagation to provide high-confidence data. Modern VISAR systems can provide <1% velocity measurements in transparent samples,[36] yielding precise EOS data.[26] Opaque or translucent samples like NCD present a considerably different challenge. The methods used to obtain average shock velocities (i.e., transit times) and to correct those velocities for unsteadiness are described below.

1. Measurements of Shock Transit Times

Average shock velocities in the NCD samples were determined using the measured thicknesses and shock transit times presented in Table 148.II. VISAR and SOP were used to measure the times that the shock exited the quartz pusher (t_1) and the NCD (t_2). This defined the total time ($\Delta t_{\mathrm{total}} = t_2 - t_1$) that the shock spent in the NCD sample and the glue layer preceding it. The transit time across the NCD sample alone is calculated by

$$\Delta t_{\mathrm{NCD}} = \Delta t_{\mathrm{total}} - \Delta x_{\mathrm{glue}} \big/ U_s^{\mathrm{glue}},$$

where Δx_{glue} is the estimated glue thickness (described in **Measurements of Thickness**, below) and U_s^{glue} is the shock

velocity in the glue estimated using the *SESAME* 7603 table for epoxy and the known pressure and particle velocity at the quartz pusher/glue interface.

For targets with an uncovered NCD step, as shown in Fig. 148.1(a), shock breakout times were measured using the drop in the VISAR reflectivity across the step/vacuum interface seen in Fig. 148.1(b). The peak in the derivative of the reflectivity, denoting the steepest slope in the drop in signal, defined the shock breakout time. This method yielded the most-consistent and most-precise transit times since the peaks were measured to ~5 ps. For targets without the steps, breakout times were defined by the rapid change in thermal emission recorded by the SOP at the quartz pusher/glue/witness interface (t_1) and the NCD/glue/standard interface (t_2). The steepest slope of the SOP signal was used to define t_1 and t_2. An additional uncertainty up to 50 ps was applied to these measurements because the location of the peak defining t_1 or t_2 was not as consistent since it varied with the thickness of the glue layer. The SOP signal does not drop to zero at the glue (or liquid D_2) interface, as was observed in the VISAR reflectivity at the step/vacuum interface. As the shock approached the rear surface of the NCD sample, the VISAR reflectivity and the SOP signal increased exponentially because of reduced volumetric scattering. This contributed to the uncertainty in t_2 because the emission continuously increased across the NCD/glue/standard (or liquid D_2) interface.

2. Measurements of Thickness

The step heights of the NCD samples glued to the quartz pushers ($\Delta x_{\mathrm{total}}$) were measured using white-light interferometry with a Zygo NexView 3-D optical surface profiler. The average NCD step height was referenced to the quartz pusher in the areas where the breakout times were measured. The glue thicknesses were estimated by combining these measurements with the thickness profiles of the individual samples (Δx_{NCD}), measured using a dual confocal microscope. Glue layers were kept to ~1 μm and are defined by $\Delta x_{\mathrm{glue}} = \Delta x_{\mathrm{total}} - \Delta x_{\mathrm{NCD}}$. For some targets, Δx_{glue} was set to 0 μm because a negative glue thickness was inferred; the uncertainty always permitted a positive glue thickness. The average shock velocity in NCD alone was determined using $\left\langle U_s^{\mathrm{NCD}}\right\rangle = \left(\Delta x_{\mathrm{total}} - \Delta x_{\mathrm{glue}}\right) \big/ \Delta t_{\mathrm{NCD}}$.

3. Nonsteady Wave Correction

In laser-driven experiments, steady shocks are difficult to attain because of the expanding ablation plasma. A technique for correcting the average shock velocity to account for nonsteadiness was developed for use in laser-driven experiments.[34] For a large planar drive, the shock-velocity history in an opaque sample is related to and corrected by the observed history in

Table 148.II: NCD transit time data and Hugoniot data from impedance matching (IM) with a quartz standard. The shock transit times (Δt_{total}) and thicknesses (Δx_{total} and Δx_{NCD}), where "total" denotes the combined NCD sample and preceding glue layer, were used to determine the average shock velocity in NCD ($\langle U_s^{NCD}\rangle$). $\langle U_s^{NCD}\rangle$ was corrected using the method described in **Nonsteady Wave Correction** (p. 164) to determine $U_s^{NCD}(t_1)$ at the IM interface. The shock velocity in quartz $[U_s^Q(t_1)]$ and $U_s^{NCD}(t_1)$ were used in the IM analysis to determine the particle velocity (u_p^{NCD}), pressure (P^{NCD}), and density (ρ_{NCD}) on the NCD Hugoniot.

Shot	Δt_{total} (ns)	Δx_{total} (μm)	Δx_{NCD} (μm)	$\langle U_s^{NCD}\rangle$	$U_s^Q(t_1)$	$U_s^{NCD}(t_1)$	u_p^{NCD}	P^{NCD} (Mbar)	ρ^{NCD} (g/cm^3)
77001	2.035±0.020	64.24±0.44	63.29±0.45	31.10±0.36	29.54±0.09	31.25±0.36	17.62±0.13	18.50±0.17	7.71±0.17
77002	1.890±0.023	62.27±0.38	61.89±0.29	32.75±0.45	31.59±0.09	33.03±0.42	19.29±0.16	21.40±0.22	8.08±0.22
77004*	2.384±0.069	64.80±0.54	64.97±0.50	27.19±0.82	25.94±0.09	27.79±0.80	14.86±0.18	13.87±0.26	7.25±0.34
77005	2.082±0.020	63.03±0.31	62.69±0.28	30.10±0.33	30.17±0.09	31.26±0.31	18.25±0.13	19.17±0.16	8.07±0.17
77006*	2.051±0.063	64.19±0.23	63.31±0.50	30.89±0.96	29.27±0.09	31.20±0.96	17.36±0.23	18.19±0.36	7.61±0.41
77007	2.109±0.019	63.44±0.39	63.71±0.33	30.08±0.32	29.81±0.09	31.28±0.31	17.88±0.12	18.80±0.16	7.85±0.14
77861	2.263±0.021	63.06±0.43	62.61±0.30	27.67±0.31	27.44±0.09	28.89±0.29	16.11±0.11	15.63±0.13	7.60±0.14
77862	2.319±0.019	61.72±0.30	61.43±0.27	26.49±0.25	26.51±0.09	27.66±0.24	15.44±0.10	14.35±0.11	7.61±0.13
79048	2.704±0.011	62.18±0.41	62.14±0.27	22.97±0.17	23.57±0.17	24.52±0.17	13.29±0.16	10.95±0.15	7.34±0.12
79049	1.951±0.008	62.07±0.48	62.17±0.26	31.79±0.26	33.87±0.16	35.10±0.26	20.98±0.21	24.74±0.27	8.36±0.17
79051	2.502±0.011	62.65±0.58	63.00±0.25	25.04±0.25	26.06±0.16	27.57±0.24	15.02±0.16	13.92±0.17	7.39±0.14
79052	2.517±0.011	63.58±0.30	62.45±0.34	24.81±0.15	25.61±0.16	27.06±0.15	14.69±0.15	13.36±0.15	7.35±0.11
79054	2.481±0.011	61.31±0.73	61.83±0.28	24.70±0.30	26.80±0.16	27.15±0.30	15.82±0.17	14.43±0.18	8.06±0.21
79055	2.263±0.010	61.54±0.68	61.39±0.25	27.11±0.30	28.22±016	29.70±0.31	16.67±0.17	16.63±0.19	7.66±0.17
79056	2.315±0.008	65.17±0.66	62.45±0.30	26.98±0.26	28.02±0.16	29.52±0.28	16.51±0.17	16.38±0.18	7.63±0.16
79057	2.196±0.010	61.60±0.44	61.22±0.25	27.87±0.22	28.56±0.16	29.93±0.22	16.97±0.17	17.07±0.18	7.76±0.15
79058	2.142±0.015	62.72±0.36	62.87±0.25	29.28±0.26	31.00±0.16	32.42±0.25	18.81±0.18	20.49±0.21	8.01±0.16
79059	2.398±0.010	61.66±0.46	61.84±0.25	25.70±0.21	26.91±0.16	28.40±0.21	15.65±0.16	14.94±0.16	7.49±0.13
79060	2.571±0.015	61.89±0.32	62.16±0.42	24.07±0.18	25.49±0.16	26.77±0.21	14.64±0.17	13.16±0.13	7.42±0.16
21233 (EP)	1.917±0.011	61.95±0.41	61.40±0.33	32.03±0.26	33.95±0.16	35.29±0.25	21.04±0.22	24.94±0.28	8.32±0.17
21237 (EP)	2.079±0.010	63.02±0.48	62.63±0.26	30.12±0.25	31.82±0.16	33.41±0.25	19.37±0.19	21.75±0.23	8.00±0.15

*Shots 77004 and 77006, which used liquid D_2–filled targets, were not included in the NCD Hugoniot fit because of the large uncertainty in measuring Δt_{total} from the lack of step/vacuum interfaces and contractions of the glue layers in the cryogenic cell.

an adjacent transparent witness.[34] This requires that the EOS of the witness and witness be known.

The amplitudes and temporal spacing of perturbations originating at the laser drive and arriving at the shock fronts in NCD and the adjacent quartz witness depend on their relative equations of state. Deviations from $\langle U_s^{NCD} \rangle$ are correlated to the observed velocity profile in the witness by $\delta U_s^{NCD}(t - t_1) = G \delta U_s^Q[(t - t_1)/F]$, where G and F are linear scaling factors that describe the relative amplitude and time history, respectively, of the shock-velocity profiles; δU_s^Q is the deviation from the average shock velocity in the quartz witness over the time period $\Delta t_{NCD}/F$, which corresponds to the same set of temporal perturbations experienced by the NCD; F is determined by the relative sound speeds and Hugoniots in the two materials; and G is additionally affected by the Grüneisen parameters. The quartz Hugoniot and $\Gamma = \Gamma_{eff}(U_s)$ were taken from Ref. 25, and quartz sound speeds were determined from the derivatives of the release paths calculated using that construct. Since the intention of this work was to measure the NCD Hugoniot, an iterative process was used where initial estimates for the Hugoniot, Γ's, and sound speeds were taken from a tabular EOS (LEOS 9061) (Ref. 23). This EOS model was chosen because the high-pressure SCD Hugoniot data best agree with LEOS 9061 predictions. The NCD velocity histories for the entire data set were first determined using the correction with these initial estimates. Then, impedance matching was done using the measured U_s^Q and inferred U_s^{NCD} at the IM interface to produce a linear U_s–u_p relation in NCD. The process was repeated using the updated Hugoniot fit so that the NCD velocity profiles were iteratively corrected until the linear U_s–u_p relation converged. An example of an NCD velocity history determined using this method is shown by the black curve in Fig. 148.1(c).

Velocity extrapolation across the glue layer at the quartz/ NCD interface was treated differently to take advantage of the quartz witness. A continuous velocity profile was inferred across the glue layer at the quartz pusher/witness interface. Using this interpolation, the velocity profile in the witness beginning at the time the shock enters the NCD,

$$\left(t_1 + \Delta x_{glue}/U_s^{glue}\right),$$

was used in the nonsteady wave correction to determine F and G. With knowledge of F and G,

$$U_s^{NCD}(t) = \langle U_s^{NCD} \rangle + G \delta U_s^Q[(t - t_1)/F]$$

was used to calculate the NCD shock velocities at times t_1 and t_2 needed for impedance matching.

Results

1. Hugoniot Data

a. SCD: The SCD Hugoniot data are listed in Table 148.III and plotted in Fig. 148.3 with existing diamond data by Knudson *et al.*[8] and Hicks *et al.*[15] The Knudson *et al.* experiments primarily used full-density (3.515-g/cm³) microcrystalline diamond and were performed using magnetically driven flyer-plate techniques. The Hicks experiments and this work, both IM experiments carried out using the OMEGA laser, used $\langle 110 \rangle$-oriented SCD and a quartz standard. The existing data in Fig. 148.3 suggest that *SESAME* 7830 best models the Hugoniot across the coexistence region (6 to 10.5 Mbar) and beyond the melt (>10.5 Mbar). This work measured less compressibility, however, than *SESAME* 7830 above 15 Mbar; this stiffer behavior is predicted by a DFT-MD EOS model (LEOS 9061).[23]

The Hicks data plotted in Fig. 148.3 are not the same as presented in the original publication; the data were re-analyzed using the updated quartz Hugoniot and the same re-shock formulation presented here. For a given pressure, this re-analysis decreased the density by ~3%. For $P^C > 20$ Mbar (corresponding to $P^Q > 16$ Mbar at the IM point), the quartz Hugoniot fit used in impedance matching was extrapolated to higher pressures than given in the quartz data set.[24,25] If the extrapolation of the quartz Hugoniot is not valid at higher pressure, this could contribute to the apparent stiffening of the Hugoniot data that relied on a quartz standard.

b. NCD: The NCD Hugoniot was measured between 10 and 25 Mbar. The data are presented in Table 148.II and plotted in the U_s–u_p and P–ρ planes in Fig. 148.4. The Hugoniot curves derived from the EOS tables in Fig. 148.4 were modeled using the appropriate lower initial density $\left(\rho_0^{NCD} = 3.36 \text{ g}/\text{cm}^3\right)$. The NCD U_s–u_p Hugoniot data are approximately linear and were fit to $U_s = a_0 + a_1(u_p - \beta)$, where the coefficients and their standard deviations are listed in Table 148.IV. An orthogonally weighted least-squares linear fit was taken about the centroid of the data (β) so that the uncertainties in a_0 and a_1 are uncorrelated.[39] The standard deviation in the fit is given by[39]

$$\sigma_{U_s}(u_p) = \left[\sigma_{a_0}^2 + \sigma_{a_1}^2(u_p - \beta)^2\right]^{1/2}.$$

The NCD data are slightly stiffer than predictions using LEOS 9061 [Fig. 148.4(b)], which well-represented the SCD

Table 148.III: ⟨110⟩ SCD Hugoniot data from impedance matching with a quartz standard.

Shot	U_s^Q	U_s^{SCD}	P^{SC} (Mbar)	U_p^{SCD}	ρ^{SCD} (g/cm^3)
79050	27.54±0.16	28.47±0.10	16.00±0.16	15.98±0.16	8.02±0.11
79053	28.68±0.16	29.56±0.10	17.51±0.17	16.85±0.16	8.17±0.12
77848	32.94±0.11	33.84±0.06	23.79±0.19	20.00±0.16	8.59±0.10
77858	33.17±0.09	34.07±0.06	24.15±0.18	20.16±0.15	8.61±0.10
77860	33.77±0.10	34.24±0.06	24.92±0.20	20.70±0.17	8.89±0.12
77851	34.62±0.09	35.06±0.06	26.27±0.24	21.32±0.19	8.97±0.13
77856	34.82±0.09	35.29±0.07	26.62±0.25	21.46±0.20	8.97±0.14

E25540JR
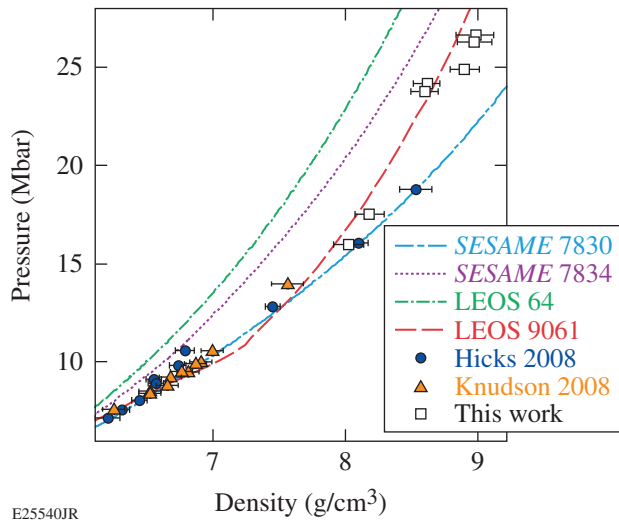
Figure 148.3
Full-density (ρ_0 = 3.515 g/cm^3) diamond Hugoniot data from this work (open squares), Knudson[8] (orange triangles), and Hicks[15] re-analyzed using the updated quartz equation of state (EOS)[25] (blue circles). The data are compared to Hugoniots modeled using diamond EOS tables.
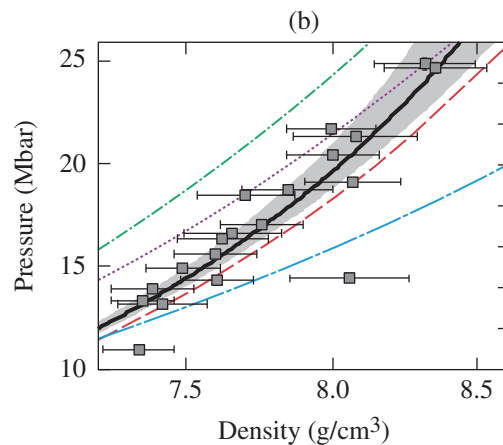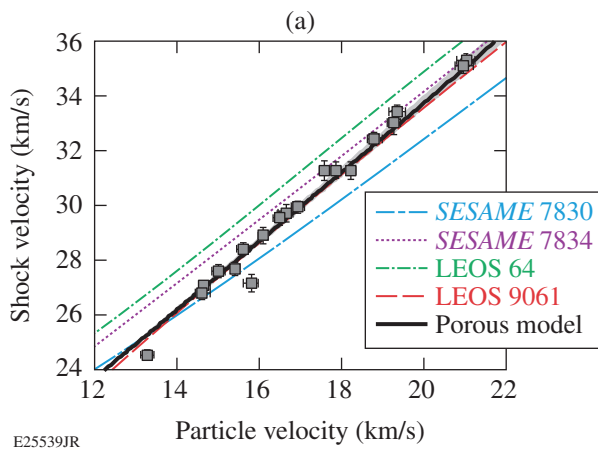

E25539JR

Figure 148.4
NCD (ρ_0 = 3.36 g/cm^3) Hugoniot data (gray squares) from impedance matching with a quartz standard. (a) The shock velocity versus particle velocity data and (b) the pressure versus density data are compared to Hugoniots modeled using diamond EOS tables and a porous model (solid black line) modeled using Eq. (6) with Γ = 1.03. The porous model using Γ = 1.03±0.1 is shown by the gray-shaded areas.

Table 148.IV: Coefficients and uncertainties to the orthogonally weighted least-squares fit to the NCD U_s–u_p data of the form $U_s = a_0 + a_1 (u_p - \beta)$.

a_0 (km/s)	a_1	β (km/s)	σ_{a_0}	σ_{a_1}
29.424	1.361	16.62	0.077	0.037

Hugoniot in the same pressure range (Fig. 148.3). NCD's lower initial density and reduced compressibility compared to SCD are consistent with that of a porous sample:

$$\left(m = \rho_0^{SCD} \Big/ \rho_0^{NCD} = 1.046 \right).$$

Porous samples exhibit stiffer and even "reverse" Hugoniots as a result of added entropy during the pore-collapse phase of compression.[22]

We find that NCD's Hugoniot can be described using a simple porosity model from McQueen[21] (black line in Fig. 148.4), given by

$$P_H^{NCD}(\rho) = P_H^{SCD}(\rho) \frac{1 - \dfrac{\Gamma}{2}\left(\dfrac{\rho}{\rho_0^{SCD}} - 1\right)}{1 - \dfrac{\Gamma}{2}\left(\dfrac{\rho}{\rho_0^{NCD}} - 1\right)}, \qquad (6)$$

where P_H^{SCD} is the SCD Hugoniot, $\rho_0^{SCD} = 3.515$ g/cm^3, $\rho_0^{NCD} = 3.36$ g/cm^3, and $\Gamma = 1.03$. This model is derived from the definition of the Grüneisen parameter, such that the Hugoniots of the porous and crystal-density materials are related through Γ. The reference Hugoniot $\left(P_H^{SCD}\right)$ was established by fitting the SCD U_s–u_p Hugoniot data in the same high-pressure fluid region (>11 Mbar) as where the NCD data were obtained. This orthogonally weighted linear fit is given by $U_s = (30.018 \pm 0.057) + (1.208 \pm 0.020) (u_p - 17.12)$. For simplicity, Γ was assumed to be constant and was optimized at 1.03. The range of the porous model using $\Gamma = 1.03 \pm 0.1$ is represented by the gray-shaded area in Fig. 148.4. $\Gamma \sim 1$ is ~20% higher than predicted by the DFT-MD model, which predicts $\Gamma \sim 0.8$ over the same density range as the data. This suggests that compared to the DFT-MD model, more energy goes into ΔP than other degrees of freedom for a given ΔE. This difference is related to the discrepancy between the DFT-MD Hugoniot (using ρ_0^{NCD}) and the NCD data despite agreement with the SCD Hugoniot data.

c. Error analysis: The values and errors in the Hugoniot data (Tables 148.II and 148.III) represent the mean and standard deviation of each parameter determined using a Monte Carlo error analysis with 10,000 runs for NCD and 100,000 runs for SCD. For each run, the observable parameters $\left(U_s^Q \text{ and } U_s^{SCD} \text{ for SCD, or } U_s^Q, \Delta x_{NCD}, \Delta x_{total}, \Delta t_{total}, \text{ and } \rho_0^{NCD} \text{ for NCD}\right)$ were varied within their error estimates. The cubic quartz U_s–u_p coefficients and Γ_{eff} used in impedance matching were varied once per run using the co-variance matrices listed in Ref. 25. For NCD, the nonsteady wave correction and impedance matching were done each time until convergence was met, yielding 10,000 possible sets of Hugoniot data. The total error bars in ρ^{NCD} are between 1.5% and 3%, with the dominating error caused by the uncertainty in target metrology and transit times.

2. Release Data

The diamond release data (Table 148.I) are plotted in Fig. 148.5 in terms of the observables, i.e., shock velocities on either side of the IM interface. The U_s^C and U_s^{Stan} data are shown for the release of diamond into liquid D$_2$, SiO$_2$ foam, CH, and quartz (the blue triangles, green diamonds, red squares, and orange circles, and respectively). The data are compared to the velocities predicted at the IM interface (lines) using the diamond EOS models. These lines were created using states on the diamond Hugoniot (abscissa) from which release paths were calculated. The intersections of release paths with the Hugoniot of the known standard provided the final states (ordinate).

The SCD release data in Fig. 148.5(a) show that _SESAME_ 7830 (black lines) and LEOS 9061 (colored lines) are best for modeling the overall behavior of the diamond release at the pressures where their respective Hugoniots are most valid, i.e., _SESAME_ 7830 below $U_s^C < 28$ km/s and LEOS 9061 above that velocity. The SCD data with $U_s^C < 24.4$ km/s, which corresponds to the completion of melt along the Hugoniot,[7] should be in the coexistence region upon release. The data do not deviate from the _SESAME_ 7830 predictions, which do not include strength effects, indicating that strength does not play a significant role in the release from >8 Mbar. Shock-wave splitting into an elastic precursor and an inelastic wave should not occur until U_s^C decays below ~22.3 km/s in the $\langle 110 \rangle$ SCD and ~21.6 km/s in polycrystalline diamond,[16] and therefore should not affect the SCD or NCD data sets.

For the NCD [Fig. 148.5(b)], the data are well represented using a Mie–Grüneisen release model referencing the porous Hugoniot shown in Fig. 148.4 with a constant $\Gamma = 1.03$ along the
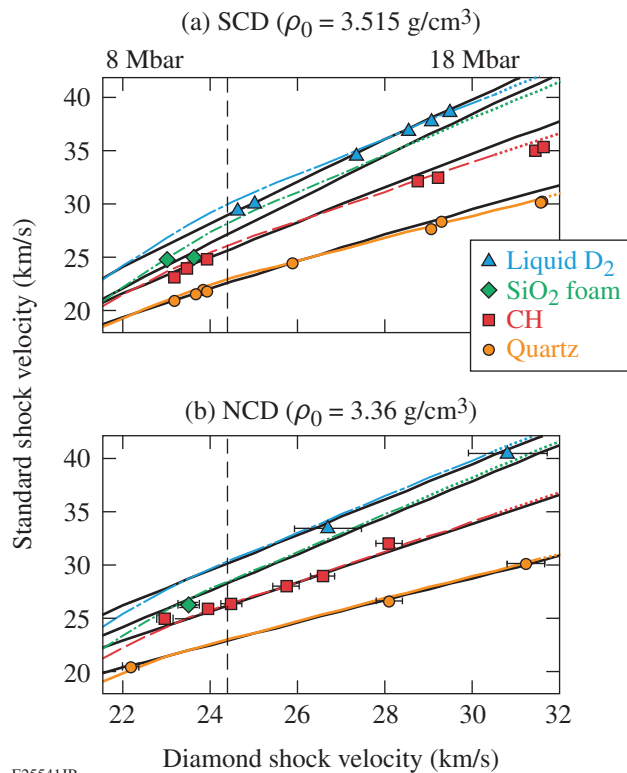
Figure 148.5

(a) SCD and (b) NCD release data compared to predictions using diamond EOS models and existing Hugoniot fits for the standards. Data points are shock velocities for diamond releasing into liquid D_2 (blue triangles), SiO_2 foam (green diamonds), CH (red squares), and quartz (orange circles). Predicted $U_s^C - U_s^{Stan}$ relationships using LEOS 9061 (colored lines) to model the diamond Hugoniot and release paths and existing Hugoniot fits for the standards: liquid D_2 (Refs. 28 ad 29) (dashed–dotted blue line), SiO_2 foam[27] (dashed–dotted green line), CH (Ref. 26) (dashed red line), and quartz[24,25] (solid orange line). Dotted portions of lines indicate that an extrapolation of the Hugoniot fit outside the standard's data range was used. The black lines in (a) are predicted $U_s^C - U_s^{Stan}$ relationships using *SESAME* 7830 to model the diamond Hugoniot and release paths. The black lines in (b) are predicted $U_s^C - U_s^{Stan}$ relationships using a Mie–Grüneisen model for the diamond Hugoniot and release paths with the same $\Gamma = 1.03$. The dashed vertical lines in (a) and (b) indicate the completion of melt on the diamond Hugoniot at 24.4($\pm$0.4) km/s (Ref. 7). For data to the left of the line, diamond released from the coexistence region. For data to the right of the line, diamond released from the liquid phase.

release path (black lines). This is consistent with the $\Gamma = 1.03$ used in the porous model that fits the Hugoniot data. LEOS 9061 (colored lines) is also adequate for predicting the release data, despite a slight 1% to 2% offset in inferred density for a given pressure on the initial Hugoniot state. The NCD data in the range $24 < U_s^{NCD} < 32$ km/s (~12 < P^{NCD} < ~20 Mbar) release from an initial state where LEOS 9061 is within the error of the NCD Hugoniot measurements. While LEOS 9061

does not fully capture the NCD Hugoniot, it does represent the release data. This indicates that LEOS 9061 correctly models the NCD ablator's release into surrogate liquid D_2 fuel when the experimental liquid D_2 Hugoniot (Hicks[28] re-analyzed by Knudson[29]) is used. For comparison, the Kerley deuterium model[40] predicts faster shock velocities at the IM interface than the Hicks Hugoniot fit.

The NCD was most likely shocked into the liquid phase at the front NCD surface where the Hugoniot was measured. In the shots to the left of the melt line in Fig. 148.5(b), the shock decayed sufficiently enough during its transit that the NCD was at least partially solid upon release at its rear surface. This was apparent from the VISAR data of the unobstructed NCD step, which showed finite reflectivity at the NCD free surface after shock breakout, indicating a solid rather than a liquid state. The U_s^{Stan} data still follow the LEOS 9061 predictions, whereas when SCD released from the solid phase, the U_s^{Stan} data were slower than the LEOS 9061 predictions. Thermal effects from NCD's porosity could be contributing to the different response when NCD releases from the coexistence region.

Conclusions

The Hugoniot and release behavior of diamond were measured at multimegabar pressures and the Grüneisen parameter for high-pressure fluid carbon was extracted from the experimental data sets. These measurements are important to constrain models used in planetary astrophysics and to design ICF targets with NCD ablators. The SCD Hugoniot above 15 Mbar agrees with DFT-MD calculations (LEOS 9061) in liquid carbon. NCD's response to shock compression is slightly stiffer than that of SCD and the DFT-MD predictions, even when taking into account its lower initial density. This behavior can be described using a standard porosity model,[21] indicating that thermal effects from the initial pore collapse affect NCD's high-pressure Hugoniot. This effect must be included when using the EOS tables to model NCD. The stiffer NCD response compared to the DFT-MD EOS model (LEOS 9061) has implications for ICF target designs because additional heating raises the adiabat of the implosion. A Grüneisen parameter of ~1 in the liquid phase (11 to 26 Mbar) was derived from the experimental NCD and SCD Hugoniot fits. This value is consistent with a Mie–Grüneisen EOS that accurately models the NCD release data.

We measured two data points of NCD releasing into liquid D_2 and six SCD/liquid D_2 data points, which are especially valuable for constraining ICF models that describe the NCD ablator release into the hydrogen fuel.[41,42] The diamond–liquid

D_2 IM data can be reproduced when using the appropriate diamond EOS model (*SESAME* 7830 or LEOS 9061 based on the diamond type and U_s^C) and the experimental liquid D_2 Hugoniot.[28,29] Overall, the release response of both types of diamond are adequately modeled using existing EOS tables, which do not include strength effects. Strength may affect the diamond release behavior at lower pressure when the elastic precursor is separated from the main shock wave. Some difference in behavior exists between SCD and NCD when releasing from the coexistence region. Thermal effects from NCD's porosity could be the source of this difference.

ACKNOWLEDGMENT

REFERENCES

1. M. Ross, Nature **292**, 435 (1981).

2. N. Madhusudhan, K. K. M. Lee, and O. Mousis, Astrophys. J. Lett. **759**, L40 (2012).

3. H. M. Van Horn, *Unlocking the Secrets of White Dwarf Stars* (Springer International Publishing, Switzerland, 2015).

4. T. S. Metcalfe, M. H. Montgomery, and A. Kanaan, Astrophys. J. **605**, L133 (2004).

5. F. Ancilotto *et al.*, Science **275**, 1288 (1997).

6. T. Guillot, Annu. Rev. Earth Planet. Sci. **33**, 493 (2005).

7. J. H. Eggert, D. G. Hicks, P. M. Celliers, D. K. Bradley, R. S. McWilliams, R. Jeanloz, J. E. Miller, T. R. Boehly, and G. W. Collins, Nat. Phys. **6**, 40 (2010).

8. M. D. Knudson, M. P. Desjarlais, and D. H. Dolan, Science **322**, 1822 (2008).

9. A. A. Correa *et al.*, Phys. Rev. B **78**, 024101 (2008).

10. A. J. MacKinnon, N. B. Meezan, J. S. Ross, S. Le Pape, L. Berzak Hopkins, L. Divol, D. Ho, J. Milovich, A. Pak, J. Ralph, T. Döppner, P. K. Patel, C. Thomas, R. Tommasini, S. Haan, A. G. MacPhee, J. McNaney, J. Caggiano, R. Hatarik, R. Bionta, T. Ma, B. Spears, J. R. Rygg, L. R. Benedetti, R. P. J. Town, D. K. Bradley, E. L. Dewald, D. Fittinghoff, O. S. Jones, H. R. Robey, J. D. Moody, S. Khan, D. A. Callahan, A. Hamza, J. Biener, P. M. Celliers, D. G. Braun, D. J. Erskine, S. T. Prisbrey, R. J. Wallace, B. Kozioziemski, R. Dylla-Spears, J. Sater, G. Collins, E. Storm, W. Hsing, O. Landen, J. L. Atherton, J. D. Lindl, M. J. Edwards, J. A. Frenje, M. Gatu-Johnson, C. K. Li, R. Petrasso, H. Rinderknecht, M. Rosenberg, F. H. Séguin, A. Zylstra, J. P. Knauer, G. Grim, N. Guler, F. Merrill, R. Olson, G. A. Kyrala, J. D. Kilkenny, A. Nikroo, K. Moreno, D. E. Hoover, C. Wild, and E. Werner, Phys. Plasmas **21**, 056318 (2014).

11. J. Biener, D. D. Ho, C. Wild, E. Woerner, M. M. Biener, B. S. El-dasher, D. G. Hicks, J. H. Eggert, P. M. Celliers, G. W. Collins, and N. E. Teslich, Jr., Nucl. Fusion **49**, 112001 (2009).

12. C. Dawedeit *et al.*, Diam. Relat. Mater. **40**, 75 (2013).

13. H. Nagao *et al.*, Phys. Plasmas **13**, 052705 (2006).

14. S. Brygoo *et al.*, Nature Materials **6**, 274 (2007).

15. D. G. Hicks, T. R. Boehly, P. M. Celliers, D. K. Bradley, J. H. Eggert, R. S. McWilliams, R. Jeanloz, and G. W. Collins, Phys. Rev. B **78**, 174102 (2008).

16. R. S. McWilliams, J. H. Eggert, D. G. Hicks, D. K. Bradley, P. M. Celliers, D. K. Spaulding, T. R. Boehly, G. W. Collins, and R. Jeanloz, Phys. Rev. B **81**, 014111 (2010).

17. K. Kondo and T. J. Ahrens, Geophys. Res. Lett. **10**, 281 (1983).

18. M. N. Pavlovskii, Sov. Phys.-Solid State **13**, 741 (1971).

19. R. F. Smith, J. H. Eggert, R. Jeanloz, T. S. Duffy, D. G. Braun, J. R. Patterson, R. E. Rudd, J. Biener, A. E. Lazicki, A. V. Hamza, J. Wang, T. Braun, L. X. Benedict, P. M. Celliers, and G. W. Collins, Nature **511**, 330 (2014).

20. D. K. Bradley, J. H. Eggert, R. F. Smith, S. T. Prisbrey, D. G. Hicks, D. G. Braun, J. Biener, A. V. Hamza, R. E. Rudd, and G. W. Collins, Phys. Rev. Lett. **102**, 075503 (2009).

21. R. G. McQueen *et al.*, in *High-Velocity Impact Phenomena*, edited by R. Kinslow (Academic Press, New York, 1970).

22. Ya. B. Zel'dovich and Yu. P. Raĭzer, in *Physics of Shock Waves and High-Temperature Hydrodynamic Phenomena*, edited by W. D. Hayes and R. F. Probstein (Academic Press, New York, 1966).

23. L. X. Benedict *et al.*, Phys. Rev. B **89**, 224109 (2014).

24. M. D. Knudson and M. P. Desjarlais, Phys. Rev. Lett. **103**, 225501 (2009).

25. M. D. Knudson and M. P. Desjarlais, Phys. Rev. B **88**, 184107 (2013).

26. M. A. Barrios, D. G. Hicks, T. R. Boehly, D. E. Fratanduono, J. H. Eggert, P. M. Celliers, G. W. Collins, and D. D. Meyerhofer, Phys. Plasmas **17**, 056307 (2010).

27. M. D. Knudson and R. W. Lemke, J. Appl. Phys. **114**, 053510 (2013).

28. D. G. Hicks, T. R. Boehly, P. M. Celliers, J. H. Eggert, S. J. Moon, D. D. Meyerhofer, and G. W. Collins, Phys. Rev. B **79**, 014112 (2009).

29. M. D. Knudson, M. P. Desjarlais, and A. Pribram-Jones, Phys. Rev. B **91**, 224105 (2015).

30. T. R. Boehly, D. L. Brown, R. S. Craxton, R. L. Keck, J. P. Knauer, J. H. Kelly, T. J. Kessler, S. A. Kumpan, S. J. Loucks, S. A. Letzring, F. J. Marshall, R. L. McCrory, S. F. B. Morse, W. Seka, J. M. Soures, and C. P. Verdon, Opt. Commun. **133**, 495 (1997).

31. S. Skupsky, R. W. Short, T. Kessler, R. S. Craxton, S. Letzring, and J. M. Soures, J. Appl. Phys. **66**, 3456 (1989).

32. Y. Lin, T. J. Kessler, and G. N. Lawrence, Opt. Lett. **20**, 764 (1995).

33. E. I. Moses *et al*., Phys. Plasmas **16**, 041006 (2009).

34. D. E. Fratanduono, D. H. Munro, P. M. Celliers, and G. W. Collins, J. Appl. Phys. **116**, 033517 (2014).

35. P. C. Souers, *Hydrogen Properties for Fusion Energy* (University of California Press, Berkeley, CA, 1986).

36. P. M. Celliers, D. K. Bradley, G. W. Collins, D. G. Hicks, T. R. Boehly, and W. J. Armstrong, Rev. Sci. Instrum. **75**, 4916 (2004).

37. M. C. Gregor, R. Boni, A. Sorce, J. Kendrick, C. A. McCoy, D. N. Polsin, T. R. Boehly, P. M. Celliers, G. W. Collins, D. E. Fratanduono, J. H. Eggert, and M. Millot, Rev. Sci. Instrum. **87**, 114903 (2016).

38. A. Lazicki, R. A. London, F. Coppari, D. Erskine, J. Hawreliak, D. Fratanduono, P. Celliers, J. Eggert, M. Millot, D. Swift, G. Collins, M. Morales, K. Capersen, S. Kucheyev, H. Whitley, J. Caster, and J. Nilsen, "Shock Equation of State of LiH to 1100 GPa," submitted to Physical Review E.

39. P. M. Celliers, G. W. Collins, D. G. Hicks, and J. H. Eggert, J. Appl. Phys. **98**, 113529 (2005).

40. G. I. Kerley, Sandia National Laboratory, Albuquerque, NM, Report SAND2003-3613 (2003).

41. H. F. Robey, T. R. Boehly, P. M. Celliers, J. H. Eggert, D. Hicks, R. F. Smith, R. Collins, M. W. Bowers, K. G. Krauter, P. S. Datte, D. H. Munro, J. L. Milovich, O. S. Jones, P. A. Michel, C. A. Thomas, R. E. Olson, S. Pollaine, R. P. J. Town, S. Haan, D. Callahan, D. Clark, J. Edwards, J. L. Kline, S. Dixit, M. B. Schneider, E. L. Dewald, K. Widmann, J. D. Moody, T. Döppner, H. B. Radousky, A. Throop, D. Kalantar, P. DiNicola, A. Nikroo, J. J. Kroll, A. V. Hamza, J. B. Horner, S. D. Bhandarkar, E. Dzenitis, E. Alger, E. Giraldez, C. Castro, K. Moreno, C. Haynam, K. N. LaFortune, C. Widmayer, M. Shaw, K. Jancaitis, T. Parham, D. M. Holungal, C. F. Walters, B. Haid, E. R. Mapoles, J. Sater, C. R. Gibson, T. Malsbury, J. Fair, D. Trummer, K. R. Coffee, B. Burr, L. V. Berzins, C. Choate, S. J. Brereton, S. Azevedo, H. Chandrasekaran, D. C. Eder, N. D. Masters, A. C. Fisher, P. A. Sterne, B. K. Young, O. L. Landen, B. M. Van Wonterghem, B. J. MacGowan, J. Atherton, J. D. Lindl, D. D. Meyerhofer, and E. Moses, Phys. Plasmas **19**, 042706 (2012).

42. S. Hamel, L. X. Benedict, P. M. Celliers, M. A. Barrios, T. R. Boehly, G. W. Collins, T. Döppner, J. H. Eggert, D. R. Farley, D. G. Hicks, J. L. Kline, A. Lazicki, S. LePape, A. J. Mackinnon, J. D. Moody, H. F. Robey, E. Schwegler, and P. A. Sterne, Phys. Rev. B **86**, 094113 (2012).

The National Direct-Drive Program on OMEGA and at the National Ignition Facility

Introduction

The main approach to ignition by means of laser-driven inertial confinement fusion (ICF)[1] currently pursued at the National Ignition Facility (NIF)[2] is x-ray (or indirect) drive (ID), where the laser energy absorbed in a high-Z hohlraum is re-emitted in the form of x rays that drive the fuel capsule. In the other mainline ICF laser approach, direct drive (DD),[3] the target is driven by laser irradiation directly coupled to the plasma ablated from the imploding capsule. The main advantage of ID is reduced sensitivity of implosions to short-scale beam nonuniformities. The main advantage of DD is higher coupling efficiency (by a factor of 3 to 5) of the laser energy into kinetic energy of the shell (hydrodynamic efficiency) compared to that of ID. The OMEGA Laser System[4] and the KrF laser NIKE at the Naval Research laboratory (NRL)[5] have been the principal facilities for DD experiments in the U.S. When the decision to pursue ID as the main ICF approach was made by the U.S. ICF program back in 1976, single-beam laser quality was a major concern for achieving high compression in DD implosions without the shell breaking apart from the Rayleigh–Taylor (RT) instability[1] seeded by laser imprint. Early challenges in improving beam uniformity have been resolved over the last several decades by introducing several beam-smoothing techniques. These include distributed phase plates (DPP's),[6] polarization smoothing with birefringent wedges,[7] and smoothing by spectral dispersion (SSD).[8] In addition, implementing adiabat-shaping techniques[9,10] significantly reduced the impact of RT instability growth during shell acceleration. Also, imprint reduction was demonstrated by using mid-Z–doped ablators[11] and high-Z target overcoats.[12] Such progress along with the challenges in achieving ignition on the NIF using ID[13] suggests considering direct drive as a viable alternative for developing a burning-plasma platform in a laboratory. In addition to the conventional "hot-spot" ignition designs, several alternative direct-drive–ignition schemes have been proposed in the past. Shock ignition,[14] the most-promising approach, is currently being considered as an alternative symmetric direct-drive–ignition design for the NIF.

Compared to x-ray drive, direct-drive targets couple a larger fraction of laser energy into shell kinetic energy and internal energy of the neutron-producing central region of the target (hot spot) at peak fuel compression. This relaxes the requirement on shell convergence and hot-spot pressure in an igniting target. The ignition condition follows from Lawson criterion,[15,16] which can be written in a form commonly used in the ICF community as[1]

$$(\rho R)_{\text{hs}} \times T \gtrsim 0.3 \; \text{g}\big/\text{cm}^3 \times 5 \; \text{keV}, \tag{1}$$

where ρ, R_{hs}, and T are the hot-spot density, radius, and ion temperature, respectively. The requirement shown in Eq. (1) is intuitively simple: the hot-spot temperature must be ~5 keV for PdV work of the incoming shell to overcome radiation losses and have an alpha-particle production rate sufficient to create bootstrap heating; an areal density of ~0.3 g/cm^2 is required to stop alpha particles inside the hot spot at these temperatures. A product of these two quantities enters into the ignition condition since ignition at lower temperatures and higher areal densities is still possible because the cold shell becomes more opaque to radiation at higher shell areal densities (assuming that larger hot-spot areal density leads to larger shell areal densities), limiting radiation losses from the hot spot.[16] Substituting expressions for the pressure $p_{\text{hs}} = (1 + Z)\rho T/m_{\text{i}}$ (Z is the average ion charge and m_{i} is the average ion mass) and internal energy $E_{\text{hs}} = 3/2 \, p_{\text{hs}} V_{\text{hs}}$ (V_{hs} is the neutron-averaged hot-spot volume) into Eq. (1) gives a minimum pressure requirement (threshold) for ignition:

$$p_{\text{hs}} > p_{\text{thr}} \equiv 250 \; \text{Gbar} \left(\frac{E_{\text{hs}}}{10 \; \text{kJ}} \right)^{-1/2},$$

$$\text{or} \tag{2}$$

$$\overline{P} \equiv \frac{p_{\text{hs}}}{p_{\text{thr}}} = \left(\frac{p_{\text{hs}}}{250 \; \text{Gbar}} \right) \sqrt{\frac{E_{\text{hs}}}{10 \; \text{kJ}}} > 1,$$

where $\overline{P}$ is the ignition pressure parameter. Equation (2) also sets the limit on the hot-spot volume in an igniting target:

$$V_{hs} < V_{40}\left(\frac{E_{hs}}{10 \text{ kJ}}\right)^{3/2}, \text{ or max } (R_{hs}) \sim \sqrt{E_{hs}}, \quad (3)$$

where $V_{40} = 4\pi/3 \, (40 \, \mu\text{m})^3$ is the volume of a 40-μm sphere. Figure 148.6 plots the alpha-amplification factor ($Y_\alpha/Y_{no \, \alpha} - 1$, where Y_α and $Y_{no \, \alpha}$ are the target yields with and without alpha-particle deposition and fuel heating, respectively) as a function of ignition pressure parameter $\overline{P}$. The plot is obtained using 1-D *LILAC*[17] simulations of cryogenic targets at different laser drive energies (from OMEGA- to the NIF-scale designs). The solid line in the figure shows a fit to the simulation results at $\overline{P} < 1$, $\delta Y/Y = \overline{P} \exp(1.7 \overline{P}^{2/3})$. $\overline{P} \sim 1$ defines the ignition threshold. When $\overline{P} > 1$ and the fuel areal density at peak compression is large enough [$(\rho R)_{fuel} > 1 \text{ g/cm}^2$] to burn a significant fraction of the main fuel, the target gain greatly exceeds unity ($G > 10$). In simulations where the main fuel areal density is low, the shell burnup fraction is not significant and the yield amplification continues to follow the fit even for $\overline{P} > 1$.

Spherically symmetric DD cryogenic designs on OMEGA presently couple up to 0.44 kJ (out of 26-kJ incident laser energy) into the hot-spot internal energy.[18] When hydro-dynamically scaled to the NIF-size laser energy (1.5 MJ to

$$\text{Ignition parameter } \overline{P} = (p_{hs}/250 \text{ Gbar})\sqrt{E_{hs}/10 \text{ kJ}}$$

TC12864JR

Figure 148.6
Alpha-amplification factor $\delta Y/Y$ as function of the ignition pressure parameter $\overline{P}$. The points represent the results of 1-D *LILAC* simulations of designs at different laser energies in the range of OMEGA to National Ignition Facility (NIF) scale. The solid line shows a fit to the simulation results at $\overline{P} < 1$, $\delta Y/Y = \overline{P}\exp(1.7 \overline{P}^{2/3})$.

1.8 MJ), these designs are predicted to couple 5× to 10× more energy into the hot spot [25 kJ to 40 kJ for DD designs, depending on the laser-coupling efficiency] compared to that of ID (4 kJ to 5 kJ is inferred in the current best-performing ID implosions on the NIF), resulting in 2.5× to 3× lower hot-spot pressures required for DD ignition. The hot-spot size also gets larger with E_{hs} [see Eq. (3)], leading to smaller shell convergence ratio (CR ~ 22 compared to 35 to 40 in the ID ignition designs) and resulting in less-demanding long-wavelength drive-uniformity requirements.

With the goal of a successful ignition demonstration using direct drive, the recently established national DD strategy has several elements and involves the following facilities and institutions: Omega (a leading facility for DD research); NRL [which leads the effort on laser imprint reduction and plays a major role in the mitigation of coupling losses caused by laser–plasma interaction (LPI)]; Lawrence Livermore National Laboratory (which recently established a DD working group concentrating its effort on understanding LPI at ignition-relevant scales, developing DD target designs with yields in the range from 100 kJ to a few MJ, and developing 3-D computational capability for DD applications); and Los Alamos National Laboratory (which leads the effort in simulating high-*Z* overcoats, experimental study of long-wavelength drive asymmetry, and developing platforms to study material properties in the warm-dense-matter regime). The elements of DD strategy include experimentally demonstrating on OMEGA the hot-spot conditions ($p_{hs} > 100$ Gbar) relevant for ignition at MJ-scale laser energies available on the NIF and developing an understanding of LPI and laser coupling using DD experiments on the NIF in the current indirect-drive configuration.

OMEGA Cryogenic Implosions
The target performance depends on both the drive and uniformity conditions. We begin this section with a discussion on the one-dimensional (1-D) physics.

1. One-Dimensional Physics
To emphasize the importance of drive conditions in designing ignition targets, the 1-D scaling laws (which exclude multidimensional effects) for peak pressure and hot-spot energy are written in terms of implosion parameters: implosion velocity v_{imp} (the peak mass-averaged shell velocity), peak drive (ablation) pressure p_{abl}, adiabat α of the unablated fuel mass (ratio of the shell pressure to Fermi pressure at shell density), and peak in shell kinetic energy E_{kin} (Ref. 19):
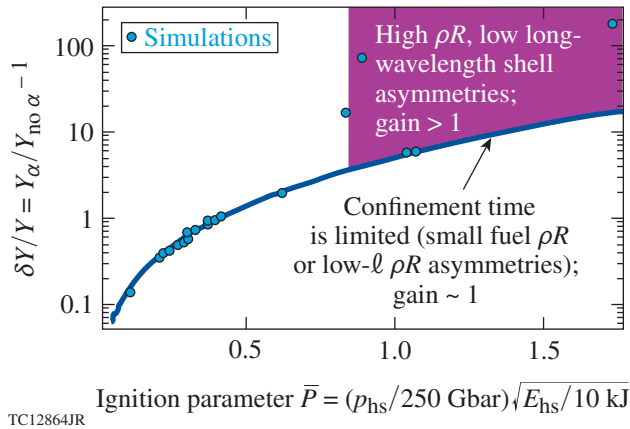
$$p_{hs}^{1\text{-}D} \sim \frac{p_{abl}^{1/3} v_{imp}^{10/3}}{\alpha},$$

$$E_{hs}^{1\text{-}D} \sim E_{kin} \frac{v_{imp}^{4/3}}{\alpha^{2/5} p_{abl}^{4/15}},$$

$$\overline{P}_{1\text{-}D} \sim \frac{\sqrt{E_{kin}} v_{imp}^4 p_{abl}^{1/5}}{\alpha^{6/5}}. \tag{4}$$

Modeling these critical implosion parameters must be experimentally validated before an assessment of the importance of multidimensional effects on the target performance can be made. The implosion velocity and shell kinetic energy are inferred in an experiment by measuring ablation-front trajectory and mass ablation rate using self-emission imaging.[20] The ablation pressure is inferred from simulations that match the measured ablation-front trajectory, mass ablation rate, bang time,[21] and scattered-light power and spectrum.[19,22] Finally, the shock-induced adiabat is inferred by measuring shock velocities early in the pulse using the velocity interferometer system for any reflector (VISAR).[23] An additional increase in the fuel adiabat caused by hot-electron preheat is estimated by measuring the hard x-ray signal[24] and areal density[25,26] in mid- to high-adiabat implosions (the areal density in 1-D, for a given laser energy, depends mainly on shell adiabat,[27] $\rho R \sim \alpha^{-0.5}$). A detailed comparison of 1-D simulation results using *LILAC* with the data shows good agreement between the two for a variety of target designs and drive conditions.[19] One-dimensional simulations include a nonlocal thermal-transport model,[28] a ray-based cross-beam energy transfer (CBET) model[29] (see discussion on CBET in **Laser Coupling and CBET**, p. 177), and first-principles equation-of-state (FPEOS) models[30] for both the DT ice and CD ablator.

2. Multidimensional Effects

The stability properties of indirect- and direct-drive designs are different. In direct drive, a thin CH layer is ablated from the shell early in the pulse to take advantage of the higher hydrodynamic efficiency of DT.[19] Since the shell consists mainly of DT during acceleration, the fuel adiabat α [which enters into the ignition scaling laws shown in Eqs. (4)] and the average in-flight shell adiabat α_{shell} (which determines shell stability property) are approximately equal, $\alpha \sim \alpha_{shell}$ ($\alpha_{shell} \gtrsim \alpha$ in adiabat-shaped designs[10]). Then, the shell's in-flight aspect ratio (IFAR, defined as ratio of the target radius to the shell thickness) can be written as[31]

$$\text{IFAR}_{DD} \sim \frac{v_{imp}^2}{\left(p_{abl}^{2/5} \alpha_{shell}^{3/5}\right)} \sim \frac{v_{imp}^2}{\left(p_{abl}^{2/5} \alpha^{3/5}\right)}. \tag{5}$$

While the in-flight shell adiabat in DD designs is determined primarily by the strength of initial shocks (the radiation preheat in DD cryogenic implosions raises the fuel adiabat by ~20%), the shell adiabat and IFAR in ID designs are determined mainly by the radiation transport, ablator opacity, and x-ray drive spectrum (the majority of shell mass during acceleration in indirect drive consists of the ablator material; ablator and main fuel masses become approximately equal at the end of acceleration). As a result,

$$\text{IFAR}_{ID} \sim \frac{v_{imp}^2}{\left(p_{abl}^{2/5} \alpha_{shell}^{3/5}\right)}. \tag{6}$$

Note that even though IFAR and the ablation-front RT growth in ID are determined by the x-ray heating of the ablator and not by the strength of initial shocks, the initial condition for RT instability is set during the shock propagation through the shell early in the drive, the so-called Richtmyer–Meshkov (RM) phase of perturbation evolution.[32] Therefore, the difference in the stability properties of indirectly driven shells for $\alpha = 1.4$ and "high-foot" $\alpha = 2.5$ designs[13] is caused mainly by differences in nonuniformity growth during the RM phase.[33]

Substituting Eq. (5) into Eq. (4) gives the following hot-spot scaling laws for DD implosions:

$$p_{hs}^{1\text{-}D} \sim p_{abl}\text{IFAR}^{5/3},$$

$$V_{hs}^{1\text{-}D} \sim \frac{E_{kin}}{p_{abl}\text{IFAR}},$$

$$E_{hs}^{1\text{-}D} \sim E_{kin}\text{IFAR}^{2/3},$$

$$\overline{P}_{1\text{-}D} \sim p_{abl}\sqrt{E_{kin}}\text{IFAR}^2. \tag{7}$$

Equations (7) shows that the hot-spot pressure and the ignition pressure parameter $\overline{P}$ can be increased in 1-D mainly by raising the shell IFAR (by reducing the shell mass, for example) and by making the laser drive more efficient (by increasing the ablation pressure and shell kinetic energy). The maximum value of IFAR in a design is set by the target stability properties and the level of nonuniformity seeds: the short-scale modes (which

satisfy $k\Delta < 1$, where k is the perturbation wave number and Δ is the in-flight shell thickness) disrupt the shell during the implosion if IFAR is too large [current cryogenic implosions on OMEGA are unstable if IFAR > 20 $(\alpha/3)^{1.1}$ (Ref. 19)]. The long-wavelength perturbations ($k\Delta > 1$) seeded by the laser power imbalance, laser mispointing, and target misalignment can prevent the hot spot from reaching the 1-D stagnation pressures if the RT instability and Bell–Plesset (BP)[1] nonuniformity growth are excessively large during deceleration. The design IFAR can be increased, nevertheless, if (1) the short-scale nonuniformities seeded by target imperfections and imprint are reduced and (2) the source of the long-wavelength perturbations (beam imbalance, target offset, and beam mispointing) is minimized.

3. Target Performance

Figure 148.7 shows the scaled ignition pressure parameter $\overline{P}$ inferred in OMEGA cryogenic implosions. Since v_{imp}, p_{abl}, and α are invariants with respect to laser energy E_L and E_{kin} is proportional to E_L (assuming constant laser-coupling efficiency for different E_L), $\overline{P}$ scales as $\sqrt{E_{\mathrm{kin}}}$ [see Eq. (2)]. Therefore, extrapolating the OMEGA results to the NIF-scale laser energy leads to $\overline{P}_{\mathrm{scaled}} = \overline{P}_{\mathrm{OMEGA}} \left(E_L^{\mathrm{NIF}} / E_L^{\mathrm{OMEGA}} \right)^{1/2}$.

The latter quantity is plotted in Fig. 148.7 for OMEGA cryogenic implosions driven at different values of the fuel adiabat (calculated using *LILAC* simulations). The hot-spot pressure and
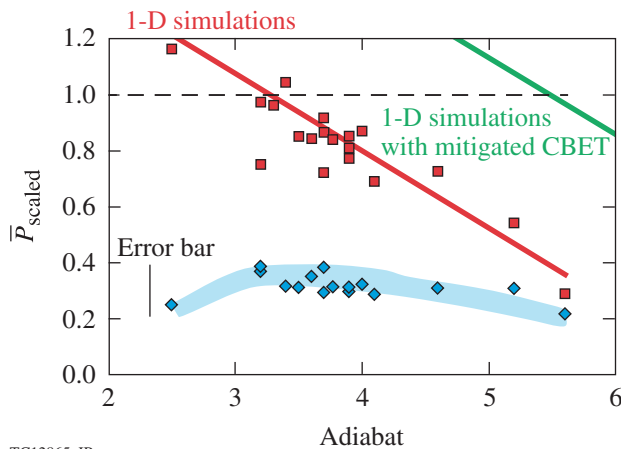

TC12865cJR

Figure 148.7
Ignition pressure parameter scaled to 1.8-MJ laser energy. Diamonds represent values inferred from the experimental data, squares show the 1-D simulation results with the full cross-beam energy transfer (CBET) effect, and the solid green line represents a linear fit through simulations with CBET fully mitigated. The short vertical line shows a typical error bar for the inferred values of $\overline{P}$. To ignite, $\overline{P}_{\mathrm{scaled}}$ in a design must exceed unity (dashed line).

internal energy are inferred[18,34] by using the measured neutron yield, the burn duration Δt_{burn} (Ref. 21), the neutron-averaged ion temperature $\langle T_i \rangle_n$, and the hot-spot size. Diamonds represent the experimentally inferred $\overline{P}_{\mathrm{scaled}}$ and squares represent the 1-D *LILAC* predictions. The trend lines represent the best linear fit to the simulation data. The highest hot-spot pressure inferred in these experiments is 56±7 Gbar (Ref. 18). According to Fig. 148.7, when scaled to the laser energy available on the NIF, the current OMEGA implosions reach up to ~40% of the pressure required for ignition. Then, using the alpha amplification scaling shown in Fig. 148.6, these implosions would yield a 2× yield amplification because of alpha heating. Similar conclusions were reached using an independent calculation recently performed based on the $P\tau$ analysis.[35]

To understand the trends shown in Fig. 148.7, the effects of shell nonuniformity must be considered. As the shell adiabat increases, the target performance becomes less sensitive to the nonuniformity growth and the inferred $\overline{P}$ approaches the 1-D–predicted values. For lower values of shell adiabat, however, the deviation of the observed $\overline{P}$ from the predictions increases. Since the 1-D value of $\overline{P}$ decreases with the adiabat [see Eq. (4)], the inferred value has a maximum at $\alpha \sim 3.5$, which is a consequence of the interplay between a 1-D reduction in $\overline{P}$ and a shell stability improvement as the adiabat increases.

The performance-degradation mechanisms in cryogenic DD implosions include both the long-wavelength modes and the short-scale growth (which breaks up the shell during acceleration and introduces mix between the ablator and the hot spot as well as between the cold, denser part of the fuel and the hot spot). The long-wavelength modes increase the volume of a central, lower-density region (which forms the hot spot when the effects of asymmetry growth are negligible but might contain colder regions excluded from the hot spot in a perturbed implosion) as well as create thin spots in the cold shell during deceleration, producing expanding bubbles that reduce pusher efficiency and limit hot-spot confinement.[18,36]

4. Three-Dimensional Results

The evolution of long-wavelength nonuniformities seeded by the target offset, beam geometry, beam-power imbalance, and mispointing is studied using the 3-D hydrocode *ASTER*.[36] These simulations show that such nonuniformities form bubbles (regions of low-density material that protrude from the central region into the higher-density shell) that develop because of the deceleration in RT and BP growth. As the shell continues to converge, the bubbles eventually break out of the shell, prematurely quenching the hot-spot confinement and neutron

yield.[34,36] Because nonuniformities cause the peak burn to occur earlier, our observations based on the fusion products sample the implosion conditions when the shell convergence has not yet reached the peak value. This effect and nonradial flows caused by the 3-D effects prevent the fuel from reaching stagnation, limiting conversion efficiency of shell kinetic energy into internal energy of the hot spot at peak burn.

The experimental evidence of low-mode asymmetries includes the x-ray self-emission imaging from a tracer Ti layer embedded into the CH shell.[37] This technique shows that significant low-mode nonuniformities developed during deceleration. Another self-emission imaging technique that maps the implosion shape during the acceleration indicates the growth of low-ℓ modes while the target is being driven by laser illumination.[38] In addition, significant variations in the measured ion temperature along different lines of sight (LOS's) in cryogenic implosions are also indicative of asymmetry flows. The ion temperature is inferred in an experiment by measuring the spectral width of neutrons created as a result of fusing D and T. The spectral broadening, however, is caused not only by the thermal effects but also by the bulk motion with velocity distribution not aligned in a single direction. This results in higher temperature inferred from the fit $\langle T \rangle_{\text{fit}}$ compared to the true thermal ion temperature T (Refs. 31 and 39): $\langle T \rangle_{\text{fit}} \simeq T + 2 / 3\, m_i V_f^2$, where m_i is the average mass of fusion-reaction products and V_f is the bulk velocity. Since asymmetry growth creates different V_f along different LOS's, different values of ion temperature are inferred along multiple LOS's in a highly distorted implosion. The maximum measured temperature difference along three LOS's in OMEGA cryogenic implosions is shown in Fig. 148.8(a). The inferred temperature differences, up to 1 keV, correspond to nonradial flow velocities of $V_f \sim 2.5 \times 10^7$ cm/s. This is consistent with the results of 3-D *ASTER* simulations that include the effect of power imbalance and target offset. The plot in Fig. 148.8(b) shows the calculated neutron spectra at three perpendicular views (solid lines) together with neutron spectrum calculated without the effect of bulk motion (dashed line). Figure 148.8(a) also shows that the measured temperature variation strongly correlates with the yield degradation relative to the 1-D predictions, suggesting that the residual kinetic energy plays a detrimental role in reducing the target performance.

The performance degradation in lower-adiabat implosions ($\alpha < 2.5$) is caused by both the long wavelengths (as described above) and the short-scale nonuniformities. The latter are seeded mainly by laser imprint, nonuniformities caused by target fabrication, and debris accumulated during cryogenic

target production. Simulations indicate that the surface defects are the most damaging since they quickly evolve into nonlinear bubbles (modulations that produce local depressions in shell density) at the ablation front that are not stabilized by ablation[40] and grow at a rate exceeding the classical limit. Such growth leads to the ablator mixing into the main fuel and the vapor region.[41] These effects are directly observed in experiments. The ablator/cold shell mix is inferred from the backlit images obtained using a monochromatic x-ray imager.[42] The observed enhancement in x-ray attenuation by the main fuel in the low-adiabat implosion, not predicted by 1-D calculations,
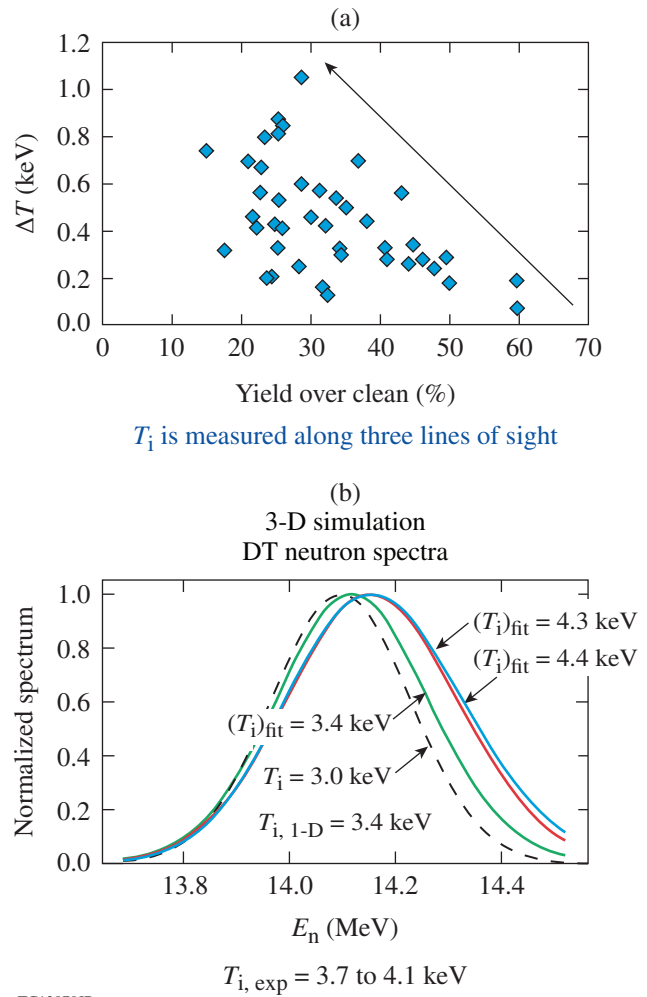

(a)

T_i is measured along three lines of sight

(b)
3-D simulation
DT neutron spectra

$(T_i)_{\text{fit}} = 4.3$ keV
$(T_i)_{\text{fit}} = 4.4$ keV
$(T_i)_{\text{fit}} = 3.4$ keV
$T_i = 3.0$ keV
$T_{i,\,1\text{-D}} = 3.4$ keV

$T_{i,\,\text{exp}} = 3.7$ to 4.1 keV

TC12870JR

Figure 148.8
(a) The measured variation in ion temperature ΔT (keV) among three lines of sight in cryogenic implosions on OMEGA as a function of yield-over-predictions. (b) Neutron spectra along three perpendicular views (solid lines) as calculated using *ASTER* simulations of an OMEGA cryogenic implosion assuming ~20-μm target offset and 15%-root-mean-square (rms) power imbalance. The dashed line shows the neutron spectrum without the effects of the bulk fuel motion.

is consistent with 0.1% to 0.2% atomic mixing of C into DT. No mixing is required to explain the observed fuel opacity in higher-adiabat implosions ($\alpha > 3.5$). In addition, the x-ray core emission at peak compression is also enhanced when the fuel adiabat is reduced to $\alpha < 2.5$, indicating that ablator carbon penetrates all the way into the hot spot during the implosion.[43] The plastic ablator in direct-drive designs is thin and gets ablated in the middle of the drive pulse. The presence of the ablator in the hot spot suggests therefore a significant growth in local surface features that produce jet-like structures in the shell early in the implosion and bring the ablator material into the hot spot.[41]

5. Laser Coupling and CBET

The shell's stability properties can be significantly improved by increasing laser coupling and making the shell thicker. This can be accomplished by increasing the drive hydroefficiency. An analysis of direct-drive implosions on OMEGA has shown that coupling losses related to CBET[29] significantly limit the ablation pressure (as much as 40% on OMEGA and up to 60% on NIF-scale targets), implosion velocity, and shell kinetic energy. CBET results from the scattering of incoming laser light caused by stimulated Brillouin scatter. The reduction in the ablation pressure caused by CBET is shown in Fig. 148.9, where the ablation pressure, calculated at the time when the ablation surface had converged by a factor of 2.5, is plotted for OMEGA and NIF-scale symmetric designs at different drive intensities. Considering such losses, demonstrating the hydrodynamic equivalence of implosions on OMEGA to ignition designs on the NIF requires the shell IFAR to exceed the current stability threshold level (~22) (Ref. 19).

One of the CBET mitigation strategies[44] involves reducing the laser beam size relative to the initial target size. This strategy, as demonstrated both theoretically and experimentally, recovers some coupling losses and increases the ablation

pressure.[29,34,45] The benefit of reducing beam size to enhance laser coupling is illustrated in Fig. 148.10, where the predicted time-dependent ablation pressure (plotted as a function of shell convergence) is shown for different ratios of R_b / R_t (R_b is defined as the radius of a 95% beam-energy contour). Figure 148.10 shows that the largest increase in coupling occurs early in the implosion when the critical surface is at a larger radius and the refraction effects prevent beams from intersecting in regions where CBET is effective (Mach ~ 1 surface in plasma corona). Later in the implosion when the critical surface has moved inward a sufficient distance, beams start to intersect in the CBET-resonant regions and exchange their energy, increasing CBET losses. When CBET is fully mitigated, the shell's kinetic and hot-spot internal energies increase, allowing implosions to reach ignition condition at a higher adiabat. This is illustrated in Fig. 148.7, where the green trend line shows the ignition pressure parameter with the enhanced laser
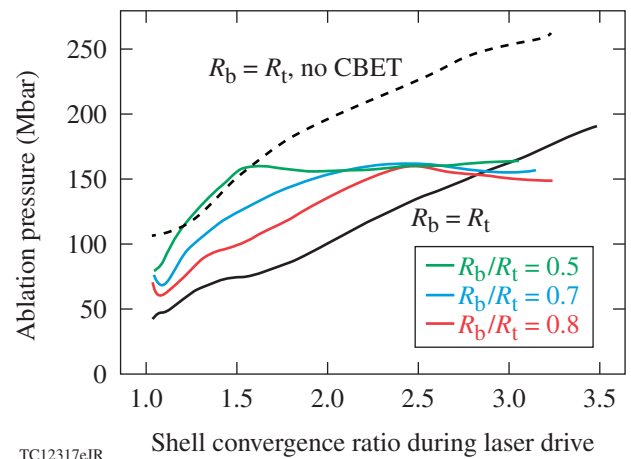

TC12317eJR

Figure 148.10
Time-dependent ablation pressure as a function of shell convergence for designs driven at $I = 9 \times 10^{14}$ W/cm^2.
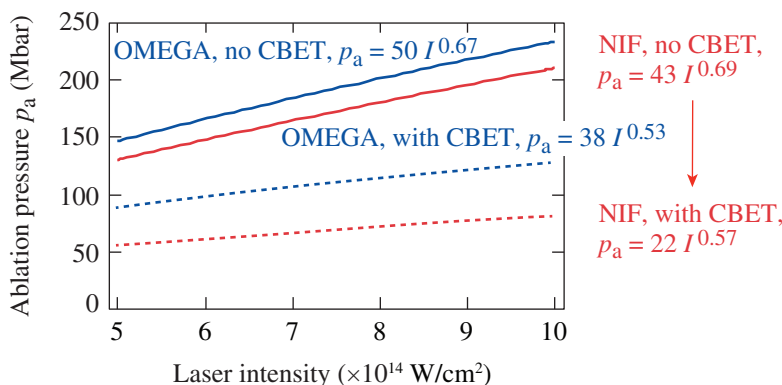

TC12872JR

Figure 148.9
Ablation pressure as a function of incident laser intensity for OMEGA and NIF-scale designs. Solid lines show the calculation results without the effect of CBET; dashed lines include the effect of CBET. The ablation pressure was calculated when the ablation front had converged by a factor of 2.5 from its initial radius.

coupling. The adiabat in the ignition designs can be increased in this case up to $\alpha \sim 5.5$, significantly improving the shell's stability properties.

Experimental campaigns performed on OMEGA with the reduced R_b/R_t have demonstrated increased hydrodynamic efficiency.[34] The target performance in such implosions, however, was degraded. This was explained, based on the results of 3-D *ASTER* simulations,[36] by asymmetries caused by power imbalance, enhanced in these implosions because of reduced beam overlap.

Conclusions

The direct-drive approach to ignition, when compared to indirect-drive designs, offers a significant increase (by a factor of 3 to 5) in laser coupling to the shell kinetic energy. Cryogenic implosions on OMEGA have reached hot-spot pressures of 56 Gbar, which is ~40% of what is required for ignition. Extrapolating these results to NIF-scale laser energy is predicted to enhance the yield caused by alpha heating by a factor of 2. The cryogenic campaigns with reduced beam size relative to the target size $\left(R_b/R_t < 1\right)$, performed on OMEGA to reduce CBET losses, demonstrated increased laser coupling and hydrodynamic efficiency; however, this coupling enhancement did not improve the target performance. Numerical simulations indicate that long-wavelength nonuniformities caused by target offset and power imbalance lead to an increased target central volume and early burn truncation. Reaching the goal of demonstrating hydrodynamic equivalence on OMEGA must include improving laser power balance, target position, and target quality at shot time. CBET must also be reduced to increase the fuel mass and improve shell stability. CBET mitigation strategies include reduction in the beam size relative to the target size and laser wavelength separation.[46]

REFERENCES

1. S. Atzeni and J. Meyer-ter-Vehn, *The Physics of Inertial Fusion: Beam Plasma Interaction, Hydrodynamics, Hot Dense Matter*, International Series of Monographs on Physics (Clarendon Press, Oxford, 2004).

2. J. Paisner *et al.*, Laser Focus World **30**, 75 (1994).

3. R. S. Craxton, K. S. Anderson, T. R. Boehly, V. N. Goncharov, D. R. Harding, J. P. Knauer, R. L. McCrory, P. W. McKenty, D. D. Meyerhofer, J. F. Myatt, A. J. Schmitt, J. D. Sethian, R. W. Short, S. Skupsky, W. Theobald, W. L. Kruer, K. Tanaka, R. Betti, T. J. B. Collins, J. A. Delettrez, S. X. Hu, J. A. Marozas, A. V. Maximov, D. T. Michel, P. B. Radha, S. P. Regan, T. C. Sangster, W. Seka, A. A. Solodov, J. M. Soures, C. Stoeckl, and J. D. Zuegel, Phys. Plasmas **22**, 110501 (2015).

4. T. R. Boehly, D. L. Brown, R. S. Craxton, R. L. Keck, J. P. Knauer, J. H. Kelly, T. J. Kessler, S. A. Kumpan, S. J. Loucks, S. A. Letzring, F. J. Marshall, R. L. McCrory, S. F. B. Morse, W. Seka, J. M. Soures, and C. P. Verdon, Opt. Commun. **133**, 495 (1997).

5. S. P. Obenschain *et al.*, Phys. Plasmas **3**, 2098 (1996).

6. T. J. Kessler, Y. Lin, J. J. Armstrong, and B. Velazquez, Proc. SPIE **1870**, 95 (1993).

7. T. R. Boehly, V. A. Smalyuk, D. D. Meyerhofer, J. P. Knauer, D. K. Bradley, R. S. Craxton, M. J. Guardalben, S. Skupsky, and T. J. Kessler, J. Appl. Phys. **85**, 3444 (1999).

8. S. Skupsky, R. W. Short, T. Kessler, R. S. Craxton, S. Letzring, and J. M. Soures, J. Appl. Phys. **66**, 3456 (1989).

9. V. N. Goncharov, J. P. Knauer, P. W. McKenty, P. B. Radha, T. C. Sangster, S. Skupsky, R. Betti, R. L. McCrory, and D. D. Meyerhofer, Phys. Plasmas **10**, 1906 (2003).

10. V. N. Goncharov, T. C. Sangster, T. R. Boehly, S. X. Hu, I. V. Igumenshchev, F. J. Marshall, R. L. McCrory, D. D. Meyerhofer, P. B. Radha, W. Seka, S. Skupsky, C. Stoeckl, D. T. Casey, J. A. Frenje, and R. D. Petrasso, Phys. Rev. Lett. **104**, 165001 (2010).

11. S. X. Hu, G. Fiksel, V. N. Goncharov, S. Skupsky, D. D. Meyerhofer, and V. A. Smalyuk, Phys. Rev. Lett. **108**, 195003 (2012).

12. S. P. Obenschain *et al.*, Phys. Plasmas **9**, 2234 (2002).

13. O. A. Hurricane *et al.*, Nature **506**, 343 (2014).

14. R. Betti, C. D. Zhou, K. S. Anderson, L. J. Perkins, W. Theobald, and A. A. Solodov, Phys. Rev. Lett. **98**, 155001 (2007).

15. J. D. Lawson, Proc. Phys. Soc. Lond. B **70**, 6 (1957).

16. R. Betti, P. Y. Chang, B. K. Spears, K. S. Anderson, J. Edwards, M. Fatenejad, J. D. Lindl, R. L. McCrory, R. Nora, and D. Shvarts, Phys. Plasmas **17**, 058102 (2010).

17. J. Delettrez, R. Epstein, M. C. Richardson, P. A. Jaanimagi, and B. L. Henke, Phys. Rev. A **36**, 3926 (1987).

18. S. P. Regan, V. N. Goncharov, I. V. Igumenshchev, T. C. Sangster, R. Betti, A. Bose, T. R. Boehly, M. J. Bonino, E. M. Campbell, D. Cao, T. J. B. Collins, R. S. Craxton, A. K. Davis, J. A. Delettrez, D. H. Edgell, R. Epstein, C. J. Forrest, J. A. Frenje, D. H. Froula, M. Gatu Johnson, V. Yu. Glebov, D. R. Harding, M. Hohenberger, S. X. Hu, D. Jacobs-Perkins, R. T. Janezic, M. Karasik, R. L. Keck, J. H. Kelly, T. J. Kessler,

J. P. Knauer, T. Z. Kosc, S. J. Loucks, J. A. Marozas, F. J. Marshall, R. L. McCrory, P. W. McKenty, D. D. Meyerhofer, D. T. Michel, J. F. Myatt, S. P. Obenschain, R. D. Petrasso, R. B. Radha, B. Rice, M. Rosenberg, A. J. Schmitt, M. J. Schmitt, W. Seka, W. T. Shmayda, M. J. Shoup III, A. Shvydky, S. Skupsky, S. Solodov, C. Stoeckl, W. Theobald, J. Ulreich, M. D. Wittman, K. M. Woo, B. Yaakobi, and J. D. Zuegel, Phys. Rev. Lett. **117**, 025001 (2016).

19. V. N. Goncharov, T. C. Sangster, R. Betti, T. R. Boehly, M. J. Bonino, T. J. B. Collins, R. S. Craxton, J. A. Delettrez, D. H. Edgell, R. Epstein, R. K. Follet, C. J. Forrest, D. H. Froula, V. Yu. Glebov, D. R. Harding, R. J. Henchen, S. X. Hu, I. V. Igumenshchev, R. Janezic, J. H. Kelly, T. J. Kessler, T. Z. Kosc, S. J. Loucks, J. A. Marozas, F. J. Marshall, A. V. Maximov, R. L. McCrory, P. W. McKenty, D. D. Meyerhofer, D. T. Michel, J. F. Myatt, R. Nora, P. B. Radha, S. P. Regan, W. Seka, W. T. Shmayda, R. W. Short, A. Shvydky, S. Skupsky, C. Stoeckl, B. Yaakobi, J. A. Frenje, M. Gatu-Johnson, R. D. Petrasso, and D. T. Casey, Phys. Plasmas **21**, 056315 (2014).

20. D. T. Michel, C. Sorce, R. Epstein, N. Whiting, I. V. Igumenshchev, R. Jungquist, and D. H. Froula, Rev. Sci. Instrum. **83**, 10E530 (2012).

21. C. Stoeckl, V. Yu. Glebov, S. Roberts, T. C. Sangster, R. A. Lerche, R. L. Griffith, and C. Sorce, Rev. Sci. Instrum. **74**, 1713 (2003).

22. W. Seka, D. H. Edgell, J. P. Knauer, J. F. Myatt, A. V. Maximov, R. W. Short, T. C. Sangster, C. Stoeckl, R. E. Bahr, R. S. Craxton, J. A. Delettrez, V. N. Goncharov, I. V. Igumenshchev, and D. Shvarts, Phys. Plasmas **15**, 056312 (2008).

23. L. M. Barker and R. E. Hollenbach, J. Appl. Phys. **43**, 4669 (1972).

24. C. Stoeckl, V. Yu. Glebov, D. D. Meyerhofer, W. Seka, B. Yaakobi, R. P. J. Town, and J. D. Zuegel, Rev. Sci. Instrum. **72**, 1197 (2001).

25. J. A. Frenje, C. K. Li, F. H. Séguin, D. T. Casey, R. D. Petrasso, T. C. Sangster, R. Betti, V. Yu. Glebov, and D. D. Meyerhofer, Phys. Plasmas **16**, 042704 (2009).

26. C. J. Forrest, P. B. Radha, V. Yu. Glebov, V. N. Goncharov, J. P. Knauer, A. Pruyne, M. Romanofsky, T. C. Sangster, M. J. Shoup III, C. Stoeckl, D. T. Casey, M. Gatu-Johnson, and S. Gardner, Rev. Sci. Instrum. **83**, 10D919 (2012).

27. R. Betti and C. Zhou, Phys. Plasmas **12**, 110702 (2005).

28. V. N. Goncharov, T. C. Sangster, P. B. Radha, R. Betti, T. R. Boehly, T. J. B. Collins, R. S. Craxton, J. A. Delettrez, R. Epstein, V. Yu. Glebov, S. X. Hu, I. V. Igumenshchev, J. P. Knauer, S. J. Loucks, J. A. Marozas, F. J. Marshall, R. L. McCrory, P. W. McKenty, D. D. Meyerhofer, S. P. Regan, W. Seka, S. Skupsky, V. A. Smalyuk, J. M. Soures, C. Stoeckl, D. Shvarts, J. A. Frenje, R. D. Petrasso, C. K. Li, F. Séguin, W. Manheimer, and D. G. Colombant, Phys. Plasmas **15**, 056310 (2008).

29. I. V. Igumenshchev, D. H. Edgell, V. N. Goncharov, J. A. Delettrez, A. V. Maximov, J. F. Myatt, W. Seka, A. Shvydky, S. Skupsky, and C. Stoeckl, Phys. Plasmas **17**, 122708 (2010).

30. S. X. Hu, B. Militzer, V. N. Goncharov, and S. Skupsky, Phys. Rev. Lett. **104**, 235003 (2010); S. X. Hu, L. A. Collins, V. N. Goncharov, J. D. Kress, R. L. McCrory, and S. Skupsky, Phys. Rev. E **92**, 043104 (2015).

31. V. N. Goncharov, in *Laser-Plasma Interactions and Applications*, edited by P. McKenna, D. Neely, R. Bingham, and D. A. Jaroszynski, Scottish Graduate Series (Springer, Switzerland, 2013), Chap. 7, pp. 135–183.

32. V. N. Goncharov, O. V. Gotchev, E. Vianello, T. R. Boehly, J. P. Knauer, P. W. McKenty, P. B. Radha, S. P. Regan, T. C. Sangster, S. Skupsky, V. A. Smalyuk, R. Betti, R. L. McCrory, D. D. Meyerhofer, and C. Cherfils-Clérouin, Phys. Plasmas **13**, 012702 (2006).

33. D. S. Clark *et al.*, Phys. Plasmas **21**, 112705 (2014).

34. V. N. Goncharov, S. P. Regan, T. C. Sangster, R. Betti, T. R. Boehly, E. M. Campbell, J. A. Delettrez, D. H. Edgell, R. Epstein, C. J. Forrest, D. H. Froula, V. Yu. Glebov, D. R. Harding, S. X. Hu, I. V. Igumenshchev, F. J. Marshall, R. L. McCrory, D. T. Michel, J. F. Myatt, P. B. Radha, W. Seka, A. Shvydky, C. Stoeckl, W. Theobald, B. Yaakobi, and M. Gatu-Johnson, J. Phys.: Conf. Ser. **717**, 012008 (2016).

35. A. Bose, K. M. Woo, R. Betti, E. M. Campbell, D. Mangino, A. R. Christopherson, R. L. McCrory, R. Nora, S. P. Regan, V. N. Goncharov, T. C. Sangster, C. J. Forrest, J. Frenje, M. Gatu Johnson, V. Yu. Glebov, J. P. Knauer, F. J. Marshall, C. Stoeckl, and W. Theobald, Phys. Rev. E **94**, 011201(R) (2016).

36. I. V. Igumenshchev, V. N. Goncharov, F. J. Marshall, J. P. Knauer, E. M. Campbell, C. J. Forrest, D. H. Froula, V. Yu. Glebov, R. L. McCrory, S. P. Regan, T. C. Sangster, S. Skupsky, and C. Stoeckl, Phys. Plasmas **23**, 052702 (2016).

37. R. C. Shah, B. M. Haines, F. J. Wysocki, J. F. Benage, J. Fooks, V. Glebov, P. Hakel, M. Hoppe, I. V. Igumenshchev, G. Kagan, R. C. Mancini, F. J. Marshall, D. T. Michel, T. J. Murphy, M. E. Schoff, C. Stoeckl, and B. Yaakobi, "Systematic Fuel Cavity Asymmetries in Directly Driven ICF Implosions," submitted to Physical Review Letters.

38. D. T. Michel, A. K. Davis, W. Armstrong, R. Bahr, R. Epstein, V. N. Goncharov, M. Hohenberger, I. V. Igumenshchev, R. Jungquist, D. D. Meyerhofer, P. B. Radha, T. C. Sangster, C. Sorce, and D. H. Froula, High Power Laser Science and Engineering **3**, e19 (2015).

39. T. J. Murphy, Phys. Plasmas **21**, 072701 (2014).

40. R. Betti and J. Sanz, Phys. Rev. Lett. **97**, 205002 (2006).

41. I. V. Igumenshchev, V. N. Goncharov, W. T. Shmayda, D. R. Harding, T. C. Sangster, and D. D. Meyerhofer, Phys. Plasmas **20**, 082703 (2013).

42. C. Stoeckl, M. Bedzyk, G. Brent, R. Epstein, G. Fiksel, D. Guy, V. N. Goncharov, S. X. Hu, S. Ingraham, D. W. Jacobs-Perkins, R. K. Jungquist, F. J. Marshall, C. Mileham, P. M. Nilson, T. C. Sangster, M. J. Shoup III, and W. Theobald, Rev. Sci. Instrum. **85**, 11E501 (2014).

43. T. C. Sangster, V. N. Goncharov, R. Betti, P. B. Radha, T. R. Boehly, D. T. Casey, T. J. B. Collins, R. S. Craxton, J. A. Delettrez, D. H.

Edgell, R. Epstein, C. J. Forrest, J. A. Frenje, D. H. Froula, M. Gatu-Johnson, V. Yu. Glebov, D. R. Harding, M. Hohenberger, S. X. Hu, I. V. Igumenshchev, R. Janezic, J. H. Kelly, T. J. Kessler, C. Kingsley, T. Z. Kosc, J. P. Knauer, S. J. Loucks, J. A. Marozas, F. J. Marshall, A. V. Maximov, R. L. McCrory, P. W. McKenty, D. D. Meyerhofer, D. T. Michel, J. F. Myatt, R. D. Petrasso, S. P. Regan, W. Seka, W. T. Shmayda, R. W. Short, A. Shvydky, S. Skupsky, J. M. Soures, C. Stoeckl, W. Theobald, V. Versteeg, B. Yaakobi, and J. D. Zuegel, Phys. Plasmas **20**, 056317 (2013).

44. I. V. Igumenshchev, D. H. Froula, D. H. Edgell, V. N. Goncharov, T. J. Kessler, F. J. Marshall, R. L. McCrory, P. W. McKenty, D. D. Meyerhofer, D. T. Michel, T. C. Sangster, W. Seka, and S. Skupsky, Phys. Rev. Lett. **110**, 145001 (2013).

45. D. H. Froula, T. J. Kessler, I. V. Igumenshchev, R. Betti, V. N. Goncharov, H. Huang, S. X. Hu, E. Hill, J. H. Kelly, D. D. Meyerhofer, A. Shvydky, and J. D. Zuegel, Phys. Plasmas **20**, 082704 (2013).

46. I. V. Igumenshchev, W. Seka, D. H. Edgell, D. T. Michel, D. H. Froula, V. N. Goncharov, R. S. Craxton, L. Divol, R. Epstein, R. Follett, J. H. Kelly, T. Z. Kosc, A. V. Maximov, R. L. McCrory, D. D. Meyerhofer, P. Michel, J. F. Myatt, T. C. Sangster, A. Shvydky, S. Skupsky, and C. Stoeckl, Phys. Plasmas **19**, 056314 (2012).

Measuring the Refractive Index of a Laser-Plasma Optical System

Using laser-plasma optical systems to manipulate the basic properties of light waves has caused a recent surge of interest.[1–4] Plasma-based photonic devices are attractive because they can be ultrafast, damage resistant, and easily tunable. Alleviating concerns about optic damage by replacing conventional optics with plasma-based components could lead to the next generation of high-power, large-scale laser facilities. Plasma gratings in particular have received a great deal of attention because they are routinely used to mediate cross-beam energy transfer in indirect-drive inertial confinement fusion (ICF) experiments at the National Ignition Facility (NIF).[5–7] Multiple experiments[8,9]—including ICF experiments at the NIF[10,11]—have consistently failed, however, to observe the level of energy transfer expected on the basis of linear theory.

Recently, that theory was revisited when it was recognized that plasma gratings could also be used to dynamically control the polarization of light waves.[1] The effect of a laser-plasma system on an independent probe laser beam can be described by a complex refractive-index perturbation that is a function of the wavelength shift between the interacting beams; the system can consequently (anisotropically) modify both the phase and the amplitude of the probe and therefore act as a wave plate and/or a polarizer.[1] Turnbull *et al.* recently presented the first demonstration of a laser-plasma wave plate utilizing the system's nonzero real refractive-index perturbation that exists even in the absence of a wavelength shift between the beams. This article reports on our use of wavelength tuning to more fully map out the complete refractive-index perturbation. For the first time the real component is measured as a function of the wavelength shift. The imaginary component, which underlies cross-beam energy transfer (CBET) experiments at the NIF, is measured with sufficient accuracy to resolve both nonresonant and resonant energy transfer and is found to be in excellent agreement with linear theory (both for the first time), yielding implications for ICF experiments. The data also include the first demonstration of a laser-plasma polarizer with 85% to 87% extinction, further complementing the existing suite of plasma-based photonic devices.

Our laser-plasma optical system consists of a plasma with electron density n_e, electron temperature T_e, and ion temperature T_i, as well as a "pump" laser beam with electric field E_0 and frequency ω_0. A probe laser beam with E_1 and ω_1 will encounter resonances if $\omega_1 - \omega_0 = \pm\omega_{IAW}$; i.e., the frequency difference between the two beams is equal to the frequency of an ion-acoustic wave (IAW) with wave number $k_b = |\mathbf{k}_0 - \mathbf{k}_1|$. The driven ion-acoustic wave mediates energy transfer between the two beams, thereby modifying the probe's amplitude. As described by the Kramers–Kronig relations, any frequency-dependent variation of the probe's amplitude in the vicinity of an optical resonance must be accompanied by variation in the real refractive index seen by the probe. The net impact of the pump on the probe beam can be described as a complex refractive-index perturbation $\delta\eta$ such that $E_1' = E_1 \exp\left(ik_1\delta\eta L/\eta_0\right)$ after interacting with the laser-plasma system, where L is the interaction length and η_0 is the unperturbed plasma refractive index. The full expression for the refractive-index perturbation was derived in Michel *et al.*[1] using a kinetic plasma model. Critically, it was also shown in that work that the perturbation is seen only by the component of the probe's electric field that is parallel to the projection of the pump's electric field in the probe's plane of polarization (cf., Fig. 148.11). The ability to induce anisotropy via the relative orientation of the pump and probe polarizations can be exploited for precise manipulation of the probe's polarization.[1,2] Here we present measurements that show excellent agreement with linear theory for both the real and imaginary components of the refractive-index perturbation as a function of the wavelength shift between the pump and probe. Previously, the real component had been measured only at zero-wavelength shift,[2] and measurements of the imaginary component were not found to agree with linear theory.[8]

The experiment was conducted at Lawrence Livermore National Laboratory's Jupiter Laser Facility. A gas jet equipped with a 3-mm-outlet-diam supersonic nozzle released methane gas prior to the arrival of the pump and probe, which were focused over the nozzle with a relative crossing angle of 27°. Two different phase plates were used to give the pump and
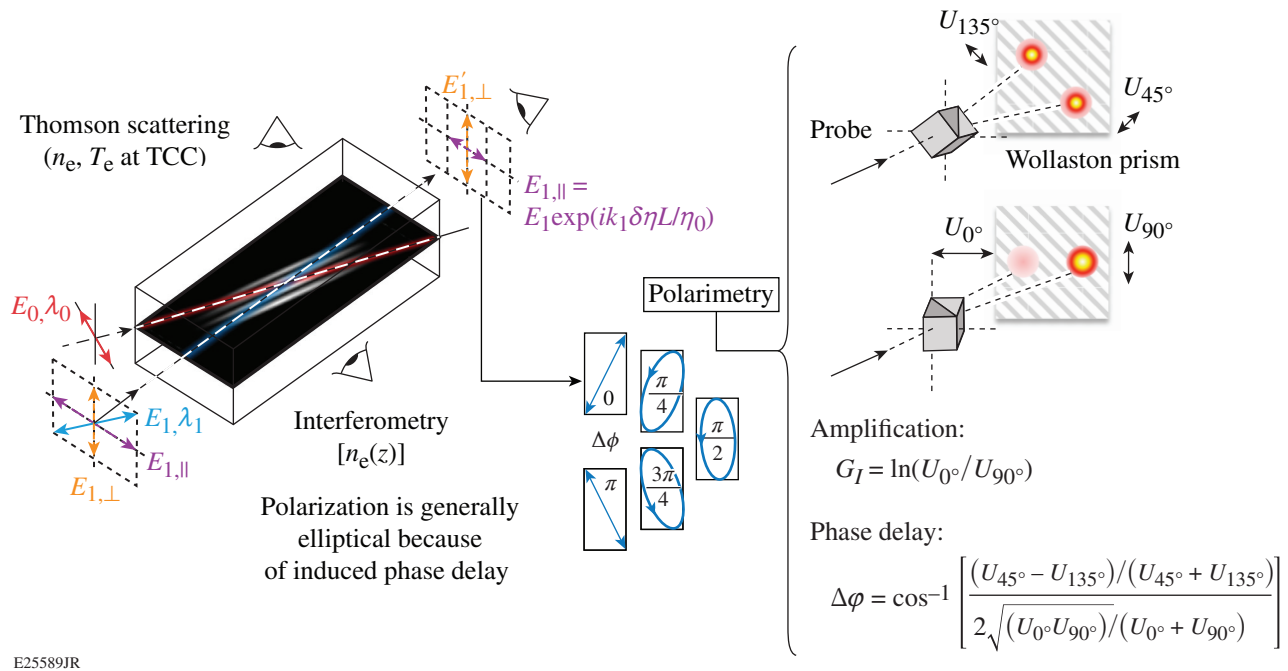
Figure 148.11
The presence of the pump introduces anisotropy to the plasma as seen by an independent probe beam. Only the component of the probe's polarization that is aligned with the pump polarization will have its amplitude and/or phase modified by the interaction, both of which can be measured using polarimetry. TCC: target chamber center.

probe speckled but roughly flattop (in an average sense) intensity distributions with 600-μm and 200-μm diameters at best focus, respectively. The pump had an $\approx$3-ns square pulse shape and established the plasma conditions prior to the arrival of the probe, which had an $\approx$250-ps Gaussian pulse shape with the peak delayed $\approx$1.3 ns from the rise of the pump. Using the nominal pump energies (292±8 J), fast-diode–based, pulse-shape measurements, and an assumed spot size based on the phase-plate properties, the pump intensity was expected to be in the range of $I_0 = (3.6\pm0.2) \times 10^{13}$ W/cm^2 averaged over the interaction region. The initial probe energy and intensity were $\approx$27 mJ and 3.4×10^{11} W/cm^2, respectively. Both beams used the fundamental frequency of an Nd:YLF laser ($\lambda \approx 1053$ nm), but different front ends allowed wavelength tuning within the bandwidth of the gain medium; here, a range of $-3 \le \Delta\lambda \le +3$ Å was used, where $\Delta\lambda$ is the wavelength difference between pump and probe. A polarizer was used before the last turning mirror to orient the probe polarization close to 45° relative to the horizontal pump polarization. This provides a convenient and novel method of diagnosing probe amplitude changes induced by the laser-plasma system; exploiting the anisotropic nature of the interaction, only the horizontal component of the probe's polarization will either grow or decay under the influence of the pump, and the orthogonal vertical polarization

provides a baseline that factors in shot-to-shot variation of the incident probe-beam energy as well as inverse bremsstrahlung absorption in the plasma, as shown in Fig. 148.11. Separating the polarizations with a Wollaston prism subsequent to the interaction and taking their ratio provides a direct measure of the amplification. To compare with linear theory, the plasma electron density and temperature were measured with Thomson scattering. The scattered light was dominated by the high-energy pump beam, collected at a scattering angle of 90°, and directed to a streaked spectrometer measuring the blue-shifted electron plasma wave feature. To obtain additional information about density gradients in the plasma, optical interferometry was used, employing a dedicated diagnostic beam that was incident on the plasma orthogonal to the pump beam. Both diagnostics were analyzed at the time of the pump–probe interaction. The experimental setup is shown in Fig. 148.11.

The effect of the refractive-index perturbation's imaginary component can be expressed as a gain exponent G, where $E'_{1,\parallel} = E_1\exp(G)$ and $G = k_1\mathfrak{F}[\delta\eta]L/\eta_0$. Intensity being proportional to the square of the electric field, the intensity gain exponent is $G_I = 2G$ and is related to amplification, the ratio of intensity in each polarization subsequent to the interaction, by $G_I = \ln(A)$. Figure 148.12 shows the experimental data

plotted with a calculation using the linear theory developed to compute CBET in indirect-drive ICF experiments on the NIF.[5] The electron density and temperature inputs used in the calculation were $n_e/n_c = 0.0104$ and $T_e = 220$ eV, where n_c is the critical density, consistent with the experimentally measured values of $n_e/n_c = 0.011\pm0.001$, and $T_e = 224\pm24$ eV. Since several necessary inputs were not directly measured, three-dimensional radiation–hydrodynamic simulations using *HYDRA*[12] were performed to obtain estimates for ion temperature and flow velocity. The pump-beam energy, spatial profile, and pulse shape used in the simulation closely reproduced the experimental conditions, and the initial methane gas density and the flux limiter were then adjusted to match the measured electron density and temperature. The simulations predicted an ion temperature of $T_i/T_e \approx 0.09$, whereas $T_i/T_e \approx 0.12$ is used in the linear theory best fit. The small difference is comparable to the level of ion heating expected from thermalizing the energy in the driven ion-acoustic waves, which is not included in the simulations. *HYDRA* also predicts an outwardly directed radial flow resulting from the expansion of the plasma channel formed by the pump beam, which broadens the ion-acoustic resonance by shifting the peak in different portions of the interaction region; this was directly imported into the linear theory calculation because of the lack of a flow velocity measurement. The effective pump intensity was also reduced 20% from the expected value (to $I_0 = 2.9 \times 10^{13}$ W/cm²), which

we attribute to unmeasured transport losses through the final optics, inverse bremsstrahlung absorption in the plasma, pump depletion effects, and/or imperfect focusing of the pump beam. In specifying the crossing angle, the calculation takes into account the finite spread given by the $f/6.7$ and $f/10$ pump and probe beams, respectively, which also broadens the ion-acoustic resonance. Finally, the peak location of the ion-acoustic resonance was most easily matched by specifying the ion species fractions as $f_C = 0.4$ and $f_H = 0.6$, whereas $f_C = 0.2$ and $f_H = 0.8$ were expected based on the initial methane-gas composition. This implies that species separation is occurring in this system. In principle, hydrogen—being lighter and having a higher charge-to-mass ratio—is expected to lead the plasma channel expansion, leaving a higher concentration of carbon in the interaction region. This effect has been observed previously using simultaneous electron and ion feature Thomson scattering in an expanding CH plasma.[13,14] Assessing this effect quantitatively requires multi-ion-fluid simulations, however, and is considered outside the scope of this study. Species separation is an increasingly active field of research in the ICF community.[15–19]

It is evident that the linear theory accurately reproduces the data both near the resonance peaks and in the off-resonant region between the Stokes and anti-Stokes peaks. Previous work utilizing a simple geometry had determined that CBET was maximized near the ion-acoustic resonance, but the peak location was not predicted accurately; the data lacked the precision to measure off-resonant transfer. It was also determined that the gain was lower than expected from the linear theory by a factor of 20 (Ref. 8). ICF hohlraums have also provided evidence that the amount of energy transfer is less than expected from linear theory.[10,11] In both previous examples, the linear theory calculations used plasma conditions taken entirely from radiation–hydrodynamic simulations. The agreement found in this better-characterized experiment suggests that inaccuracies in the assumed density and temperature may be one source of discrepancy. Weak turbulence effects associated with having many of these coupled-beam interactions in the same region of plasma may also be a factor in indirect-drive ICF.[10] Note that while the conditions of this experiment are very different from an ICF environment in terms of wavelength, intensity, density, and temperature, it can still be considered a good surrogate by several metrics. Gain was larger in this experiment than even the most resonant of interactions in an ICF hohlraum, so this can be considered an upper bound on the parameter space relevant to ICF. Furthermore, the normalized ion-acoustic–wave damping is $\nu/\omega_{IAW} \approx 0.1$ to 0.2 (i.e., strongly damped) in both cases; achieving this in the present experiment motivated the use of the multispecies methane gas.[20]
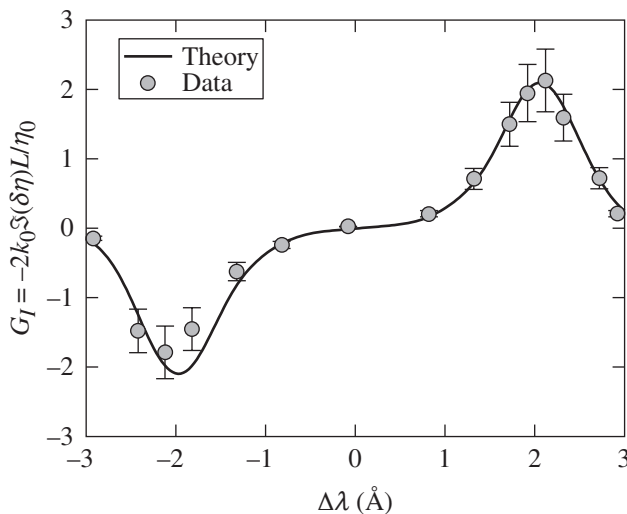
E25591JR

Figure 148.12
The intensity gain exponent is plotted as a function of the relative wavelength shift between the probe and pump. The parameters used in the linear theory calculation are listed in the text and are quite consistent with measured values (where available) and three-dimensional *HYDRA* simulations.

As mentioned, the imaginary refractive-index perturbation component is accompanied by a real refractive-index change, which introduces a phase delay between the probe's vertical (noninteracting) and horizontal (interacting) components. While amplification was determined by separating the vertical and horizontal components and taking their ratio (which is insensitive to the phase delay), inferring the phase delay $\Delta\phi$ requires a second measurement in which the Wollaston prism is rotated 45° in order to separate the 45° and 135° polarization components. With each signal's energy in arbitrary units given by U_j, where j is the polarization angle, the phase delay for each pair of measurements (assuming polarized light and perfect shot-to-shot reproducibility) is given by

$$\Delta\phi = \cos^{-1}\left[\frac{(U_{45°} - U_{135°})/(U_{45°} + U_{135°})}{2\sqrt{U_{0°}U_{90°}}/(U_{0°} + U_{90°})}\right]. \qquad (1)$$

Unlike the imaginary component, the real component of the refractive-index perturbation is nonzero even in the absence of a wavelength shift between the pump and probe. Turnbull *et al.* exploited this property previously in the first demonstration of a laser-plasma wave plate, converting an initially elliptical polarization into a nearly ideal circular polarization.[2] Here, wavelength tuning capability allows us to validate other points along the real refractive-index perturbation curve, as shown in Fig. 148.13. Again, the linear theory provides a good match to the experimental data using the same parameters that were used to fit the amplification data, with key features—nonzero phase delay at zero wavelength shift, larger dephasing on either side of the resonance, and zero dephasing at the peak—evident in the data. Note that the measurement does not actually discriminate between positive and negative phase delay, but since the data are consistent with the shape of the curve as predicted by linear theory, we assume that those points to the left of the peak are positive and points to the right of the peak are negative. This is the first (to our knowledge) measurement of a laser-plasma optical system's real refractive-index perturbation as a function of wavelength tuning.

The experiment was designed in such a way to test the concept of a "plasma polarizer," which was proposed by Michel *et al.*[1] When $\lambda_1 - \lambda_0 < 0$, the probe transfers energy to the pump but only out of its horizontal component (which is aligned with the pump polarization) resulting from the anisotropy of the laser-plasma system, so the system is effectively a linear polarizer. The data point at the negative peak of Fig. 148.12
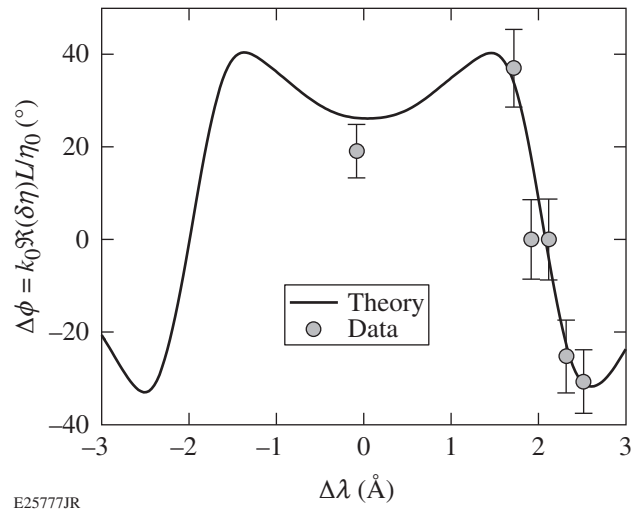
Figure 148.13
The phase delay induced by the real refractive-index perturbation is plotted as a function of the wavelength shift between the pump and probe. The linear theory is once again in good agreement with the experimental data.

represents an extinction of 85%. The data are shown in Fig. 148.14; the incident polarization was oriented in order to have nearly equal horizontal and vertical components, but after propagating through the system, the horizontal polarization is significantly attenuated. Additional shots were conducted in which the incident probe intensity was increased up to $I_1 \approx 3 \times 10^{12}$ W/cm^2, and the extinction stayed in the range of 85% to 87%. Note that the probe is otherwise minimally affected by the system because the phase delay induced between the vertical polarization and what is left of the horizontal polarization is close to zero near the resonance peak, absorption in this fairly tenuous plasma is calculated to be modest, and the probe is not degraded by other laser–plasma instabilities. Maintaining similar plasma conditions, the extinction could be increased or decreased by changing the pump intensity. This demonstrates another ultrafast, damage-resistant, and tunable laser-plasma photonic device. Having now achieved both a wave plate and a polarizer, it is possible to design a laser Q switch using only laser-plasma systems.

In summary, a laser-plasma optical system's complete refractive index—both its imaginary and real components—was mapped out for the first time, using a consistent set of laser and plasma parameters. It was found to be in excellent agreement with the linear theory for coupled beams in a plasma that is used to compute cross-beam energy transfer in indirect-drive ICF experiments. The ability to correctly predict energy transfer in this well-characterized context, but not in ICF experiments,[10,11] points to possible errors in the hydrodynamic inputs to the ICF

Vertical (preshot)   Horizontal (preshot)

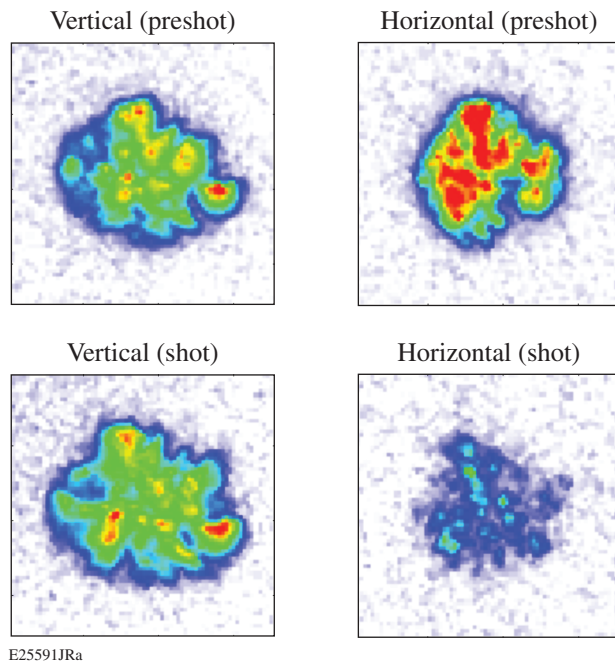Vertical (shot)   Horizontal (shot)

E25591JRa

Figure 148.14
The anisotropic laser-plasma system acts like a pure linear polarizer at the negative resonance peak, depleting the probe's horizontal polarization component. The color scale for each pair is normalized to the vertical polarization. The vertical and horizontal spots appear to be different because the Wollaston prism slightly affects the imaging. The pre-shot images were obtained without any plasma, and the horizontal polarization was brighter than the vertical polarization because the polarizer setting the incident polarization was not quite oriented at 45°; 85% to 87% of the horizontal polarization was then extinguished by the laser-plasma polarizer, whereas the vertical polarization was minimally perturbed by the system.

calculations and/or weak turbulence effects from having many such coupled beam interactions in the same volume of plasma. We also achieved the first demonstration of a laser-plasma polarizer, which extinguished 85% to 87% of an independent probe beam's horizontal polarization.

ACKNOWLEDGMENT

REFERENCES

1. P. Michel, L. Divol, D. Turnbull, and J. D Moody, Phys. Rev. Lett. **113**, 205001 (2014).

2. D. Turnbull, P. Michel, T. Chapman, E. Tubman, B. B Pollock, C. Y. Chen, C. Goyon, J. S Ross, L. Divol, N. Woolsey, and J. D Moody, Phys. Rev. Lett. **116**, 205001 (2016).

3. D. J. Stark *et al.*, Phys. Rev. Lett. **115**, 025002 (2015).

4. G. Lehmann and K. H. Spatschek, Phys. Rev. Lett. **116**, 225002 (2016).

5. P. Michel *et al.*, Phys. Rev. Lett. **102**, 025004 (2009).

6. S. H. Glenzer *et al.*, Science **327**, 1228 (2010).

7. J. D. Moody *et al.*, Nat. Phys. **8**, 344 (2012).

8. R. K. Kirkwood *et al.*, Phys. Rev. Lett. **76**, 2065 (1996).

9. R. K. Kirkwood, J. D. Moody, A. B. Langdon, B. I. Cohen, E. A. Williams, M. R. Dorr, J. A. Hittinger, R. Berger, P. E. Young, L. J. Suter, L. Divol, S. H. Glenzer, O. L. Landen, and W. Seka, Phys. Rev. Lett. **89**, 215003 (2002).

10. P. Michel *et al.*, Phys. Rev. Lett. **109**, 195004 (2012).

11. R. P. J. Town *et al.*, Phys. Plasmas **18**, 056302 (2011).

12. M. M. Marinak *et al.*, Phys. Plasmas **8**, 2275 (2001).

13. J. S. Ross *et al.*, Rev. Sci. Instrum. **83**, 10E323 (2012).

14. P. Amendt *et al.*, Phys. Rev. E **91**, 023103 (2015).

15. J. R. Rygg, J. A. Frenje, C. K. Li, F. H. Séguin, R. D. Petrasso, J. A. Delettrez, V. Yu. Glebov, V. N. Goncharov, D. D. Meyerhofer, S. P. Regan, T. C. Sangster, and C. Stoeckl, Phys. Plasmas **13**, 052702 (2006).

16. G. Kagan and X.-Z. Tang, Phys. Plasmas **19**, 082709 (2012).

17. C. Bellei and P. A. Amendt, Phys. Rev. E **90**, 013101 (2014).

18. M. J. Rosenberg, A. B. Zylstra, F. H. Séguin, H. G. Rinderknecht, J. A. Frenje, M. Gatu Johnson, H. Sio, C. J. Waugh, N. Sinenian, C. K. Li, R. D. Petrasso, P. W. McKenty, M. Hohenberger, P. B. Radha, J. A. Delettrez, V. Yu. Glebov, R. Betti, V. N. Goncharov, J. P. Knauer, T. C. Sangster, S. LePape, A. J. Mackinnon, J. Pino, J. M. McNaney, J. R. Rygg, P. A. Amendt, C. Bellei, L. R. Benedetti, L. Berzak Hopkins, R. M. Bionta, D. T. Casey, L. Divol, M. J. Edwards, S. Glenn, S. H. Glenzer, D. G. Hicks, J. R. Kimbrough, O. L. Landen, J. D. Lindl, T. Ma, A. MacPhee, N. B. Meezan, J. D. Moody, M. J. Moran, H.-S. Park, B. A. Remington, H. Robey, M. D. Rosen, S. C. Wilks, R. A. Zacharias, H. W. Herrmann, N. M. Hoffman, G. A. Kyrala, R. J. Leeper, R. E. Olson, J. D. Kilkenny, and A. Nikroo, Phys. Plasmas **21**, 122712 (2014).

19. H. G. Rinderknecht, M. J. Rosenberg, C. K. Li, N. M. Hoffman, G. Kagan, A. B. Zylstra, H. Sio, J. A. Frenje, M. Gatu Johnson, F. H. Séguin, R. D. Petrasso, P. Amendt, C. Bellei, S. Wilks, J. Delettrez, V. Yu. Glebov, C. Stoeckl, T. C. Sangster, D. D. Meyerhofer, and A. Nikroo, Phys. Rev. Lett. **114**, 025001 (2014).

20. E. A. Williams *et al.*, Phys. Plasmas **2**, 129 (1995).

Commissioning an X-Ray Detector System for Spectral Analysis of Tritium-Filled Targets

Introduction

Both glass and plastic targets filled with deuterium–tritium mixtures (DT) are used at LLE for research into inertial confinement fusion experiments. These targets are imploded with the 60-beam OMEGA Laser System. The permeation-filling process can take up to a week since the targets must be pressurized to tens of atmospheres without crushing the fragile, thin-wall shells. The overall time required to fill targets depends on the permeation time constant. Typically five or six permeation time constants are used to fill targets to the desired pressure. Although the fill pressure and DT ratio are known precisely, a nondestructive method to verify that the targets actually contain the expected fill pressure at shot time is currently unavailable. Two factors can lead to underfilling a target: (1) The permeation time constant is underestimated so sufficient time is not allowed for the charging pressure to equilibrate with the gas pressure inside the target, or (2) a defect develops in the shell, causing the target to depressurize more rapidly than predicted by the permeation time constant.

An x-ray detection system (XDS) originally developed to measure bremsstrahlung of tritium β decay from the surface of metals[1–3] has been modified and developed with the capability of measuring the pressure of DT fuel inside a target just prior to the shot. This system permits rapid, nondestructive identification of underpressurized targets. This article details the design of the system, discusses preliminary measurements of x-ray emission from glass and plastic targets, and demonstrates that the method can achieve accurate, repeatable measurements.

Equipment Design Features

The XDS comprises three primary components: a high-resolution, dual-axes imaging system for repeatable, accurate target positioning; a helium enclosure with triple-axes micrometer positioning; and an Amptek silicon drift detector (SDD). The SDD was fit with a silicon nitrate (Si_3N_4) window to measure x-ray energies from 200 eV to 40 keV. The detector features a 25-mm^2 silicon drift diode with a measured 130-eV full-width-at-half-maximum resolution at 5.9 keV.

The arrangement of the equipment is illustrated in Fig. 148.15. The origin of the optical axes was defined by centering the window of the detector on the x, y origin in one camera's field of view (FOV) and the side view of the detector window in the z origin of the other camera. The detector was then retracted 25.4 mm in the z direction so that targets placed in the center of both cameras' FOV would be positioned 25.4 mm in front of the detector with a repeatable precision of 10 μm. During all measurement campaigns, the environment was purged with helium at a flow rate of 4 L/min to provide a
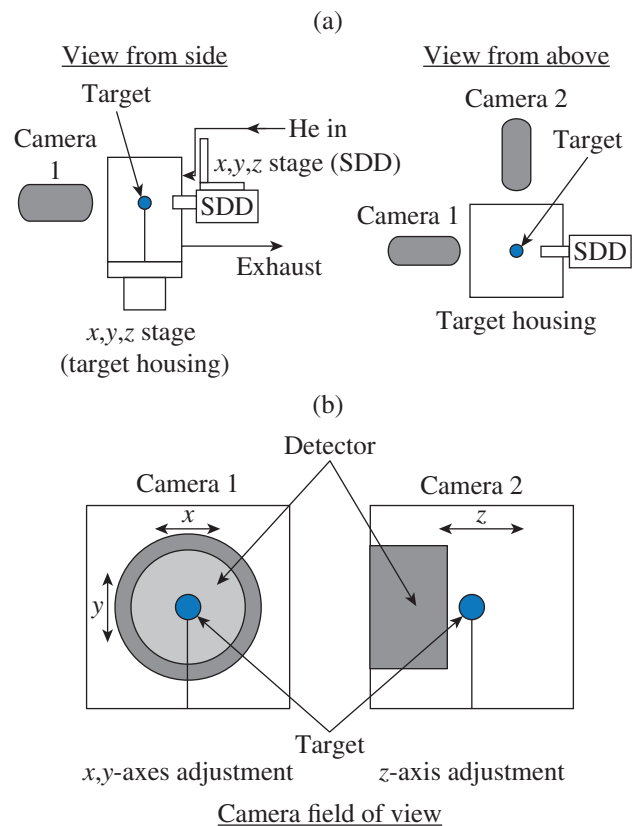
Figure 148.15
Layout of the x-ray detection system. SDD: silicon drift detector.

tenfold volume exchange per minute within the enclosure to minimize air contamination of the chamber and to purge any tritium that permeated from plastic targets.

The response of the SDD was calibrated in air and helium using an ^{55}Fe source. The resulting spectrum is shown in Fig. 148.16. Calibration in air shows the suppression of lower-energy K_α lines such as aluminum and the presence of the argon K_α, as expected. K_α lines from manganese, the ^{55}Fe decay product, are also clearly visible in both the air and helium cover gases. A ^{109}Cd source was used to calibrate the detector over the full energy range of the tritium spectrum.

E22973JR
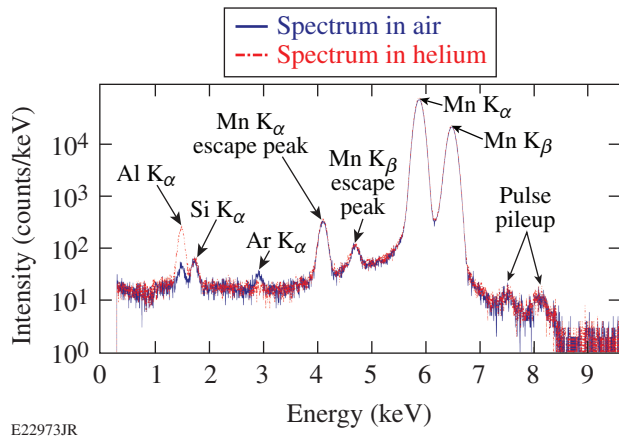
Figure 148.16
The response of the silicon drift detector to an ^{55}Fe source in air and helium.

Spectral Analysis of SiO$_2$, CH, and CD Targets
Decay betas in tritium-filled targets generate both fluorescent and bremsstrahlung x rays as they interact with the shell material. These interactions are illustrated in Fig. 148.17 for both glass (SiO$_2$) and plastic targets. The permeability of tritium through glass is very low at room temperature and very little tritium is present in the enclosure. Additionally, the solubility of tritium in glass is very low and very little tritium resides inside the glass wall of the shell. Almost all decay betas originate in the DT gas and interact with the glass to generate x rays. These electrons have insufficient energy to penetrate the glass wall. By contrast, plastic is highly soluble and permeable to tritium. A 100-nm Al permeation barrier is applied to the shell's exterior to reduce tritium losses from the targets to manageable levels. The plastic contains a significant amount of tritium, and measureable amounts of tritium escape into the enclosure. In this case, decay betas originate in the gas and the plastic and can penetrate the aluminum overcoat together with x rays and tritium molecules.

The emission spectra of glass targets are dominated by the fluorescence from silicon and oxygen atoms in the shell's wall. Two spectra from a glass target filled with 10 atm of 38.3% tritium in DT are shown in Fig. 148.18: one for a 5-min measurement time and one for a 15-h measurement time. The longer measurement time yielded a higher-resolution spectrum with more-discernible features, notably the Al K_α line from the housing of the detector itself. Figure 148.19 illustrates that once the DT gas has leaked out of the glass target, the emission spectrum drops to background levels, demonstrating that the amount of tritium dissolved into the glass is negligible.

Three glass-target silicon K_α lines were measured for 5 min and compared. Two of these targets were imploded on OMEGA later on the same day. As shown in Fig. 148.20, the two silica targets had a Si K_α count rate within 5% of each other and produced neutron yields within 10% of each other on OMEGA.

E22974JR
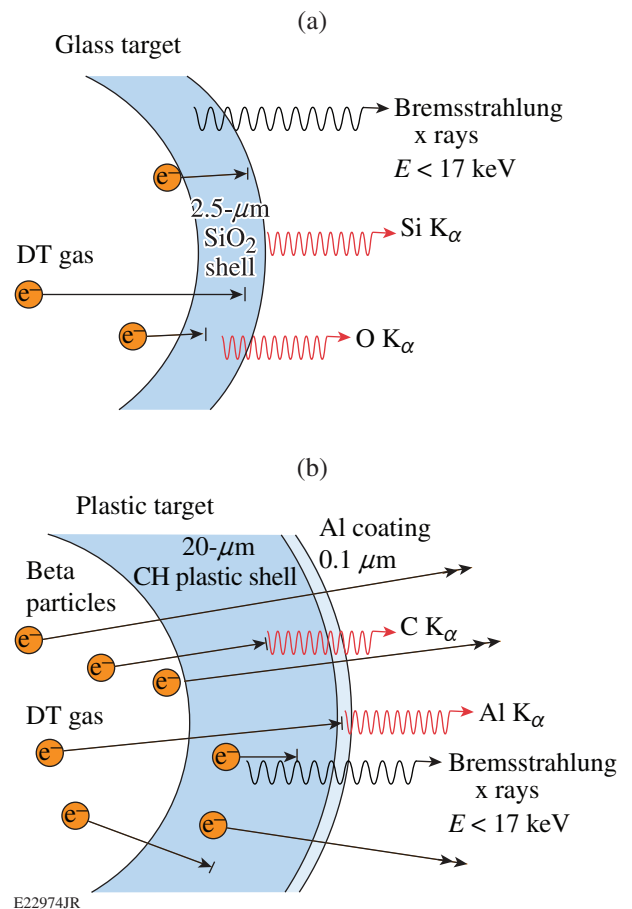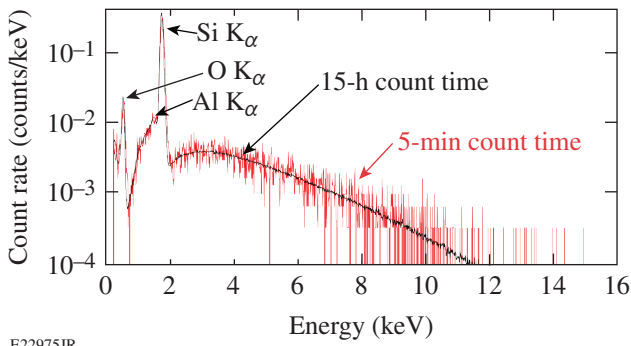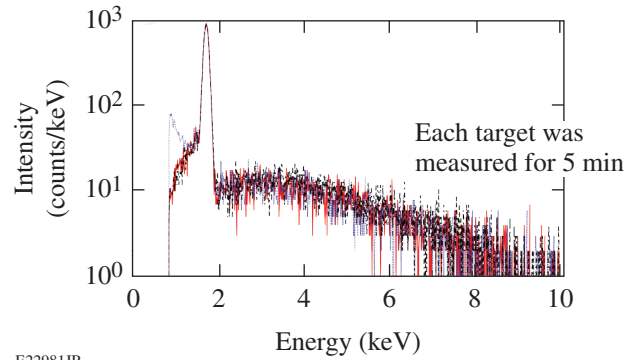
Figure 148.17
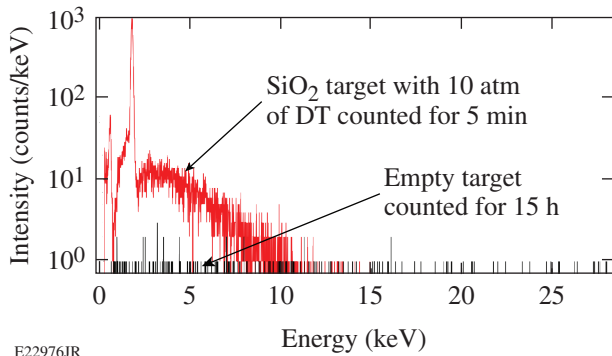Illustration of the interactions decay betas undergo in glass and plastic targets.

Figure 148.18
Comparison of a 5-min emission spectrum and a 15-h emission spectrum collected from a glass target containing 3.83 atm of T.

Figure 148.19
A 5-min spectrum collected from a glass target containing 10 atm of DT compared to a 15-h spectrum collected from glass target that has lost its DT.

Target number	Target ID	Si K_α rate	Neutron yield ($\times 10^{13}$)
SiO$_2$–1	ISE-3Q14-01-8	31.9	3.02
SiO$_2$–2	ISE-3Q14-01-5	31.3	n/a
SiO$_2$–3	ISE-3Q14-01-27	33.5	3.42

Figure 148.20
Five-minute spectra of the three glass targets listed in the table. These targets were fielded on OMEGA.

Figure 148.21
Five-minute spectra collected from two plastic targets: one filled to 3.2 atm of T$_2$; the other filled with 4.2 atm of T$_2$.

Fluorescence does not dominate emission spectra from plastic targets. Figure 148.21 compares two plastic targets in the energy range from 2.5 keV to 12 keV. One target was filled with 4.2 atm of T$_2$ at Lawrence Livermore National Laboratory (LLNL) and then shipped to LLE at liquid nitrogen temperature for attachment to a stalk. The second target was filled at LLE with 16.7 atm of 38.3% tritium in DT, or an equivalence of 3.2 atm of T$_2$ gas. This target was attached to its support stalk using ~80 ng of epoxy prior to filling with DT. Both targets exhibited strong bremsstrahlung emission with fluorescence K$_\alpha$ peaks for aluminum and oxygen. Additionally, the target filled at LLE presented silicon and sulfur K$_\alpha$ lines. Tritium soaked into the silicon stalk and the epoxy while the target was filled with tritium at LLE and subsequently fluoresced the silicon and the sulfur present in the epoxy. The larger amplitude of the aluminum K$_\alpha$ line found in the emission spectrum of the LLNL target may be attributed to the higher tritium pressure and thinner shell wall in that target by comparison to the LLE target.

Beta particles that emerge from the plastic targets can interact with the detector window if the detector is within the beta range. This effect is demonstrated in Fig. 148.22, where emission spectra from plastic and silica targets are compared at 2.54 cm and 1.27 cm from the detector. The silica target exhibits the same bremsstrahlung spectrum at 1.27 cm as it does at 2.54 cm since no betas escape the shell. On the other hand, the emission spectrum from the plastic target develops a more-pronounced bremsstrahlung signature than the silica target at 1.27 cm when the target is close enough to the detector for escape betas to interact with the detector window.
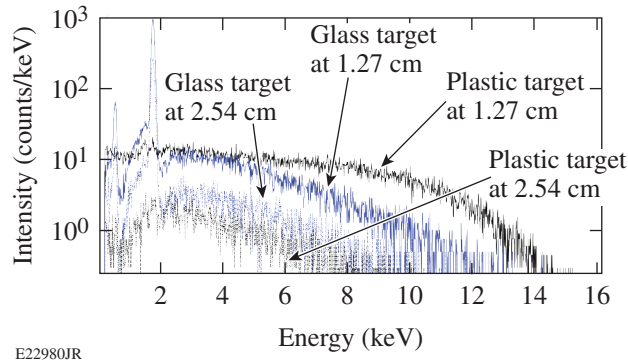
Figure 148.22

Comparison of spectra collected from glass and plastic targets at two distances from the detector to illustrate how decay betas escape from plastic targets interacting with the detector.

Correlation Between Plastic Target Activity and Pressure

Gas loss from plastic targets is approximately exponential. The permeation time constant is measured for each target using D_2 gas at General Atomics after fabrication. These time constants are then used to guide the tritium-filling rate. Once charged to the desired pressure with tritium gas, the targets are placed in cold storage to reduce permeant losses. Targets at LLNL are stored at 77 K, increasing the permeation time constant by a factor of about 1100, while targets at LLE are stored at 150 K, increasing the permeation time constant by a factor of about 800.

The x-ray spectra of five plastic targets were taken continuously while they were outgassing at room temperature to correlate the tritium activity against the gas pressure. All targets were measured at 2.54 cm from the detector face to suppress bremsstrahlung from the detector membrane. The environment was purged with helium at a flow rate of 4 L/min during measurements to prevent a buildup of tritium in the housing as targets outgassed. Two targets (A1 and B1) were measured immediately after removal from cold storage during the diagnostic development campaign and then again after five days of outgassing at 24-h intervals for an additional five days. Three targets (A2, B2, and B3) were measured continuously upon removal from cold storage for a period of six days to obtain the energy/time spectrum. The targets in Group A were filled at LLE with 16.7 atm of DT (38.3% tritium) or an equivalent T_2 fill pressure of 3.2 atm while the targets in Group B were filled at LLNL with T_2. Estimates of tritium content in the targets at the time of the initial x-ray emission measurement and the shell composition are provided in Table 148.V.

All targets were mounted at LLE. For the ease of comparison, DT-filled targets are from here on reported in their equivalent T_2 concentrations.

The time evolution of the spatially integrated count rate of the targets takes on the shape of a double-exponential function as seen in Fig. 148.23. Decay betas from two sources are most likely responsible for the shape of the activity–time curve: decay betas from tritium gas inside the shell and decay betas from tritium dissolved in the target shell. The decay in activity is the result of losing tritium through diffusion through the shell or the dissolution of tritium out of the shell into the helium gas flow away from the detector. The two sources are referred to as the "gas activity" and the "shell activity" to differentiate between the two sources and their effect on the time evolution of the spectrum. The time constant for the gas activity component is expected to be short and dependent on the gas pressure in the target. The shell activity is expected to have a very long time constant since the tritons are most likely chemically bound in the plastic. A 40-h measurement of the change in the baseline activity suggests the time constant for the shell activity is of the order of 3.6 years.

Table 148.V: Tritium-fill pressure and the estimated tritium pressure in each target at the time of the x-ray measurement.

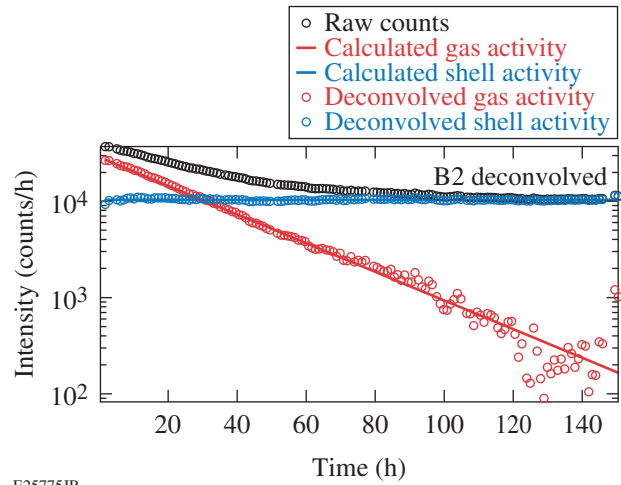| Target ID	Tritium-fill pressure (atm)	Estimated target pressure at time of x-ray measurement (atm)	Shell composition
A1	3.2*	2.9	CD
A2	3.2*	2.4	CH
B1	5.0	3.6	CH
B2	5.1	3.2	CD
B3	12.2	12.2	CD

*Actual fill pressure of 16.7 atm using 38.3% T in DT.
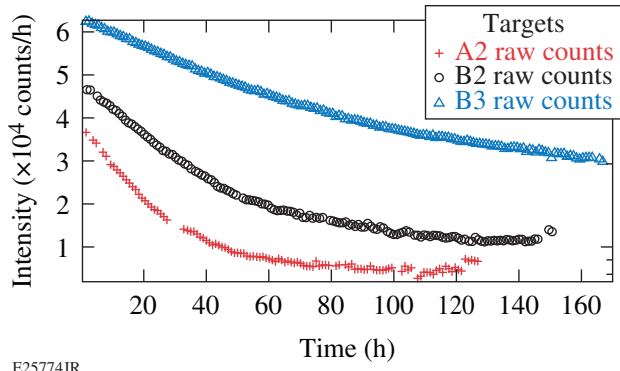
Figure 148.23
The time evolution of the spectrally integrated count rate of three plastic targets outgassing at room temperature.

Figure 148.24
The continuous x-ray spectrum from a plastic target deconvoluted to show the contributions from the DT gas inside the target and from DT gas dissolved in the plastic.
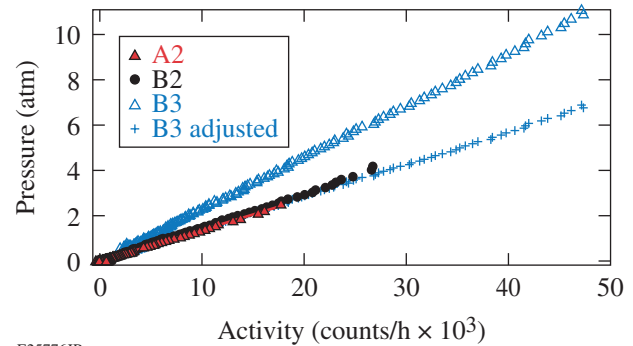
The spectra were fit with weighted double-exponential functions after reaching the baseline shell activity and using 3.6 years as the half-life for the shell's exponential function. Using the measured coefficients, the gas and shell activity were deconvolved from the spectra by subtracting each from the raw data as shown in Fig. 148.24. The measured permeation time constants for the gas activity source are provided in Table 148.VI and compared against the values provided by General Atomics. In each case the DT time constants are longer by at least 50% than the reported time constants determined with D_2 gas.

The pressure of the targets at each measurement interval was calculated using the reported soak time and fill pressures and the measured DT time constant, assuming the tritium loss rate from the target to be exponential. Table 148.VII compares the soak and fill pressures. The calculated target pressure evolution was plotted against the deconvolved gas activity evolution and is shown in Fig. 148.25. Pressure correlates linearly with activity as expected. The slopes of the pressure–activity curves

Figure 148.25
The calculated DT pressure loss from a plastic target compared against the x-ray emission from the residual DT inside the plastic target.

Table 148.VI: Comparison of the D_2 reported time constant with the measured time constant using DT.

Target ID	D_2 reported time constant (h)	Mass-adjusted time constant (h)[*]	DT time constant (h)	Ratio of measured/reported
A2	5.1	5.7	12.8	2.3
B2	11.3	13.8	20.2	1.5
B3	23.7	26.5	39.0	1.5

[*]GA reported half-lives converted to a DT-equivalent time constant using a root-mass difference of the hydrogen isotopologues: D_2, DT, and T_2, i.e., $\sqrt{5/4}$ and T_2 by $\sqrt{3/2}$.

for targets A2 and B2 lie within 8% of one another, while the slope for target B3 is $1.6\times$ greater than the average slopes of the other two targets. Taking the measured tritium activity to be accurate with <1% error in the counting statistics, the initial fill pressure of B3 should be closer to 7.6 atm of T_2 as opposed to the reported 12.2 atm. The pressure–activity curve for B3 using a fill pressure of 7.6 atm of T_2 (shown in Fig. 148.25) is observed to fall in line with the curves for the other two targets. The reduced fill pressure is being determined under the assumption that targets A2 and B2 had more accurately reported fill pressures since their slopes were within 8% of each other.

The shell activity of each target was measured independently using liquid scintillation counting at the end of each measurement campaign. Each target was crushed in liquid scintillation fluid to capture any residual tritium. Each crushed shell was soaked in the liquid scintillation fluid for several days to leach tritium from the plastic. A 1-mL aliquot was extracted from the leachate and measured in the liquid scintillation counter. These activities are also summarized in Table 148.VII. The shell activity was found to be linearly proportionate to the fill pressure of the target, or the initial total activity. Additionally, the plastic walls retained ~30% of the initial target activity.

Conclusions

An XDS has been developed and successfully commissioned with an intended application of nondestructively measuring the activity in tritium-filled targets. The XDS allows for an expedient verification of tritium content in a target prior to it being loaded into the OMEGA target chamber. The measured activities of two of the glass targets have been measured to have a Si K_α activity rate within 5% of each other, which corresponded to neutron yields within 10% after being imploded by the 60-beam OMEGA Laser System. This activity in glass targets is believed to provide a suitable initial baseline for comparison with future glass targets, allowing targets to be screened for low, or vacant, tritium content.

The T_2 permeation half-life has been measured for three plastic targets by continuously measuring the decrease in activity over a period of six days each. The measured half-lives were observed to be between $1.5\times$ and $2.3\times$ longer than the corresponding D_2 half-life values measured by the manufacturer, after taking into account the root–mass difference for DT and T_2. The activity of the tritium bound to the shell was observed to be proportionate to the initial fill pressure. The shell activity was ~30% of the total activity in the target.

The target fill pressure at the time of x-ray measurement was calculated taking into account the different half-lives, fill pressures, and storage times of the targets. Based on the target fill pressure, the activity of A2 was calculated to be 17% lower than A1. The measured activity of A2 was 16% less than A1 for a +1% difference. The targets from Group B exhibited significant deviation from their expected activities. The difference between the expected and measured activities is attributed to an underestimate in the permeation time constant. Adjusting for the longer time constant in the activity of B3 reconciles the apparent discrepancy in the pressure–activity curve when the B3 curve is compared against the curves measured for A2 and B2. The fill pressure of B2 at the time of measurement was calculated to be 7% less than B1, with an expected similar difference in activity. The actual measured activity for B2 was 11% greater than B1 for a difference of +18%. The actual fill pressure of B3 was calculated to be ~33% less than the value reported by General Atomic, based on the slope of the pressure versus activity over time when compared with targets A2 and B2.

The XDS is a robust, nondestructive technique for confirming the actual tritium fill pressure in either glass or plastic targets.

Table 148.VII: Comparison of the shell activity to fill pressure and total target activity.

Target ID	Soak pressure (atm)	Target pressure (atm)	Fill-to-destruction duration	Shell activity (kBq)	Shell activity/ target pressure (kBq/atm)	Shell/total activity (%)
A2	3.2*	2.4	48	926	386	31
B2	5.1	3.2	46	950	297	28
B3	12.2	7.6**	53	1259	166	29

*Adjusted for the actual T_2 content.
**Fill pressure based on known soak time and DT measured time constant.

REFERENCES

1. L. Mao *et al*., Nucl. Instrum. Methods Phys. Res. B **269**, 105 (2011).

2. M. Matsuyama, K. Watanabe, and K. Hasegawa, Fusion Eng. Des. **39–40**, 929 (1998).

3. M. Matsuyama, H. Nakatani, and K. Watanabe, Fusion Eng. Des. **10**, 405 (1989).

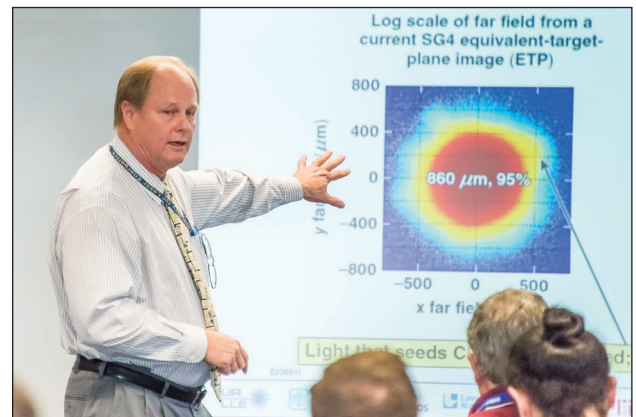# The Eighth Omega Laser Facility Users Group Workshop

Introduction

The Eighth Omega Laser Facility Users Group (OLUG) Workshop was held at the Laboratory for Laser Energetics (LLE) on 27–29 April 2016. More than 110 scientists, postdoctoral fellows (postdocs), and students from institutions in the U.S. and abroad attended the workshop. As has been the case in previous workshops, postdocs and students received travel support for the workshop from the Department of Energy's (DOE's) National Nuclear Security Administration (NNSA).

The Workshop Program

The workshop program included an overview on the National Inertial Confinement Fusion (ICF) Program presented by Keith LeChien from NNSA; four review and science talks by Craig Sangster (National ICF Direct-Drive Program), Carlo Graziani (Inferring Morphology and Strength of Magnetic Fields from Proton Radiographs), Philip Nilson (High-Resolving-Power, Ultrafast Streaked X-Ray Spectroscopy on OMEGA EP), and Jonathan Davies (An Overview on Laser-Driven Magnetized Liner Inertial Fusion on OMEGA); one Omega Laser Facility talk given Samuel Morse (Progress on Recommendations and Items of General Interest); three poster sessions including a total

U2046JR

Figure 148.26
Craig Sangster (LLE) discussed the National ICF Direct-Drive Program.

U2045JR

Figure 148.27
Attendees at the Eighth Omega Laser Facility Users Group Workshop.

of 76 research posters and 15 Omega Laser Facility posters (the majority of the contributed posters were presented by postdocs and students) two mini-workshop sessions dedicated to streak cameras (organized by Charles Sorce) and magneto-inertial fusion electrical discharge system (MIFEDS) (organized by Gennady Fiksel); a students and postdocs panel discussion; a discussion and presentation of the **Findings and Recommendations** (p. 197); and research and career opportunity talks by representatives from Lawrence Livermore National Laboratory (LLNL) (Robert Heeter), Los Alamos National Laboratory (LANL) (S. Batha), Sandia National Laboratories (SNL) (P. Knapp), and LLE (Michael Campbell).

Student and Postdoctoral Poster Awards

In an effort to motivate and reward excellence in young researchers, the posters presented at the OLUG Workshop by students and postdocs are reviewed and ranked by a committee of scientists. As a result, prizes and honorable mentions are given to those posters at the top of the ranking. The following are the awards granted at this OLUG Workshop:

Student Awards

1st prize: Scott Feister, Ohio State University, "Acquisition and Analysis for High-Repetition-Rate HEDP (10 Hz to 1 kHz)"

U2047JR

Figure 148.28
Carlo Graziani (University of Chicago) gave a talk on inferring morphology and the strength of magnetic fields from proton radiographs.

U2054JR

Figure 148.30
Patrick Knapp discussed research and career opportunities at Sandia National Laboratories.

U2048JR

Figure 148.29
Philip Nilson (LLE) gave a talk on high-resolving-power, ultrafast streaked x-ray spectroscopy on OMEGA EP.

U2053JR

Figure 148.31
Michael Campbell discussed research and career opportunities at LLE.

2nd prize: Jeffrey Fein, University of Michigan, "Modeling of OMEGA EP Experiments Studying Z Dependence of the Two-Plasmon–Decay Instability"

3rd prize: Samuel Totorica, Stanford University, "Non-Thermal Electron Energization from Magnetic Reconnection in Laser-Driven Plasmas"

Honorable-Mention Awards

Kevin George, Ohio State University, "Modifying the TNSA Ion Spectrum with Front-Surface Microstructures"

Amina Hussein, University of Michigan, "Optimization of Cold K-alpha Emission Using Copper Foams"

U2055JR

Figure 148.32
Student and postdoc poster awardees. From left to right, back row: Hans Rinderknecht, Alex Zylstra, Scott Feister, Jeffrey Fein, Samuel Totorica, and Hong Sio; front row: Willow Wan, Theodore Lane, and Amina Hussein. Also on the far right, front row are Maria Gatu Johnson and Craig Sangster who led the poster awardees selection process.
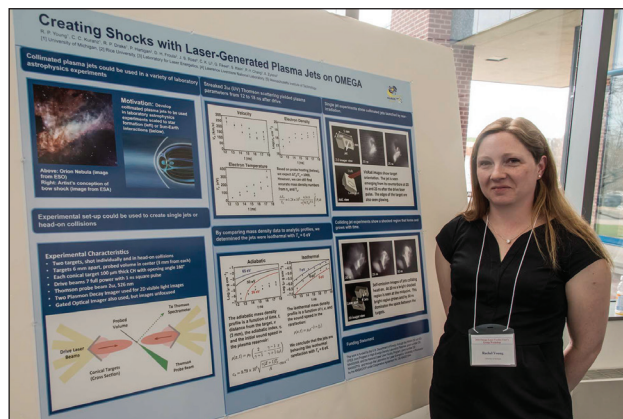
U2049JR

Figure 148.33
Rachel Young (University of Michigan) presented a poster on laser-generated plasma jets.

U2050JR

Figure 148.34
Federica Coppari (LLNL) discusses her poster on equation-of-state measurements on OMEGA.
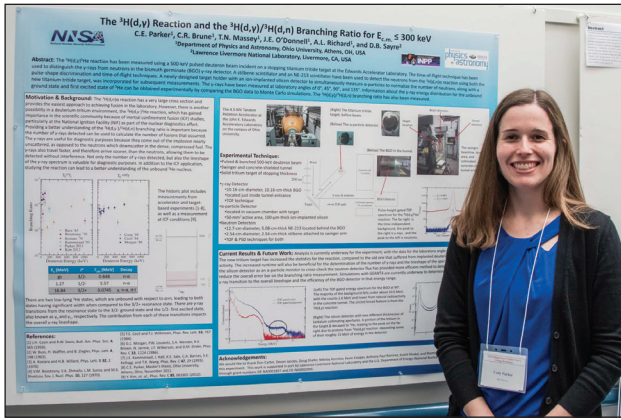
U2051JR

Figure 148.35
Cody Parker (Ohio State University) presented a poster on nuclear reactions with application for ICF diagnostics.

Theodore Lane, West Virginia University, "Improving the Fidelity of Interpreting Time-Averaged Spectra on Z for Development of a Multi-Element Stark-Broadening Diagnostic"

Mary Kate Ginnane and Ethan Turner, State University of New York at Geneseo, "Time-Resolved Tandem Faraday Cup Development for High-Energy TNSA Particles"

Willow Wan, University of Michigan, "Observation of Vortex Merger and Growth Inhibition in a Dual-Mode, Supersonic Kelvin–Helmholtz Instability Experiment"

Hong Sio, Massachusetts Institute of Technology, "Studies of Kinetic/Multi-Ion–Fluid Effects and Ion–Electron Equilibration in ICF Plasmas Using Multiple Nuclear and X-Ray Emission Histories"

Postdoctoral Fellow Awards
1st prize: Hans Rinderknecht, Lawrence Livermore National Laboratory, "Studies of Ion Species Separation in ICF-Relevant Plasmas at Omega"

2nd prize: Alex Zylstra, Los Alamos National Laboratory, "Studying Astrophysical Nucleosynthesis Using Inertially Confined Plasmas at Omega"

3rd prize: Siddarth Patankar, Lawrence Livermore National Laboratory, "Initial Results of Short-Pulse Laser Interactions with Optically Levitated Microdroplets"

Bylaws, Nominations, and Election

In the fall of 2015, members of OLUG approved the first set of bylaws for OLUG. Paul Drake (University of Michigan) gave a presentation on the bylaws and the approval process. Based on the guidelines established by the bylaws, Roberto Mancini (University of Nevada, Reno) led in the winter of 2016 the first nomination and election to select two new members for OLUG's Executive Committee (EC): one representative from a U.S. university/small business and one representative from a national laboratory/major business. To this end, a nominations committee was set up comprised of Roberto Mancini (Chair),

U2056JR

Figure 148.36
Paul Drake (University of Michigan) discussed the OLUG bylaws approved in the fall of 2015.

U2057JR

Figure 148.37
Roberto Mancini (University of Nevada, Reno) explained the nomination and election process carried out in the winter of 2016.

Tammy Ma (LLNL), and Farhat Beg (University of California, San Diego). This committee requested nominations from OLUG members from mid-January through mid-February of 2016. The election, which followed in February and March, resulted in the selection of Johan Frenje (MIT) and Mingsheng Wei (GA) as new members of the EC. Current members of OLUG's EC for April 2016–April 2017 include the following:
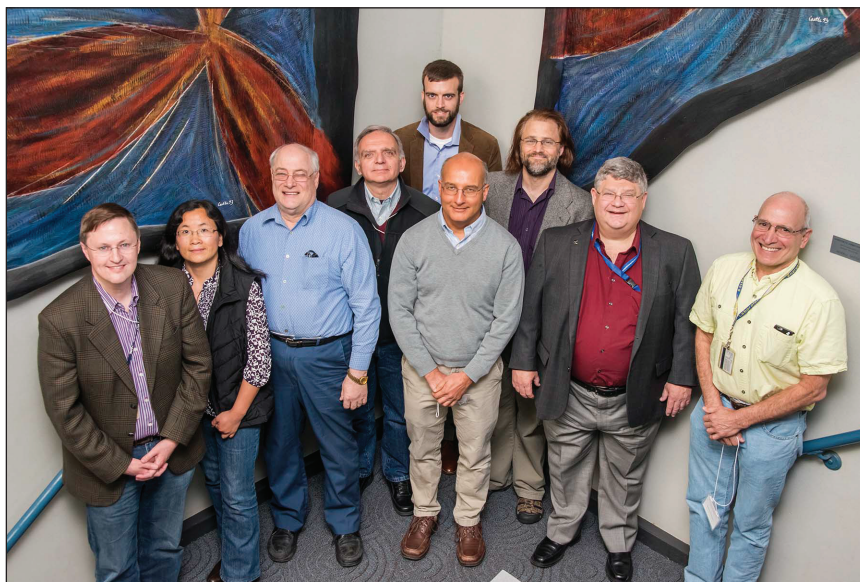
- Chair: Roberto Mancini (University of Nevada, Reno)

- University/small business: Paul Drake (University of Michigan), Johan Frenje (MIT), and Mark Koepke (West Virginia University)

- National laboratory/major business: Peter Celliers (LLNL), Kirk Flippo (LANL), and Mingsheng Wei (GA)

- Junior researcher: Alex Zylstra (LANL)

- Non-U.S. researcher: Peter Norreys (Rutherford Laboratory, U.K.)

- LLE, ex-officio: James Knauer

The first chairperson of OLUG, Richard Petrasso, has stepped down after leading OLUG for the eight years since its creation. The EC and the members of OLUG are very grateful to Richard Petrasso for his leadership, commitment, and generous dedication to making OLUG a success and serving as a role model for other facility users groups in the U.S. in the area of high-energy-density science.

Summary of Findings and Recommendations

An important outcome of OLUG's annual workshop is the list of Findings and Recommendations that OLUG submits for consideration to LLE's management. The list of 2016 Recommendations is summarized below, including those put forward by the postdocs and student panel.

1. A two-step upgrade of the magnetic-field capability on OMEGA: first, increase the magnetic field to 30 T within the next two years; second, a future enhancement to increase to 50 T.

2. Investigate the "straight-through" issue with the streaked x-ray spectrometer (SXS-SSCA) including the option of replacing the TIM-based streak camera (SSCA) with a newer/better camera.

U2058JR

Figure 148.38
OLUG Executive Committee for April 2016–April 2017. From left to right: Johan Frenje (MIT), Mingsheng Wei (GA), James Knauer (LLE), Roberto Mancini (University of Nevada, Reno, Chair), Alex Zylstra (LANL), Peter Celliers (LLNL), Kirk Flippo (LANL), Paul Drake (University of Michigan), and past-chair Richard Petrasso (MIT). Not shown in the photo: Mark Koepke (West Virginia University) and Peter Norreys (Rutherford Laboratory, U.K.).

U2059JR

Figure 148.39
Paul Drake led the discussion on the **Findings and Recommendations**.

U2052JR

Figure 148.40
Students and postdocs are shown during their panel discussion session.

3. Make a second x-ray streak camera available on OMEGA with capabilities similar to those of SSCA.

4. Implement a Rochester Optical Streak System (ROSS) streak camera on OMEGA for the particle and x-ray temporal diagnostic (PXTD).

5. Use charge-coupled–device (CCD) detectors with the x-ray framing cameras on OMEGA EP.

6. Implement a standardized calibration procedure of the OMEGA optical Thomson-scattering system.

7. Implement faster framing cameras for Thomson-scattering measurements on OMEGA.

8. Undertake the necessary modifications on frequency conversion, final focusing optics, and distributed phase plates to enable a 2ω operation on one of the long-pulse beams of OMEGA EP.

9. Implement near-backscatter–imager (NBI) and time-integrated scatter calorimeter (SCAL) diagnostics on OMEGA EP.

10. Reconfigure the spherical-crystal-imaging (SCI) diagnostic hardware on OMEGA EP to a design similar to the SCI operational on OMEGA, where the line-of-sight block is a component held by the same ten-inch manipulator (TIM) and the detector is outside of the TIM.

11. Improve the projection capability of the OLUG Workshop conference room so that material being used in the discussion sessions can be projected from any Windows laptop or MacBook in the room.

12. Make several improvements to OMEGA's capability to measure low-energy neutron spectra in a DT background.

13. Enhance the active shock breakout (ASBO)/streaked optical pyrometer (SOP) diagnostic.

14. Install a planar cryogenic system on OMEGA EP to provide an additional capability that could complement the National Ignition Facility (NIF) capability and significantly broaden the possibilities for experiments in this area of study.

15. Consider adding plasma sacrificial mirrors to OMEGA EP.

16. Investigate the implementation of an enhanced laser pulse-shaping capability on OMEGA.

17. Allocate more resources to the CR39 etch/lab group to better support the increasing demand of this detector system on OMEGA and OMEGA EP experiments.

18. Consider making gas jet targets available for OMEGA and OMEGA EP.

19. Consider the development of a high-spectral-resolution x-ray spectrometer for OMEGA.

20. If possible, avoid parallel OLUG Workshop sessions in the future. We recommend that next year's evening session focus on x-ray imaging techniques. We appreciate the reinstatement of the national labs session on Friday and recommend additional opportunities for career-oriented interaction between young researchers and representatives of the laboratories—for example, during lunch or by creating an employment-opportunities board. The student/postdoc representative will organize these events at the 2017 workshop in consultation with the rest of the executive committee.

21. Continue the effort to improve and modernize web-based resources. We also recommend that LLE commits resources to development in two new areas: first, enhance the data downloading capability: exporting shot request form (SRF) configuration data as a "parseable file" (e.g., XML), providing diagnostic characterization information, and moving all results and analysis to the Principal Investigator (PI) computer; second, overhaul the data access permissions so that they are more reliable and potentially more granular, rather than blanket institution-based access.

LLE's Summer High School Research Program

During the summer of 2016, 13 students from Rochester-area high schools participated in the Laboratory for Laser Energetics' Summer High School Research Program. The goal of this program is to excite a group of high school students about careers in the areas of science and technology by exposing them to research in a state-of-the-art environment. Too often, students are exposed to "research" only through classroom laboratories, which have prescribed procedures and predictable results. In LLE's summer program, the students experience many of the trials, tribulations, and rewards of scientific research. By participating in research in a real environment, the students often become more excited about careers in science and technology. In addition, LLE gains from the contributions of the many highly talented students who are attracted to the program.

The students spent most of their time working on their individual research projects with members of LLE's technical staff. The projects were related to current research activities at LLE and covered a broad range of areas of interest including laser physics, computational modeling of implosion physics, experimental diagnostic development, experimental modeling and data analysis, physical chemistry, optical design, tritium capture and storage, cryogenic target characterization, and scientific web page development (see Table 148.VIII).

The students attended weekly seminars on technical topics associated with LLE's research. Topics this year included laser physics, fusion, holography, nonlinear optics, atomic force microscopy, optical instruments, and pulsed power. The students also received safety training, learned how to give scientific presentations, and were introduced to LLE's resources, especially the computational facilities.

The program culminated on 24 August with the "High School Student Summer Research Symposium," at which the students presented the results of their research to an audience including parents, teachers, and LLE staff. The students' written reports will be made available on the LLE Website and bound into a permanent record of their work that can be cited in scientific publications.

Three hundred and fifty-three high school students have now participated in the program since it began in 1989. This year's students were selected from approximately 60 applicants.

At the symposium LLE presented its 20th annual William D. Ryan Inspirational Teacher Award to Mrs. Shayne Watterson, a chemistry teacher at Penfield High School. This award is presented to a teacher who motivated one of the participants in LLE's Summer High School Research Program to study science, mathematics, or technology and includes a $1000 cash prize. Teachers are nominated by alumni of the summer program. Mrs. Watterson was nominated by Emma Garcia and Felix Weilacher, participants in the 2014 program. Emma wrote, "Mrs. Watterson inspired me and the rest of her classes every single day, regardless of the difficulty of the topic… Mrs. Watterson's enthusiasm for her subject is unmistakable… Plenty of times she came up with creative and fun ways for us to learn new concepts. For example, she made up an electromagnetic wave dance to show how the electric wave and the magnetic wave combine and move together." She noted that Mrs. Watterson "is concerned with the success of each of her students as individuals" and concluded by saying, "Mrs. Watterson is probably the best teacher I have ever had, and has showed me both how much fun science can be and how I can pursue it as a career." Felix said of Mrs. Watterson, "There are those who choose to make lives out of leading and inspiring future generations, and for their efforts our communities are certainly and greatly enriched." He noted that Mrs. Watterson "spent huge amounts of time with individual students, be it after school or during free periods, helping them steadily through areas they did not understand." He described Mrs. Watterson as "a truly inspirational teacher, who can affect a student in wonderful ways, pushing the student into new experiences, guiding the student through new layers of learning, and unlocking that student's potential."

Table 148.VIII: High School Student and Projects—Summer 2016.

Name	High School	Supervisor	Project Title
Kyle Bensink	Victor	D. W. Jacobs-Perkins	Post-Shot Data Analysis Tools for Cryogenic Target Shots
Lindsay Browning	Penfield	R. S. Craxton	Development of a Standardized Saturn Ring for Proton Backlighter Targets at the National Ignition Facility
James Hu	Brighton	R. W. Kidder	Using Social Media Technologies for Online Scientific Analysis and Collaboration
Webster Kehoe	Wilson Magnet	R. S. Craxton	Beam-Pointing Optimizations for OMEGA Implosions
Grace Lenhard	Prattsburgh	W. T. Shmayda	Characterizing a Cu/Mn Alloy for Extracting Oxygen from Inert Gas Streams
Joseph Mastrandrea	Webster Thomas	W. T. Shmayda	Measuring Hydrogen Pressure over a Palladium Bed
Nathan Morse	Allendale Columbia	M. J. Guardalben	OMEGA Frequency-Conversion Crystal Designs for Improved Power Balance
Sapna Ramesh	Pittsford Mendon	K. L. Marshall	Characterization of the Electrical Properties of Contaminated Dielectric Oils for Pulsed-Power Research
Archana Sharma	Webster Schroeder	A. Kalb	Design and Optimization of a Portable Wavefront Measurement System for Short-Coherent-Length Laser Beams
Jonah Simpson	Brighton	C. Stoeckl	Validating the Fast-Ion Energy Loss Model in the Monte Carlo Simulation Toolkit Geant4 and Simulating Laser-Driven Nuclear Reaction Experiments on OMEGA EP
Matthew Wang	Pittsford Sutherland	C. Stoeckl	Impulse Response Calibration of a Neutron Temporal Diagnostic Using the Multi-Terawatt Laser
Leah Xiao	Webster Schroeder	R. S. Craxton	Simulations of Laser-Driven Magnetized-Liner Inertial Fusion
Joy Zhang	Penfield	R. T. Janezic	Development of a Digital Microscope for the Characterization of Defects in Cryogenic DT-Filled Targets

FY16 Laser Facility Report

During FY16, the Omega Facility conducted 1414 target shots on OMEGA and 779 target shots on OMEGA EP for a total of 2193 target shots (Tables 148.IX and 148.X). OMEGA averaged 11.7 target shots per operating day with Availability and Experimental Effectiveness averages for FY16 of 95.6% and 96.6%, respectively.

OMEGA EP was operated extensively in FY16 for a variety of internal and external users. A total of 718 target shots were taken into the OMEGA EP target chamber and 61 joint target shots were taken into the OMEGA target chamber. OMEGA EP averaged 7.9 target shots per operating day with Availability and Experimental Effectiveness averages for FY16 of 96.9% and 95.8%, respectively.

Table 148.IX: OMEGA Laser System target shot summary for FY16.

Laboratory/ Program	Planned Number of Target Shots	Actual Number of Target Shots	ICF	Shots in Support of ICF	Non-ICF
CEA	44	55	—	—	55
HED	423.5	491	—	—	491
LANL	44	52	52	—	—
LBS	115.5	136	—	—	136
LLE	352	327	—	327	—
LLNL	77	75	75	—	—
NLUF	198	232	—	—	232
SNL	22	22	22	—	—
Calibration	0	24	—	24	—
Total	1276	1414	149	351	914

Table 148.X: OMEGA EP Laser System target shot summary for FY16.

Laboratory/ Program	Planned Number of Target Shots	Actual Number of Target Shots	ICF	Shots in Support of ICF	Non-ICF
HED	180	292	—	—	292
LBS	54	82	—	—	82
LLE	120	161	—	161	—
LLNL	12	14	14	—	—
NLUF	90	110	—	—	110
NRL	18	25	25	—	—
SNL	24	37	37	—	—
Calibration	0	58	—	58	—
Total	498	779	76	219	484

Highlights of Achievements in FY16

Spherical implosions on the OMEGA Laser System benefit from symmetric laser drive and uniform beam focal spots. As we continue to seek higher implosion pressures, we have embarked upon a system-wide campaign for improvements in subsystems to achieve improved power balance and uniformity.

In FY16, efforts have focused on temporally balancing the energy over 100-ps intervals of the pulse shape. To achieve this, each stage of beam splitters, spatial filters, and amplifiers must have the passive transmission losses and active gain balanced. An observed visible scatter (haze) has developed on several amplifier disks over 21 years of service, prompting investigation of transmission *in situ*. The haze is a scattering source for IR light and is a primary loss mechanism in the OMEGA system. Efforts in FY16 led to the discovery that this haze can be cleaned and the disks restored to pristine transmission characteristics. Since each amplifier exhibits a unique amount of haze, we will utilize system time in FY17 to systematically address the losses. Additionally, the spatial-filter transmission is affected by damage sites in the lenses. A tighter threshold for replacement was adopted in FY16 to minimize contributions to imbalance. We also completed development of a characterization tool to ensure quantitative measurement of the lens-damage site area within the beam aperture.

The OMEGA equivalent-target-plane diagnostic is a precision far-field laser instrument for characterizing the on-target beam uniformity. It has existed since FY01 and had been used to sample Beam 46 for 15 years. During FY16 it was changed from Beam 46 to Beam 56 to allow a second sample of the laser system. This capability will be used in FY17 to further study the on-target focal spot compared to x-ray images of the same beam recorded on an x-ray charge-coupled–device (CCD) diagnostic.

The relative phase of OMEGA smoothing by spectral dispersion (SSD) modulators gives an effective pointing shift to the on-target focal spot when SSD is used on picket pulses. This phenomenon led LLE to synchronize the modulators to the pulse shape. Previously, the co-timing has been set at the beginning of the day using target shots in an operationally costly manner. This year, a pulse shape was created that has a temporal profile matching the modulation period so that the majority of setup can be achieved before target shots and verified during the standard setup shots such as the pointing shot. Additionally, a streaked spectrometer at the output of the system has been fabricated and dedicated to SSD phase

measurement, ensuring that drift does not limit this key aspect of focal-spot position during the campaign.

Several efforts have also been pursued to improve laser capabilities on OMEGA. The beam-to-beam timing system has been optimized to reduce the mean arrival time of the pulse to <3-ps root mean square (rms).[1] This method was demonstrated in FY15 and refined to enable quarterly calibration runs during FY16. The UV spectrometer focus was improved and spectrally calibrated using an in-house laser source matched to the primary wavelength. The OMEGA users identified a need for additional beam blocks to prevent blowthrough on the target chamber. Nine additional units were acquired, increasing the total available to 15.

LLE has supported laser-driven MagLIF (magnetized liner inertial fusion) experiments on OMEGA, including experiments where preheating the gas within a magnetized cylindrical target during compression is required. MagLIF on OMEGA utilizes 40 laser beams to compress a cylindrical target, one beam to preheat the fuel, and the magneto inertial fusion electrical discharge system (MIFEDS) to provide an axial magnetic field. A project was implemented in FY16 to improve the symmetry by properly orienting a single laser beam with respect to the compression beams. This symmetry is not readily available with the spherical symmetry of beams on OMEGA. The Beamline 35 pulse is redirected with the use of multiple mirrors to Port P9 and focused onto the cylindrical target using a newly acquired focus lens for the third-harmonic (351-nm) light. The energetics of Beam 35 are controlled by detuning frequency-conversion efficiency to achieve ~200 J in a 2-ns pulse.

The OMEGA EP short-pulse laser presents a number of challenges to operation because of the high fluence of the beam. Early in FY16, the lower-compressor diagnostic beam path was augmented with a large-aperture, neutral-density (ND) filter to reduce the accumulated *B*-integral distortions and enable the ability to diagnose the temporal and spectral characteristics of the signal path beam at higher energies. Significant improvements in the available uniformity of filter glass made it possible to calibrate the spatial transmission of this optic. This action ensured the safe operation of the laser at energies much closer to the upper-compressor capabilities.

Numerous improvements have been made to the OMEGA EP Laser System including an overhaul of the SBSS (stimulated Brillouin scattering suppression) system. This system ensures

that acoustic waves are not generated during propagation of laser pulses by giving the beam a small amount of bandwidth to avoid the nonlinear Brillouin scattering effect. This effort reduced the amount of lost shot time from >600 min to <40 min per quarter. The short-pulse diagnostic package scanning autocorrelator was upgraded with an improved CCD detector replacing a photodiode, and the ultrafast temporal diagnostics (UTD) upgrade continued to explore the capabilities of pulse lengths between best compression (~700 fs) and 10 ps. The UTD scopes were ordered and will be installed in early FY17.

Additional diagnostic capabilities added in FY16 include a low-yield neutron time-of-flight diagnostic on the H15 port of OMEGA, covering a new range of neutron energies. The proton temporal diagnostic received a 3-cm nose cone, enabling one to more precisely measure DD and D^3He reaction history.

LLE has taken important steps in the development of future target diagnostics, one of which is the OMEGA EP subaperture backscatter system—an initial capability established in FY16. This hardware will measure the stimulated Brillouin and stimulated Raman scattering bands on a UV beam from the target. Measurements began in the fourth quarter and will be used to define the final system architecture.

Important time-integrated measurements of the high-resolution spectrometer diagnostic were completed in FY16. The shots collected data on scientific cameras (future use will include a streak camera for time-resolved measurements) using the two crystal options and paved the way for final design of the system.

The Experimental Operations and support groups have integrated several new key features to improve operational efficiency. The OMEGA Target Bay structure has been augmented with 600 ft^2 of additional decking space to make storage of the increasing ten-inch–manipulator diagnostic inventory more readily available. Additionally, the darkrooms have been outfitted with digital scanners to rapidly provide a moderate resolution image of film-based data to the Principal Investigator and aid in experimental direction during the campaign.

REFERENCES

1. W. R. Donaldson, J. Katz, R. Huff, E. M. Hill, J. H. Kelly, J. Kwiatkowski, R. B. Brannon, and R. Boni, Rev. Sci. Instrum. **87**, 053511 (2016).

National Laser Users' Facility and External Users' Programs

Under the facility governance plan implemented in FY08 to formalize the scheduling of the Omega Laser Facility as a National Nuclear Security Administration (NNSA) User Facility, Omega Laser Facility shots are allocated by campaign. The majority (68.2%) of the FY16 target shots were allocated to the Inertial Confinement Fusion (ICF) Campaign conducted by integrated teams from Lawrence Livermore National Laboratory (LLNL), Los Alamos National Laboratory (LANL), Naval Research Laboratory (NRL), Sandia National Laboratories (SNL), and LLE and the High-Energy-Density (HED) Campaigns conducted by teams led by scientists from the national laboratories, some with support from LLE.

The Fundamental Science Campaigns accounted for 25.5% of the Omega Facility target shots taken in FY16. Over 61% of these shots were dedicated experiments under the National Laser Users' Facility (NLUF) Program, and the remaining shots were allotted to the Laboratory Basic Science (LBS) Program, comprising peer-reviewed fundamental science experiments conducted by the national laboratories and by LLE.

The Omega Laser Facility was also used for several campaigns by teams from the Commissariat à l'énergie atomique et aux energies (CEA) of France. These programs are conducted at the facility on the basis of special agreements put in place by Department of Energy (DOE)/NNSA and participating institutions.

The facility users during this year included 13 collaborative teams participating in the NLUF Program; 14 teams led by LLNL and LLE scientists participating in the LBS Program; many collaborative teams from the national laboratories and LLE conducting ICF experiments; investigators from LLNL, LANL, and LLE conducting experiments for high-energy-density–physics programs; and scientists and engineers from CEA.

In this article, we briefly review all the external user activity on OMEGA during FY16.

FY16 NLUF Program

FY16 was the second of a two-year period of performance for the NLUF projects approved for FY15–FY16 funding and Omega Laser Facility shot allocation. Thirteen NLUF projects (see Table 148.XI) were allotted Omega Laser Facility shot time and conducted a total of 342 target shots at the facility. The FY16 NLUF experiments are summarized in this section.

Fast-Electron Energy Coupling and Transport in Warm Dense Plasmas

Principal Investigators: F. N. Beg and C. M. Krauland (University of California, San Diego)
Co-investigators: M. S. Wei (General Atomics); J. J. Santos (Centre Lasers Intenses et Applications, Université Bordeaux); and W. Theobald (LLE)
Graduate Students: S. Zhang and J. Peebles (University of California, San Diego)

Understanding the transport physics of an intense relativistic electron beam in plasmas of varying density and temperature is crucial for many high-energy-density systems, including advanced ignition schemes (e.g., fast ignition and shock ignition) and energetic proton source generation. The fast-electron current (>MA) produced from petawatt laser–matter interaction is much greater than the Alfvén current, and while propagating in plasmas, this super-Alfvénic electron beam draws a return current of background electrons that acts as a neutralizing force. As the return current propagates in the target, resulting joule heating causes variations in the resistivity. Depending on the medium and the current density, either divergence-causing resistive filamentation instabilities or collimating resistive magnetic fields can occur. This award investigates fast-electron propagation in cold and pre-assembled large-volume plasmas to understand the role of resistive effects.

In FY16 experiments, we used OMEGA EP to examine electron-beam transport in allotropes of carbon. Samples of

Table 148.XI: NLUF proposals approved for shots at the Omega Laser Facility for FY15–FY16.

Principal Investigator	Institution	Title
F. N. Beg	University of California, San Diego	Fast-Electron Energy Coupling and Transport in Warm Dense Plasmas
A. Bhattacharjee	Princeton University	Dynamics of Magnetic Reconnection and Instabilities of Current Sheets in High-Energy-Density Plasmas
R. P. Drake	University of Michigan	Experimental Astrophysics on the Omega Laser Facility
T. Duffy	Princeton University	Dynamic Compression of Earth and Planetary Materials Using the OMEGA Laser
P. Hartigan	Rice University	Magnetic Accretion Shocks and Magnetospheres in the Laboratory
R. Jeanloz	University of California, Berkeley	Exploring the Quantum Mechanics of Dense Matter
K. Krushelnick	University of Michigan	X-Ray Measurements of Laser-Driven Relativistic Magnetic Reconnection Using OMEGA EP
D. Q. Lamb	University of Chicago	Nonlinear Amplification of Magnetic Fields in Laser-Produced Plasmas
E. P. Liang	Rice University	Creation of a Magnetized Jet Using a Hollow Ring of Laser Beams
R. D. Petrasso	Massachusetts Institute of Technology	Explorations of Inertial Confinement Fusion, High-Energy-Density Physics, and Laboratory Astrophysics
A. Spitkovsky	Princeton University	Generation of Collisionless Shocks in Laser-Produced Plasmas
M.-S. Wei	General Atomics	Hot-Electron Scaling in Long-Pulse Laser–Plasma Interactions Relevant to Shock Ignition
L. Willingale	University of Michigan	High-Energy Electron-Beam Acceleration from Underdense Plasma Using OMEGA EP

both single-crystal, chemical-vapor–deposition diamond and vitreous carbon were compared since the atomic ordering of a material can have a significant impact on resistivity itself. If the ions are highly disordered, as in the case of vitreous carbon, then electrons scatter incoherently and their mean free path limited to the mean inter-ionic distance results in high resistivity. We used the OMEGA EP IR sidelighter beam (850 J, 10 ps) to irradiate a 10-μm-thick coating of Al on both targets to produce the electron beam. Transport and energy deposition are inferred from the measured fast-electron–induced fluorescence emission of a Cu tracer layer on the opposite side of the carbon, seen in the target schematic of Fig. 148.41. We also compared the initially cold target shots to those that were shock heated from the high-energy, 4-ns-long pulse laser irradiation (~2 × 10^{14} W/cm^2) onto a 30-μm CH ablator. The shock propagated through the carbon layer toward the Al, creating a roughly uniform heated medium behind the front. The electron beam was then injected at various times relative to the shock location.

Our results show distinct differences in the divergence of hot electrons between the two initially cold samples. In data from a spherical crystal imager (SCI) tuned to Cu K$_\alpha$ (~8 keV), the short-pulse interaction with the Al target layer is recorded by the bright bremsstrahlung spot produced at the interaction. This provides a spatial fiducial for the 2-D, time-integrated Cu fluorescence images resulting from electrons moving through the target and impacting the Cu layer. SCI shows that strong resistive filamentation occurs in the vitreous carbon but not the diamond [Figs. 148.42(a) and 148.42(b)]. This is expected from the instability growth analysis that shows the higher resistivity leading to faster growth rates. When both targets are first heated via long-pulse irradiation, the background and high-angle divergence emission is significantly reduced and a more-focused beam is evidenced in the diagnostics. Figure 148.43(a) shows the difference in profiles for the cold versus heated high-density carbon, suggesting a collimating effect from magnetic-field growth. Similarly, in the vitreous
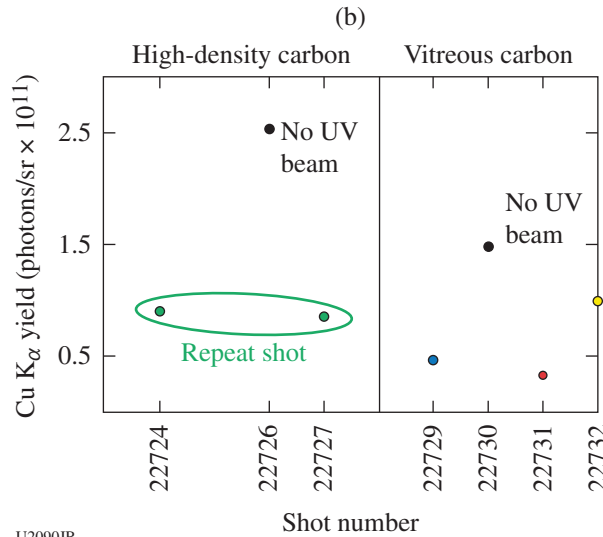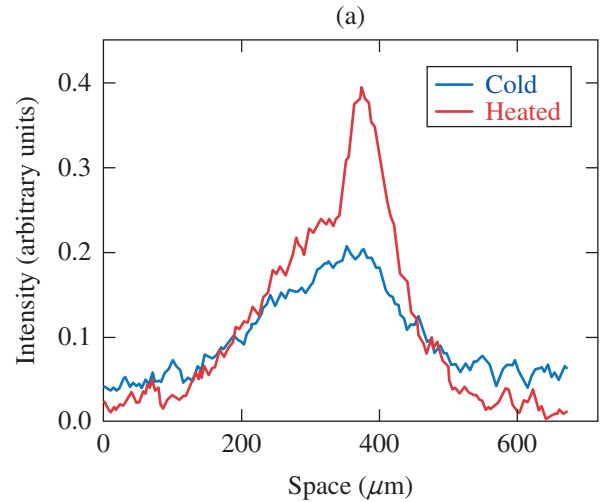
carbon case, a more-localized emission is observed along the target axis but there is no evidence of filamentation. When the electron beam is injected into a fully shocked vitreous carbon layer, the Cu K_α yield is comparable to the high-density car-

bon case. Spectral analysis is ongoing but preliminary results suggest significant variation in temperature when the electron beam is injected at different delays. Particle-in-cell simulations are being performed to separate the effects of resistive heating and magnetic-field growth, including at target layer interfaces.
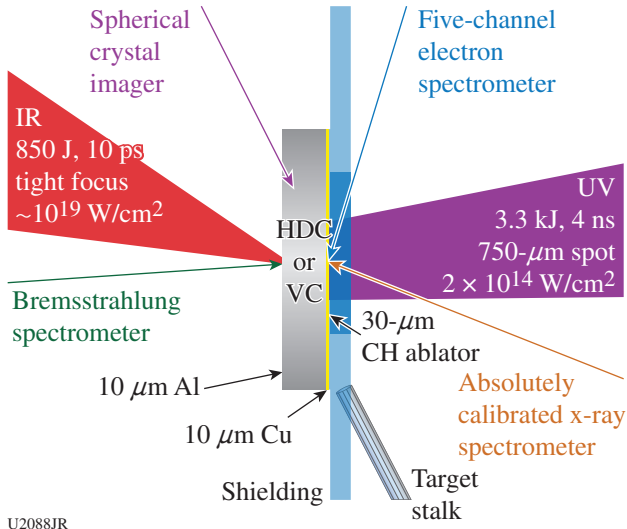
Figure 148.41
Schematic of the shock-heated sample experiment in the OMEGA EP chamber and the primary diagnostics detecting hot-electron characteristics. The targets were either high-density carbon (HDC) or vitreous carbon (VC). Some shots were performed without the UV beam in an otherwise identical configuration.

Figure 148.42
Spherical crystal imager (SCI)–measured Cu K_α images from short-pulse–only shots for (a) HDC and (b) VC. A spherical crystal imager (SCI) views the target 73.4° off of target normal.

Figure 148.43
(a) SCI spatial profile of fluorescence emission from copper in HDC shots, showing evidence of a focused electron beam with bright localized emission when the target is initially shock heated. (b) Plot of Cu K_α photon yield calculated from spectra recorded on the calibrated zinc von Hamos x-ray spectrometer. While the overall signal drops when the targets are initially heated, this is likely caused by the refluxing of electrons over the entire target, as seen in the SCI data. The red, blue, and yellow dots correspond to a shock position 1/5, 2/3, and fully through the carbon target layer, respectively.

Multi-Nanosecond X-Ray Source Characterization on OMEGA

Principal Investigators: R. P. Drake, P. A. Keiter, and C. C. Kuranz (University of Michigan)
Co-investigators: D. Shvarts, Y. Elbaz, and G. Malamud (Negev Research Center); A. Frank and E. Blackman (University of Rochester); and B. van der Holst (University of Michigan)
Graduate students: J. Davis and R. Van Dervort (University of Michigan)

Soft x-ray sources provide a unique tool for probing and driving matter in high-energy-density systems. Our specific interest is using them for laboratory-astrophysics experiments driven by soft x rays at below 1 keV. To produce a readily characterized source of such x rays, we used a gold conversion foil, heated by high-energy laser beams, then acting as a quasi-blackbody emitter. Previous sources of this type had durations of 1 ns or less. Here, we used OMEGA to demonstrate a source with a duration of 6 ns. To optimize the source for this duration, we characterized the temporal and spatial emission from laser-heated foils of varying thickness.

Figure 148.44 shows a schematic of the experiments. The experiments used 0.5-, 0.75-, 1.0-, and 1.5-μm-thick foils, which were directly heated by a 2.0-kJ, 6-ns laser pulse produced by overlapping laser beams that were smoothed using SG5 phase plates, to produce a laser energy flux of 1×10^{14} W/cm^2. We measured the spatial profile of the x-ray emission using an x-ray framing camera with a soft x-ray nose cone to be able to image the x-ray emission in the 200- to 300-eV and 400- to 500-eV bands in addition to imaging the harder x rays. The Dante photodiode array measured the temporal characteristics of the emission with particular focus on the sub-keV energy bands [Fig. 148.44(b)].

We measured emission from both the irradiated and non-irradiated sides of the foil. The measurements of the irradiated side provided a baseline for future comparison when the source is used with a physics package and the emission from the non-irradiated side cannot be measured. From the Dante output we inferred a time-varying effective temperature, defined as the temperature of a blackbody source that would produce the observed energy flux. The thinnest foils (0.5 μm) produce an ~6-ns, 100-eV source. Thicker foils result in a lower effective temperature as well as a delay in the onset of emission. We were surprised to find the emission to be sustained for 6 ns with a foil as thin as 0.5 μm. Modeling of this case suggests that the laser heating creates and sustains a heated region throughout

the gold, and that the foil density remains high enough to prevent the laser from penetrating through the foil up to 6 ns. As foil thickness increases, the effective temperature decreases significantly. The results were very reproducible.

We therefore have demonstrated that one can produce a simple, reliable x-ray source near 100-eV effective temperature, several nanoseconds in duration on OMEGA. We intend to use this source for laboratory-astrophysics experiments.
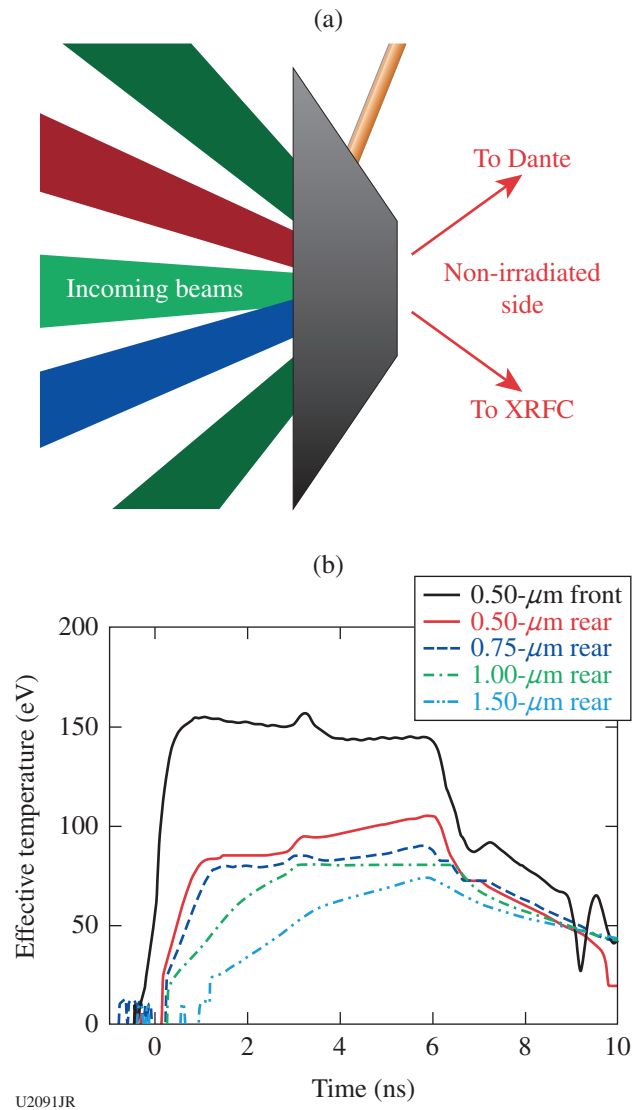

Figure 148.44
(a) Experimental schematic. The laser irradiates the left side of the gold, with Dante and the x-ray framing camera (XRFC) performing most measurements on the non-irradiated side. (b) Effective temperature versus time calculated from the Dante voltage signals. The onset slows and the peak effective temperature decreases as foil thickness increases.

Crystal Structure and Melting of a Laser-Shocked Fe–Si Alloy

Principal Investigators: T. S. Duffy (Princeton University) and R. G. Kraus (LLNL)

Co-investigators: R. F. Smith and F. Coppari (LLNL); J. K. Wicks (Princeton); and T. R. Boehly (LLE)

Graduate Student: M. G. Newman (California Institute of Technology)

The equations of state of potential Earth core alloys at pressures and temperatures near the solid–liquid coexistence curve are important for understanding dynamics at the inner core boundaries of the Earth and super-Earth extrasolar planets. Silicon is one of the most-promising candidates for the light element of the core. An iron–silicon alloy with composition Fe–15wt% Si (Fe–15Si) has been shown to phase separate at static high pressures into an Fe-rich hexagonal close-packed (hcp) phase and a cesium chloride structured (B2) phase.[1] This decomposition requires chemical diffusion of atoms, which is an inherently slow process. Previous studies of the structure and melting behavior of the iron silicide system have been limited to the more-modest temperatures and pressures that are attainable with a laser-heated diamond anvil cell. The OMEGA and OMEGA EP Laser Systems offer the capability to probe the iron silicide system at higher pressures and temperatures as well as dramatically different time scales (~1 ns versus ~1 h).

We have conducted a series of laser-driven shock-melt experiments on textured polycrystalline Fe–15Si samples on OMEGA and OMEGA EP. Measured particle velocities in the Fe–15Si samples using the line velocity interferometer system for any reflector (VISAR) were used to infer the thermodynamic state of the shocked samples. *In-situ* x-ray diffraction measurements using the powder x-ray diffraction image-plate (PXRDIP) diagnostic (Fig. 148.45) were used to probe the melting transition and investigate the decomposition of Fe–15Si into a Si-poor hcp phase and Si-rich B2 phase. Our work addresses potential kinetic effects of decomposition caused by the short time scale of laser-shock experiments. In addition, the thermodynamic data collected in these experiments add to our understanding of the equation of state of Fe–15Si, which is a candidate for the composition in Earth's outer core.

Our experimental results show a highly textured solid phase upon shock compression to pressures ranging from 170 to 300 GPa. The high degree of texturing makes it difficult to definitively identify the structure of the high-pressure solid phases, and both hcp and B2 phases are considered candidate
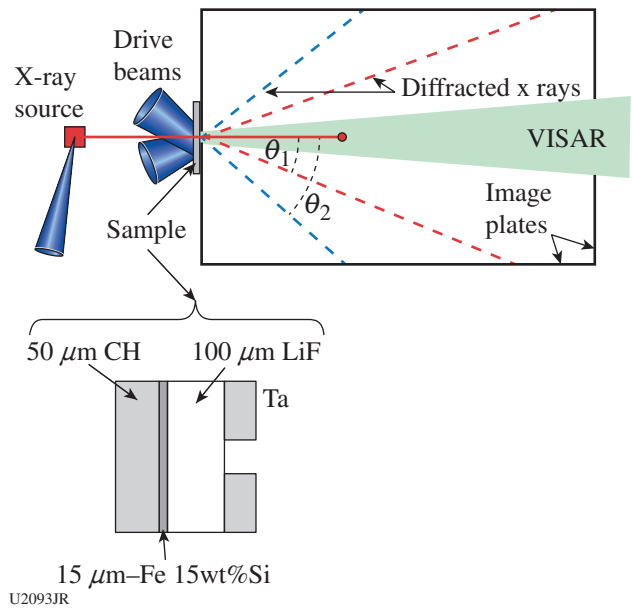

Figure 148.45
Schematic illustration of powder x-ray diffraction image-plate (PXRDIP) diagnostic for x-ray diffraction measurements on OMEGA and OMEGA EP. The diagnostic consists of a rectangular box whose interior is lined with image plates. X rays from a backlight source are used to probe the crystal structure of the laser-driven Fe–Si sample. The target package consists of an ablator, Fe–Si sample, and a LiF window mounted on a pinhole that serves to collimate the incident x rays. VISAR: velocity interferometer system for any reflector.

structures. Upon shock compression above 300 GPa, the intense and highly textured solid diffraction peaks give way to diffuse scattering and loss of texture, consistent with melting along the Hugoniot (Fig. 148.46). This is the first direct determination of Hugoniot melting of a Fe–Si alloy. These measurements will enable us to place new constraints on the effect of alloying on the melting temperature and crystal structure of iron near-Earth core conditions.

Dynamics of Magnetic Reconnection in High-Energy-Density Plasmas

Principal Investigators: W. Fox, D. Schaeffer, and A. Bhattacharjee (Princeton University); G. Fiksel (University of Michigan); and D. Haberberger (LLE)

We have developed and conducted experiments on OMEGA EP to study the phenomenon of magnetic reconnection. Magnetic reconnection occurs when regions of opposite directed magnetic fields in a plasma can interact and relax to a lower-energy state; it is an essential plasma-physics process in many systems that governs the storage and explosive release of magnetic energy in systems such as the Earth's magnetosphere,
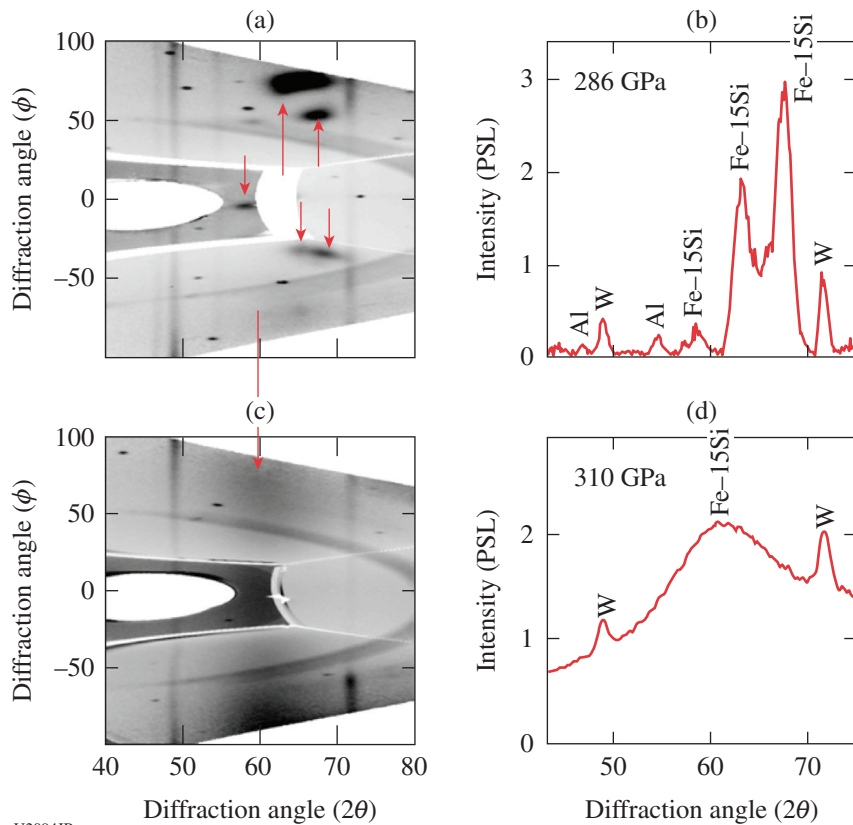
Figure 148.46

(a) Representative x-ray diffraction data for shocked Fe–15Si projected into 2θ versus ϕ space, which correspond to the polar and azimuthal angles about the incident wave vector, respectively. The red arrows point to the diffraction peaks associated with the shock-compressed sample. (b) The corresponding 1-D integrated diffraction patterns for these experiments. [(a) and (b)] At 286 GPa, textured diffraction peaks consistent with hcp/B2 Fe–Si are observed. [(c) and (d)] At 317 GPa, we observe diffuse scattering consistent with shock melting of the sample.

U2094JR

the solar corona, and magnetic-fusion devices. The energy thereby liberated can produce heat and flows and can cause a large number of particles to accelerate to high energies.

These experiments on OMEGA EP used an externally applied magnetic field of the order of 10 T as the seed field for reconnection. With an externally applied field, the fields undergoing reconnection are under experimental control, so it is possible to conduct experiments with variable fields and topologies.

We have successfully carried out two experimental shot days on OMEGA EP. These experiments used the magnetized colliding plasma platform developed by our group and first published in Ref. 2.

The first shot day used the angular filter refractometry diagnostic to observe the density evolution of the expanding plumes. These experimental results provide a measurement of the plasma density flowing with the magnetic field. This determines the plasma regime for reconnection and the flows and allows us to apply accurate initial conditions in our computation models of the colliding plumes and reconnection.

On the second shot day we used the proton radiography to obtain high-resolution images of the magnetic fields in the colliding plasmas. We successfully obtained data at both high- and low-temperature plasma conditions. These results were obtained very recently and are under analysis, but sample data are shown in Fig. 148.47. The data show proton-radiography measurements that are sensitive to the magnetic fields. Light to dark represents increasing fluence of the protons. We observe white "ribbons" on the edge of each expanding plume; each plume is a region of compressed magnetic field that is sufficiently strong enough ($B \sim 25$ T) to deflect the diagnostic protons off-detector and leave a white low-fluence area. We also observe thin, dark "caustics," which are regions where the protons are focused owing to large gradients of magnetic field. The results show a very rapid evolution of the current sheet from laminar to breaking up as the two plasmas collide, over only a very short time span (3.8 ns versus 4.0 ns). The fast breakup includes the generation of horizontal caustics, indicating the generation of multiple islands resulting from multiple reconnection sites. These results are presently being analyzed and compared with our particle-in-cell code.

(a)

(b)
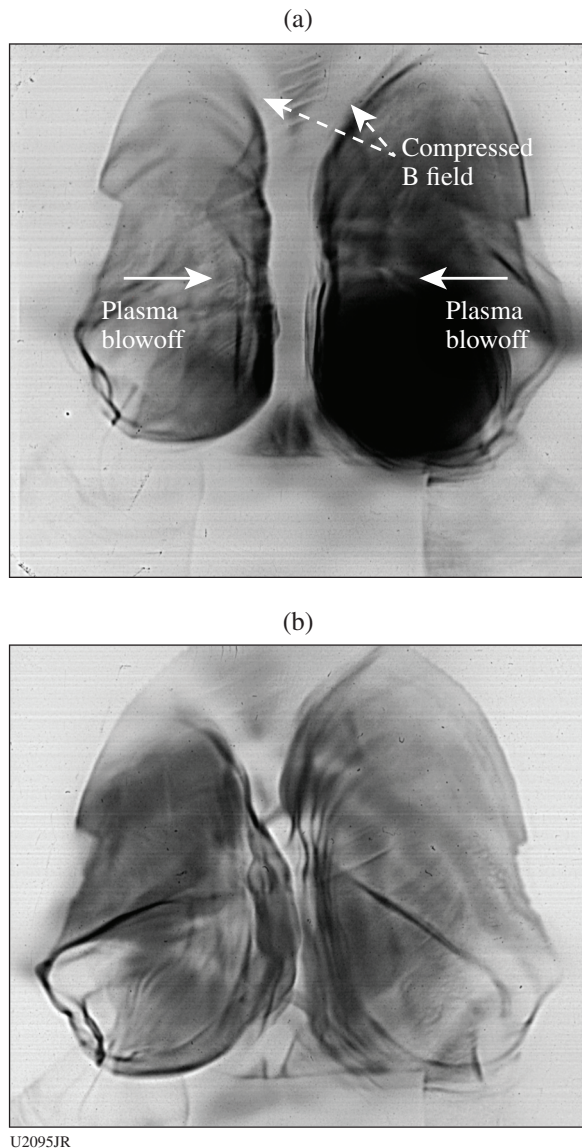
U2095JR

Figure 148.47

Fast evolution of the current sheet measure with proton radiography. The contrast indicates fluence of diagnostic protons, and white areas indicate regions where the magnetic field frozen into the plasma is strong enough to deflect the diagnostic protons off-film. (a) Evolution at 3.8 ns showing the formation of the current sheet as two plumes collide. (b) Evolution a short time later at 4.0 ns showing the fast breakup of the current sheet into smaller-scale structures.

Magnetized Accretion Shocks and Magnetospheres in the Laboratory

Principal Investigator: P. Hartigan (Rice University)
Co-investigators: C. C. Kuranz, G. Fiksel, J. Levesque, and R. Young (University of Michigan); J. M. Foster and P. Graham (Atomic Weapons Establishment; A. Frank (University of Rochester); A. Liao (Rice University); and C. K. Li and R. D. Petrasso [Massachusetts Institute of Technology (MIT)]

Our campaign seeks to develop experiments that feature strongly magnetized, high-Mach-number shock waves in a controlled laboratory environment. These experiments are motivated by the many astrophysical systems where magnetic fields play a key role in determining how supersonic flows interact with their surroundings. Examples include stellar winds, jets from young stars and black holes, interacting binary systems, accretion disks around young stars, planetary magnetospheres, and exoplanetary atmospheres that are subjected to both radiation and winds from their host stars.

Our previous work succeeded in making analogues for both a magnetized-accretion column and a planetary magnetosphere. The accretion-column experiments impacted a magnetized plume of supersonic plasma onto a surface, while the magnetosphere designs drove a supersonic flow (the laboratory equivalent of a solar wind) past a current-carrying wire (a planetary magnetosphere), with the goal to see if we could observe the enhanced magnetic pressure influence the offset of the bow shock from the surface of the wire. While both experiments showed promise, in both cases it was clear that the flow was too dense and too impulsive—the flow simply pushed the shock onto the surface of the obstacle.

To address this issue, we developed a new drive (Fig. 148.48) and performed a series of Thomson-scattering measurements in October 2015 to verify that the numerical models provided the desired ranges of density and velocity. Figure 148.48(b) highlights several regions in density and velocity that are unsuitable for the study of magnetized dynamical effects because the gas is too dense to be a plasma (mauve area), the field diffuses out of the material (green area), a shock does not form (blue area), the field is too strong to allow a shock to form (gray area), or the field is too weak to show dynamical effects (red area). We have found diagrams like that in Fig. 148.48 to be very useful in providing a broad overview of the plasma parameters associated with any experimental design. Our numerical models, verified by the Thomson-scattering data, show that the wind from the colliding flows remains in the desired range of parameter space for over 100 ns, equivalently $20\times$ the characteristic dynamical time scale for laminar flow past the wire.

During the most recently completed shot day (in August 2016), we successfully acquired our first proton radiography images of the system (Fig. 148.49). These experiments used a dual-wire configuration for the target: one wire carrying current and the other one inactive. The images, still being analyzed, reveal a very sharp feature that we believe is a compressed magnetic layer in the dense zone behind the bow shock. These images have

significantly better spatial resolution than the two-photon–decay imager (TPDI) optical images we have been using to date and appear to be an excellent diagnostic for these types of experiments. Our preliminary analysis implies that a radial flow from the wire, driven by irradiation from the foils, also affects the

system dynamics. If confirmed, the system would then resemble an irradiated exoplanetary atmosphere embedded within a strong stellar wind. Differences between the thicknesses and intensities of the caustics for the 3-MeV and 15-MeV protons should provide clues as to the thickness of the magnetized shocked layer.

(a)

(b)
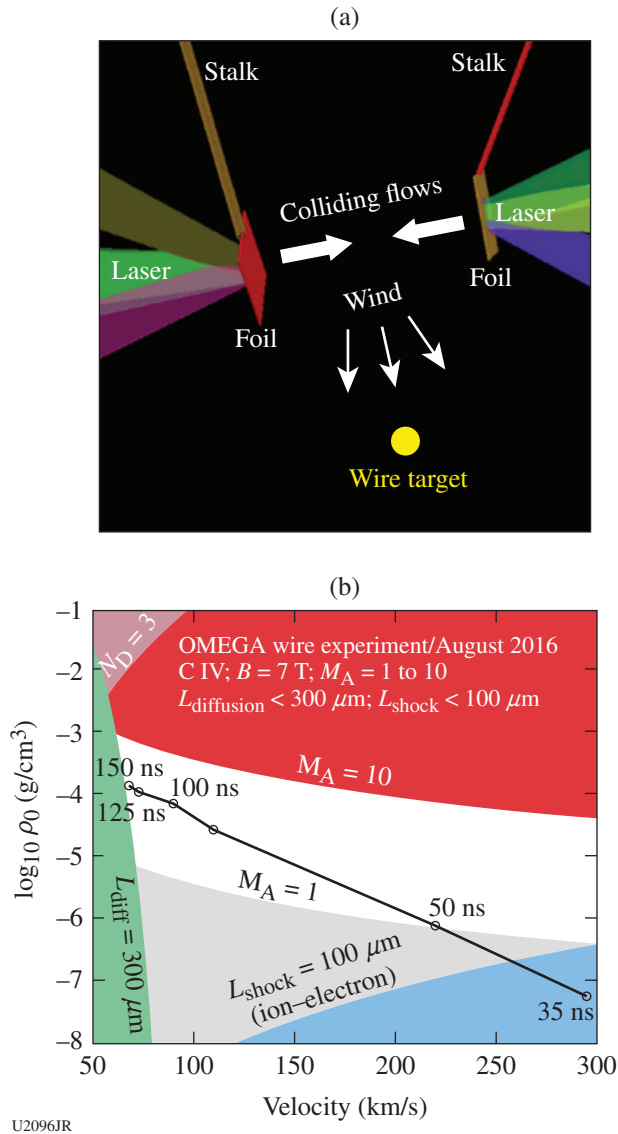
Figure 148.48
New drive design. (a) Design concept showing two colliding flows. Lasers irradiate graphite foils and create oppositely directed impulsive flows that collide and make a more-steady supersonic wind. Adjusting the angle between the two flows allows one control over both the density and velocity. (b) Parameter space for the drive. Shaded areas (green: magnetic diffusion; mauve: warm dense matter; blue: no shock formation; gray: sub-Alfvénic; and red: weak field) are not optimal for observing dynamical effects of fields. The line shows that the drive parameters remain in the correct regime for a time interval of over 100 ns.

(a)

(b)
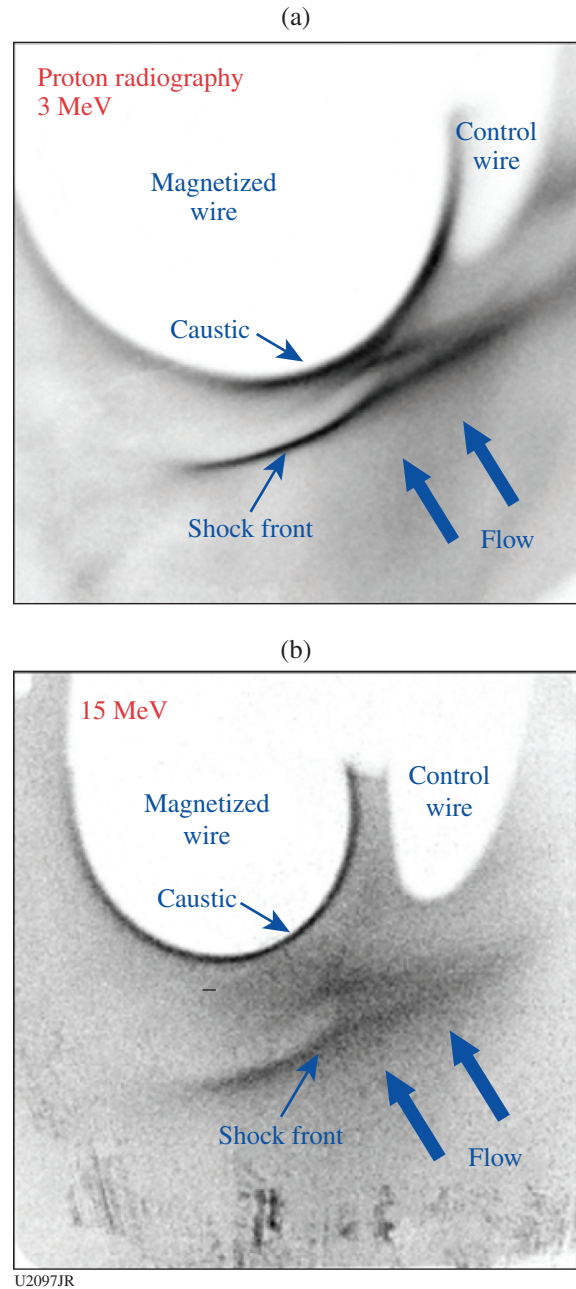
Figure 148.49
Proton radiographs of the wire magnetosphere experiment. The magnetic field from the current in the wire bends protons away from the wire to form a caustic, which is displaced more when the protons are less energetic. A second caustic forms as the magnetic field is compressed in the post-shock region.

The program currently supports the thesis work of three graduate students: R. Pierson and J. Levesque (University of Michigan) and A. Liao (Rice University). These students have been directly involved in the target designs, data analysis, and numerical modeling and on shot days have traveled to the Omega Laser Facility, where they have been involved with real-time decisions concerning the experiment.

Quantum Mechanical and Indirect Diamond Anvil Cell Campaigns
Principal Investigator: R. Jeanloz (University of California, Berkeley)
Co-investigators: P. Loubeyre and S. Brygoo (CEA); and M. Millot, J. R. Rygg, J. H. Eggert, P. M. Celliers, and G. W. Collins (LLNL)

In FY16, the University of California, Berkeley–CEA–LLNL team continued to explore the properties of warm dense hydrogen isotopes at extreme density using ultrafast optical diagnostics under shock compression. We conducted three half-days of experiments, using several-kJ, 1-ns drives to launch strong shocks in hydrogen precompressed to 15 GPa. Active shock breakout (ASBO, velocimetry) and streaked optical pyrometry (SOP) were used to monitor the shock-front velocity, reflectivity/absorptivity, and thermal emission during its travel in the hydrogen layer and in the quartz reference plate. Using impedance matching, new pressure–density–temperature equation-of-state data were obtained, and new data were collected on the metallization of hydrogen at unprecedented conditions approaching the predicted plasma-phase transition (PPT) (Fig. 148.50). In parallel, the team also developed a new approach for collecting multishock data on precompressed samples that allowed us to reach even higher densities in the vicinity of the PPT.
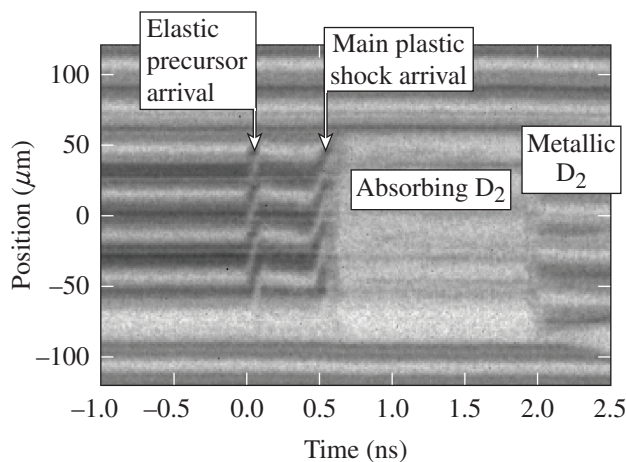
To pave the way for future National Ignition Facility (NIF) experiments, our team also started to develop an indirect-drive diamond anvil cell (DAC) platform on OMEGA using gold halfraums. Three half-day campaigns provided a wealth of information on this new platform and showed that a higher-pressure, highly planar shock could be obtained. Strong photoionization was always observed, however, even when using different halfraum geometries of drive configurations.

X-Ray Measurements of Laser-Driven Relativistic Magnetic Reconnection Using OMEGA EP
Principal Investigators: K. Krushelnick, A. Raymond, L. Willingale, A. Thomas, and T. Batson (University of Michigan); P. M. Nilson and C. Mileham (LLE); G. J. Williams and H. Chen (LLNL); and W. Fox (Princeton University)

Previous laser-driven magnetic-reconnection experiments used kilojoule-class, nanosecond-duration laser pulses (long-pulse regime) focused to moderate intensities $I \sim 10^{14}$ to 10^{15} W/cm^2 to heat a solid target and create two colliding plasmas. Azimuthal megagauss magnetic fields in each are driven together by frozen-in-flow, i.e., the bulk motion of the plasma, or hot-electron flows, resulting in electron acceleration by the reconnection fields to energies exceeding an order of magnitude larger than the thermal energy. This experimental regime allows for dimensionless parameter scalings with many astrophysical systems. Until now, however, the extremely energetic class of astrophysical phenomena, including high-energy pulsar winds, gamma-ray bursts, and jets from galactic nuclei, where the energy density of the reconnecting fields exceeds the rest mass energy density, has been inaccessible in the laboratory. This is the regime of relativistic reconnection, which results in much higher energies of accelerated electrons because of longer confinement of the charged particles within

U2098JR

Figure 148.50
Raw velocimetry [active shock breakout (ASBO)] data for a multishock in deuterium precompressed to 13 GPa that will provide new insight into hydrogen's insulator-to-metal transition near the predicted plasma-phase transition. After the breakout of a two-shock structure from the diamond into the deuterium layer, D_2 becomes opaque before becoming reflecting (metallic) when the shock bounces off the second diamond anvil and sends a second shock into the D_2.

the acceleration region. With OMEGA EP we have been able to use laser pulses of much higher intensity ($I > 10^{18}$ W/cm^2) that generate a dense, relativistic electron plasma within the focal volume during the interaction with a solid foil target. In this regime, magnetic-field–generation mechanisms and transport are governed by the relativistic electron population and its dynamics. The expansion of the hot-electron plasma rapidly sets up a space-charge field at the target–vacuum interface, confining a large portion of the electrons to expand radially along the target surface. These currents generate an azimuthal magnetic field with ~100-MG magnitude expanding radially at about the speed of light. Generating two such interaction sites produces a reconnection geometry with plasma characteristics of the relativistic reconnection regime.

In these experiments an x-ray (copper K$_\alpha$) imaging technique visualized the fast electrons accelerated in the reconnection region to provide spatial information about the extent of the current sheet and also allowed us to take time-resolved measurements of the x-ray emission. Our simulations show that the plasma density and magnetic-field characteristics in the reconnection region satisfy $\sigma > 1$, indicating these experiments are in the relativistic reconnection regime. The experiments focused two short-pulse laser beams onto micron-scale thick copper foil targets to focal spots separated by a distance x_{sep}. A generalized experimental schematic and diagram of the two-spot field geometry with corresponding magnetic and electric fields are depicted in Fig. 148.51. When the antiparallel magnetic fields meet in the midplane between the interaction sites, the field lines can break and reconnect within a reconnection layer, deflecting inflowing electrons and supporting a target-normal electric field supported by the Hall effect and by thermal pressure. This localized electric field generates a current sheet, with electrons being accelerated into the dense regions of the plasma. These fast electrons undergo ionizing collisions with atoms in the target and K-shell electrons are emitted (these atoms recombining on femtosecond time scales). K$_\alpha$ x-ray emission occurs as the L-shell electrons transition to

U2099JR
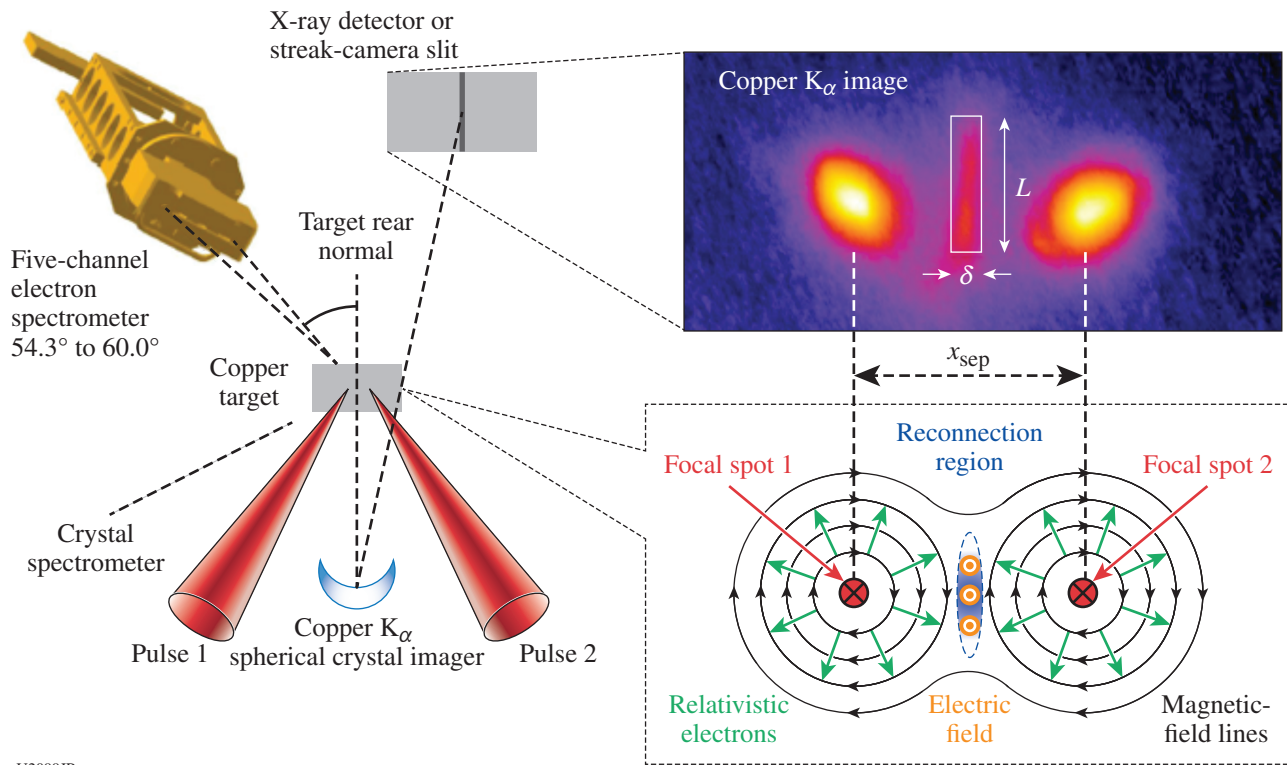
Figure 148.51

A schematic of the experimental geometry for the OMEGA EP experiments. The spherical crystal images x rays from the front side of the target onto a detector. A typical K$_\alpha$ image is shown with the reconnection layer highlighted in the white box with length (L) and width (δ) labeled. A physical picture of the interaction illustrates the two azimuthal magnetic fields expanding into the reconnection region where a target normal electric field accelerates the electrons into the dense target to generate the copper K$_\alpha$ emission in the midplane.

the K shell. Therefore, by imaging the K$_\alpha$ (8.048-keV) emission with a spherically bent quartz x-ray crystal, we are able to produce a map of the current sheet generated between the magnetic-field regions and therefore diagnose the reconnection process.

With this experimental geometry, separation scans of the focal spots were performed with the HERCULES laser at the University of Michigan (2-J, 40-fs pulses focused to extreme intensities 2×10^{18} W/cm^2 onto 12-μm copper foils) and OMEGA EP at LLE [500 J/1000 J, 20 ps focused to comparable intensities of (1 to 2) $\times 10^{18}$ W/cm^2 onto 50-μm copper foils]. Two bright K$_\alpha$ sources corresponding to the target heating within the focal volume were observed on both systems (Fig. 148.52). Additionally a separation-dependent enhancement of the K$_\alpha$ radiation at the midplane was measured corresponding to the current sheet. Detailed analysis of the midplane K photons with a von Hamos crystal spectrometer

allowed us to estimate that they originated from within a cold, relatively deep plasma, consistent with a population of accelerated electrons in the midplane by the reconnection electric field. Further, x-ray pinhole camera images found no midplane emission between 2 to 6 keV, ruling out collisional heating between the two plasmas as a source of the K$_\alpha$ enhancement. Figure 148.53 shows the measured midplane signal (a) width and length and (b) normalized signal as a function of the focal separation. To search for additional signatures of electrons accelerated by the reconnection electric field, a five-channel electron spectrometer was utilized on OMEGA EP at the target rear (Fig. 148.54). It showed angularly dependent nonthermal features super-imposed on a quasi-Maxwellian energy distribution, suggesting rear target-normal accelerated electrons propagated through the target and escaped into vacuum. The nonthermal features were suppressed when a 100-ps delay was introduced between the pulses, supporting their association with reconnection.
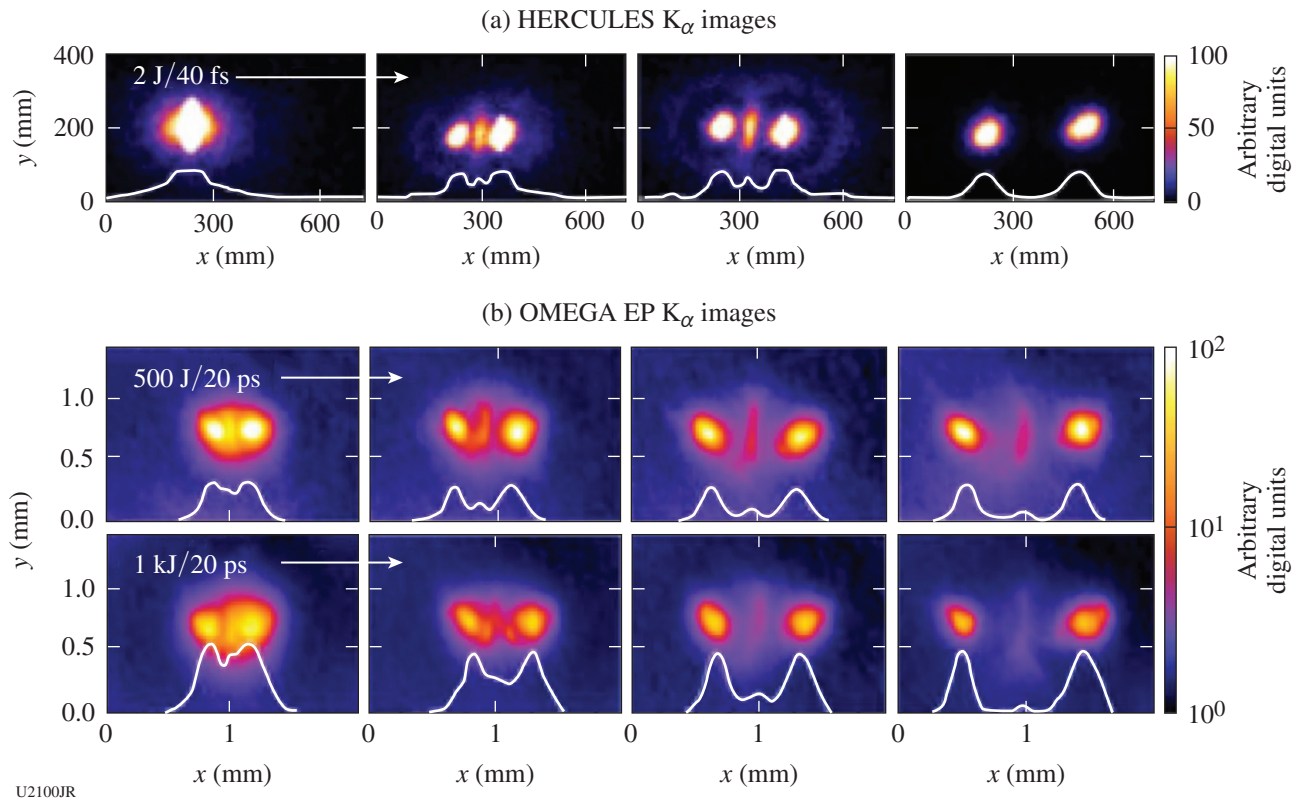
Figure 148.52
Front-side copper K$_\alpha$ images from focal-spot separation scans using (a) the HERCULES laser and (b) the OMEGA EP laser. The 50-μm horizontal lineouts are superimposed.
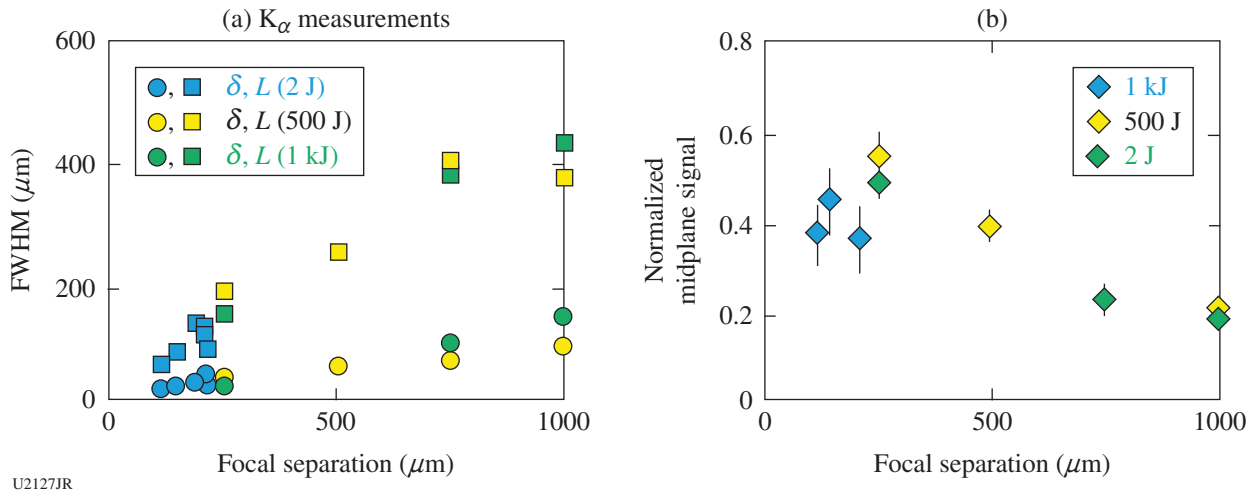
Figure 148.53
(a) The enhanced midplane signal full width at half maximum (FWHM) width (δ) and length (L) and (b) integrated signal normalized to the per-shot average of the integrated signal density from the focal-spot regions.
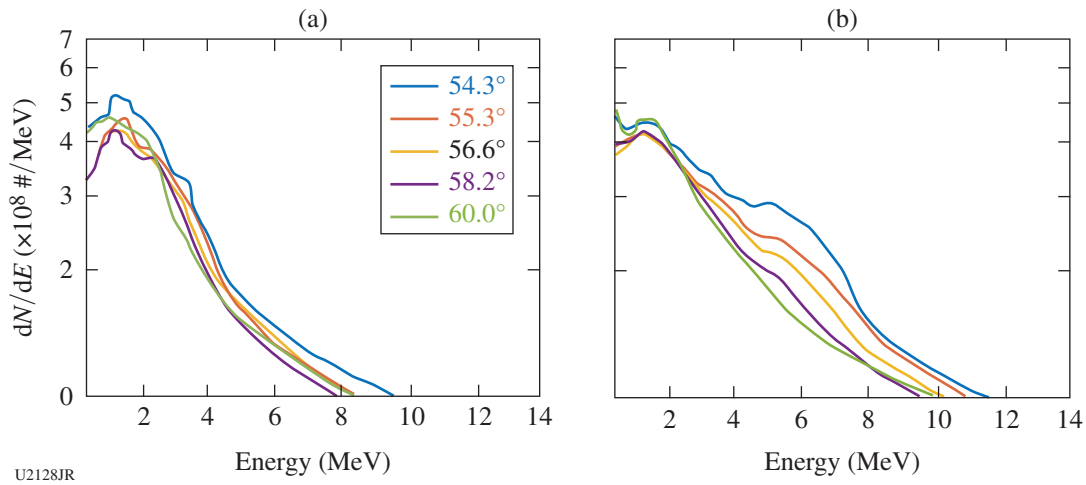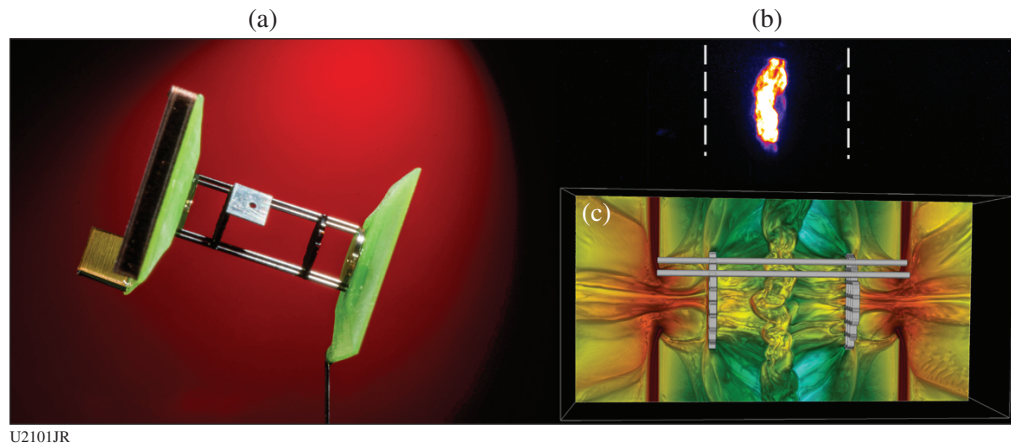

Figure 148.54
The electron spectra (for 500-μm separation) from the OMEGA EP multichannel spectrometer at angles from the transmitted laser axis in the case of (a) a 100-ps pulse-to-pulse delay (no reconnection) and (b) no pulse-to-pulse delay (reconnection).

Nonlinear Amplification of Magnetic Fields in Laser-Produced Plasmas
Principal Investigator: D. Lamb (University of Chicago)

The experiments we performed during our second shot day (10 August 2016) on the OMEGA laser studied the turbulent dynamo amplification of magnetic fields, a ubiquitous process in astrophysical systems, and the effects of magnetized turbulent plasmas on nonthermal particle diffusion and acceleration processes relevant to cosmic rays. The experiments utilized a platform [Fig. 148.55(a)] very similar to the one fielded on OMEGA during our very successful first shot day, during which we demonstrated nonlinear amplification by turbulent dynamo for the first time in a laboratory environment. We designed the experimental platform aided by numerical modeling effort on one of the nation's leading supercomputers [Fig. 148.55(c)] and it is uniquely fitted to generate turbulent plasmas in the large magnetic Reynolds numbers regime, where dynamo can operate. The configuration consists of two diametrically opposed foil targets, 8 mm apart, that are backlit with temporally

U2101JR

Figure 148.55

(a) Experimental platform of the National Laser Users' Facility (NLUF) Campaign to study turbulent dynamo amplification and nonthermal particle acceleration and diffusion, processes that occur in astrophysical environments like galaxy clusters. The assembly consisted of two polystyrene foils and a pair of meshes, held together by four boron rods. The foils and meshes were carefully designed and machined to optimize the conditions in the interaction region for turbulent field amplification. By changing the specifications of the grids, we are able to control the injection scale of the turbulence and the shape of the interaction region. The shields and flaps protect the interaction region, the imploding D^3He capsule, and the diagnostics from the direct view of the laser spots. The shield with the pinhole—on the side of one of the grids—made it possible to create collimated proton beams to investigate diffusion of charged particles by magnetized turbulence. (b) X-ray image of the interaction region after the collision. The flow exhibits strong turbulence and is considerably hot. The wealth of experimental diagnostics has made it possible to characterize the magnetized plasma, study the turbulent dynamo mechanism, and probe the physics behind the interaction of magnetized turbulence with charged particles. (c) Three-dimensional radiation–magnetohydrodynamic simulation of the experimental platform, performed with the multiphysics code *FLASH*. A large simulation campaign on Argonne National Laboratory's *Mira* BG/Q supercomputer guided us in the design of a platform capable of probing the turbulent dynamo regime. The figure displays a 3-D rendering of the simulated electron density (in cm^{-3}), after the jets collide.

stacked beams that deliver 5 kJ of energy on each side. The beams drive a pair of colliding plasma flows that carry seed magnetic fields, generated by the Biermann battery effect. The flows propagate through a pair of grids that destabilize the flow and produce turbulence with a driving scale defined by the grid specifications. By varying the latter we can assess the properties of turbulence injection. The turbulent flows meet at the center of the chamber to form a hot, turbulent interaction region where seed magnetic fields are amplified to saturation values. The magnetized turbulent flow is probed with pinhole-collimated proton beams to study spatial diffusion; we also measure the electron energy spectrum in search of particle acceleration signatures.

Our 13 shots have yielded a wealth of experimental data. The diagnostics we fielded made it possible to fully characterize the turbulent interaction region, quantify its energy budget and power spectrum, and study the effects of magnetized turbulence on diffusing and accelerating charged particles. More specifically, x-ray imaging [Fig. 148.55(b)] made it possible to directly visualize the turbulent region and explore how different grid specifications altered the dynamics of the flow interaction.

From the x-ray intensity fluctuations we also reconstructed the density power spectrum of the turbulence and inferred its power law. Moreover, the time-resolved spectrum from the Thomson-scattering diagnostic yielded clear ion-acoustic features that allowed us to characterize the plasma properties, including ion and electron temperatures, turbulent and bulk flow velocity, and electron density. By coupling the Thomson-scattering diagnostic with a Wollaston prism, we were also able to separate the light's polarization into two orthogonal components and measure Faraday rotation caused by the magnetic field. In conjunction with proton radiography and the novel mapping techniques we developed, we were able to reconstruct the strength and topology of the magnetic field in space and time. By introducing a pinhole [Fig. 148.55(a)] in the path of the protons, we were also able to create a collimated proton beam that interacted with the electromagnetic fields of the turbulent plasma and spatially diffused, as cosmic rays would, with astrophysical turbulence. Lastly, by fielding the Osaka multichannel spectrometer, we were able to recover the energy spectrum of the electrons. This plenitude of experimental data is still under analysis and scrutiny and promises to expand our understanding of the puzzle that is astrophysical turbulence.

Creation of Magnetized Jet Using a Hollow Ring of Laser Beams
Principal Investigator: E. Liang (Rice University)

Progress toward the objectives of the project as listed in the original application has exceeded expectations. We carried out a one-day OMEGA laser experiment in December 2015, using 20 beams to form a hollow-ring focal pattern to create a magnetized jet from a flat plastic target. The hollow-ring radius varied from 0 to 800 μm. Eleven shots were completed successfully. Thomson-scattering (TS) diagnostics were used to measure the on-axis electron and ion densities, temperature, and flow velocity at 2.5 mm from laser target for each shot. The TS results confirmed the predictions of *FLASH* 2-D simulations, namely that the on-axis density, temperature, and velocity are highest for the 800-μm-radius ring and lowest for the 0-radius ring. Both 3-MeV and 14-MeV monoenergetic protons from D^{3}He capsule implosions were used to measure the magnetic-field geometry and magnitude in the jet via proton radiography. The results show much stronger and more filamentary magnetic fields embedded in the jet than *FLASH* 2-D simulation predictions. We deduced peak magnetic fields exceeding 10 T. This important and unexpected result means that the plasma properties of the hollow-ring jet, including its collisionality, will be significantly impacted by the self-generated magnetic field. Posters on the preliminary results were presented at both the Omega Laser Facility Users Group Workshop in April 2016 and the High-Energy-Density Laboratory Astrophysics (HEDLA) Stanford Linear Accelerator (SLAC) meeting in June 2016. A more-updated poster will be presented at the American Physical Society Division of Plasma Physics Conference in November 2016, in which details of the proton-radiography results and magnetic-field deconvolution will be discussed.

Explorations of Inertial Confinement Fusion, High-Energy-Density Physics, and Laboratory Astrophysics
Principal Investigators: R. D. Petrasso C. K. Li, and J. A. Frenje (MIT)
Co-investigators: F. H. Séguin and M. Gatu Johnson (MIT)

MIT work in FY16 included a wide range of experiments that applied proton radiography, charged-particle spectrometry, and neutron-spectrometry methods developed by MIT and collaborators to the study of laboratory astrophysics, high-energy-density physics (HEDP), and inertial confinement fusion (ICF) plasmas. Seventeen papers[3–19] about NLUF-related research were published in FY16 (four by students[4–7]) and many invited talks and contributed talks were presented at conferences.

Former MIT Ph.D. student Dr. M. J. Rosenberg (Fig. 148.56) won the 2016 Marshall N. Rosenbluth Outstanding Doctoral Thesis Award based on his 2014 thesis[20] entitled "Studies of Ion Kinetic Effects in Shock-Driven Inertial Confinement Fusion Implosions at OMEGA and the NIF and Magnetic Reconnections Using Laser-Produced Plasmas at OMEGA." He is only the second Ph.D. student supported by NNSA and/or the joint program to ever receive this prestigious award (the first was Dr. M. J.-E. Manuel, whose 2013 MIT thesis was also based on NLUF research). Dr. Rosenberg is now a Research Scientist at LLE.

U2102JR

Figure 148.56
Dr. M. J. Rosenberg, who won the 2016 Marshall N. Rosenbluth Outstanding Doctoral Thesis Award based on his 2014 thesis[20] entitled "Studies of Ion Kinetic Effects in Shock-Driven Inertial Confinement Fusion Implosions at OMEGA and the NIF and Magnetic Reconnections Using Laser-Produced Plasmas at OMEGA."

Two new Ph.D. students (R. Simpson and A. Rosenthal) and one new postdoc (C. Parker) have joined our division and are becoming active participants in the NLUF program. They work alongside continuing graduate students N. Kabadi, B. Lahmann, H. Sio, G. Sutcliffe, and C. Wink.

One of the major areas of research was the study of plasma jets and the effects of magnetic fields on their propagation. Of particular importance was a scaled laboratory experiment designed to shed light on jet dynamics in the Crab-nebula (as described in Ref. 3). The remarkable discovery by the Chandra X-Ray Observatory that the Crab nebula's jet periodically

changes direction provides a challenge to our understanding of astrophysical jet dynamics. It had been suggested that this phenomenon may be the consequence of magnetic fields and magnetohydrodynamic instabilities, but experimental demonstration in a controlled laboratory environment was lacking. In the experiment (shown schematically in Fig. 148.57), high-power lasers were used to create a plasma jet that could be directly compared with the Crab jet through well-defined physical scaling laws. The jet generated its own embedded toroidal magnetic fields; as it moved, plasma instabilities resulted in multiple deflections of the propagation direction, mimicking the kink behavior of the Crab jet. The experiment was modeled with 3-D numerical simulations that showed exactly how the instability develops and results in changes of direction of the jet.

Other research and publication topics included the stopping of ions in plasmas,[19] utilizing charged fusion products from ICF implosions and measurements of their energy losses in passing through the ICF-capsule plasma with charged-particle spectrometers; this work is of great importance for ignition since it is relevant to the deposition of alpha-particle energy in burning fuel. In addition, studies of kinetic, multi-ion effects and ion–electron equilibration rates in ICF plasmas (e.g., Ref. 4) continued in the ongoing series of developments evolving from Ref. 20. Thermonuclear reactions at energies relevant to stellar nucleosynthesis and big-bang nucleosynthesis were studied using ICF implosions.[9] Effects of fuel-capsule shimming and drive asymmetry on ICF symmetry and yield were studied on OMEGA.[15,16]

Generation of Collisionless Shocks in Laser-Produced Plasmas
Principal Investigators: A. Spitkovsky (Princeton University) and C. Huntington (LLNL)

The FY16 MagShock EP Campaign was dedicated to the detection of collisionless magnetized shocks in ablated plasma flows. Such shocks form in supernova remnants and in the heliosphere, among others. The shock thickness is determined by the Larmor radius of the incoming protons, and the mean free path must be much longer. The setup is shown on Fig. 148.58. The experiments used the OMEGA EP Laser System in which a 3-D–printed Helmholz coil powered by MIFEDS (magneto-inertial fusion electrical discharge system) was inserted. Three targets were mounted on MIFEDS. A 400-J, 1-ns pulse was used to ablate plasma that propagated along the coil's magnetic field (this component is called "background" plasma). A 1.3-kJ, 1-ns pulse was used to drive fast flow orthogonal to the magnetic field [this component is called "piston" plasma (see Fig. 148.58)]. On some shots two piston plasmas were ablated with different time delays, but most shots
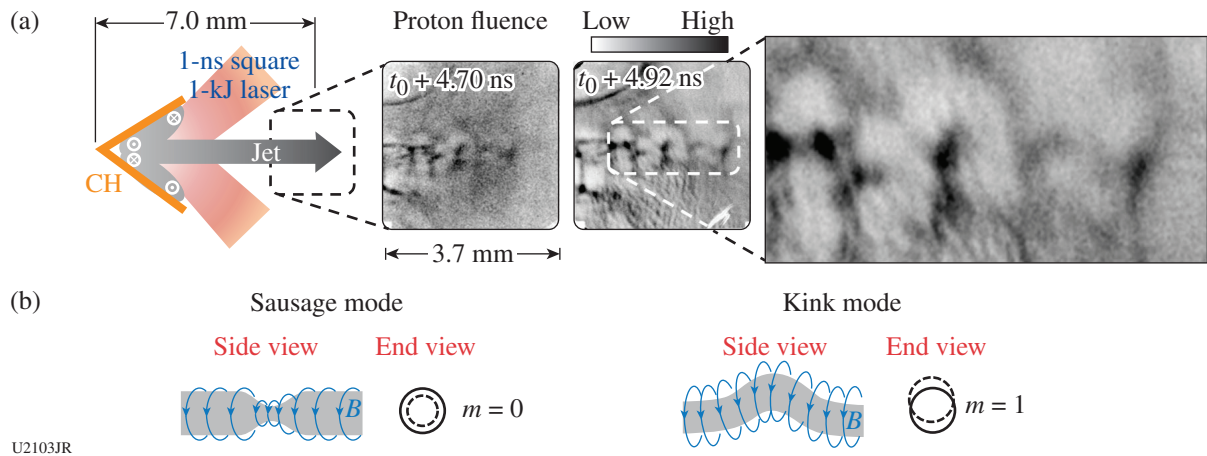

Figure 148.57
A scaled laboratory experiment that sheds light on the Crab-nebula jet dynamics.[1] (a) Schematic of a laser-beam–irradiated, cone-shaped target and the resulting plasma jet. Side-on (proton flux into the paper) radiographic images show the proton fluence distribution at $t_0 + 4.70$ ns with 14.7-MeV protons and at $t_0 + 4.92$ ns with 3-MeV protons, where t_0 is the time when the lasers turned on. The enlarged image shows a sequence of clumps and changes of jet direction. (b) Schematic illustrations of the fastest-growing magnetohydrodynamic current-driven instabilities: mode $m = 0$ (sausage, leading to jet propagation clumping) and $m = 1$ (kink, leading to jet direction changing). Higher modes ($m > 1$) are also expected to be excited, but they will have smaller effects and are not illustrated here.

used only one piston plasma. The interaction between the flows was expected to drive a compression in the background plasma and the magnetic field (see Fig. 148.59). At a strong-enough drive, this compression becomes a collisionless shock. We diagnosed this compression using proton radiography with target normal sheath acceleration (TNSA) from a short 10-ps laser pulse. The protons were recorded on CR39 film, which was our primary diagnostic. On some shots, a 4ω optical probe was also utilized.

Our experiments resulted in the detection of a magnetized collisionless shock propagating through the plasma. The main feature of the magnetic compression in the data was the appearance of a white band in the proton image, indicating additional deflection of the protons. The band was followed by a sharp

caustic of enhanced proton concentration (Fig. 148.59). The band and the caustic propagated at 300 km/s. The thickness of the band allowed us to constrain the magnetic compression to 2.3, and the caustic was interpreted as the signature of the contact discontinuity between the piston and compressed background plasma. This compression ratio corresponds to a Mach-3 shock. The shock is in the collisionless regime since

Figure 148.58
(a) Schematic of fast piston plasma interacting with a magnetized background plasma; (b) experimental setup.
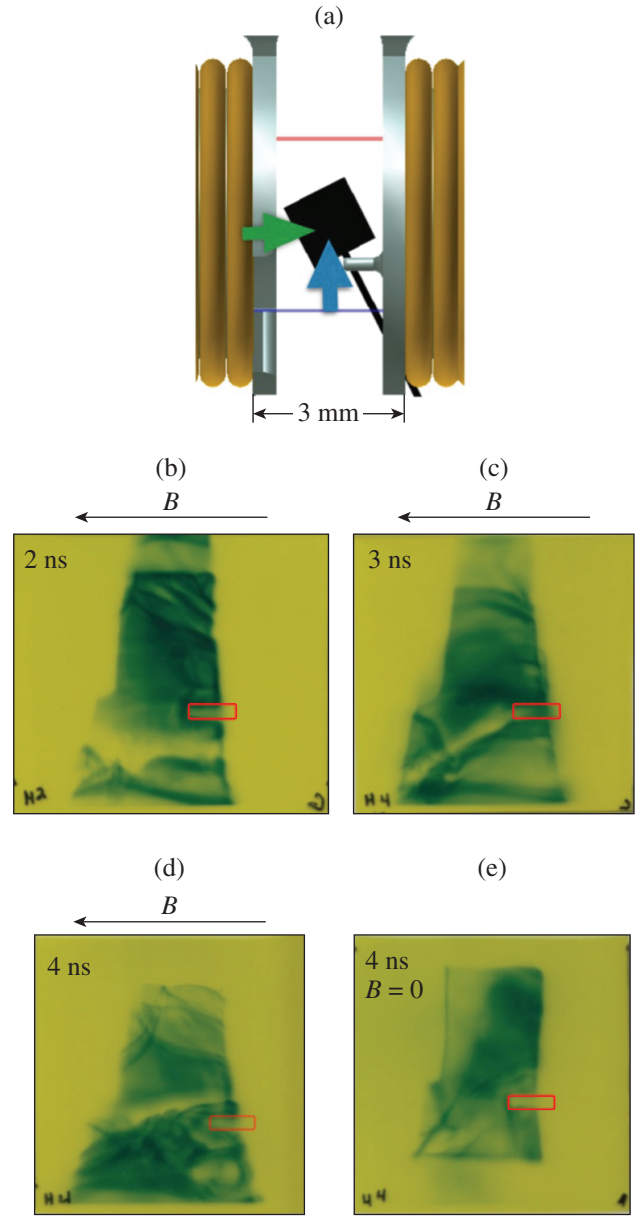
Figure 148.59
(a) View of the setup from the film. [(b)–(d)] Proton radiography of the interaction at different times. Notice the movement of the white band and the sharp caustic feature behind it. (e) The band is not present when the B field is off.

the mean free path of the background protons is larger than the size of the plasma. We have confirmed these results on several shots and have performed the time series study and the null shots of no B field, reverse B field, and individual piston and background plasma shots. These shots did not display the white compressional band, indicating that this feature is unique to the magnetized compressed plasma. We performed extensive numerical simulations of the experiment with particle-in-cell (PIC) simulations, including simulated proton radiography through the fields of the simulation. The experimental results agree quite well with the predictions of the simulations.

These findings are currently being readied for publication in Physical Review Letters. Some preliminary results from this campaign were presented at the 2016 HEDLA Conference.

We thank the OMEGA EP personnel for their assistance in planning and executing this campaign.

Hot-Electron Scaling in Long-Pulse Laser–Plasma Interaction Relevant to Shock Ignition

Principal Investigator: M. S. Wei (General Atomics)
Co-investigators: C. M. Krauland (General Atomics); S. Zhang, J. Peebles, F. N. Beg (University of California, San Diego); and W. Theobald, C. Ren, E. Borwick, J. Li, W. Seka, C. Stoeckl, R. Betti, and E. M. Campbell (LLE)

The shock-ignition (SI) fusion scheme requires launching a strong shock via a short-duration (0.5 to 1 ns), high-intensity ($>5 \times 10^{15}$ W/cm^2) spike laser pulse into a pre-assembled fuel to achieve ignition. Surpassing the threshold intensity for laser–plasma instabilities (LPI's) such as stimulated Brillouin scattering (SBS), stimulated Raman scattering (SRS), and two-plasmon decay (TPD), the coupling of spike pulse energy to the target is uncertain. Under these laser and plasma conditions, copious hot electrons can be produced. While very energetic electrons (>200 keV) could preheat the fuel and degrade compression, it is suggested that moderate energy electrons (50 to 100 keV) could benefit the SI scheme by increasing ablation pressure and augmenting the ignitor shock strength as they are stopped in the compressed high-density, low-Z ablator region. The objective of this General Atomics (GA) NLUF project in collaboration with the University of California, San Diego, and LLE is to systematically study the scaling of hot-electron generation with laser intensity, wavelength, and plasma condition (including target ablator material) in the SI-relevant regimes. Understanding LPI and the resultant hot-electron characteristics (total energy, temperature, and divergence) is important for the viability of the SI concept.

Our second-year NLUF experiment in 2016 was successfully conducted in the OMEGA chamber including both OMEGA-only shots and joint OMEGA and OMEGA EP shots, which provided the opportunity to evaluate hot-electron production and energy coupling in the SI-required spherical geometry. The experiment was built off of the strong spherical shock platform by using the same OMEGA 60 UV beams' pulse shape [0.35-TW, 0.8-ns square pulse with 1-ns low-power foot shown in Fig. 148.60(b)], but adding the high-energy OMEGA EP IR beam (0.1 ns, 2.7 kJ with nominal vacuum laser intensity of 2×10^{17} W/cm^2) at various timing delays in joint shots. Changing the injection time of the IR beam allowed us to alter the scale length and temperature of the corona plasma with which it interacted. In addition to measuring the IR-generated hot electrons and their energy coupling to the compressed target, we also measured electrons generated by the 60 UV beams alone with their overlapped high intensity of ~3×10^{15} W/cm^2 by employing smoothing by spectral dispersion (SSD), a distributed polarization rotator (DPR), and an assortment of small phase plates. A schematic of the campaign is shown in Fig. 148.60(a). To facilitate hot-electron characterization including the spatial distribution in the target, experiments used a 485-μm-outer-diam sphere target [Fig. 148.60(c)] consisting of a 30-μm CH ablator layer and a low-density Cu foam ball. The novel GA-produced low-density, pure-Cu foam has a density of 1.2 g/cm^3 (~13% of solid Cu) with ≤1-μm pore size.

Our results resolve successful coupling of IR beam energy to the spherically compressing target under various laser and target conditions. Figure 148.61 shows the measured Cu K$_\alpha$ emission from three different shots: (a) OMEGA only; (b) a joint shot with the IR beam at 0.9 ns, corresponding to the end of the low-intensity foot of the UV driver pulse; and (c) a joint shot with the IR beam at 1.8 ns, corresponding to the end of the UV beams. In the OMEGA-only shot, the observed Cu K$_\alpha$ emission spot excited by the UV beam–produced hot electrons had a characteristic ringlike pattern with a radius of ~150 μm corresponding to the location of the shock-compressed, high-density Cu foam region at 1.8 ns. In the joint shot with the OMEGA EP beam injected at the end of the OMEGA driver, additional Cu K$_\alpha$ emission caused by the OMEGA EP beam–produced hot electrons can be clearly seen on the compressed high-density Cu foam region along the OMEGA EP beam-propagation direction. The localized energy deposition shown in Figs. 148.61(a) and 148.61(c) suggests effective stopping of the UV beam– and IR beam–produced hot electrons by the high-density, compressed Cu foam shell with an areal density of 25 to 30 mg/cm^2, within which <100-keV electrons will be ranged out. In contrast, Cu K$_\alpha$ emission caused by
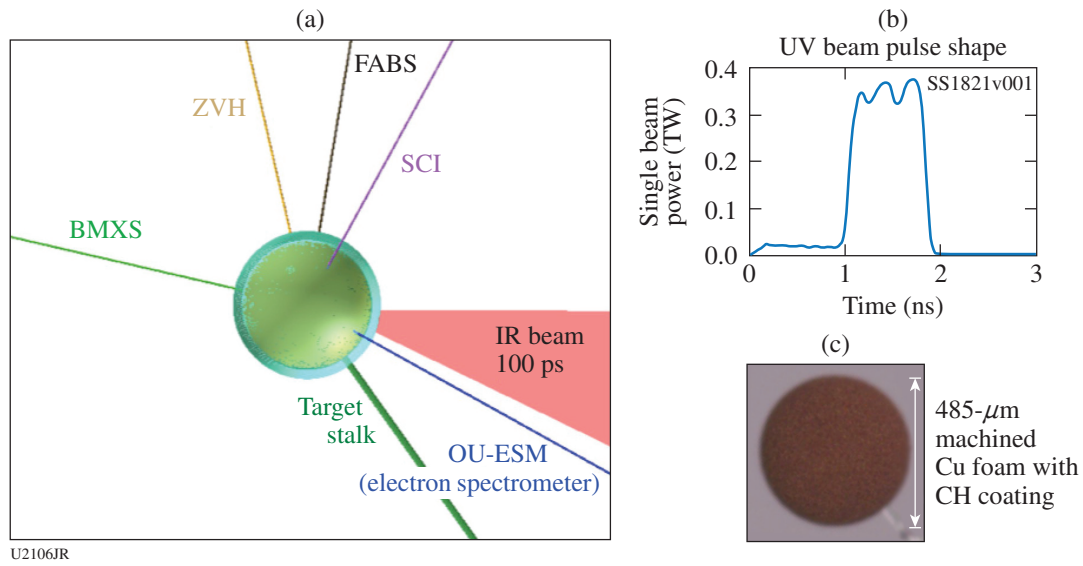
Figure 148.60

(a) Schematic of the joint shot experiment in the OMEGA chamber and the primary diagnostics detecting hot-electron–induced Cu K-shell fluorescence and bremsstrahlung radiation as a result of target irradiation by the OMEGA UV driver and OMEGA EP IR beam; (b) OMEGA pulse shape for 60 UV beams; (c) GA-made Cu foam sphere that is coated with 30 μm of CH as ablator. FABS: full-aperture backscatter station; ZVH: zinc von Hamos; BMXS: bremsstrahlung MeV x-ray spectrometer; OU EMS: Osaka University electron spectrometer.
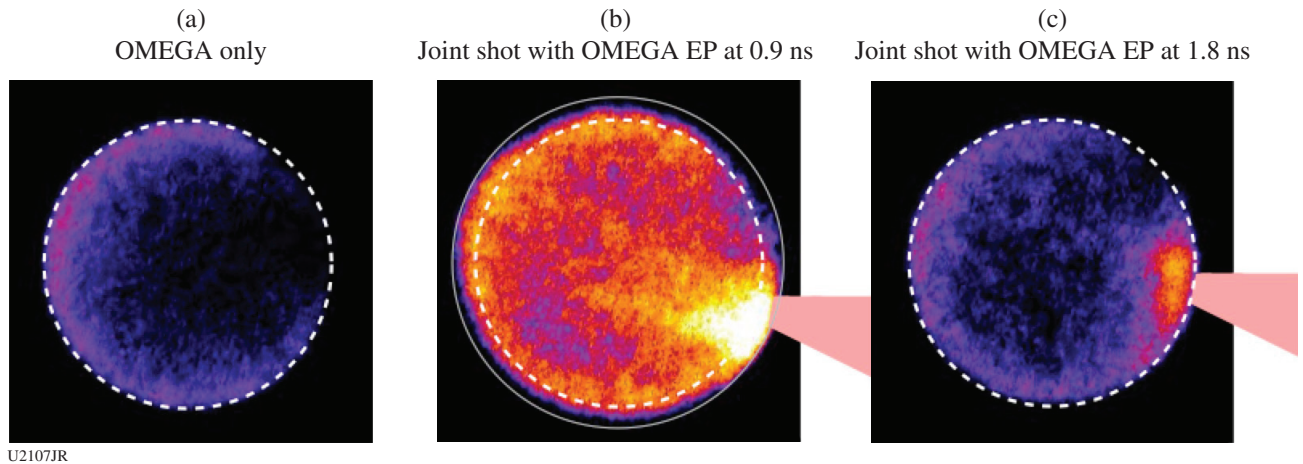
Figure 148.61

(a) SCI–measured Cu K$_\alpha$ images from an OMEGA-only shot; (b) a joint OMEGA and OMEGA EP shot with the OMEGA EP beam (represented by the red triangle with focal position in the corona plasma at $n_c/10$) at 0.9 ns; and (c) a joint shot with the OMEGA EP beam at 1.8 ns, respectively. The white dashed circle in each image has a radius of ~150 μm, corresponding to the radial location of the compressed Cu foam at 1.8 ns (the end of the OMEGA driver pulse). The solid circle in (b) has a radius of ~190 μm, indicating the compressed Cu target size at 0.9 ns.

hot electrons produced by the OMEGA EP IR beam injected at 0.9 ns into a short-scale-length, 1-keV corona plasma is observed from an ~200-μm target radius, corresponding to the location of the compressed Cu foam shell at the earlier time.

Hot electrons produced by the IR beam can be seen penetrating through the compressed, dense Cu foam shell and being transported farther into the core. This is caused by the less-than-10-mg/cm^2 areal density of the compressed Cu foam shell at

that time, where ~100-keV electrons will not be effectively stopped. It is also worth noting that this Cu K_α emission can be seen from the entire target, including the opposite side with the limb brightening. This may indicate the influence of hot-electron trajectories in the target by the self-generated electromagnetic fields. This phenomenon is much less prominent with the denser compressed shell in the joint shot with the OMEGA EP beam injected at 1.8 ns. The preliminary data clearly show that hot-electron generation and energy stopping strongly depend on the target conditions, which are visualized with the use of the novel low-density, mid-Z Cu foam target. The measured Cu K_α photon yield by the calibrated zinc von Hamos (ZVH) x-ray spectrometer agrees with the signal trend.

The streaked SRS data from the full-aperture backscatter station (FABS) diagnostic also captured sidescattered light from the IR beam's interaction with the long-scale-length plasma in all joint shots. Figure 148.62 shows the temporally and spectrally resolved backscattered light for the UV Beam 25 and sidescattered light from the IR beam (80° from the IR beam axis) for the same three shot cases: (a) an OMEGA-only shot, (b) a joint shot with the OMEGA EP beam at 0.9 ns, and (c) a joint shot with the OMEGA EP beam at 1.8 ns. An additional signal of the sidescattered light caused by the OMEGA EP IR beam in the joint shots is observed to emit near its 2ω (527 nm) and also in the spectrum range of 680 nm to 770 nm. An analysis of the scattered-light data is ongoing and will also be directly compared with the planned PIC simulations of LPI

and the resultant hot-electron generation and transport. Other data analyses, including the bremsstrahlung spectrum data, are also in process and will provide information on hot-electron energy spectrum, temperature, and energy-coupling efficiency in the target to be similarly compared with simulations.

High-Energy Electron Beam Acceleration from Underdense Plasmas Using OMEGA EP

Principal investigators: L. Willingale, T. Batson, A. Raymond, and K. Krushelnick (University of Michigan); P. M. Nilson, D. H. Froula, D. Haberberger, A. Davies, and W. Theobald (LLE); J. G. Williams and H. Chen (LLNL); and A. V. Arefiev (University of Texas, Austin)

For intense, picosecond-scale lasers, propagation through underdense plasmas results in forces that expel electrons from along the laser axis, resulting in the formation of channels. Electrons can then be injected from the channel walls into the laser path, which results in the direct laser acceleration (DLA) of these electrons and the occurrence of a high-energy electron beam. Experiments performed on OMEGA EP studied the formation of a laser channel in an underdense CH plasma, as well as the spatial properties and energy of an electron beam created via DLA mechanisms. The 4ω optical probe diagnostic was used to characterize the density of the plasma plume, while proton radiography was used to observe the electromagnetic fields of the channel formation.
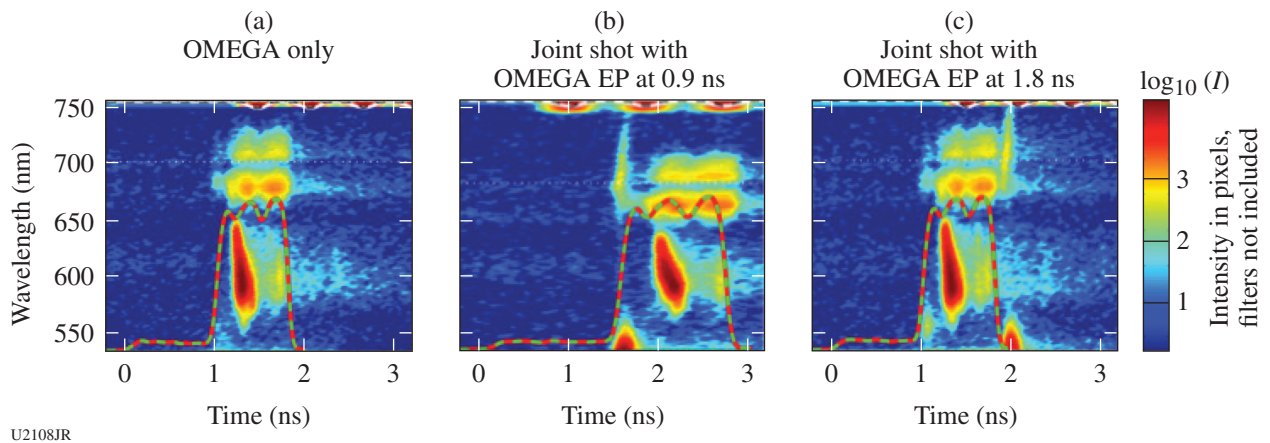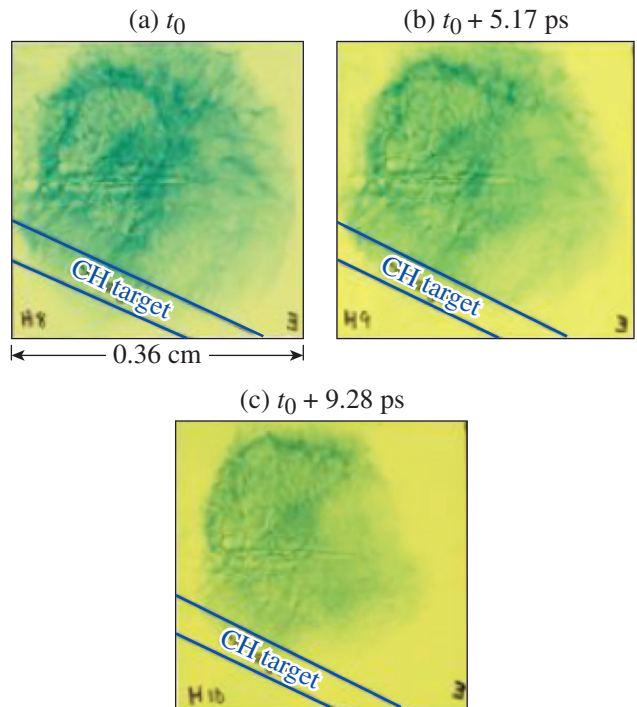

Figure 148.62
(a) Measured streaked stimulated Raman scattering (SRS) data in three typical shots: (a) OMEGA-only shot, [(b) and (c)] joint shots with the OMEGA EP beam at 0.9 ns and 1.8 ns, respectively. Sidescattered light from the OMEGA EP IR beam can be clearly seen in the joint shots.

The experiments used four of the OMEGA EP chamber's beams. A long-pulse UV beam (2.5 ns, 1200 J) ionized a CH target, creating an expanding plasma plume. After 2.5 ns, the backlighter (BL) [a short-pulse IR beam (0.7 ns, 400 J)] interacted with the plasma plume, creating a laser channel. The channel formation was imaged by two diagnostics. First, a short-pulse IR beam (sidelighter, 10 ps, 750 J) was focused on a Cu foil, creating a proton probe, which imaged electromagnetic fields onto radiochromic film (RCF). Secondly, the 4ω (263-nm) optical probe diagnostic was sent through target chamber center (TCC) to image the laser channel via shadowgraphy, the magnetic-field formation via polarimetry, and the density of the plasma channel via angular filter refractometry (AFR). The electrons propagated to a magnetic spectrometer where their energy was measured. Two target configurations have been used. In the first configuration, the CH target was ionized by the long-pulse UV beam and a plasma plume was allowed to propagate away from the target. The short-pulse main interaction beam then interacted with the plasma at a point 2 mm above the target. In the second configuration, a 1-mm-diam, 3-μm-thick CH disk was premanufactured to have a 400-μm-diam hole in the center. The pulse beam focused to a spot size of 800 μm, therefore centered on the hole. The plasma was allowed to flow toward the center of the disk, where the short-pulse main interaction beam was focused, thereby reducing diffraction of the intense laser pulse by plasma density gradients.

Protons generated via TNSA interactions with a Cu foil were deflected via the electromagnetic fields in the laser channel and imaged onto an RCF film stack located 8 cm away from the target interaction. The penetration depth of protons into the film pack was modeled with SRIM/TRIM, and time-of-flight calculations were used to map protons of a given energy to a given flight time from the Cu foil where they were born. Jitter of the order of 20 ps in the laser pulses made it impossible to achieve an exact timing relative to the short pulse; however, relative timing between each film in the proton stack was calculated. The channel was observed to have a length of 2 mm and a width of 0.49 mm (Fig. 148.63). These dimensions stayed constant over the 10 ps that they were visible on the film stack. In the normal geometry (Fig. 148.64), a region of high electric field is observed to expand from the target center at a velocity of 0.1 c. The formation of a laser channel inside an expanding plasma plume in an oblique target geometry and the resultant acceleration via DLA of high-energy electrons has been observed and appears to refract upward from the axis of the laser. Channel formation in a normal target configuration was also observed, with features specific to the presence of a high-

Figure 148.63
Proton images of a laser channel formed by oblique target geometry.
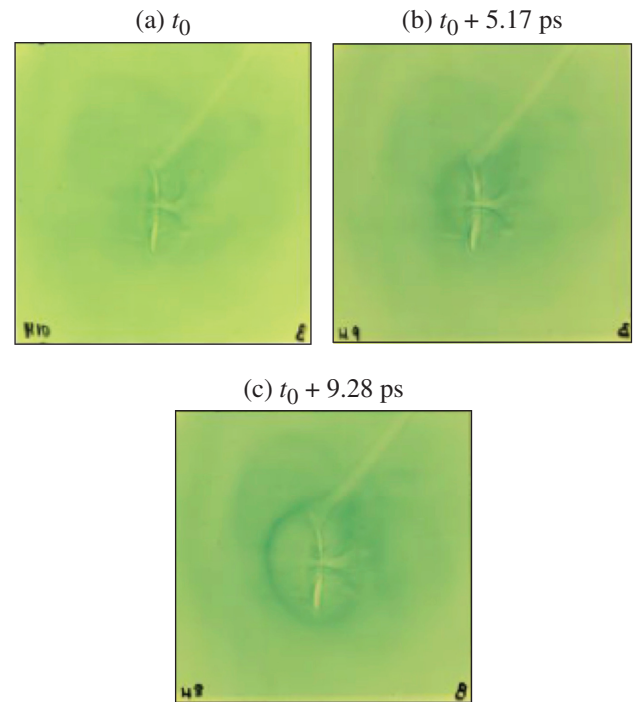
Figure 148.64
Proton images of target normal geometry

energy, short-pulse beam. Future work will focus on varying the plasma density in the channel and observing the channel in channel pointing and the energy of the accelerated electrons.

FY16 Laboratory Basic Science Studies

In FY16, LLE issued a solicitation for LBS proposals to be conducted in FY17. A total of 23 proposals were submitted. An independent committee reviewed and ranked the proposals; on the basis of these scores, 14 proposals were allocated 20 shot days at the Omega Laser Facility in FY17. Table 148.XII lists the approved FY17 LBS proposals.

Fourteen LBS projects previously approved for FY16 target shots were allotted Omega Laser Facility shot time and conducted a total of 218 target shots at the facility in FY16 (see Table 148.XIII). The FY16 LBS experiments are summarized in this section.

Ultrastrong Spherical Shocks
for Nuclear and Material Science
Principal Investigators: R. Betti and W. Theobald (LLE)

This project applied the spherical strong shock (SSS) platform[21,22] to study material science at extreme pressures (several gigabars) and densities (several g/cm^3). The platform opens a new regime for HEDP and is also useful for applications to ICF since they make it possible to study ultrastrong shock generation for the shock-ignition scheme.

In UltraSSS-16A, we conducted experiments to study fundamental physics underlying the compression of a sample material in spherical geometry using the 60-beam OMEGA laser. Figure 148.65 shows a schematic of the experimental setup. The UV beams were focused on the surface of a 430-μm-diam solid CH target, which contained a small (50-μm-diam) sample material (Ti or Cu) precisely placed in the center. The targets were fabricated by GA, which also performed an extensive characterization of all the targets in the optical and x-ray regimes to demonstrate that the sample materials were placed better than 10 μm in the center of the CH sphere. A 1-ns square laser pulse with an intensity of 5×10^{15} W/cm^2 launched the spherical shock wave that converged in the sample. The pressure strongly increased because of the convergent geometry and the sample material was strongly heated and compressed, producing a short burst of x-ray emission. The x-ray emission was measured with several x-ray diagnostics including an x-ray framing camera and a streaked x-ray spectrograph. Figure 148.66 shows a measured time-resolved spectrum from a target with a Ti sample. The photon energy ranged from 4.5 keV

to 8.5 keV and the time interval from 0.5 to 2.0 ns, where time zero is defined as the start of the laser pulse. The strong x-ray emission up to ~1.1 ns stems from the plasma corona outside of the CH sphere where most of the laser energy is absorbed. Once the laser was turned off, the coronal plasma quickly cooled and the x-ray emission from this region decayed. After
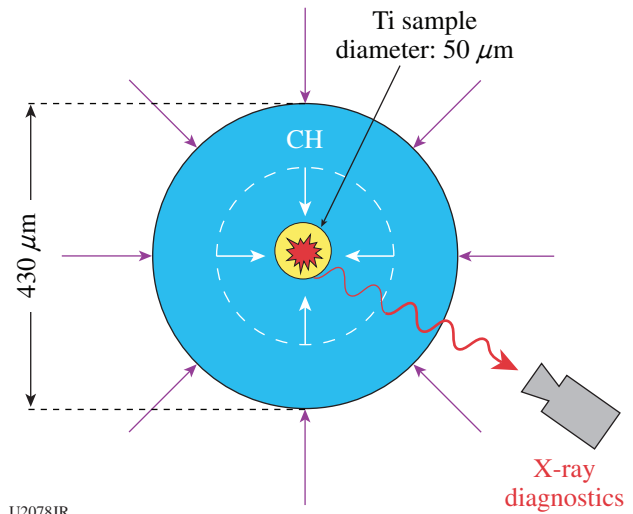

U2078JR

Figure 148.65
Schematic of the experimental setup of the ultrastrong spherical shock experiment. All 60 beams of the OMEGA laser were focused on the surface of a solid CH target, which contained a small sample material (Ti or Cu) precisely placed in the center. The x-ray emission from the sample material was measured and analyzed to obtain information on the achieved material condition.
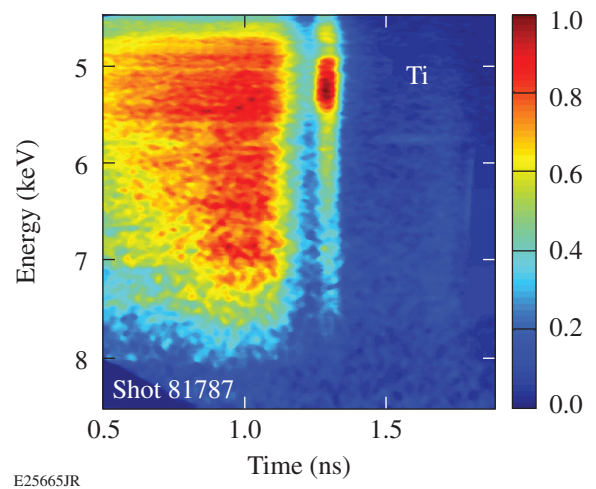

E25665JR

Figure 148.66
Measured time-resolved x-ray spectrum from a target with a Ti sample. The emission up to ~1.1 ns comes from the plasma corona, while the short burst at 1.3 ns is emitted from the heated and compressed Ti sample.

Table 148.XII: LBS Experiments approved for target shots at the Omega Laser Facility in FY17.

Principal Investigator	Title	Institution	Facility required	OMEGA shot days allocated	OMEGA EP shot days allocated
H. Chen	Exploring the Applications of Laser-Produced Relativistic Electron–Positron Pair-Plasma Jets	LLNL	OMEGA EP	0	1
A. R. Christopherson	Shock-Ignition Timing Measurements on OMEGA	LLE	OMEGA	1	0
J. R. Davies	Measuring the Nerst Effect and the Thermal Dynamo	LLE	OMEGA	1	0
T. Doeppner	Ionization Potential Lowering in Dense Plasma at Multi-100 Mbar	LLNL	OMEGA	1	0
D. E. Fratanduono	High-Pressure Polymorphism of Two High-Strength Ceramics: Boron Carbide (B_4C) and Silicon Carbide (SiC)	LLNL	OMEGA, OMEGA EP (not joint)	0	1
S. Jiang	Characterizing Pressure Ionization in Ramp-Compressed Materials with Electron-Induced Fluorescence	LLNL	OMEGA EP	0	1
D. Martinez	Imaging Cometary and Jet Flows on OMEGA EP	LLNL	OMEGA EP	0	1
M. Millot	Equation of State, Structure, and Optical Properties of Silicates	LLNL	OMEGA/ OMEGA EP	0	2
A. Pak	Probing the Field and Accelerated Ion Dynamics of Laser-Driven Electrostatic Shock Waves	LLNL	OMEGA EP	0	1
H.-S. Park	Study of the Dynamics of High Alfvénic Mach Number Plasma Interactions and Collisionless Shocks from Laser-Produced Plasmas	LLNL	OMEGA	2	0
H. G. Rinderknecht	Measurements of Kinetic Shock-Front Structure in Plasmas	LLNL	OMEGA	1	0
M. J. Rosenberg	Electron Energization During Magnetic Reconnection in HED Plasmas	LLE	OMEGA	1	0
M. B. Schneider	Radiative Properties of an Open L-Shell, non-LTE Plasma	LLNL	OMEGA	1	0
R. Smith	Thermal Conductivity of Fe and Fe-Si at Earth Core Conditions	LLNL	OMEGA	1.5	0
C. Wehrenberg	Probing the Extreme Deformation Mechanisms of Covalently Bonded Solids	LLNL	OMEGA	0.5	0
A. B. Zylstra	Charged-Particle Stopping Power and Scattering Measurements in Warm Dense Plasma	LANL	OMEGA	1	0

Table 148.XIII: LBS experiments approved for target shots at the Omega Laser Facility in FY16.

Principal Investigator	Title	Institution	Facility required	OMEGA shot days allocated	OMEGA EP shot days allocated	Joint shot days allocated
R. Betti	Ultrastrong Spherical Shocks for Nuclear and Materials Studies	LLE	OMEGA	1	0	–
J. H. Eggert	Development of Compressed Ultrafast Photography (CUP) Diagnostic for Dynamic Laser-Compression Experiments	LLNL	OMEGA EP	0	1	–
C. J. Forrest	Studies of (n,2n) Reactions of Light Nuclei at E_n = 14 MeV Using High-Energy-Density Laser Plasmas	LLE	OMEGA	1	0	–
P. Gourdain	High-Field–Assisted X-Ray Source	LLE	Joint	1	1	1
S. T. Ivancic	Integrated Channeling of High-Intensity Laser Beams in Implosions	LLE	Joint	1	1	1
A. E. Lazicki	Structural Studies of Electride Phases of High-Density Matter: Structures of Mg to Above 10 Mbar	LLNL	OMEGA	2	0	–
J. D. Moody	Characterization of Laser-Driven Magnetic Fields Using Proton Deflectometry	LLNL	OMEGA EP	0	2	–
P. M. Nilson	Study of Particle Energization During Magnetic Reconnection in High-Energy-Density Plasmas	LLE	OMEGA EP	0	2	–
A. Pak	Ion Acceleration from Laser-Driven Electrostatic Shock Waves	LLNL	OMEGA EP	0	1	–
H.-S. Park	Weibel Instabilities and Astrophysical Collisionless Shocks from Laser-Produced Plasmas	LLNL	OMEGA	2	0	–
Y. Ping	Pressure Ionization in Ramp-Compressed Materials	LLNL	OMEGA	1	0	–
C. Stoeckl	Spectroscopy of Neutrons Generated Through Nuclear Reactions with Light Ions in Short-Pulse Laser Experiments	LLE	OMEGA EP	0	1	–
W. Theobald	Proton Transport and Coupling into Shock-Compressed CH Targets for Proton Fast Ignition	LLE	OMEGA EP	0	1	–
C. E. Wehrenberg	Kinetics, Mechanism, and Shear Strain of the bcc-to-hcp Transition in Shock-Compressed Iron from Laue Diffraction	LLNL	OMEGA	1	0	–

a short time period of decreased x-ray emission, a short and intense burst is observed at 1.3 ns, indicative of the shock heating of the sample. The x-ray flash at 1.3 ns was emitted from the compressed and heated Ti sample.

Figure 148.67 shows the x-ray spectrum at 1.3 ns (blue) together with simulated spectra (red, yellow, and purple). Preliminary calculations were performed by our collaborators from the University of Las Palmas (Spain) with their code *ABAKO* to analyze the data. Assuming uniform conditions, a database of Ti spectra was computed within a range of mass densities of $\rho = 20$ to 200 g/cm^3 and temperatures $T = 400$ to 2400 eV for a uniformly compressed Ti sphere with radius $R = 10$ μm. The assumed radius approximately matches the Ti core radius at the flash time according to a *LILAC* simulation of shot 81787. *ABAKO* calculations include a continuum-lowering effect, which has a strong impact for Ti conditions of interest, opacity effects based on escape factors to compute the atomic kinetics, and continuum broadening consistent with continuum lowering in order to calculate the emergent intensity. A simple χ^2 minimization was performed to obtain the best fit compared to the experimental spectrum (see Fig. 148.67). The comparison between measured and simulated spectra indicate that the core has been heated to a temperature of ~800 eV and compressed to a mass density of $\rho = 100$ g/cm^3. The analysis is ongoing and will include the input from radiation–hydrodynamic simulations. The *ABAKO* code will be used to post-process the *LILAC*
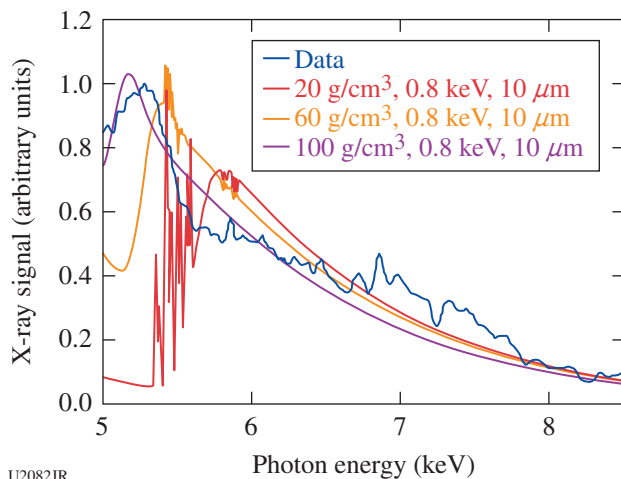
simulation of shot 81787 and to compute the collection of emergent spectra during the flash time interval. A temperature of ~1 keV and a mass density of 100 g/cm^3 indicate that a pressure exceeding 1 Gbar has been reached inside the Ti sample.

Development of a Compressed Ultrafast Photography Diagnostic for Time-Resolved Imaging of Dynamically Compressed Samples
Principal Investigators: J. H. Eggert and S. Ali (LLNL)
Co-investigator: D. E. Fratanduono (LLNL)

Late in FY16, one day on OMEGA EP was used to assess the feasibility of ultrafast optical imaging using coded images recorded by a Hamamatsu C7700 streak camera. The target design consisted of a plastic ablator and aluminum pusher driving a shock wave into a 2×2 grid of quartz samples of varying thicknesses, resulting in large-scale, spatially varying reflectivity changes as a function of time. A subset of the targets had an additional feature etched into the aluminum pusher layer to assess the resolution of the reconstructed series of images. Over the course of the day, data were collected with four different coded mask resolutions, three different streak-camera slit widths, and three different intensity levels on the camera. The full data set will enable one to assess the viability of the diagnostic and better determine the ideal experimental parameters for the diagnostic setup. Further analysis is required since the reconstruction of the images is nontrivial; however, the initial results are promising and suggest that this compressed ultrafast photography (CUP) diagnostic can provide images of the target with roughly 100-ps resolution.

Evaluation of the D(n,2n)p Reaction at 14.03 MeV with Modern **ab initio** *Calculations*
Principal Investigator: C. J. Forrest (LLE)

Nucleonic interactions with deuterium leading to a three-body breakup present important testing grounds for modern microscopic nuclear theory. The nuclear community has been studying these particular nucleon–nucleon (N–N) interactions over the past several decades. An accurate understanding of these processes is also of fundamental technological importance for the advancement of ICF research, tasked with demonstrating sustained thermonuclear D–T fusion in the laboratory. However, experimental data are scarce and incomplete, in particular, for energy spectra of neutrons from nD breakup occurring in thermonuclear ICF environment.

The neutron energy spectrum of the D(n,2n)p reaction has been measured (Fig. 148.68) using 14.03-MeV neutrons at a lab

U2082JR

Figure 148.67
Comparison of the experimental x-ray spectrum from the Ti sample (blue) with calculations with the code *ABAKO*. A reasonable agreement was obtained for a temperature of ~800 eV and a mass density of $\rho = 100$ g/cm^3.
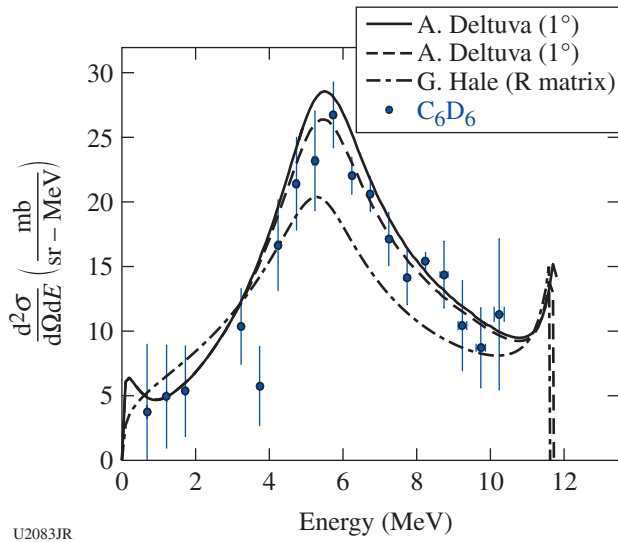
Figure 148.68
The measured cross section from a hexadeuterobenzene (C_6D_6) target (blue data points) shows good agreement with the modern *ab initio* calculation[23] outside the region at 3.75 MeV. An R-Matrix approach[24] is also compared with the inferred cross section with a larger discrepancy in the peak energy region ~5.5 MeV.

angle covering 0° to 7° using an ICF platform on OMEGA.[25] An ~100-ps-duration neutron burst from an imploding DT-filled glass-shell target was used to induce the breakup reaction in a nuclear interaction vessel that contained deuterated compounds positioned in-line with a high-resolution time-of-flight spectrometer. In these experiments, the double-differential cross section from deuterium breakup was measured in a lower-energy region (<2 MeV) and at a near-zero lab angle as compared to previous accelerator experiments. The results compare well with modern *ab initio* calculations, demonstrating that this theory can provide an accurate description of light-ion reactions.

High-Field–Assisted X-Ray Source
Principal Investigator: P.-A. Gourdain (LLE)

This experiment aimed at developing an assisted x-ray source using OMEGA as the imploder/pre-ionizer and OMEGA EP as the final ionizer. The goal of the 2016 campaign was to tune a cylindrical implosion driven by 36 beams and determine its quality, find the optimum timing to shoot OMEGA EP, and demonstrate feasibility of integration between MIFEDS coils/OMEGA/OMEGA EP to implode cylindrical geometries. All these goals were achieved successfully in one shot day.

Figure 148.69 shows that cylindrical implosions were achieved by using only 36 beams. The optimal timing was determined accurately. While we were able to record the Ar K-shell spectrum when OMEGA EP was turned off (shown in Fig. 148.70), spectra recorded with OMEGA EP turned on have a very poor signal-to-noise ratio. X rays from an unknown source, possibly e-beam bremsstrahlung, are believed to be responsible.
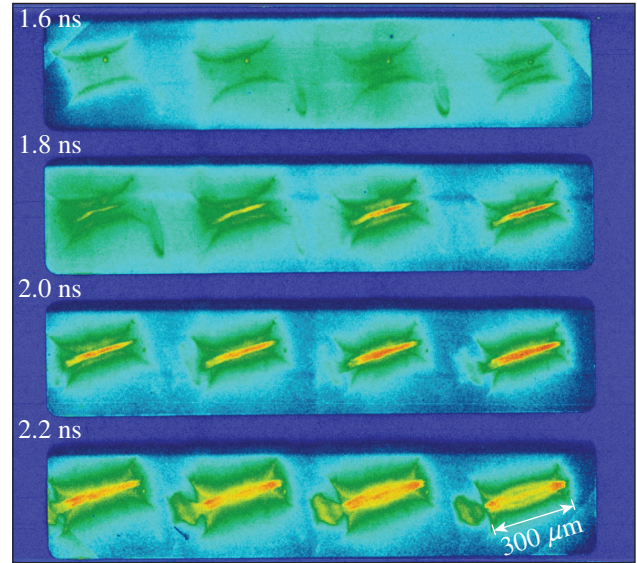
Figure 148.69
Framing-camera images showing the excellent cylindrical implosions. The last set of four frames shows a plasma plume created by OMEGA EP.
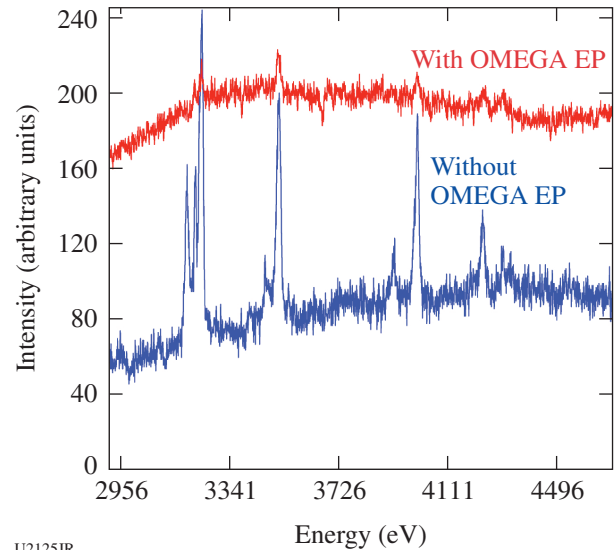
Figure 148.70
X-ray spectrum recorded by the end-on spectrometer in the Ar K-shell range with and without OMEGA EP.

Integrated Channeling of High-Intensity Laser Beams in Implosions
Principal Investigator: S. T. Ivancic (LLE)

This campaign studied the efficacy of heating a compressed OMEGA implosion with a co-propagated OMEGA EP channeling and heating beam. Sixty OMEGA beams imploded a CD capsule to a high areal density. The channeling and heating beams were timed to arrive at peak compression of the capsule. A new pulse shape that minimizes the coasting phase by using a triple-picket pulse and faster implosion velocity was implemented. The neutron yield from heated cores showed minimal additional neutrons generated from the addition of the heating pulse. Figure 148.71 displays a schematic of the experimental setup of the joint OMEGA/OMEGA EP experiment. A plastic shell is imploded by the 60 UV beams to create a high-density plasma with an extended corona. A 100-ps ("channeling") IR pulse is injected into the plasma, forming a channel followed by a high-intensity, 10-ps ("heating") pulse generating fast electrons at the channel wall. The shell consists of a 17-μm outer CH layer and a 23-μm inner deuterated plastic layer that is doped with 1% atomic density of Cu. The Cu doping provides K_α fluorescence x-ray emission at 8.048 keV when excited by fast electrons, which is imaged by an SCI. This technique visualizes the fast-electron energy deposition in the compressed shell. The 17-μm-thick CH ablator reduces the excitation of K_α fluorescence from direct interaction of the driver beams and eliminates the neutron background from the hot corona. Our experiments showed, however, that even with the undoped CH ablator, there is still some K_α radiation generated by the implosion. Other diagnostics include two electron spectrometers, an x-ray spectrometer, and neutron time-of-flight detectors to measure the thermonuclear fusion neutron yield from D–D reactions. The temporal evolution of the areal density was calculated with a 1-D simulation using the radiation–hydrodynamics code *LILAC* including cross-beam energy transfer (CBET) and nonlocal electron transport. Peak compression is predicted at 4.3 ns, where time zero is defined by the start of the drive pulse. The short pulses were injected at five times to bracket the peak compression. The electron spectrometers captured a very interesting trend in the spectrum of the escaped fast electrons for the different injection times. For an early injection of both pulses, copious amounts of MeV electrons were generated with a clear trend of decreasing fast-electron production for later injection times.
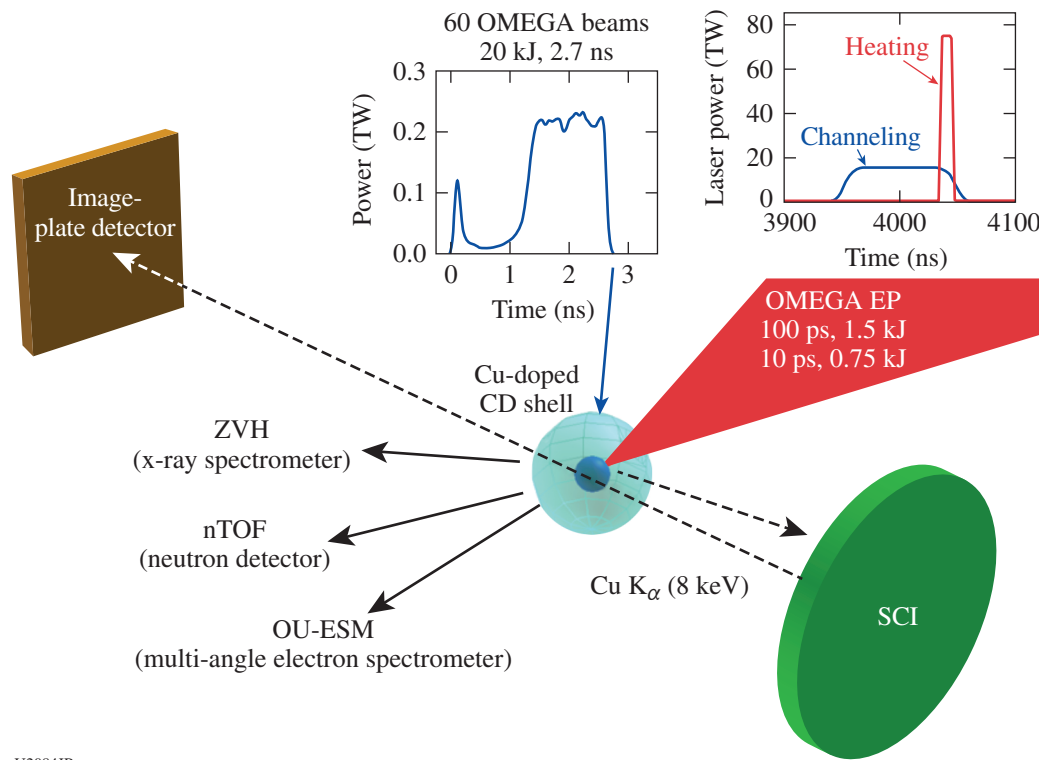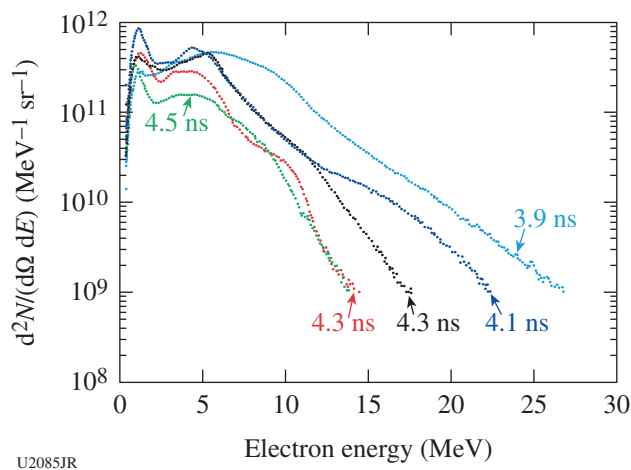

Figure 148.71
Schematic of experimental setup.
nTOF: neutron time of flight.

U2084JR

The results of the integrated experiment showed indications of electron stopping in the core as it approached peak areal density. Figure 148.72 shows the trend observed in the Osaka University electron spectrometer data for the central (on-axis) channel as a function of injected electron time. As the target approaches peak areal density (4.5 ns), there is a dip in the escaped electrons between 1 and 3 MeV. This trend was observed only in the on-axis channel and not in the ±5° or 10° channels that do not pass through the dense core of the compressed target. These data suggest that the dense core of plasma is stopping some of the electron beam. The total electron yield for later short-pulse injection times is lower as well, indicating poorer coupling of energy from the high-intensity pulse into fast electrons. However, because of the high background levels in the Cu K_α images, the contribution from the IR-produced electrons was not directly observed in this campaign. A future experiment with a thicker ablator may protect the Cu fluor layer from direct irradiation by the drive beams with the extended pulse.

This campaign sought theoretically predicted high-pressure phases of Mg, which have the interesting feature of density-driven electron localization in interstitial regions in the crystal lattice, occurring as a direct consequence of strong quantum mechanical constraints on the electronic wave functions of core and valence electrons at high compression. Three of these "electride" phases are predicted between 4 and 12 Mbar for magnesium.[26–28]

The experiment compressed solid Mg to the 10-Mbar pressure regime using ramped laser pulses and probed crystal structure using the PXRDIP diagnostic via transmission diffraction of He_α x rays from a metal foil backlighter (Fig. 148.73). Pressure in the sample was probed by measuring the target's free-surface velocity using VISAR and correlating it with a pressure state. Four half-days on OMEGA were used to optimize the target design, pulse shapes, and diagnostic filtering and timing and then to collect data between 2 and 15 Mbar. In spite of the very weak x-ray scattering strength of low-Z Mg, diffraction peaks were registered at up to 6 to 7 Mbar, above which pulse-length limitations hampered the ramp compression of the Mg, despite a high background resulting from ablation plasma x rays. Above 4 Mbar, the data indicate a new phase, albeit inconsistent with the theoretical predictions. These results are being used to design further measurements for the NIF.
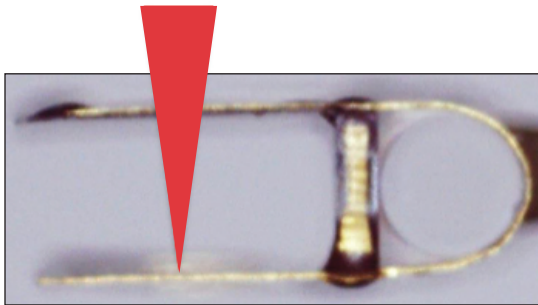

Figure 148.72
Transmitted electron spectrum through the compressed shell as a function of OMEGA EP injection time.

Structural Studies of Electride Phases of High-Density Matter: Structures of Mg to above 10 Mbar

Principal Investigator: A. E. Lazicki (LLNL)
Co-investigators: F. Coppari, R. Smith, R. Kraus, J. R. Rygg, D. E. Fratanduono, J. H. Eggert, and G. W. Collins (LLNL); M. McMahon, M. Gorman, and A. Coleman (University of Edinburgh); D. McGonegle and J. Wark (Oxford); and L. Peacock and S. Rothman (AWE)

Figure 148.73
(a) Cross section of the PXRDIP diagnostic showing the laser drive in blue and the x-ray source incident ~45° into the image-plate chamber, where diffraction peaks are registered. (b) Image plates digitally warped into a stereographic projection to show the x-ray diffraction peaks from Mg near 400 GPa (indicated with arrows) and from an ambient Ta calibrant (marked with red lines).

Hohlraum Magnetization Using Laser-Driven Currents

Principal Investigators: J. D. Moody and B. Pollock (LLNL)
Co-investigators: J. S. Ross, D. Turnbull, C. Goyon, A. Hazi, G. Swadling, and W. Farmer (LLNL)

In FY16 the two-day LDMag Campaign on OMEGA EP continued a basic science investigation of the feasibility of using laser-generated currents to self-magnetize targets, such as future ICF hohlraums. These experiments substantially improved the proton deflectometry capability of previous campaigns to probe the fringing magnetic-field structure around the outside of the half-loop target shown in Fig. 148.74. On the open side of the loop are parallel plates, into one of which holes were placed so that the OMEGA EP long-pulse beams could shine through to produce a plasma at the surface of the second plate. Hot electrons from this plasma collect around the holes in the first plate, driving a current through the half-loop that connects the plates, and producing a magnetic field on the loop axis and in the surrounding volume.

U2119JR

Figure 148.74
End-on view of geometry for hohlraum self-magnetization on OMEGA EP, with beam path shown schematically in red.

To probe these fields, protons are produced through the TNSA mechanism from the interaction of the two orthogonal OMEGA EP short-pulse beams with two separate, thin Au foil targets as shown in Fig. 148.75. Cu meshes impose fiducials in the proton images recorded on radiochromic film, providing detailed measurements of the field profile millimeters from the target. The loop structure was probed both along and across its axis by protons produced using the orthogonal short-pulse beams. Fields up to 200 T were inferred at the end of the 0.75- to 1-ns, 1-TW B-field drive laser pulses. The analysis of this recent experiment is ongoing and will inform the FY17 continuation of this effort.
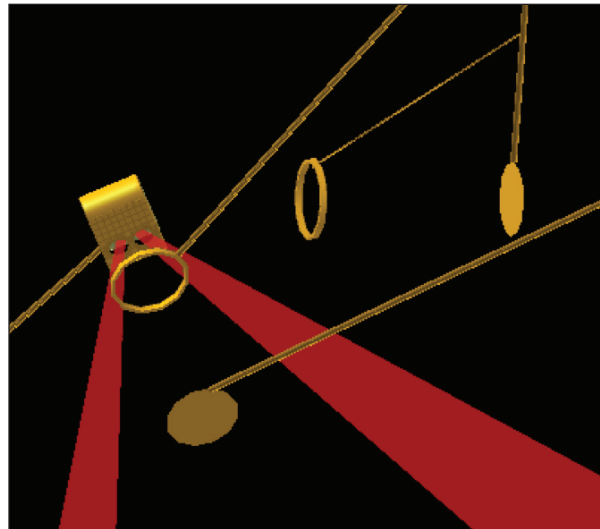
U2120JR

Figure 148.75
Geometry for proton deflectometry on OMEGA EP, with proton detectors (not shown) placed 8 cm behind and to the left of the B-field target.

Laser-Driven Electrostatic Shock-Wave Acceleration

Principal Investigator: A. Pak (LLNL)
Co-investigators: D. Haberberger (LLE) and T. Link (LLNL)

This shot day on OMEGA EP sought to create and image a relativistic collisionless electrostatic shock wave using a high-power, short-pulse laser. The astrophysical community is interested in understanding the plasma conditions under which these collisionless shocks form, the structure of their associated electric fields, and the resulting particle acceleration. It is also desirable to assess the viability of this new ion acceleration mechanism to produce an ion beam with the following properties: ~100 MeV per atomic mass unit, narrow energy spread $\Delta E/E$ ~10%, and high beam density ~10^{10} particles per bunch.

A summary of the experimental and diagnostic setup is shown in Figs. 148.76(a) and 148.76(b). An x-ray drive is first produced (or not) using a 1-ns laser pulse to irradiate a 25-μm-thick gold foil. The x-ray drive ablates and expands an initially 1.4-μm-thick CH target. After waiting ~500 ps for the peak plasma electron density to fall to ~5×10^{21} cm^{-3}, the backlighter beam drives the electrostatic shock wave to accelerate particles. The sidelighter beam then irradiates a second orthogonal proton source to probe the CH plasma. Figures 148.76(c)–148.76(e) and 148.76(f)–148.76(h) compare the accelerated proton beam profile, spectrum, and side-on proton radiography from, respec-
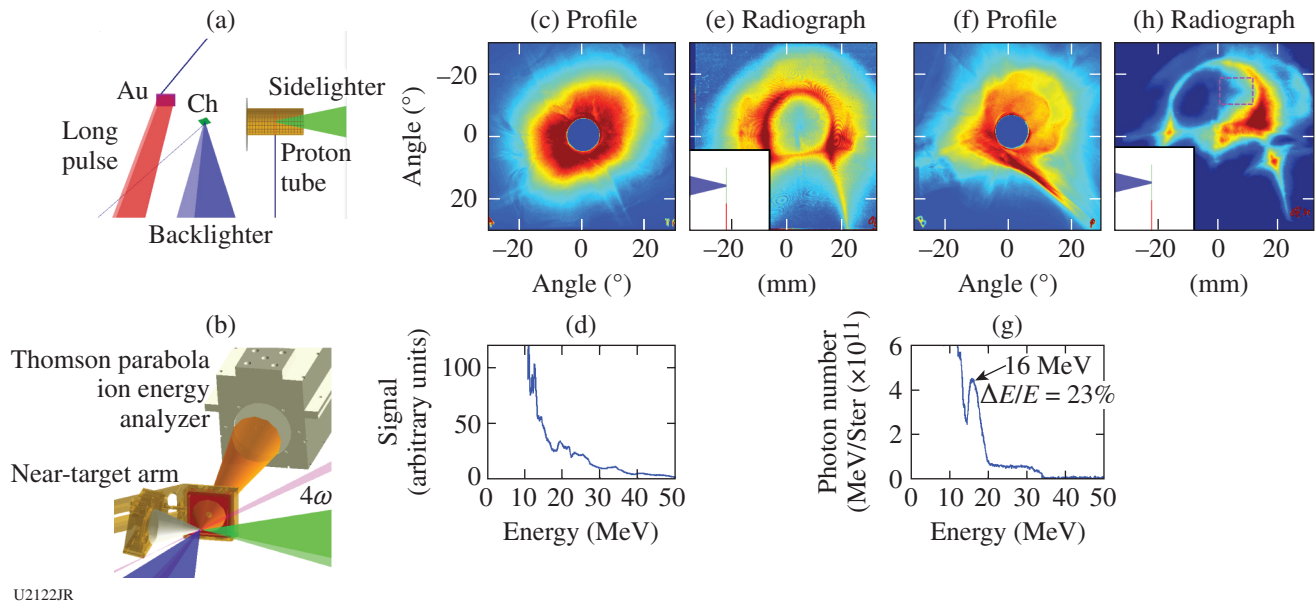
Figure 148.76

(a) Experimental configuration and (b) diagnostic suite. A long-pulse beam creates x rays to ablate an initially 1.4-μm-thick CH foil to tailor the plasma density profile. The short-pulse "backlighter" beam then drives the target, producing a proton beam via target-normal sheath acceleration (TNSA). Orthogonal to this, the "sidelighter" beam creates a second proton beam as a radiographic probe. [(c),(d)] TNSA proton beam profile and spectrum from direct drive of the CH foil, without x-ray preheat. The hole in the profile measurement transmits part of the beam to the Thomson parabola diagnostic. (e) Side-on proton radiograph of the TNSA field. [(f),(g)] TNSA beam profile and spectrum from an experiment with an x-ray tailored plasma density profile. (h) The resulting proton radiograph; the inset shows backlighter laser incident from the left, while the x-ray preheat comes from the right.

tively, an unperturbed foil and an expanded target. When the plasma density profile is first tailored with the x-ray drive, the proton spectrum exhibits a narrowband feature at ~16 MeV [Fig. 148.76(g)], and the side-on radiography shows a localized deficit in the probe beam. Both features are consistent with the generation of an electrostatic shock wave and are absent on the control experiment where an unperturbed target was used. Future work will focus on correlating the accelerated spectrum to the velocity of the electrostatic shock wave as inferred from the proton radiography data.

***Astrophysical Collisionless Shock Experiments
with Lasers (ACSEL)***
Principal Investigators: H.-S. Park, C. M. Huntington, and G. F. Swadling (LLNL)

The ACSEL-16A and -16B experiments continued to investigate the formation of astrophysically relevant collisionless shocks in a diagnosable laboratory environment. These shots were carried out in support of the ongoing ACSEL effort at LLNL and with support of the broad, cross-institutional ACSEL collaboration. A total of 13 target shots were completed

during ACSEL-16A and -14 during ACSEL-16B. The experiments primarily investigated interactions between beryllium targets, which were selected to provide a low-Z, single-species blowoff plasma in order to simplify Thomson-scattering analysis. Experiments also investigated end-on proton probing using thin foil targets and a new dish-shaped plastic target.

The experiments used OMEGA to heat the surfaces of a pair of opposing targets, launching counter-propagating plumes of high-velocity (~10^6-ms^{-1}), high-temperature (~keV) plasma. The parameters of the outflows are such that they are largely collisionless but with parameters amenable to the growth of instabilities, which can mediate the formation of a collisionless shock.

The interaction of the flows is diagnosed using a combination of (a) temporally resolved, single-point optical Thomson scattering and (b) proton radiography imaging. A D^{3}He exploding-pusher capsule provides a dichromatic (3.3- and 14.4-MeV) proton source for radiography, making it possible to probe at two separate times during each experiment. Images are recorded on CR39 nuclear track detectors whose processing

and analysis are carried out by collaborators at MIT. Previous proton imaging data have detected the presence of complex magnetic-field structures. The field structures are observed to grow in strength as the experiment progresses; the observed filamentary structures are interpreted as being the result of the growth of the Weibel instability in the region where the flows collide and interpenetrate.

The primary goal of ACSEL-16A and -16B was to collect improved optical Thomson-scattering data by using the beryllium targets to provide single-species plasmas; this significantly simplifies the interpretation of the detailed structure of the scattered spectra. The Thomson-scattering diagnostic records features of both ion-acoustic waves and electron plasma waves; data from this diagnostic have been previously used to diagnose the interpenetration of the flows and to measure heating

associated with the development of the two-stream instability. Figure 148.77 shows sample Thomson-scattering data from this campaign. High-quality data of the flow interactions at target separations of 4 and 5 mm were captured. Analysis of these data will reveal trends in the evolution of the plasma parameters of the interacting flows.

New experiments carried out in ACSEL-16B investigated a new target configuration. These targets were modified to a "dish" shape, allowing a significantly larger number of beams to impinge on the target within the facility's incident-angle constraints. This modification to the target geometry increased the density of the outflows by a factor of 10, as measured via Thomson scattering. This density scaling has the potential to allow one greater control in the pursuit of the formation of a mature collisionless shock.
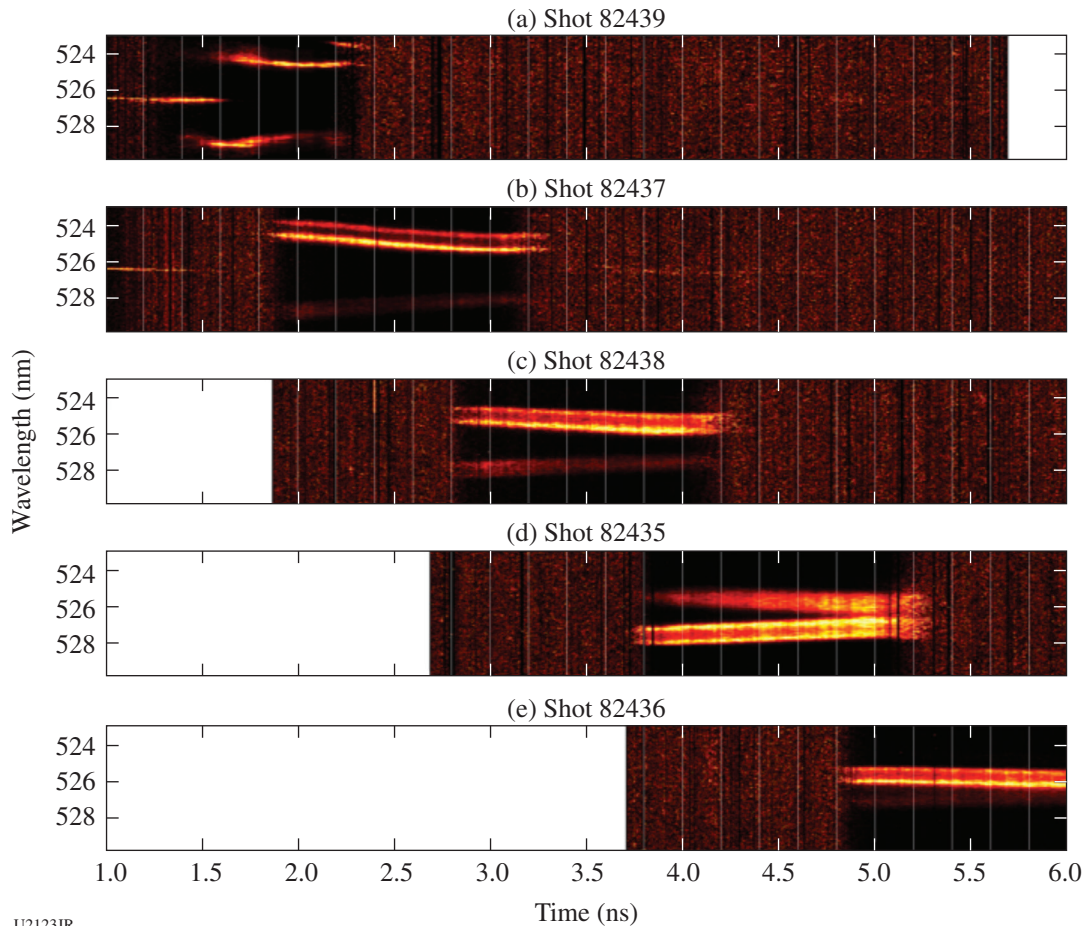
Figure 148.77
Thomson-scattering ion-acoustic wave time series, showing interpenetration of a pair of beryllium plasma flows.

Pressure Ionization in Ramp-Compressed Materials

Principal Investigators: Y. Ping and S. Jiang (LLNL)
Co-investigators: R. Shepherd and R. Heeter (LLNL)

The Pressure Ionization Campaign comprised two half-days on OMEGA during FY16. This campaign used ramp compression to compress an iron foil up to twice its original density, while keeping the temperature below 1 eV. The driver consisted of five laser pulses stacked in time. Separately, a spherical implosion provided a broadband x-ray backlighter. Both the absorption and fluorescence spectra were measured to study the energy shift of the Fe inner shells caused by pressure ionization. Figure 148.78(a) shows the measured absorption spectrum. At the top is a raw image from a 2× compression shot. X-ray filters of Fe, Mn, and Cr at the entrance slit of the spectrometer provided K-edge wavelength fiducials. The Fe K edge was measured for four different cases: undriven Fe, Fe with 2× and 1.5× compression, and liquid Fe. No obvious shift of the Fe K edge was observed in any of these cases. Figure 148.78(b) shows the fluorescence spectra measured using MSPEC (multipurpose spectrometer), in which K_α fluorescence was observed for the first time in ramp-compressed iron, despite noise and high background levels. The two top images in Fig. 148.78(b) show

raw spectra processed by a despeckling technique. The two lines from right to left correspond to Fe K_α and Cu K_α (from an undriven Cu washer used to mount the iron sample). The Cu K_α line provides a reference to compare different shots. The plot of Fig. 148.78(b) compares the K_α peaks from liquid Fe (blue) and from solid Fe with 2× compression (red). There appears to be a slight shift in the K_α energy. Future experiments will improve the signal-to-noise ratio, use a higher-resolution spectrometer to confirm the energy change, and seek to measure the weaker K_β signal, which is more prone to a shift because of pressure ionization.

Spectroscopy of Neutrons Generated Through Nuclear Reactions with Light Ions in Short-Pulse Laser-Interaction Experiments

Principal Investigators: C. Stoeckl, U. Schroeder, T. C. Sangster, and C. J. Forrest (LLE)

The experimental objective of this project is to study nuclear reactions in light ions generated in short-pulse laser-interaction experiments. Planar deuterated plastic (CD) targets were irradiated with one short-pulse (10-ps) beam focused at the target's front surface. A second low-energy (100-J), long-pulse (100-ps)
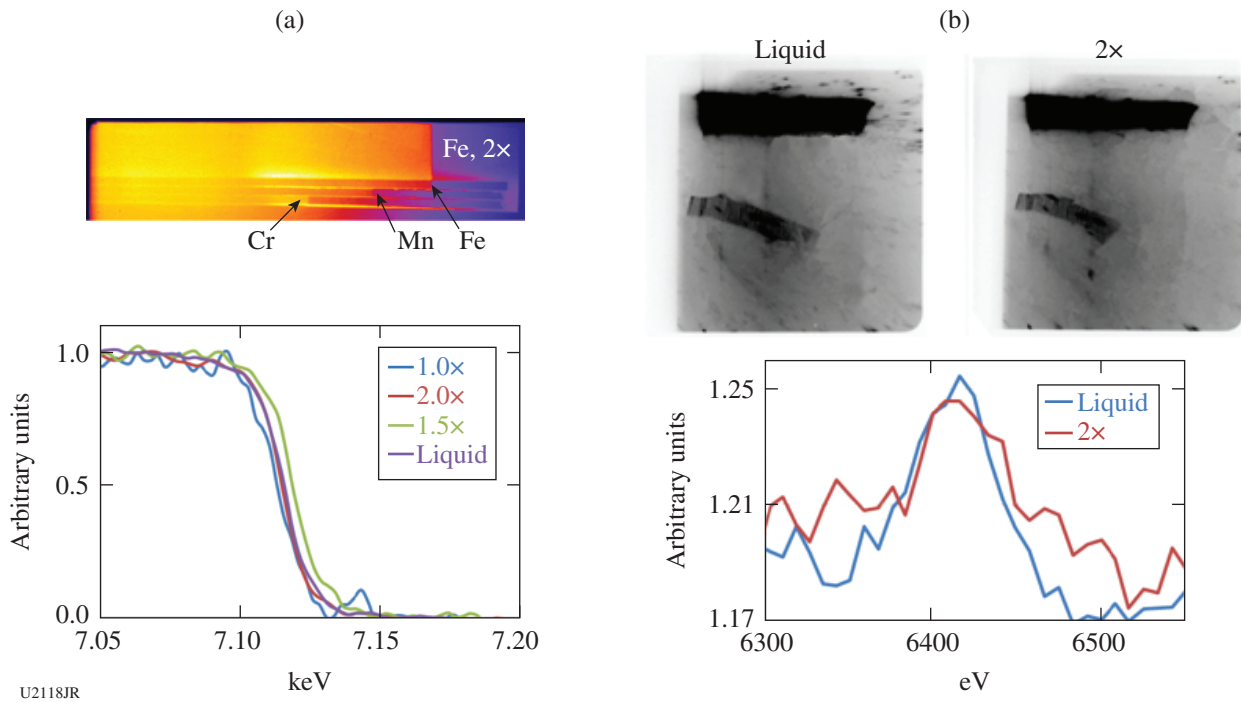

(a)

(b)

Figure 148.78

(a) A raw image of the measured absorption spectrum for 2× compressed Fe and measured Fe K edge under four different conditions. (b) Top: Measured MSPEC spectra, despeckled to reduce noise. Bottom: Lineouts of the Fe K_α feature for liquid and 2× compressed Fe.

UV beam was fired 0.5 ns ahead of the short-pulse beam to suppress proton acceleration on the front surface of the target. Charged particles, protons, and deuterons from the rear of the target create neutrons and charged particles through nuclear reactions in a second converter target placed closely behind the primary interaction target. The spectrum of the neutrons generated in the converter target is measured using a three-channel scintillator photomultiplier–based neutron time-of-flight detector system. Charged-particle detectors are used to measure the spectra of the primary particles.

The previous experiments in FY15 with CD primary and layered secondary targets with up to ten alternating layers of 25-μm-thick CD and 25-μm-thick Be foils showed clear evidence of both D–D fusion neutrons and neutrons from the $Be^9(d,n)B^{10}$ nuclear reaction. No secondary D–T fusion neutrons are observed from any tritium that would be generated in $Be^9(d,t)$ Be^8 neutron pickup reactions, which indicates that the cross section of this reaction is smaller than the calculated values.

The experiments with the layered CD/Be targets were continued in FY16, where one shot day was available. Three shots were taken with secondary targets at different laser intensities to measure the neutron spectrum and three shots without a secondary target to record the incident fast-ion spectrum. Again no neutrons from D–T fusion reactions were observed.

To be able to run realistic simulations of the OMEGA EP experiments, fusion cross sections based on the Bosch and Hale parametrization were added to the Monte Carlo particle transport framework Geant4. Geant4 already includes primary and secondary particle tracking and physics modules to describe the slowing down of the ion flow in the secondary target and neutron scattering in the target and detector.

First tests show that the Geant4 simulations correctly reproduce the relativistic kinematic of the D–D in-flight fusion reaction and the mean free path of the deuterons with respect to fusion reactions, if the simulations used enough particles that the statistical error becomes insignificant.

Figure 148.79 shows the calculated total neutron energy spectrum from a first preliminary simulation using a 4-MeV deuteron beam on a 1-g/cm^3 pure-deuterium target. A pure-deuterium target was chosen to improve the statistics.

Neutrons from both the primary D–D fusion (2 to 6 MeV) and the secondary D–T reaction (11 to 19 MeV) from the tritium
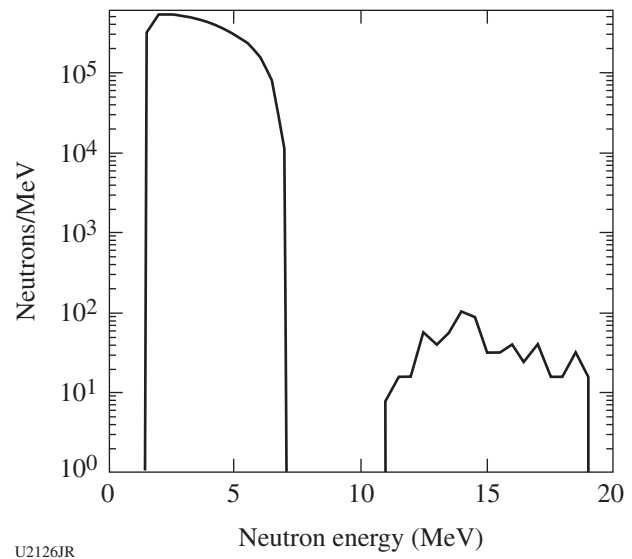
Figure 148.79
Neutron energy spectrum from a deuterium secondary target irradiated by a 4-MeV deuteron beam calculated by Geant4.

produced in the d(d,t)p branch of the D–D reaction are visible. Out of the 8×10^9 incident primary particles, ~0.1% produce a primary fusion neutron and ~0.1% of the tritons produced in the primary reactions generate a secondary neutron. Because of the complex interaction between the energy loss of the fast ions (deuterons, tritons) in the target material and the energy dependence of the fusion cross section, these conversion efficiencies are difficult to predict accurately without these detailed simulations. Given that the dynamic range of our current detectors is ~100, these simulations indicate that it might not be feasible to detect those secondary neutrons with the present detector system on OMEGA EP.

Proton Transport and Coupling into Shock-Compressed CH Targets for Proton Fast Ignition
Principal Investigator: W. Theobald (LLE)

A focused, laser-driven proton beam is an effective means for rapidly heating material and it remains a promising fast ignitor. However, there are unexplored topics that must be incorporated into an integrated proton fast-ignition scheme such as conversion efficiency to protons in a fully assembled target and transport of the high-current-density proton beam in shock-compressed fuel. In pTransEP-16A, we conducted experiments to study fundamental physics' underlying high-current proton beam production, transport, stopping, and energy coupling in reduced-scale, fast-ignition–relevant conditions using OMEGA EP. The two short-pulse beams were alternated with

700-J energy and 10-ps pulse duration to irradiate compound targets consisting of a curved source foil, a conducting cone to focus the beam, low-density resorcinol formaldehyde (RF) plastic foam (340 mg/cm^3) transport blocks, and 10-μm-thick Cu diagnostic layers on the top and rear sides. Integrated shots were also taken in which two long-pulse lasers were used to drive a quasi-planar shock to compress the RF in the probe beam path.

We shot targets of increasing complexity from a freestanding curved foil to the full compound integrated target. The proton spectrum was measured for each of the types using a stack of radiochromic film and a Thomson parabola ion energy analyzer. Figure 148.80 shows how the maximum proton energy decreased as target components were added. The maximum energy (shown here) and proton number (not shown) decreased as soon as material was added to the curved target. This is in line with our understanding from previous experimental and computational work that added target material is a sink for the energetic electrons that support accelerating fields on the target; however, the magnitude of the change is surprising. In fact, this reduction in energy gain is more significant than the stopping in the 0.34-g/cm^2 areal density of RF.
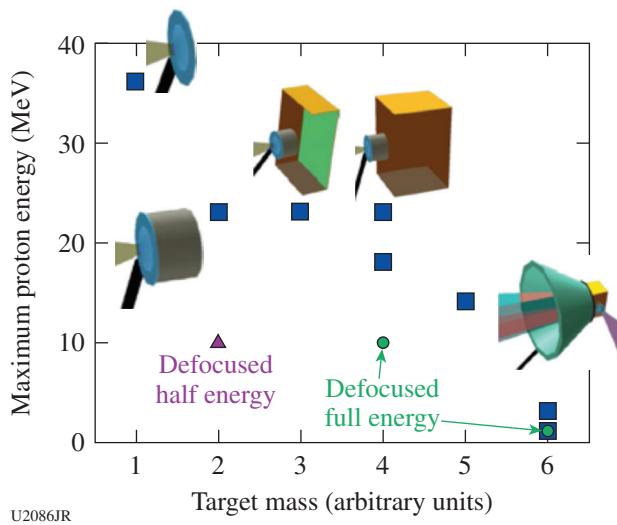
Figure 148.80
Maximum proton energy measured in the forward direction for the six target types investigated. The energy was highest for the freestanding target and lowest for the fully integrated target with a shock-compressed transport medium.

The coupling to the rear side of the target was also studied by observing Cu x-ray line emissions with a spectrometer (ZVH) and a monochromatic x-ray imager using an SCI. Example images from the latter (see Fig. 148.81) show the signature of

a moderately well collimated beam (cone angle <20°) in the laser's forward direction.

The localized emission will be compared to the results of future transport simulations. The simulations will also be compared to the proton spectral measurements with and without the RF blocks.
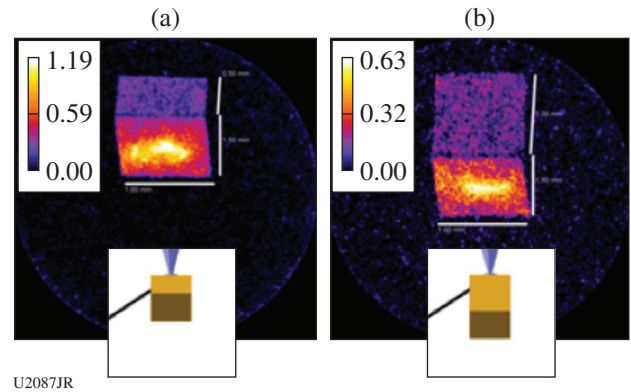

Figure 148.81
SCI images of 8.048-keV Cu K$_\alpha$ x-ray emission from Cu foils on the top and rear side of a plastic block. The block length was (a) 500 μm or (b) 1 mm. The insets show the target as viewed from the diagnostic. The signal consists of a relatively uniform background caused by refluxing energetic electrons and a forward-directed beam of protons.

Shear Stress and Mechanism of Phase Transition in Shock-Compressed Iron
Principal Investigator: C. E. Wehrenberg (LLNL)

The IronLaue-16 Campaign was the first campaign to use Laue diffraction to study the response of single-crystal iron to shock compression. As shock compression drives iron through a body-centered-cubic (bcc)–hexagonal phase transition, Laue diffraction can be used to determine the orientation of the transformed phase and therefore the mechanism of transformation. Additionally, Laue can measure the shear strain in the compressed state. In these shots, 32 OMEGA beams were used to drive an implosion of an empty CH capsule, creating a burst of broadband x rays during stagnation that are used for Laue diffraction. Separately, two beams were used to drive a shock into an ablator and the single-crystal sample. Excellent diffraction data were observed in several shots for a range of shock pressures. Figure 148.82 shows an example in which multiple diffraction spots from the shock-compressed iron are visible.
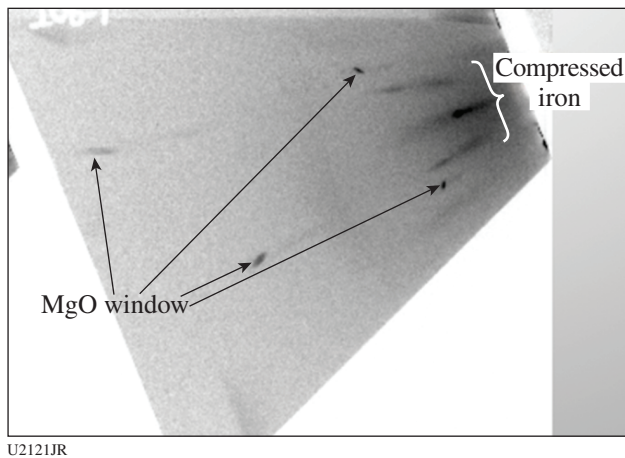
U2121JR

Figure 148.82
Example of Laue diffraction data showing multiple diffraction spots from shock-compressed iron.

FY16 LLNL Omega Facility Experiments
Principal Investigators: R. F. Heeter, S. J. Ali, P. M. Celliers, F. Coppari, J. H. Eggert, D. Erskine, A. Fernandez Panella, D. E. Fratanduono, C. M. Huntington, L. C. Jarrott, S. Jiang, R. G. Kraus, A. E. Lazicki, S. LePape, D. A. Martinez, J. M. McNaney, M. A. Millot, J. D. Moody, A. E. Pak, H.-S. Park, Y. Ping, B. B. Pollock, H. G. Rinderknecht, J. S. Ross, R. F. Smith, G. F. Swadling, C. E. Wehrenberg, G. W. Collins, O. L. Landen, A. Wan, and W. Hsing (LLNL); J. Benstead and M. Rubery (AWE); R. Hua (UCSD); and H. Sio (MIT)

In FY16, LLNL's High-Energy-Density (HED) Physics and Indirect-Drive Inertial Confinement Fusion (ICF-ID) Programs conducted several campaigns on the OMEGA and OMEGA EP Laser Systems, as well as campaigns that used the OMEGA and OMEGA EP beams jointly. Overall, these LLNL programs led 430 target shots in FY16, with 304 shots using only the OMEGA Laser System and 126 shots using only the OMEGA EP laser. Approximately 21% of the total number of shots (77 OMEGA shots and 14 OMEGA EP shots) supported the ICF-ID Campaign. The remaining 79% (227 OMEGA shots and 112 OMEGA EP shots) were dedicated to experiments for the HED Physics Campaign. Highlights of the various HED and ICF campaigns are summarized in the following reports.

In addition to these experiments, LLNL Principal Investigators (PI's) led a variety of Laboratory Basic Science Campaigns using OMEGA and OMEGA EP, including 81 target shots using only OMEGA and 42 shots using only OMEGA EP. The highlights of these are also summarized, following the ICF and HED campaigns.

Overall, LLNL PI's led a total of 553 shots at LLE in FY16. In addition, LLNL PI's also supported 57 NLUF shots on OMEGA and 31 NLUF shots on OMEGA EP, in collaboration with the academic community.

Indirect-Drive Inertial Confinement Fusion Experiments

Hydrodynamic Response from Oxygen Nonuniformities in Glow-Discharge Polymer Plastic
Principal Investigators: P. M. Celliers and S. J. Ali

Simulations and target characterization indicated that inhomogeneity in oxygen content could be a significant seed for Rayleigh–Taylor growth in NIF implosions using glow-discharge polymer (GDP) plastic shells. This has been indirectly supported by the observation of larger-than-expected in-flight modulations during NIF GDP capsule implosions along with the realization that such inhomogeneities can result from photo-induced oxygen uptake. To investigate the magnitude of the effect of these oxygen heterogeneities on the hydrodynamic response of GDP ablators, oxygen modulations were photo-induced in GDP foils by illuminating the foils with blue light through a periodic mask pattern. The foils were then fielded on OMEGA as ablators driven by a halfraum to replicate foot conditions on the NIF. The resulting optically reflective shock wave was observed using the OMEGA high-resolution velocimeter (OHRV), a 2-D single-gate measurement. Two-dimensional velocity maps were obtained for both oxygen-modulated and unmodulated samples, with the modulated samples showing clear evidence of the propagation of a rippled shock wave as a result of the photo-induced oxygen heterogeneity. A time series spanning approximately 2.3 to 4.2 ns after shock breakout from the GDP ablator into a poly (methyl methacrylate) (PMMA) witness layer was obtained and clearly showed that the decay in the amplitude of the perturbation was dependent on the perturbation wavelength, as expected.

Principal Hugoniot Measurements of Liquid Deuterium Above 100 GPa
Principal Investigator: A. Fernandez Panella

These two half-day campaigns using cryogenic targets on OMEGA investigated the principal Hugoniot of liquid deuterium at high precision above 100 GPa. This study was motivated by a systematic discrepancy between previous experimental data on different platforms (OMEGA, Z, and NIF keyhole data) and current equation-of-state (EOS) models above 100 GPa, with the data suggesting higher compression than models, including the current preferred EOS used in ICF

simulations.[29] Experimental uncertainties of the existing data are too large, however, to rule out the models unambiguously. Examining this discrepancy is relevant as the first shock in an ICF implosion lies on the principal Hugoniot of the fuel. Recent diagnostic improvements along with the availability of the recent high-accuracy calibration of the quartz EOS standard[30] result in new experiments collecting data with much higher accuracy.

The first campaign carried out three measurements of shock-compressed deuterium along the principal Hugoniot at pressures ranging from 350 to 550 GPa, the highest pressures to date. The ablator material was 90-μm-thick beryllium and the targets were driven by a 2-ns flat, square laser pulse. VISAR was used as the main diagnostic to measure shock velocities. In the alpha-quartz reference material, shock velocities of 34 to 40 km/s were measured, and velocities of 50 to 64 km/s were obtained in the deuterium (Fig. 148.83). A summary of the data is shown in Fig. 148.84. Note the improvement of the data quality with respect to previous campaigns (e.g., D. Hicks 2009); the uncertainties in the shock velocities in the present campaign are a factor of 3 smaller.

The impedance-matching analysis relies on an accurate knowledge of the EOS of the standard material (alpha quartz) to determine the particle velocity, pressure, and density of the sample (shock-compressed deuterium). Because the new data extend beyond the valid range of the quartz calibration, two tabular quartz EOS models have been used to estimate the systematic uncertainty of the new data. The results are shown in Fig. 148.84. All the experimental data show higher compression along the Hugoniot (4.5 to 4.7) than the current EOS models predict (e.g., 4 to 4.3 with LEOS 1014 Kerley). This trend is similar to the previous data obtained at different facilities (Omega, Z, and the NIF), which also showed a similar discrepancy with current models beyond 100 GPa. Further analysis is underway to understand the systematic uncertainties and to understand the underlying reasons for such discrepancy with the models.

The second half-day in August was very successful as well. The addition of an extra quartz anvil to the target design enabled us to measure a re-shock and a second impedance data point. Four shots were taken that will complete the data set at lower shock pressures ($100 < P < 350$ GPa), where the Knudson–Desjarlais quartz calibration is more accurate.

Study of Interpenetrating Plasmas on OMEGA
Principal Investigator: S. Le Pape

The Near-Vacuum Campaign on the NIF has shown that radiation–hydrodynamic codes such as *HYDRA* do not accurately describe the collision of two high-velocity flows, e.g., ablated gold from the hohlraum wall and ablated carbon from the capsule, with relative velocity of 8×10^7 cm/s at an electron density of 10^{21}/cm^3. In this parameter space, radiation–hydrodynamic simulation predicts a stagnation of the two plasmas, leading to a density ridge at the materials' boundary; however, experimental data do not support this scenario. The main hypothesis to explain the discrepancy is that the flows'
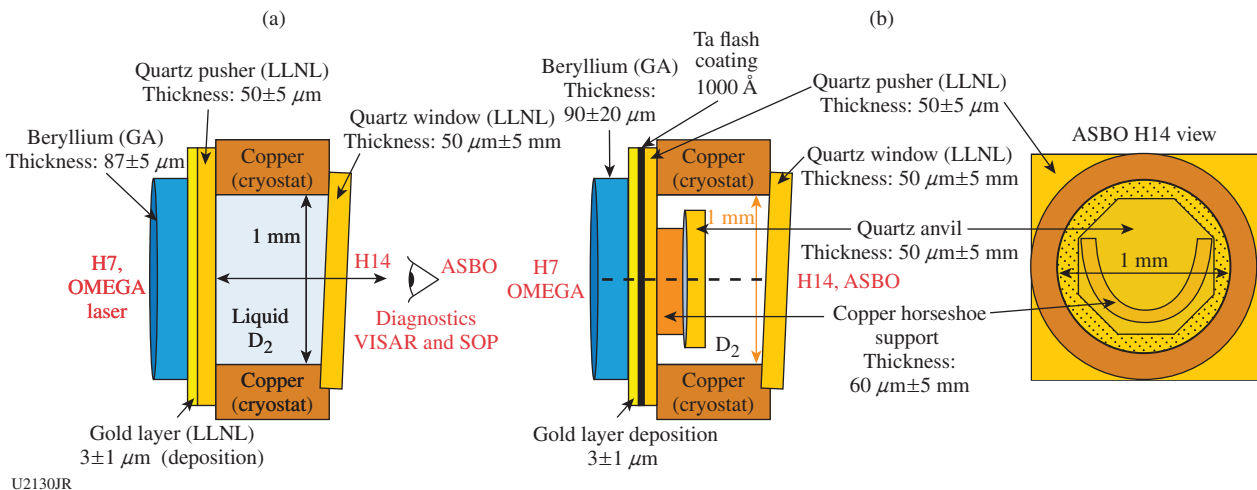

Figure 148.83
Schematic of the target design and experimental configuration for the (a) PCRYO-16A and (b) PCRYO-16B Campaigns, respectively.
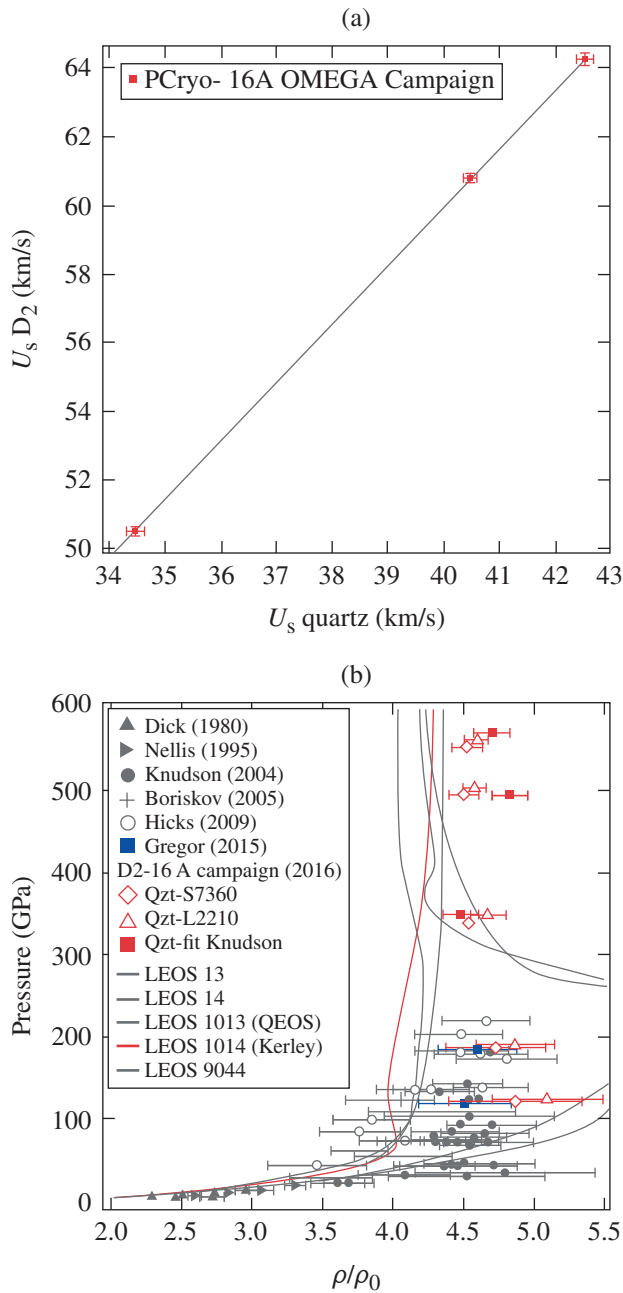
Figure 148.84

(a) Summary of the observables: transmitted shock velocity in D_2 versus incident shock velocity in quartz. (b) Pressure versus compression along the principal Hugoniot of liquid deuterium. Experimental data: vertical triangle by Dick *et al*., horizontal triangle by Nellis, filled circles by Knudson *et al*., crosses by Boriskov, open circles by Hicks *et al*., blue squares are recent data (not yet published) by M. Gregor *et al*. (LLE), red symbols this work (preliminary result) analyzed using the Knudson–Desjarlais quartz calibration and also using two tabular quartz EOS models (*SESAME* 7360, Kerley, and LEOS 2210).

interpenetration cannot be described by a fluid code but requires a full kinetic description at this high relative velocity and low density. To explore this, an OMEGA campaign was designed to emulate a near-vacuum hohlraum environment in a simpler geometry that would allow one to diagnose the material boundary using both optical Thomson scattering and time-resolved x-ray imaging. To reach NIF-relevant conditions, laser beams are used to irradiate both an outer ring of material ranging (depending on the shot) from low to high Z (carbon, aluminum, and gold) and an inner ring of high-density carbon (Fig. 148.85). The laser energy was also varied during the campaign.
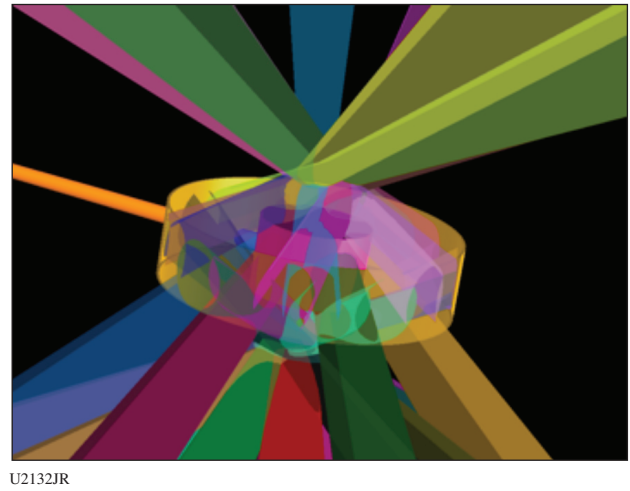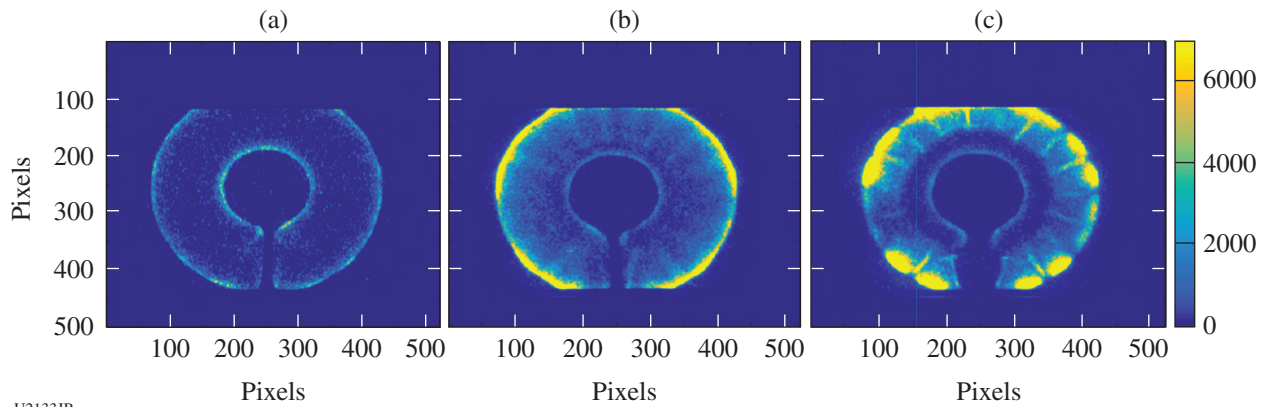

Figure 148.85
VISRAD view of the target geometry with laser beams.

High-quality data were obtained from both main diagnostics. Figure 148.86 illustrates that as the Z of the outer ring material is increased from carbon to gold, and plasma collisionality is increased, the material boundary becomes more apparent for the same laser drive and time.

Figure 148.87 shows ion-acoustic wave (IAW) and electron plasma wave (EPW) spectra. From these spectra, flow velocities, ion temperatures, electron densities, and flow compositions are deduced, providing a complete picture of the plasma parameters.

Broadband Proton Radiography of Shock Front in Gases
Principal Investigators: Y. Ping and R. Hua (LLNL)
Co-investigators: H. Sio (MIT); C. McGuffey and F. Beg (University of California–San Diego); and G. W. Collins (LLNL)

Figure 148.86
X-ray images at 0.9 ns for the three different rings: (a) carbon, (b) aluminum, and (c) gold. The center circle is the high-density carbon ring; the outer circle is the low- to high-Z ring.
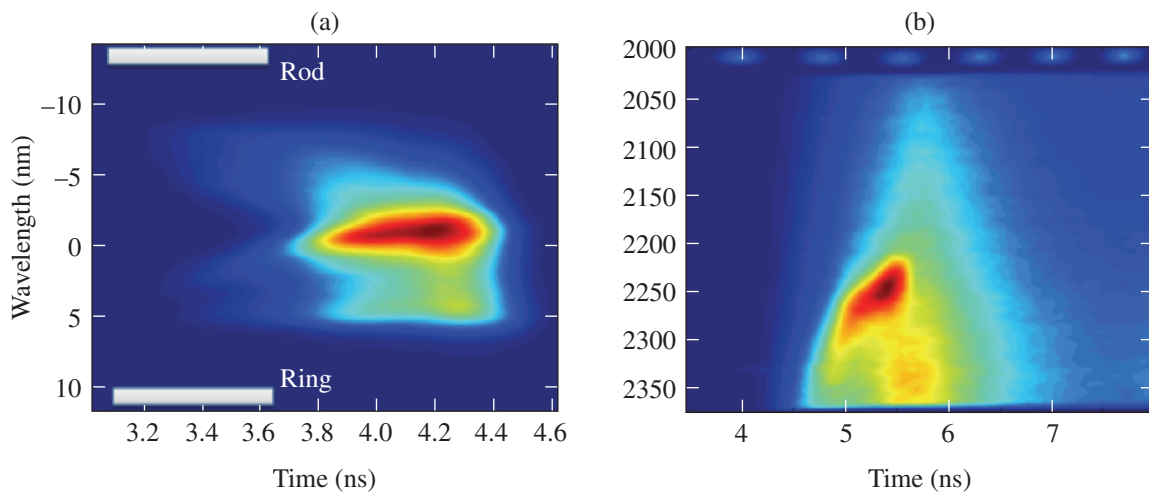
Figure 148.87
(a) Ion-acoustic wave (IAW) and (b) electron plasma wave (EPW) spectra for carbon into carbon.

This campaign is based on an experimental platform developed on OMEGA EP in FY15 to study shock-front structure and field effects in low-density systems. The broadband proton backlighter is generated by high-intensity, short-pulse interaction with metal foils through the well-known TNSA process. The shock is driven by three UV long-pulse beams in a gas cell with a CH ablator. Both shot days provided excellent proton radiographs and soft x-ray spectra of shock propagation in gases. Figure 148.88(a) displays proton radiographs with different-energy protons, showing clearly energy-dependent deflection of protons and complex structure at the shock front. A variable-spaced-grating (VSG) snout was added as a spectroscopic diagnostic for He–Ne mixtures. The spatially resolved spectra, shown in Fig. 148.88(b), provided shock velocity in a single shot and a constraint on shock temperature by Ne lines. A radiative precursor was also observed as indicated

in Fig. 148.88(b) as the He-like Ne line extended beyond the shock front. A paper on this new platform has been submitted to Review of Scientific Instruments[31] and a radiograph analysis paper is in progress.

Studies of Kinetic and Multi-Ion-Fluid Effects in Inertial Confinement Fusion Implosions Using Nuclear-Reaction and X-Ray Emission Histories
Principal Investigator: H. Sio (MIT)

The motivations for the one-day DTHe3-16A Campaign on OMEGA were (1) to measure simultaneously the DT and D^3He reaction histories on the same instrument and (2) to measure multiple x-ray emission histories in different x-ray energy bands. By measuring the nuclear reaction histories, one can make a time-resolved comparison of the nuclear

(a) Proton radiographs

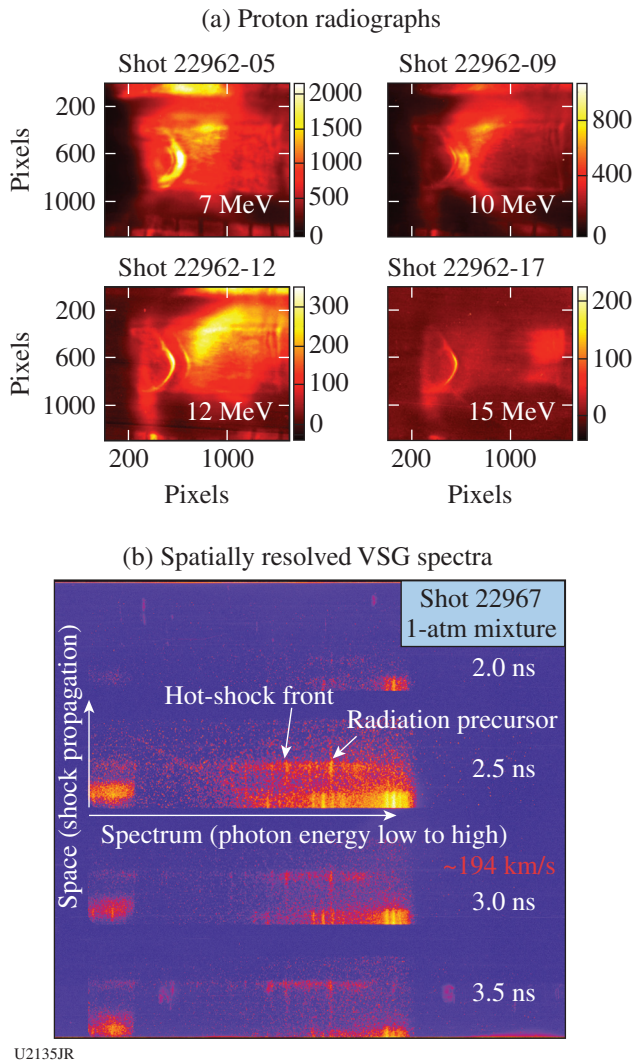### (b) Spatially resolved VSG spectra

U2135JR

Figure 148.88
(a) Proton radiographs of a shock front in He gas showing energy-dependent structure; (b) spatially resolved spectra by a variable-spaced-grating (VSG) snout. Both shock front and radiative precursor were clearly observed.

rates as implosions transition from a more-hydrodynamic ($\sim$2.3-mg/cm^3 initial gas fill) to a more-kinetic ($\sim$0.3 mg/cm^3 initial gas fill) regime. Comparison with hydrodynamic and kinetic-ion simulations will be used to understand how plasma density and temperature profiles are altered by nonhydrodynamic effects during shock burn.

At the same time, the ratio of two different nuclear reaction histories will be used to infer a spatially averaged $T_i(t)$. X-ray emission histories in different x-ray energy bands will be used to infer a spatially averaged $T_e(t)$ from the slope of the bremsstrahlung continuum. Since both the nuclear reaction histories and the x-ray emission histories are simultaneously measured

on the particle x-ray temporal diagnostic (PXTD), their relative cross timing is very well known (<10 ps). $T_i(t)$, $T_e(t)$, and their relaxation toward equilibrium will be used to measure the ion–electron (i–e) equilibration rate to experimentally validate the Coulomb logarithm for various plasma conditions.

In addition to the primary PXTD data (Fig. 148.89), other nuclear [wedge-range filter (WRF), charged-particle spectrometer (CPS), and proton-core imaging spectroscopy (PCIS)], optical (FABS), and x-ray [Dante, Sydor framing camera (SFC), and framed Kirkpatrick–Baez x-ray microscope (KB-FRAMED)] diagnostics also measured good data to constraint implosion trajectory, laser absorption, nuclear yields, ion temperatures, and x-ray output.
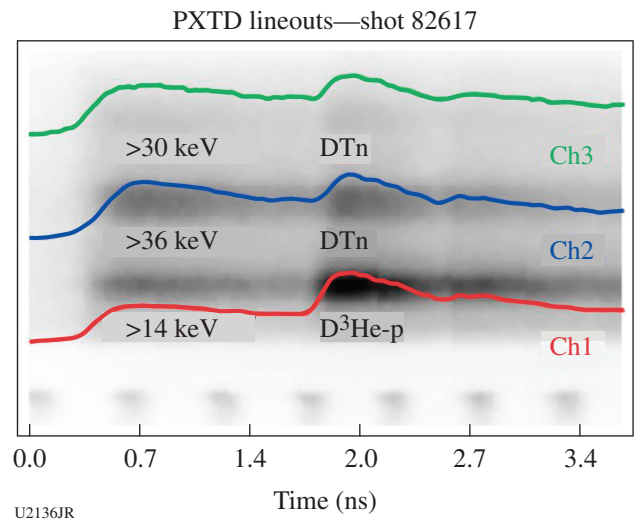
PXTD lineouts—shot 82617

U2136JR

Figure 148.89
Particle x-ray temporal diagnostic (PXTD) channel lineouts on shot 82617. X-ray emission histories (in the energy band above 14, 30, and 36 keV) and nuclear reaction histories (DT, D^{3}He) are measured simultaneously on one streak. Each streak channel has its own filtering in front of, and light attenuation filter behind, the scintillator to equalize the signal relative to the other channels.

X-Ray Blanking Mitigation Experiments for the NIF Optical Thomson-Scattering Diagnostic
Principal Investigators: G. F. Swadling and J. S. Ross

The XRayBlanking-16A experiment was carried out to assess the risk posed to the NIF optical Thomson-scattering (OTS) diagnostic by x-ray–driven "blanking" of the optical debris shield, and to test a Xe gas x-ray shield design concept. A total of 11 target shots yielded high-quality data that addressed the threshold for x-ray blanking effects and demonstrated the feasibility of the Xe gas x-ray shield concept.

The radiation environment presented by NIF hohlraums is extreme; they typically produce radiation temperatures of ~300 eV, with soft x-ray (<3-keV) fluxes of ~10 to 20 TW sr^{-1}, and total time-integrated yields of ~60 kJ sr^{-1}. An optically transparent debris shield will be installed in front of the OTS collection telescope to protect it from target debris produced during shots. The optical layout constrains this shield to be <60 cm from the target, but at this distance, during a typical ignition-scale experiment, the window could receive a total time-integrated soft x-ray fluence of up to 16 J/cm^2. This fluence raises the potential for blanking of the debris shield–induced optical opacity caused by the effects of soft x-ray irradiation.

In the XRayBlanking-16A experiments, the OMEGA Laser System was used to heat a gold sphere target to produce soft x rays with a comparable spectrum and power to that produced by NIF hohlraums. The soft x-ray flux and spectrum were diagnosed using the OMEGA Dante diagnostic. Sample optics were exposed to this soft x-ray flux and their optical transmissions were measured using a 532-nm probe laser beam. Blanking was observed over a fluence range from 0.2 to 2.5 J/cm^2. This threshold falls significantly below the expected soft x-ray fluence onto the NIF OTS debris shield, indicating that measures are required to mitigate this effect.

An optically transparent but x-ray opaque Xe gas x-ray shield concept was tested. The x-ray shield successfully mitigated x-ray blanking of glass samples, demonstrating the feasibility of this concept (see Fig. 148.90). The x-ray shield concept will be applied to the NIF OTS.

Measurements of Anisotropy in Non-LTE Low-Density Iron–Vanadium Plasmas

Principal Investigator: L. C. Jarrott
Co-Investigators: M. E. Foord, R. F. Heeter, D. A. Liedahl, M. A. Barrios Garcia, G. V. Brown, W. Gray, E. V. Marley, C. W. Mauche, K. Widmann, and M. B. Schneider

Accurate characterization of optical-depth effects, which create geometrical anisotropies in K-shell line emission from low-density non-LTE (local thermodynamic equilibrium) plasmas, is very important for improving line-ratio–based temperature measurements in hohlraums on the NIF, as well as OMEGA. This campaign built upon the established tamped-foil non-LTE platform on OMEGA, with specific goals to increase the laser intensity, verify the hydrodynamics of the target expansion, and provide a robust calibration of the x-ray spectrometers. Two target types were used: The primary target was a 10-μm-thick, 1000-μm-diam beryllium tamper containing
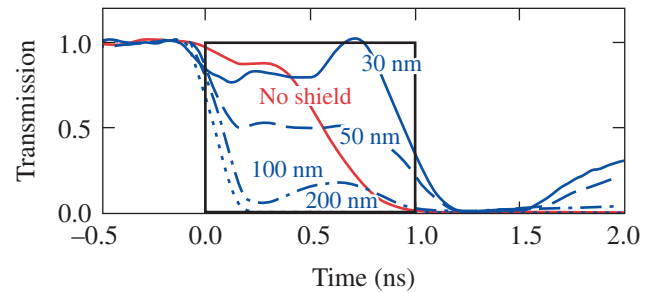
Figure 148.90
Example of 532-nm sample transmission data from XRayBlanking-16A. The black line shows the nominal square laser pulse shape. The red line shows the transmission of a sample in the absence of an x-ray shield. The sample was exposed to ~2.5 J/cm^2 of soft x rays over the duration of the experiment. The blue lines show transmission through samples protected by a 10-cm-long Xe gas shield at a pressure of 0.04 atm. The gas was contained by thin (30- to 200-nm) SiN membranes, which were themselves ablated by the soft x rays. For membranes ≤50 nm thick, the optical transmission was extended significantly relative to the unshielded sample. The thicker membranes appear not to have expanded sufficiently to allow transmission of the probe without significant absorption.

a volumetrically equal mixture of iron and vanadium, 200 nm thick and 250 μm in diameter. The second target was a "null" where the beryllium tamper contained no sample material. Three beam–target orientations were used over the course of 13 shots. In the first configuration, an MSPEC spectrometer situated in TIM-2 and a gated pinhole imager in TIM-3 had an edge-on view of the target, while another MSPEC in TIM-6 and another pinhole imager in TIM-4 had a face-on view. In the second configuration, the target orientation with respect to TIM-2 and TIM-6 was reversed. In the third configuration, all primary TIM-based diagnostics had a viewing angle of 45° with respect to target normal. These three target–beam orientations provided an *in-situ* cross-calibration of the spectrometers and pinhole imagers. The data obtained from 13 shots included simultaneous, time-resolved edge-on and face-on measurements of (1) the iron and vanadium K-shell spectra and (2) the expanding plasma volume. The K-shell spectral data provided time-resolved electron temperature measurements of the expanding plasma, with preliminary analysis indicating $T_e >$ 2 keV, higher than previous campaigns (Fig. 148.91).

Optical Thomson-Scattering Measurements from Gas-Covered Au Spheres

Principal Investigator: J. S. Ross
Co-investigators: G. Swadling, R. Heeter, M. Rosen, K. Widmann, and J. Moody (LLNL); and D. H. Froula (LLE)

The GasCoSphere-16A Campaign performed "gas-covered," high-Z sphere experiments, with a gold-coated CH sphere
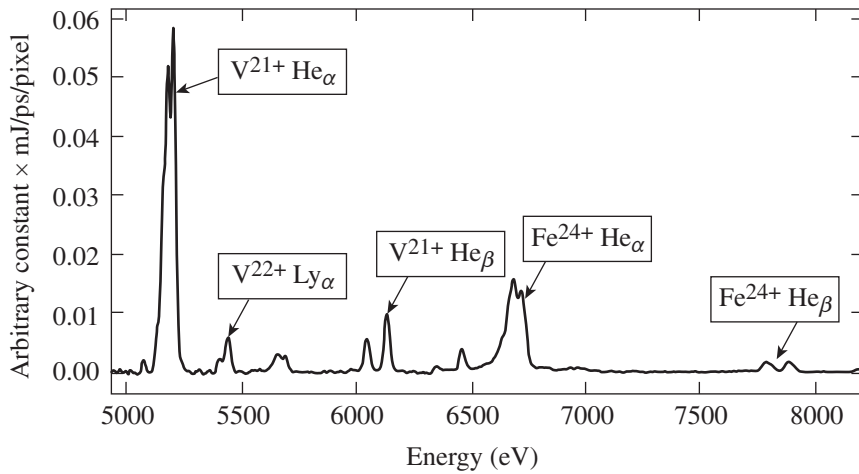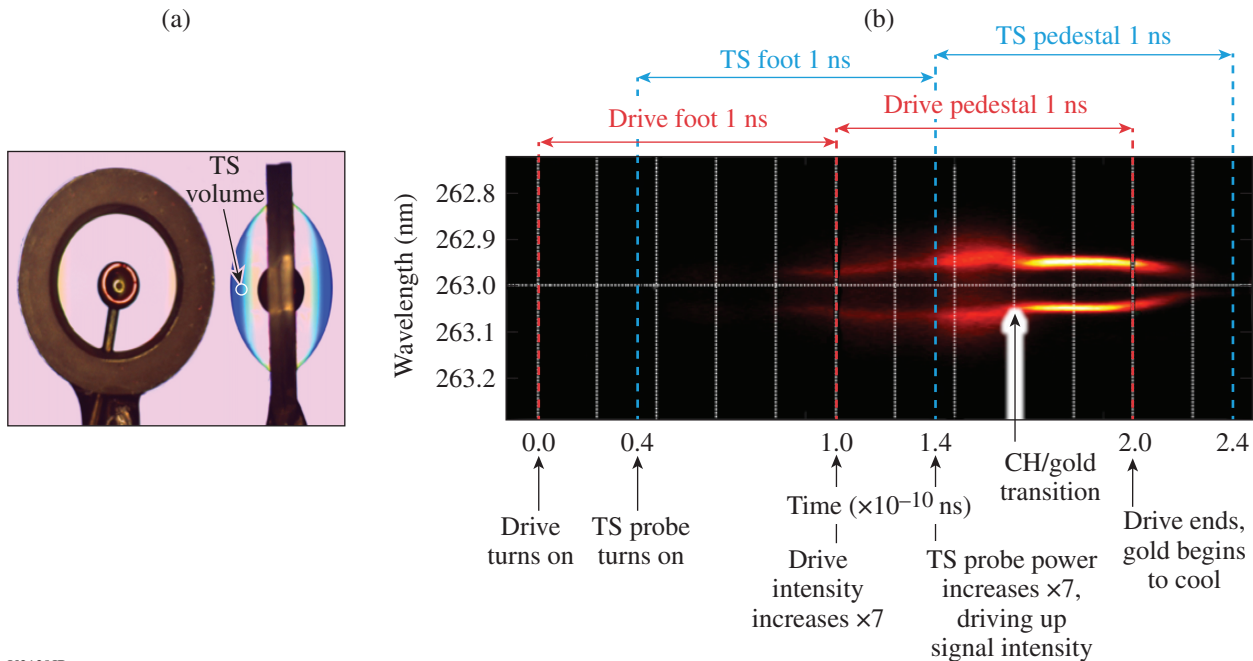
Figure 148.91
Spectrum measured by an MSPEC spectrometer of the x-ray emission from K-shell transitions in highly charged vanadium and iron. An electron temperature >2000 eV is inferred from the various line ratios.

U2138JR

placed inside of a gas bag and illuminated using a direct-drive geometry, to investigate atomic physics models, radiative properties of the laser-spot plasma, and the interpenetration of multi-ion–species plasmas relevant to ICF indirect-drive–ignition hohlraums. These experiments use a laser irradiation of 10^{14} to 10^{15} W/cm^2, similar to National Ignition Campaign hohlraums. The gas bag was filled with 1 atm of either propane or a 70/30 mix of propane and methane, achieving (respectively) initial electron densities of 7.5% and 6.0% of the critical density of the 3ω drive beams. With these conditions, the gold–gas interface mimics the interaction of a hohlraum's gold wall with the low-density hohlraum fill gas.

In these experiments, the plasma temperature and density at various radial positions in the blowoff plasma were characterized using optical Thomson scattering. The laser drive used a shaped laser pulse (1-ns square foot, 1-ns square peak) to reduce the shock produced by the gas-bag window. The electron temperature and density, the plasma flow velocity, and the average ionization state are inferred by fitting the theoretical Thomson-scattering form factor to the observed data. An example of the Thomson-scattering data from ion-acoustic fluctuations is shown in Fig. 148.92. The measured data are compared to post-shot simulations with and without a diffusion model in Fig. 148.93. The data and simulations show minimal

U2139JR

Figure 148.92
(a) A 1-mm-diam Au sphere centered in a 2.6-mm-diam gas bag. The location of the Thomson-scattering (TS) volume is shown. (b) This example of the Thomson-scattering ion feature indicates where the transition from scattering from Au to scattering from CH plasma is observed at 1.6 ns.

diffusion of Au into the low-Z CH plasma. Continued data analysis and simulations are in progress to better understand the plasma evolution and heat transport.
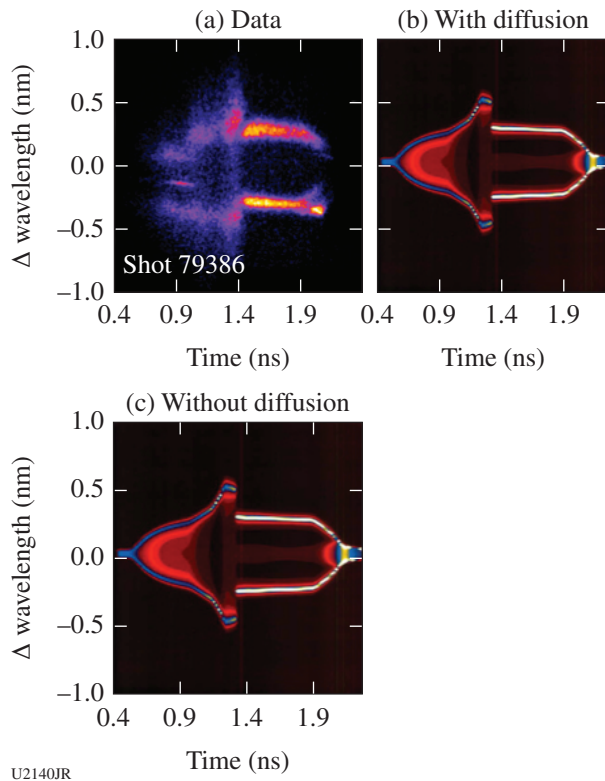
Figure 148.93
The (a) measured Thomson-scattering signal is compared to post-shot simulations (b) using or (c) not using a diffusion model to investigate the interpenetration of Au into the CH plasma.

High-Energy-Density Experiments

1. Material Equation of State Using Diffraction Techniques

Measurements of the High-Pressure Refractive Index of Magnesium Oxide Windows
Principal Investigator: R. F. Smith

Magnesium oxide (MgO) has the potential to be a good alternative to LiF as a window material in high-pressure EOS experiments. The goal of this half-day OMEGA campaign was to measure the refractive index of MgO to pressures up to 800 GPa, following the experiments and analytical techniques outlined in Ref. 32. The target design (shown in Fig. 148.94) consists of 100 μm of micrograined diamond with, on the rear surface, a half layer of 100-μm MgO [100] single crystal.
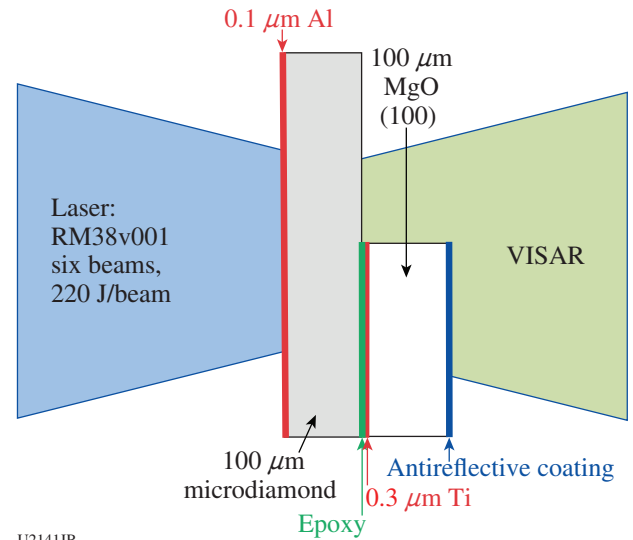
Figure 148.94
Target design for the MaxOxWindow-16A experiment.

A 0.3-μm Ti layer was coated onto the inner MgO surface to enhance reflectivity for VISAR measurements, and an antireflection coating was added to the rear surface. Target normal was oriented along the OMEGA H7–H14 axis. Six 23° beams with the RM38v001 pulse shape were incident onto the diamond ablator, using 220-J/beam, SG8 phase plates, and beam delays to achieve an ~7-ns ramped laser pulse. With this configuration a ramp compression wave with a peak pressure of 800 GPa was launched into the target assembly. The LLE-ASBO (VISAR) diagnostic could then simultaneously measure the diamond free-surface velocity and the diamond/MgO interface velocity. With knowledge of the sample thicknesses and the EOS of both diamond and MgO, one can compare the expected diamond/MgO interface velocity with the measured velocity. The discrepancies between the two can be then used to determine the density correction on the MgO refractive index with that of LiF (Ref. 32). Good-quality data were obtained on this campaign to support this analysis.

Ramp Compression of MgO and Development of Ge Diffraction Backlighter on OMEGA EP
Principal Investigator: R. F. Smith

The target and laser design for the W-MgO-DiffEP-16A Experimental Campaign is shown in Fig. 148.95(a). This campaign successfully demonstrated the capability of ramp compression of samples to high pressure on OMEGA EP [Fig. 148.95(c)]. With a slight variation of the target design

(a)

10 μm Mo
30 μm   45 μm
diamond | MgO (100)

ERM99V021

1.1-mm phase plate

VISAR

0.1-μm W coating over half the field of view

(b)
—Shot 22254 (751.6 J)
—Shot 22256 (1557.6 J)

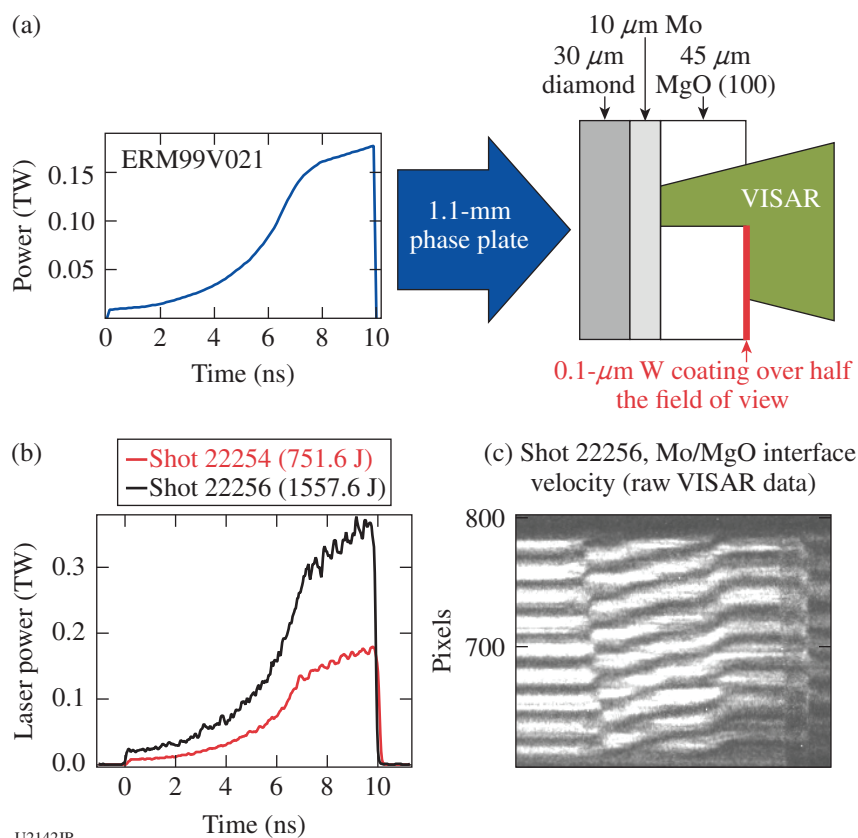(c) Shot 22256, Mo/MgO interface velocity (raw VISAR data)

U2142JR

Figure 148.95

(a) Laser and target request for the W-MgO-DiffEP-16A shots. A 10-ns pulse (ERM99v021) was designed to compress to pressures of 500 GPa and then hold at that pressure. The target package consists of a 30-μm diamond ablator, a 10-μm Mo foil, and a 45-μm-thick MgO [100] window. Half of the MgO free surface was coated with 0.1 μm of W, such that the OMEGA EP VISAR diagnostic could simultaneously measure both the Mo/MgO interface velocity and the MgO free-surface velocity. (b) As-delivered laser power for two shots. (c) VISAR data from a shot successfully ramp compressing the MgO to several hundred GPa.

in Fig. 148.95(a), a 10-ns ramped pulse shape (ERM99v006) launched a steady shock into the MgO sample. By increasing the laser power (shock pressure) on a shot-to-shot basis, it was established that along the Hugoniot single crystal, MgO loses its 532-nm transmission at ~300 GPa; this is consistent with the onset of the B1–B2 phase transformation.

Simultaneously, this campaign tested the efficacy of a Ge He$_\alpha$ 10.2-keV source for x-ray diffraction measurements. The Ge target consisted of a 6-μm layer of Ge, coated onto a graphitic carbon substrate, and then illuminated with a 1-ns flattop pulse that delivered 1250 J into a 200-μm spot. Using this configuration, a strong He$_\alpha$ peak was measured and found to be sufficiently strong for use as a source in subsequent x-ray diffraction experiments.

Development of a New Platform
for Measuring Recrystallization
Principal Investigators: F. Coppari and R. G. Kraus

The goal of this campaign is to develop a platform for measuring recrystallization of Pb through shock-ramp compression. By launching a first initial shock to compress the sample along the Hugoniot close to the melting pressure, letting it release

into the liquid phase, and then recompressing it with a ramp compression across the solid–liquid phase boundary, one can measure high-pressure melting lines of materials. The phase of the Pb upon shock, release, and ramp compression is monitored by time-resolved x-ray diffraction. The onset of melting is identified by the appearance of a diffuse scattering pattern and the disappearance of the Bragg diffraction lines characteristic of the solid. The pressure is monitored by VISAR, looking at the interface between the Pb and a LiF window. This campaign tested for the first time the use of beryllium ablators in diffraction experiments at Omega. This was possible thanks to excellent support from the Omega staff to implement special procedures to avoid Be contamination of the diffraction diagnostic hardware and the image-plate media used to record the data. The behavior of Be ablators is relatively easy to capture with hydrocode simulations, improving predictive capabilities for this class of experiments. In this experiment it was possible to accurately tune the laser pulse shape and compress the Pb sample along this complicated shock/release/ramp path. Beryllium is also a highly efficient ablator, especially compared to standard plastic ablators, so the same pressure can be obtained with lower laser energy, with the added desirable effect of reducing the ablation x-ray background that may interfere with the diffraction measurements. On this recent OMEGA EP shot

day, excellent diffraction data were obtained that will help inform future Omega and NIF campaigns.

How Much Do The Backlighter X-Rays Heat Unshocked Diffraction Samples?
Principal Investigator: D. Erskine
Co-investigator: J. H. Eggert

Recently many diffraction shots on the NIF using the TARDIS diffraction platform have successfully returned valuable information about the structure of materials under shock loading. These experiments use an x-ray backlighting source created by intensely illuminating a material such as Fe or Cu to produce K-shell x-ray lines. This illumination occurs while other laser illumination creates a pressure wave that moves through the sample. The x rays diffract from the compressed sample and the angular directions of the diffracted rays are recorded by a set of time-integrating imaging plates that surround the sample. Simultaneously, a pair of VISAR interferometers measure the Doppler velocity of the target surface and the velocity history reveals information about the shock loading of the target.

The question is, does the backlighting illumination itself cause enough heating in the sample to perturb these measurements? To find out, this experiment shot a set of diffraction targets that were *not* illuminated by the pressure drive lasers; only the backlighting x rays were used. If the temperature increase related to absorption of x rays is significant, the thermal expansion creates a velocity (and displacement) signature. The answer is yes, a small signal can be observed, but only at maximum OMEGA EP laser power to the backlighter and with thicker (50-μm) samples. This was established using one day of OMEGA EP time to deliver nine shots using various sample thicknesses and backlighter sources. No heating signature was observed for the first six shots using moderate backlighter laser power on either 5- or 50-μm-thick samples. On three shots, however, a small thermal expansion displacement was observed (Fig. 148.96) when the maximum amount of backlighter power was delivered onto a relatively thick sample. These data will be used to refine the design of upcoming diffraction measurements.

Development of in-situ Pressure Standard for Diffraction Experiments
Principal Investigator: F. Coppari
Co-investigator: J. H. Eggert

The goal of this campaign is to develop a new way to determine pressure in diffraction experiments, based on the use of
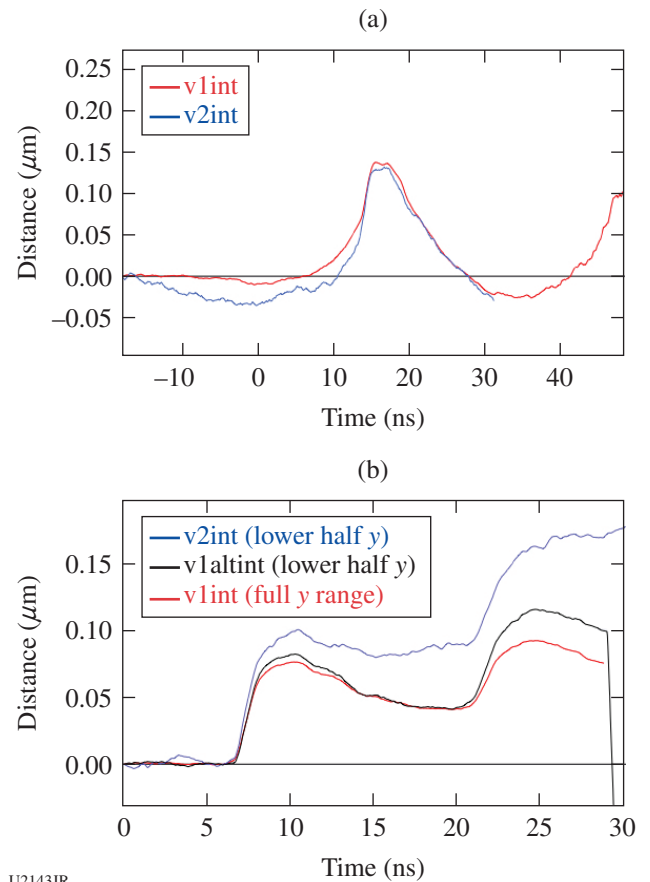
Figure 148.96
Measured displacement of diffraction sample's rear surface versus time, by integrating the VISAR velocity signal. Two VISAR's (1 = red, 2 = blue) monitor the same sample but have different record lengths. (a) Shot 22612 (Fe backlighter on 100 μm of Al). Good agreement between VISAR's was obtained. (b) Shot 22614 (Cu backlighter on 50 μm of Al). The discrepancy between the blue trace (VISAR2) and the red and black traces (integrating different regions on VISAR1) requires further investigation.

an *in-situ* pressure gauge. By measuring the diffraction signal of a standard material (whose EOS is known) that has been compressed together with the sample, one can determine the pressure reached during ramp compression.

Currently, pressure is determined with VISAR measurements of diamond free-surface velocity; this method is in some cases ambiguous (e.g., because of the lack of reflectivity or shock formation). Cross checking the VISAR measurement with *in-situ* pressure determination, using the diffraction signal of a standard material, will improve the diffraction platform by providing a complementary way of determining the pressure state within the sample. In addition, combining pressure determination from VISAR and from the *in-situ* gauge can

also provide information about the temperature of the sample by measuring the calibrant thermal expansion.

In this experiment, different pressure gauge materials (Au, Pt, and Mo) were tested in ramp compression to a moderate pressure (2 to 3 Mbar). Excellent-quality data were obtained. The Pt standard gave the best results because the diffraction signal was strong and untextured. Although this platform still needs some development effort before being used routinely in diffraction experiments, the data collected so far are extremely encouraging and suggest that the use of an *in-situ* pressure gauge can be a viable path forward in future x-ray diffraction measurements at both Omega and the NIF.

Development of Simultaneous Diffraction and EXAFS Measurements
Principal Investigator: F. Coppari
Co-investigators: Y. Ping and J. H. Eggert

Simultaneously measuring diffraction and extended x-ray absorption fine-structure (EXAFS) signals in the same shot will be an enormous advancement for laser-based materials experiments. Such capability would provide simultaneous probes of both the long-range (diffraction) and short-range (EXAFS) order of the material, as well as two complementary probes of the Debye–Waller factor to probe the temperature of a single material state.

The approach in this campaign used the PXRDIP diagnostic to measure diffraction and the x-ray spectrometer (XRS) to measure EXAFS. The challenge was to find a suitable backlighter that would generate both a monochromatic (for diffraction) and broadband (for EXAFS) x-ray source. Different schemes were tested out in the different campaigns, such as Kr-filled capsule implosions or illumination of a high-Z foil to exploit both the line and the continuum emission, but these initial schemes did not work for both diffraction and EXAFS. Success was achieved, however, in measuring simultaneous XRD and EXAFS by using a dual-material foil backlighter, where one side of the foil is optimized to generate He_α radiation for diffraction (i.e., Fe foil driven with six beams at 500 J and a 300-μm laser spot) and the other side is used to generate a broadband bremsstrahlung continuum for EXAFS (i.e., Ag foil driven with 13 beams at 500 J and best focus to maximize the laser intensity), as shown in Fig. 148.97. The sample material in these shots was a "diamond sandwich" with an Fe sample as typically used in ramp-compression experiments. Figure 148.97 also shows examples of the EXAFS and diffraction data.

Further development is needed to improve the data quality, but this result represents a big step forward in the study of dynamically compressed matter.
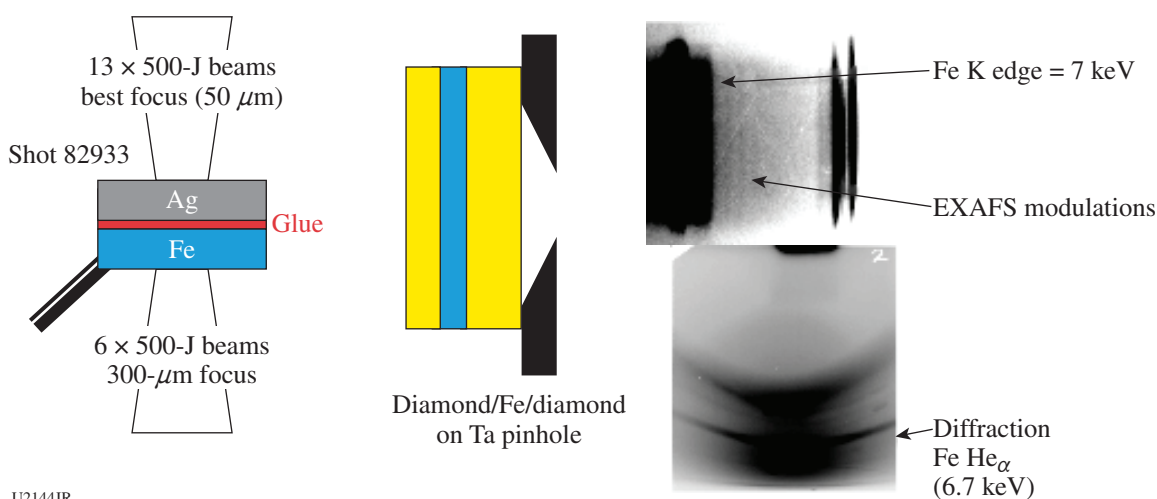

Figure 148.97
Schematic of the backlighter and target used in the XRD-EXAFS_16C Campaign to successfully measure simultaneous extended x-ray absorption fine structure (EXAFS) (top data) and diffraction (bottom) of an Fe foil sandwiched between a diamond ablator and a window.

2. Material Equation of State Using Other Techniques

Development of Spherically Convergent Equation-of-State Measurements

Principal Investigator: A. E. Lazicki

Co-investigators: D. Swift, A. Saunders, T. Doeppner, F. Coppari, R. London, D. Erskine, D. E. Fratanduono, P. M. Celliers, J. H. Eggert, G. W. Collins, H. Whitley, J. Castor, and J. Nilsen

This series of shots was designed to test and qualify a platform for measuring Hugoniot EOS at pressures much higher than can be achieved using a standard planar drive. This platform is intended to collect data in the >100-Mbar pressure regime, where currently very little data exist for any material, for the purpose of constraining EOS models.

The first two campaigns, GbarEOS-16A and -16B, used a hohlraum (indirect drive) to launch converging shock waves into solid spheres of CH_2, similar to an existing platform on the NIF but not yet in use on OMEGA. Along the axis of the hohlraum, backlit 2-D x-ray images of the imploding sphere were collected with a framing camera; streaked backlit images of a slice of the sphere, imaged through a slit in the hohlraum,

were also recorded with a streak camera (Fig. 148.98). The radiographs yield density and shock velocity, which allow one to calculate the shock state using the Rankine–Hugoniot equations. The two campaigns experimented with variations in camera configuration, hohlraum gas fill, x-ray backlighter energies, and hohlraum drive energy. Usable data were collected on all diagnostics for a subset of the shots, indicating pressures between 30 to 200 Mbar, and analysis is in progress. In a subset of the shots, x-ray Thomson-scattering measurements were made using a spectrometer with a view along the hohlraum axis in an effort to constrain temperature as well. An analysis of these results has been published.[33] The third half-day campaign (GbarEOS-16C) used the OMEGA beams to directly ablate a sphere of deuterated plastic (CD) to drive the convergent shock wave, with the core material state assessed via radiography, x-ray Thomson scattering, and neutron-yield diagnostics. Results of these campaigns are being used to further optimize the platform to make more measurements in FY17.
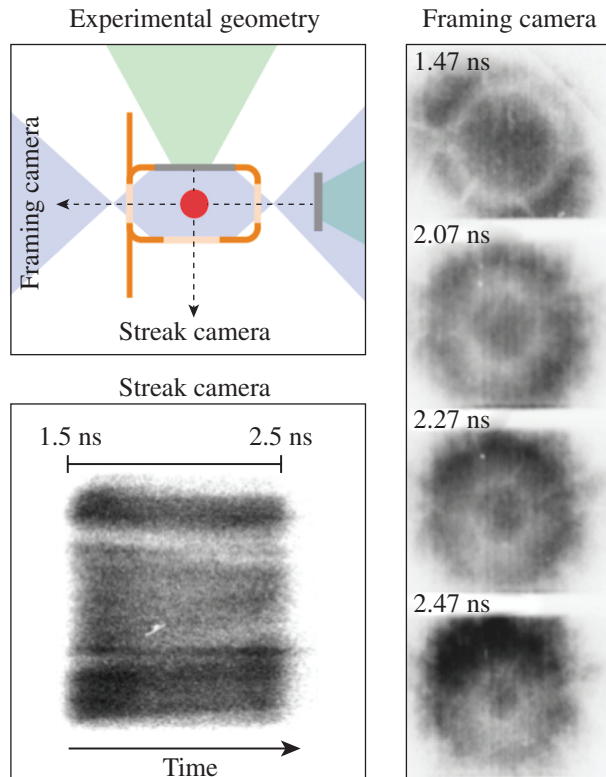
Development of Conically Convergent Equation-of-State Measurements

Principal Investigator: A. E. Lazicki

Co-investigators: D. Swift, F. Coppari, R. London, D. Erskine, D. E. Fratanduono, P. M. Celliers, J. H. Eggert, G. W. Collins, H. Whitley, J. Castor, and J. Nilsen

This campaign was designed to test a conically convergent platform for measuring the Hugoniot EOS of arbitrary materials, including high-Z materials, at much higher pressures than can be achieved using a standard planar drive. This platform is intended to collect data in the >100-Mbar pressure regime, where currently very little data exist for any material, for the purpose of constraining EOS models.

To achieve the desired pressure amplification, this campaign experimented with convergent shock waves launched into a cone inset within a halfraum (Fig. 148.99). For appropriate cone angles, nonlinear reflections of the shock wave result in the formation of a Mach stem: a planar high-pressure shock that propagates along the axis of the halfraum. This concept has previously been demonstrated on high-explosives platforms[34] and proposed for a laser drive[35] but never previously tested.

Experimental geometry — Framing camera (1.47 ns, 2.07 ns, 2.27 ns, 2.47 ns) — Streak camera (1.5 ns, 2.5 ns, Time)

U2145JR

Figure 148.98
Experimental configuration and raw radiographs from a streak camera and framing camera for shot 79708.

One advantage of this geometry over a spherically convergent geometry is that since the Mach reflection is planar, it can be launched into a planar target package to make a traditional transit-time impedance-matching measurement using a velocimetry diagnostic.

One half-day of OMEGA shots was used to test three different cone angles using the VISAR and SOP diagnostics to register shock breakout times and profiles from the free surface of a CH (rexolite polystyrene) cone. Results indicate the formation of a Mach stem at pressures exceeding 200 Mbar. The data will be used to develop an EOS measurement on OMEGA in FY17, with extension to more-extreme conditions using NIF as well.
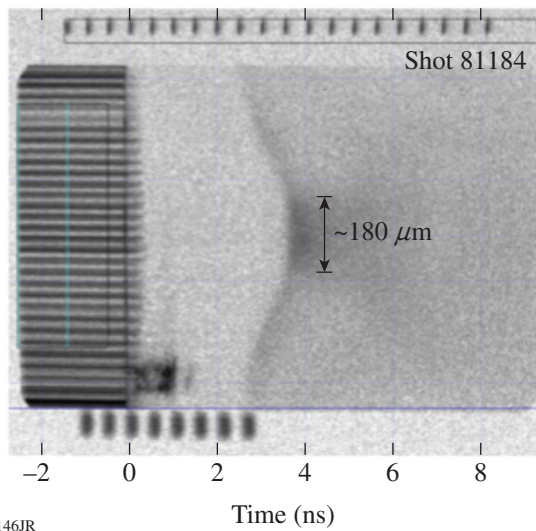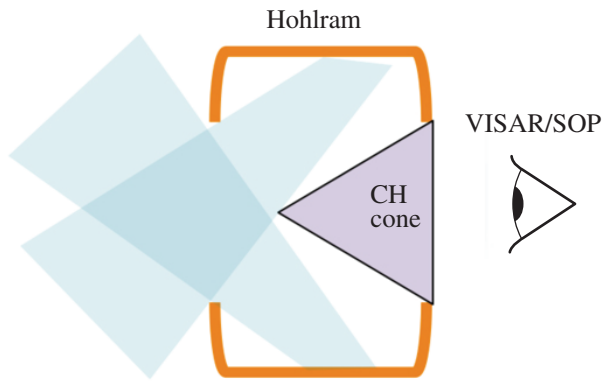
Figure 148.99
Experimental configuration and raw VISAR data showing the breakout time from a CH cone.

Ramp Equation-of-State Measurements on Gas-Encapsulated Samples
Principal Investigator: R. F. Smith
Co-investigator: D. E. Fratanduono

The goal of this campaign was to test a new target design in which the sample is encapsulated in a gaseous environment of nitrogen or argon. The target was designed to determine if the velocity at a diamond/gas interface was different from the velocity off a diamond/vacuum free surface.

The target was oriented along the H7–H14 axis (Fig. 148.100). Six OMEGA beams, incident 23° off axis with a 3.8-ns ramp laser pulse shape, were combined to generate an ~7-ns overall ramp compression drive in a diamond sample. Peak sample pressures of 800 GPa were generated. The ABSO (VISAR) diagnostic simultaneously measured the diamond/gas interface velocity and the diamond/MgO interface velocity. Using the diamond/MgO interface velocity, the known diamond thickness and the previously measured EOS of diamond, one can infer the diamond free-surface velocity. Discrepancies between the diamond/gas and calculated diamond free-surface velocities provide an indication as to the effect of gas encapsulation. During the half-day of shots, the gas pressure was varied to obtain a range of data to establish operating boundaries for future experiments with different sample materials.

Optical Blanking Test for Gas-Encapsulated Equation-of-State Measurements
Principal Investigator: D. E. Fratanduono
Co-investigator: R. Smith

Following up on the Gas-Encapsulation Ramp Campaign, this campaign continues to explore a new target design in which the sample is encapsulated in a gaseous environment. The target was designed to determine if a diamond/gas interface velocity differs from the velocity of a diamond/vacuum free surface. The new gas-fill capability on OMEGA EP was employed.

Eight experiments were performed to examine if a low-density gas would blank (become opaque to the VISAR probe beam) when ramp compressed using the UV lasers on OMEGA EP. Neon, xenon, argon, and nitrogen were examined at 1.0 atm and 1.5 atm. No issues were observed with neon, argon, and nitrogen. Blanking was observed in the xenon data. These data will be useful for designing future NIF experiments with encapsulated samples.
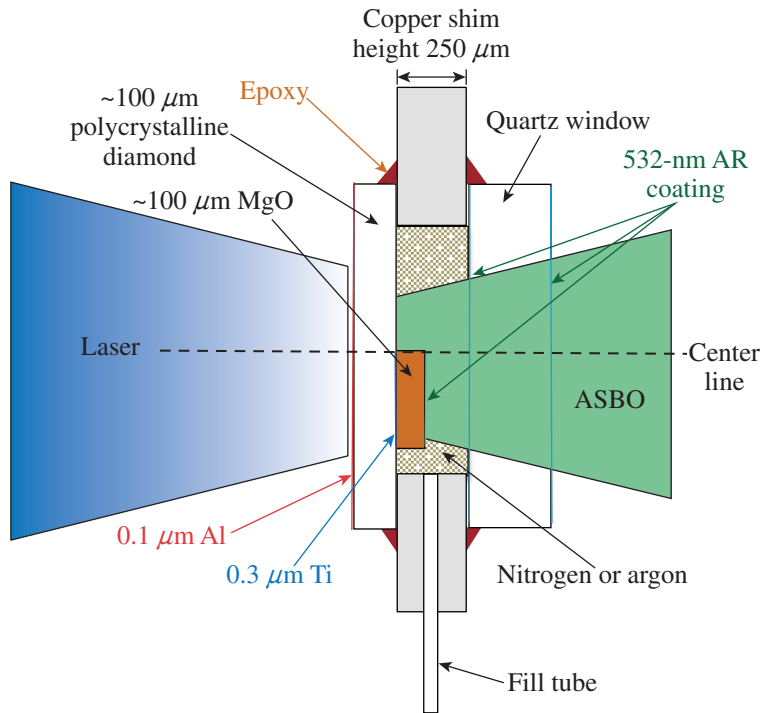
Figure 148.100
Target design for RampReverb-16B.
AR: antireflective.

U2147JR

Development of a Platform for Equation-of-State Measurements Using Flyer-Plate Impact

Principal Investigator: F. Coppari
Co-investigators: R. London, P. M. Celliers, M. Millot, D. E. Fratanduono, A. Lazicki, and J. H. Eggert

The goal of this campaign is to develop a platform to accelerate diamond flyer plates to hypervelocity for EOS measurements. The conceptual design was to ramp compress a diamond plate on the end of a halfraum, using x-ray ablation to accelerate the diamond into vacuum. After propagating a known distance, the diamond flyer impacts a transparent diamond window. By measuring the diamond flyer-plate velocity prior to impact, together with the resulting shock velocity in the diamond witness, the principal Hugoniot of diamond can be determined *absolutely* (e.g., without requiring a known pressure reference), making it possible to develop diamond as a high-pressure EOS standard.

These FY16 shots pioneered the indirect-drive approach, which greatly improved planarity and resulted in more-homogeneous, smooth flyer acceleration compared to direct-drive flyer experiments in FY15. The maximum pressure achievable on OMEGA remains, however, below the onset of diamond reflectivity, so instead quartz was used as a window and reference. Issues with the diamond flyer breaking up before impact, because of spalling, arise when attempting to reach higher

pressure. This currently prevents us from obtaining high-quality VISAR data (and high-precision EOS measurements) from a full-density diamond flyer. But since the technique appears promising, future campaigns will explore different flyer materials that could also become useful absolute EOS standards (i.e., Mo and Cu).

Backlighter Development for Extended X-Ray Absorption Fine Structure Measurements

Principal Investigator: F. Coppari
Co-investigators: Y. Ping, J. R. Rygg, and J. H. Eggert

EXAFS measurements require a bright, smooth broadband x-ray source for absorption spectroscopy near x-ray edges of the sample material. The x-ray radiation emitted by a capsule implosion meets these requirements and is currently used in laser-based EXAFS experiments. This x-ray emission decays rapidly, however, at higher photon energies, making it very challenging to measure EXAFS above 10 keV. To extend the x-ray energy range of laser-based EXAFS measurements, this campaign explored the possibility of using bremsstrahlung sources from foil backlighters driven at relatively high intensity. The specific goal of this campaign was to determine the optimum material and laser power configuration for this technique on OMEGA. Both Mo and Ag foils were tested, with laser intensity varying from 8×10^{16} W/cm^2 to 3×10^{17} W/cm^2. The source spectrum and size were measured for each shot.

The Ag foil driven with full intensity and tight laser focus is in fact somewhat brighter than the capsule backlighter above 10 keV (see Fig. 148.101). The bremsstrahlung backlighter's simplicity and potential for further improvement make this approach a valuable alternate x-ray source for high-energy EXAFS measurements.
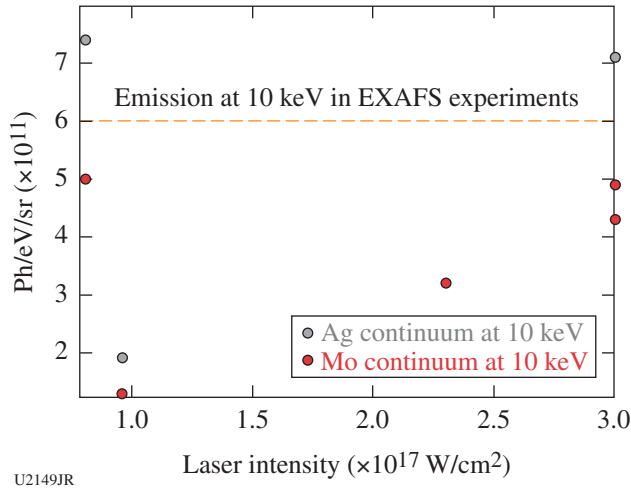

Figure 148.101
Brightness of Ag and Mo foils at 10 keV as a function of laser intensity. The dashed line represents the brightness of the capsule backlighter at 10 keV, currently used as an x-ray source for EXAFS measurements on OMEGA

Hugoniot Equation of State of Low-Density Porous Graphite

Principal Investigator: A. E. Lazicki
Co-investigators: F. Coppari, R. London, D. Swift, M. Millot, D. E. Fratanduono, H. Whitley, J. Castor, and J. Nilsen

This campaign was designed to probe a preheated Hugoniot EOS, using pore collapse of a porous material to generate preheating. The pressure and density of shocked states were determined by impedance matching with a quartz standard. As shown in Fig. 148.102, the samples were driven using the gas-filled hohlraum indirect-drive platform, and the VISAR and SOP diagnostics measured shock transit times in samples of porous graphite. Shock steadiness during transit through the graphite samples (which are opaque to the VISAR) was determined from a quartz witness sample placed next to the porous graphite, from which a continuous record of the shock speed was simultaneously recorded. High-quality data were collected for 12 shots during two half-days in FY16; detailed analysis is underway.
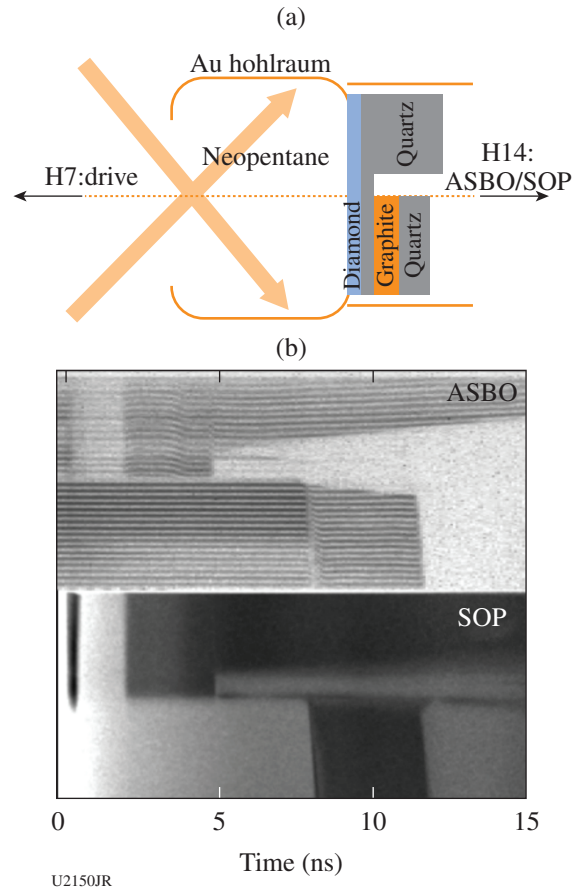

Figure 148.102
Experimental configuration and raw graphite EOS data for shot 80846.

3. Hydrodynamics

Mix-Width Measurements of Rayleigh–Taylor Bubbles in Opaque Foams

Principal Investigator: C. M. Huntington

The OMEGA Foam Bubbles Campaign addresses challenges in deeply nonlinear, multimode hydrodynamic-instability measurements. The interface between two materials of different densities may be susceptible to either Richtmyer–Meshkov (RM) or Rayleigh–Taylor (RT) instabilities if it is shocked or accelerated, respectively. These instabilities in turn drive mixing, where perturbations on the interface determine how the low- and high-density materials interpenetrate. This campaign aims to measure the extent of the interpenetration ("mix width") in cases where the perturbation is complex and the materials mix on small scales. This is achieved by carefully manipulating the properties of the materials in the system. Particular emphasis is placed on the densities, which set the

instability growth rates, and on the x-ray opacity characteristics, which determine the contrast in the x-ray image used to diagnose the mix width.

A technique developed over many previous planar RT experiments uses a high-opacity material, often iodinated plastic, embedded in the plastic portion of the target that comprises the "high-density" part of the unstable interface. When driven by indirect drive from a halfraum, and then imaged with transmission x-ray radiography, the location of the high-opacity tracer material is clear and reveals the position of the high-density material in the system. This technique can obscure, however, the shape and extent of the low-density "bubbles" when the foam mixes with the doped plastic. In contrast to this, foam bubbles use an opaque *foam*, which when set next to the more-transparent plastic, highlights the extent of the *foam penetration into the plastic*. This system has identical hydrodynamic behavior as the traditional doped plastic/foam interface, but with inverse x-ray characteristics. The target for the Foam Bubbles Campaign includes both interfaces, ensuring that the entire system experiences the same acceleration. An example of the data collected is shown in Fig. 148.103. This image was generated using tilted, tapered, point-projection x-ray imaging and clearly shows the layers on each side of the split target. The extent of bubble penetration in an RT unstable system is a fundamental quantity, and this measurement will further our understanding of hydrodynamic systems, from ICF implosions to supernovae.

Development of a Radiography/VISAR Platform for Hydrodynamics Measurements

Principal Investigators: M. Rubery (AWE)
and D. Martinez (LLNL)
Co-investigators: G. Glendinning (LLNL); and S. McAlpin, J. Benstead, and W. Garbett (AWE)

Continuing prior work on detailed radiography of hydrodynamic systems, hohlraum-driven experiments were performed over a half-day in FY16 by an LLNL/AWE collaboration using the OMEGA Laser System. The objectives for this campaign were to investigate the evolution of a driven interface using point-projection x-ray radiography, qualify a new simultaneous radiography/VISAR configuration, and obtain drive characterization data using the Dante diagnostic (Fig. 148.104).

For the radiography measurements, a point-projection backlighter was generated through a 20-μm pinhole along the "cranked" TIM-6 axis and recorded with a single-strip gated
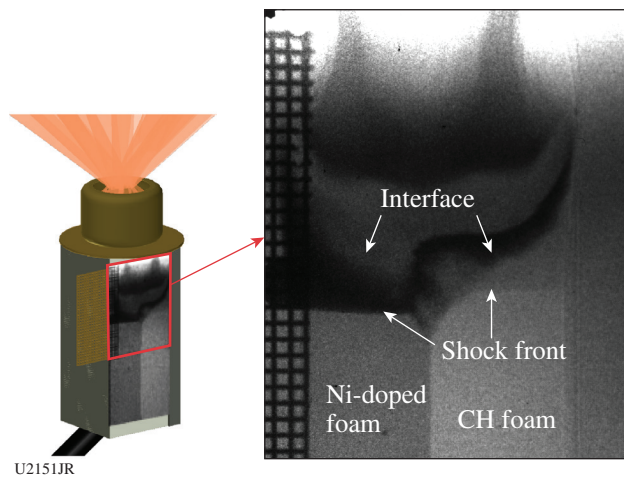

Figure 148.103

The indirectly driven target is shown, with an example of the data collected. The shock appears as a flat line across the foams, with the mixing evident at the foam/plastic interface downstream of the shock.
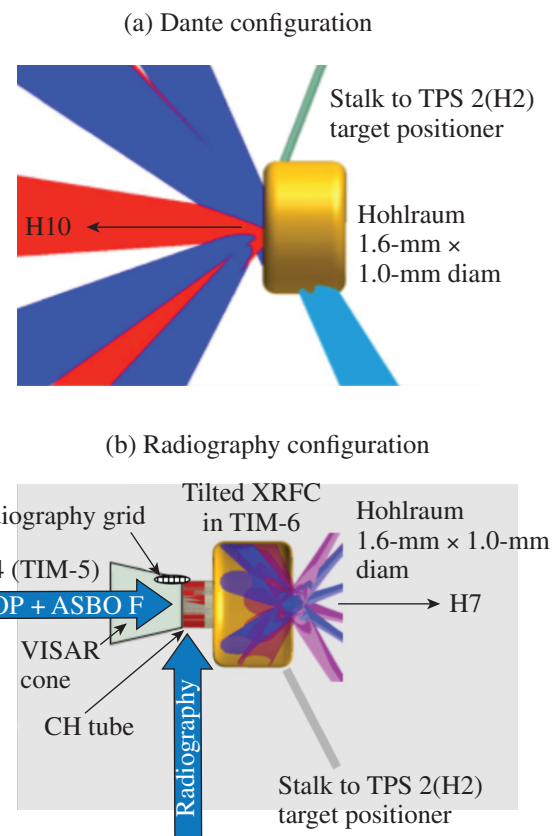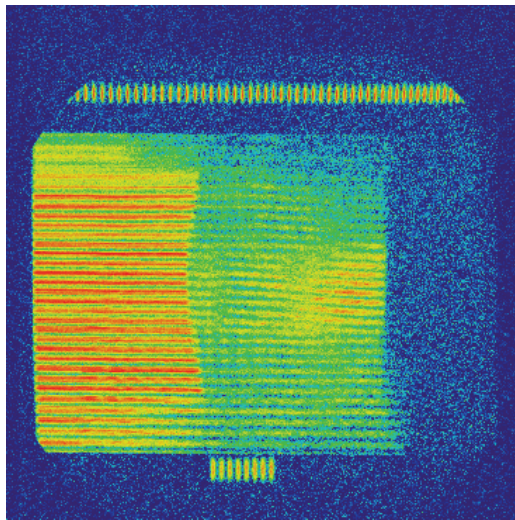

Figure 148.104

(a) Dante-optimized and (b) radiography/VISAR target configurations. TPS: Target Positioning System; XRFC: x-ray framing camera; SOP: streaked optical pyrometer; ASBO: active shock breakout; TIM: ten-inch manipulator.

imager. A quartz window with aluminum flash coating and a light shield cone were applied to the rear of one radiography target, allowing us to make a VISAR measurement along the TIM-5 (port H14) axis. Separate hohlraum drive measurements were performed with hohlraums oriented toward Dante along the H10 axis, using a simplified target with the physics package removed. A 75-J timing laser was incorporated into the Dante configuration to improve cross-timing of each Dante channel.

This half-day of experiments was successful, firing two radiography shots, four Dante shots, and one combined radiography/VISAR shot. Figure 148.105 shows the VISAR data from the combined radiography/VISAR design. Excellent data were recorded on all diagnostics and the experiments met the goals of the HED Program.


U2153JR

Figure 148.105
VISAR data confirming the success of the new dual radiography/VISAR target configuration.

Proton Heating of Copper Foam on OMEGA EP
Principal Investigator: J. Benstead (AWE)
Co-investigators: E. Gumbrell, P. Allan, S. McAlpin, M. Crook-Rubery, L. Hobbs, and W. Garbett (AWE)

This LLNL–AWE collaborative campaign studied the heating of a cylindrical puck of copper foam irradiated by a short-pulse–generated proton beam. The two major goals of the experiment were to measure the temperature distribution through the target and to quantify the extent of expansion of the rear surface.

The experimental setup is depicted in Fig. 148.106. A gold foil was irradiated with the OMEGA EP sidelighter (SL) short-pulse beam delivering 300 J over 0.7 ps. The SL produced a beam of protons and ions that were used to heat a copper foam puck positioned ~1.8 mm away. An aluminum foil was placed between the gold foil and the copper puck to improve heating by filtering out heavier ions and low-energy protons that would nonuniformly heat the target.
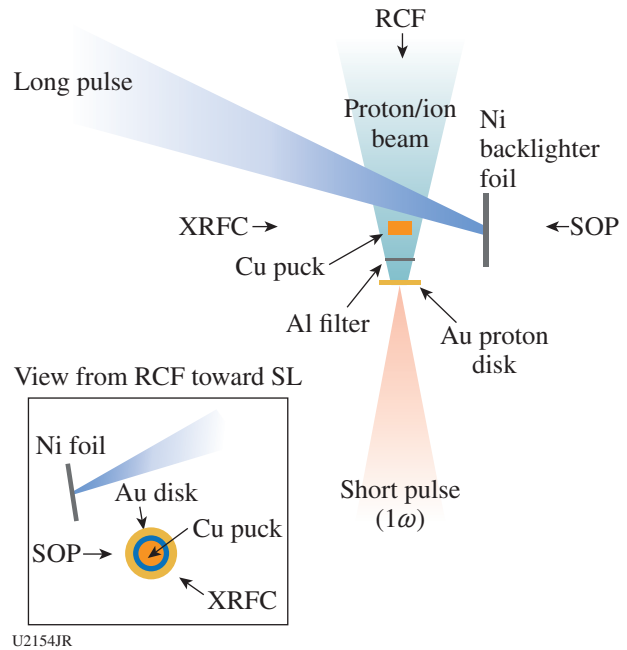
Figure 148.106
Experimental layout for proton-heating shots with combined x-ray radiography, SOP, and radiochromic film (RCF). For simplicity, only one backlighter beam (of the three used) is shown. SL: sidelighter.

The subsequent sample expansion was imaged with an x-ray radiography system. This experimental platform used a nickel area backlighter, irradiated with three long-pulse beams, coupled to an x-ray framing camera (XRFC), which imaged the backlit target. The backlighter (BL) beams were delayed with respect to the SL beam in order to observe the heated and expanded target at different times (see Fig. 148.107).

The SOP diagnostic was fielded orthogonally to the heating axis, with its imaging slit oriented such that the temperature through the central section of the disk could be measured front to rear over the first 5 ns of heating (see Fig. 148.108). In addition, an RCF stack measured the proton/ion beam spectrum on the shot.

In total, six shots were fired, with data acquired on the XRFC, RCF, and SOP diagnostics. The SOP indicated the front surface was significantly hotter, and expanding faster, than the

U2155JR

Figure 148.107
Gated x-ray imaging data from (a) an unheated and (b) a heated copper foam puck. For the heated shot, the backlighter was delayed by 20 ns. From this perspective, the protons propagate from left to right through the target. There is clear expansion of the front surface in (b).

U2156JR

Figure 148.108
SOP data from a proton-heating shot. The insert shows the position and orientation of the SOP slit relative to the target. There is a clear difference between the expansion of the front (proton-facing) and rear surfaces.

rear surface over the first 5 ns. This agreed well with the XRFC data, which showed that the front surface had expanded while there was minimal rear-surface expansion on most shots.

4. Plasma Properties

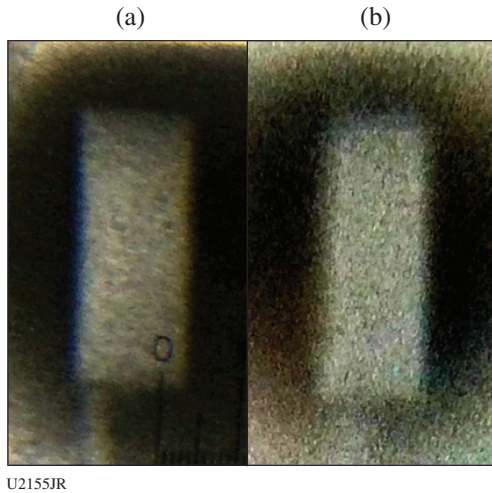#### Shock-Front Structure in Multispecies Plasmas
Principal Investigator: H. G. Rinderknecht
Co-investigators: H.-S. Park, S. Ross, S. Wilks, P. Amendt, and B. Remington (LLNL)

Two OMEGA shot days were dedicated to developing a new experimental platform for the study of shock-front structure in low-density plasmas composed of single- and multiple-ion species. In these experiments, 10 or 12 beams deliver 2.1 to 2.7 kJ in 0.6 ns to a thin ablator (2 μm SiO_2 or 5 μm CH) mounted to one end of a CH tube, launching a strong shock into a low-density gas (1 atm) contained within. After thin windows on two sides of the tube are destroyed by ~150 J of laser light, OMEGA's 4ω beam probes the shocked plasma and scatters light that is detected by the Thomson-scattering (TS) diagnostic. Figure 148.109(a) shows the experimental design used on the first day.

High-quality Thomson-scattering data were achieved on several shots, after tuning the destroyer-beam energy and the delay between the destroyer and probe beams. Figure 148.109(b) shows IAW features from a shocked plasma composed of H + 2%Ne, which shows the shock beginning to pass through the TS volume as blue-shifting of the scattered light. Lineouts shown in Fig. 148.109(c) uniquely demonstrate the evolution of a multispecies shock-front structure: the scattered-light feature associated with the hydrogen is blue-shifted (beginning to "shock up") while the peaked neon feature remains static. Analysis of these features shows the hydrogen is heated ($T \sim 0.8$ keV) and flowing ($V \sim 250$ μm/ns), while the Ne is cold ($T \sim 0.1$ keV) and still ($V \sim 0$)—a multifluid or kinetic phenomenon that cannot be captured in standard single-fluid models.
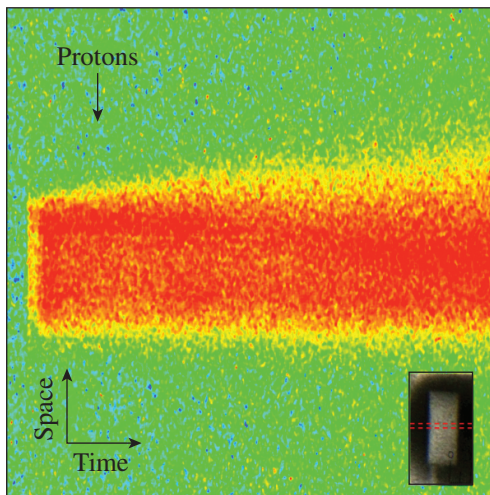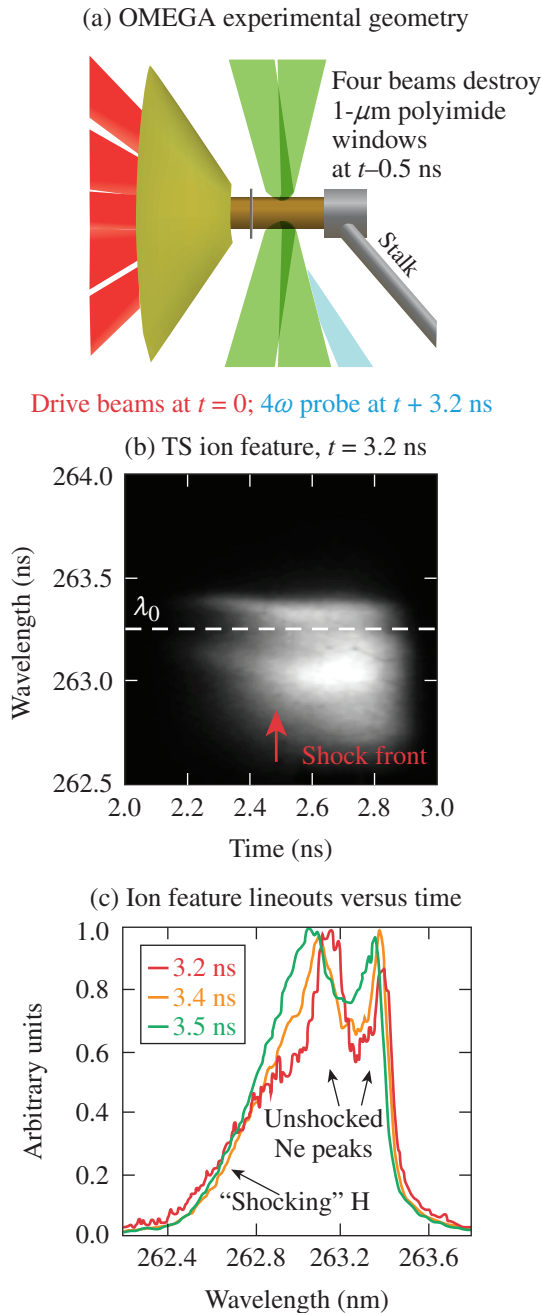
On the second shot day, single-species (H) and multispecies shocks (H + 2%C) were compared, using predominantly CH ablators. The CH ablators launched weaker shocks than the SiO_2. Further analysis of the TS data is in progress. These results will be used to constrain models of shock-front formation, which are sensitive to kinetic physics and relevant to the shock phase of capsule implosions. The shock-tube TS platform also makes more-detailed shock physics studies possible for laboratory astrophysics.

(a) OMEGA experimental geometry

Four beams destroy
1-μm polyimide
windows
at t–0.5 ns

Stalk

Drive beams at $t = 0$; 4ω probe at $t + 3.2$ ns

(b) TS ion feature, $t = 3.2$ ns

λ_0

Shock front

Wavelength (ns)

Time (ns)

(c) Ion feature lineouts versus time

— 3.2 ns
— 3.4 ns
— 3.5 ns

Arbitrary units

Unshocked
Ne peaks

"Shocking" H

Wavelength (nm)

U2157JR

Figure 148.109
Experimental design and results for Thomson scattering (TS) in a shock tube on OMEGA. (a) A 2.1-mm-diam CH tube filled with 1 atm of H(0.98) + Ne(0.02) was shocked by 12 OMEGA beams driving an SiO_2 ablator. The 1-μm-thick CH windows were destroyed using 75 J each in 0.6 ns, allowing a 4ω probe beam and scattered light to pass. (b) Thomson-scattering ion feature recorded on this experiment, showing the evolution of the shock front. (c) Lineouts of the TS ion feature showing kinetic features in the shock evolution: differential velocity and temperature between the H and Ne ion species are observed.

Magnetized Collisionless Shocks for Weapons Effects
Principal Investigator: B. B. Pollock
Co-investigators: H.-S. Park, J. S. Ross, C. Huntington, and G. Swadling

In FY16 the MCLSWEffect Campaign on OMEGA continued an investigation of interpenetrating plasma flows in the presence of background magnetic fields. This campaign employed the MIFEDS pulsed-power magnetic-field system to provide a background field. As illustrated in Fig. 148.110, the field was directed along the direction of a low-density plasma plume that was produced inside the MIFEDS structure, into which a high-density plume was then expanded after a variable delay. The interaction region was probed with Thomson scattering and proton deflectometry to measure the plasma density, temperature, flow velocity, and field structure. This campaign increased the field of view for the proton diagnostic roughly threefold by inserting the proton detector much closer to the interaction than in previous experiments. The analysis of this recent experiment is ongoing and will inform the FY17 continuation of this effort.
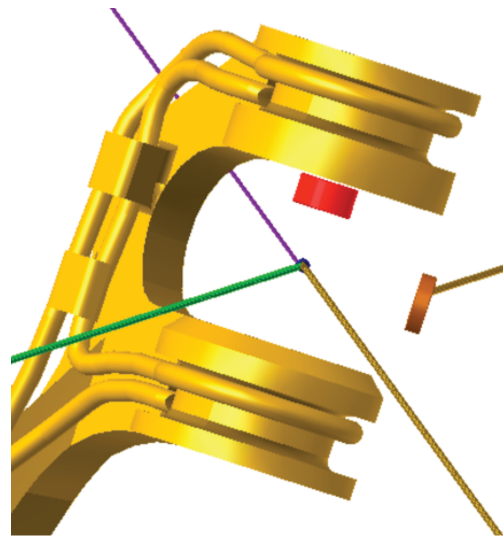
U2158JR

Figure 148.110
The magneto-inertial fusion electrical discharge system (MIFEDS) used in this campaign. The red disk on the upper surface is illuminated by four beams, producing a low-density plasma along the MIFEDS magnetic-field axis. The gold-colored disk on the right then provides the orthogonal plasma plume that interacts with the low-density plasma. The Thomson-scattering volume is at the intersection of the surface normal for these disks, while the proton radiography field of view slightly overfills the MIFEDS interior region.

X-Ray Spectroscopy of Fully Characterized Non-LTE Gold Plasmas

Principal Investigator: R. F. Heeter

Co-investigators: J. A. Emig, M. E. Foord, L. C. Jarrott, D. Liedahl, E. Marley, C. A. Mauche, M. B. Schneider, and K. Widmann

In pursuit of a more-precise understanding of the radiative properties of non-LTE gold, to improve the fidelity of hohlraum x-ray drive simulations for NIF experiments, the AuNLTE-16A Campaign continued a study of laser-heated beryllium-tamped gold/iron/vanadium foils. Prior measurements in FY13–FY15 suggest a need for refinements to an earlier benchmark,[36] involving a higher gold ionization versus temperature, but the plasma conditions and uniformity must be more fully understood. The FY16 campaign acquired both hydrodynamic expansion imaging data and detailed x-ray spectra for various laser-drive arrangements. Data obtained on 11 shots included simultaneous measurements of (1) time-resolved gold M-band spectra from 2 to 5.5 keV, (2) the plasma electron temperature via K-shell emission from helium-like and hydrogenic V and Fe ions, and (3) the plasma density from time-resolved face-on and edge-on imaging of the sample's expansion from its initial size. Preliminary analysis indicates electron temperatures at or above 1.5 keV were obtained, based on the presence of the

Ly_α lines for V and Fe. Figure 148.111 provides a sample of the imaging data, which shows highly uniform M-band emission at 1.6 ns into the 3.2-ns laser drive, followed over the next 1 ns by an evolving bright spot suggestive of a radial compression-rarefaction wave. The radial feature is undergoing further investigation. Detailed analysis is expected to deliver improved M-band benchmark spectra for non-LTE models.

5. Material Dynamics and Strength

Copper Rayleigh–Taylor (CuRT) Growth Measurements

Principal Investigator: J. M. McNaney

Co-investigators: S. Prisbrey, H.-S. Park, C. M. Huntington, and C. E. Wehrenberg

The CuRT Campaign is part of the material strength effort, which is aimed at assessing the strength of various metals at high pressure and high strain rate. The goal of the CuRT platform is to measure RT growth of samples that behave "classically," meaning they can be fully modeled using a fluid description. In this series of experiments the intent is to measure RT growth in liquid copper at high pressure, with a second goal of demonstrating the dynamic range of the technique by measuring RT growth in solid copper. The FY16 shots made significant progress toward these goals.
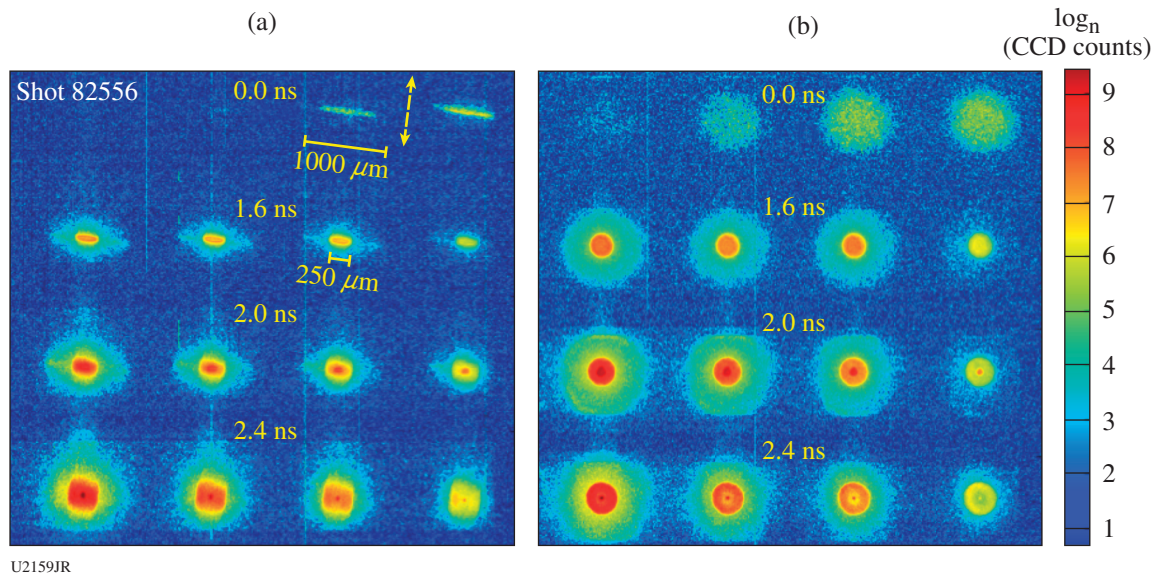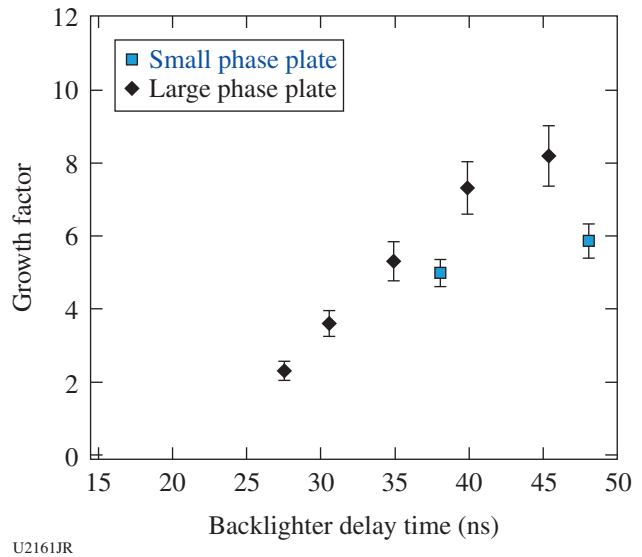

Figure 148.111

Log-scale rendering of gated x-ray images of the circular AuNLTE target. Images were obtained by viewing the target (a) edge-on and (b) face-on. The cameras were synchronized by observing laser turn-on (first row of images). Timing for each strip is labeled in the center, with the gate pulse propagating from left to right along each strip. Target dimensions are provided for the images in (a). The x-ray emission from the 250-μm-diam high-Z sample (orange–red) is visible inside the relatively weak signal from the 1000-μm-diam beryllium tamper (cyan halo). CCD: charge-coupled device.

Without the stabilization of strength, classical RT growth is characterized by a growth rate $\gamma = \sqrt{kg\mathrm{A}_n}$, where k is the wavelength of the unstable mode, g is the acceleration, and the Atwood number A_n quantifies the magnitude of the density jump at the interface. Acceleration of the sample in this OMEGA EP experiment is provided by the stagnation of a releasing shocked plastic "reservoir," which is directly driven by ~1 to 2 kJ of laser energy, depending on the desired material condition. The growth of preimposed ripples is recorded using transmission x-ray radiography from a copper He$_\alpha$ slit back-lighter source, where the opacity of the sample is calibrated to the ripple amplitude. The pre-shot metrology and measured ρr of the driven sample together yield the growth factor, which is compared to models of RT growth. A gold knife edge on the sample provides a measure of the modulation transfer function, and a step wedge creates an opacity look-up table on each shot, resulting in error bars of approximately ±10%.

In December 2015 a new set of large-spot phase plates was commissioned, and the drive was recalibrated to produce pressure conditions similar to those present during the shots earlier in 2015 with smaller laser spots. Excellent planarity was achieved (Fig. 148.112), and it was established that the laser energy was sufficient to reach the highest pressure condition necessary for the campaign.

Later in FY16, because of a target build that was out of specification, measurements of liquid phase RT growth were delayed, but the targets as built were sufficient to investigate solid-state copper behavior. RT growth data (Fig. 148.113) collected under very similar peak pressures in solid-state copper indicate that data collected using the smaller phase plate diverge from the large-phase-plate data at late times, likely caused by the loss of planarity and more-rapid drop off in ripple driving force. The analysis of this data is ongoing and modeling of the ripple growth is underway. Additional experiments are planned for FY17.

U2161JR

Figure 148.113
Growth factor data for solid copper using small and large phase plates.
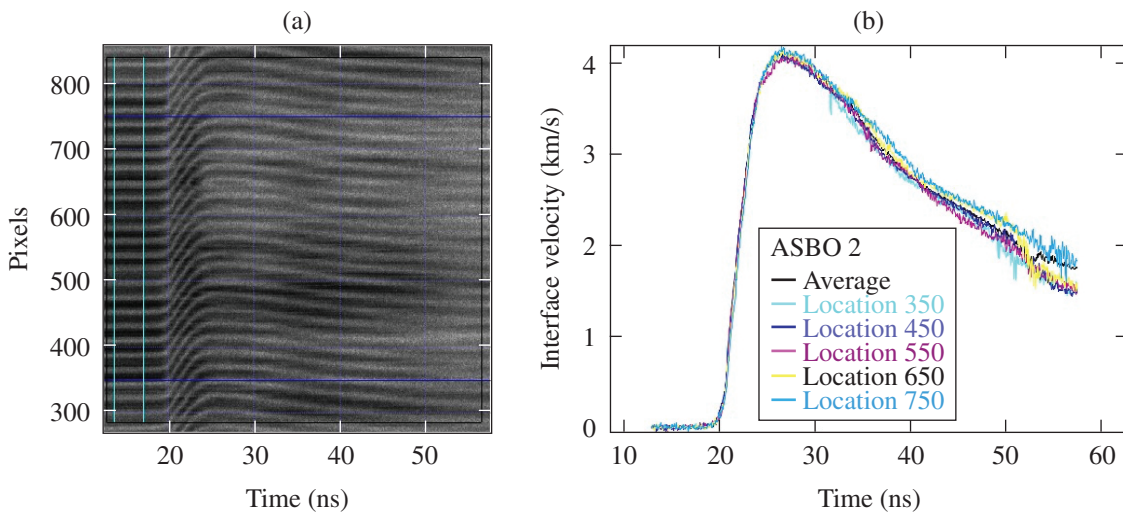
U2160JR

Figure 148.112
(a) The ASBO (VISAR) data from shot 24063 and (b) a series of lineouts taken across the image showing excellent planarity.

Evaluation of Additive-Manufactured Foams for Ramp-Compression Experiments
Principal Investigator: R. Smith

The four half-day AMFoam Campaigns evaluated the use of 3-D–printed or additive-manufactured foams as surrogates to carbonized resorcinol foams (CRF) in ramp-compression target designs, in support of ongoing material strength experiments on the NIF. The 3-D–printed foams were structured as follows: Individually printed lines were grouped into $100 \times 100 \times 16$-μm^3 "log pile" blocks, which in turn were stitched together to form 16-μm-thick, 1.7-mm-diam layers. Seven of the 16-μm layers were then stacked to arrive at cylindrical "AM foams" that were 1.7 mm in diameter and 112 μm tall. These foams were then glued onto a 25-μm Be + 180-μm 12% Br-doped CH ablator assembly. Following the ramp-compression platform described in Ref. 37, 15 beams of the OMEGA laser with 300 J in 2 ns drive through the ablator and launch the foam across a gap to send a ramp-compression wave into an Al/LiF sample (see Fig. 148.114, lower left), which is diagnosed using 1-D line VISAR viewing the sample off a semireflective mirror. In addition, at a controlled time after this compression begins, the OHRV (2-D VISAR probe) takes a 2-D snapshot of the reflectivity and velocity field with a spatial resolution of ~3 μm (Ref. 38). An example of the intensity field recorded on the 2-D VISAR is shown in Fig. 148.114, lower right. Over the course of the four campaigns the structure of the 3-D–printed foam was varied, with the goal of optimizing the temporal ramp profile.

Development of an Experimental Platform for Reflection Diffraction Measurements During Shock or Ramp Compression
Principal Investigator: C. E. Wehrenberg

This campaign seeks to develop a platform for x-ray diffraction *in situ* during shock or ramp compression in a reflection geometry. To measure the strain state of a material in detail, it is necessary to probe the strain in several directions, yet diffraction experiments to date on OMEGA and the NIF have been limited to transmission diffraction in a narrow range of angles of incidence. The ability to measure diffraction in reflection geometry would greatly increase a diffraction experiment's sensitivity to shear strain.

In this campaign, one or two UV beams drove an Fe backlighter, while one or two UV beams drove a shock into an ablator and a sample (Ta or Fe). A 3-D–printed mount
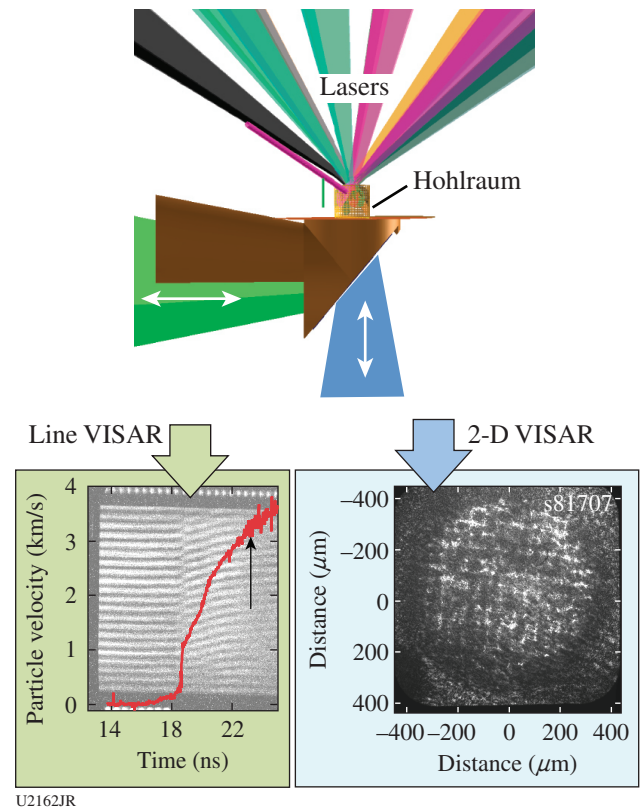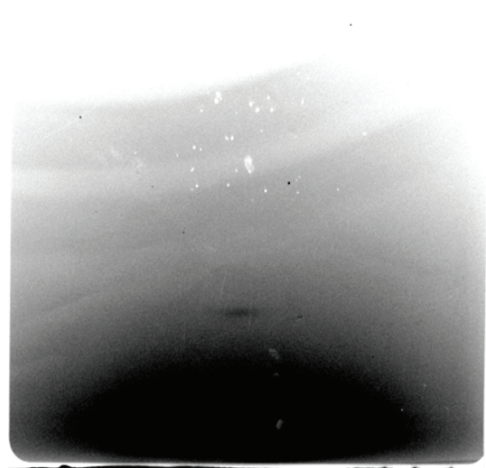

Figure 148.114
Schematic diagram describing the experimental setup for the AMFoam-17C/D campaigns, which combine the OMEGA high-resolution velocimeter (OHRV) and ASBO diagnostics on a single shot. The goal of these shots was to characterize the temporal and spatial drive associated with additive manufactured (3-D–printed) foam targets. The OHRV provided 2-D velocity measurement of the 3-D–printed foams at a snapshot in time. For the AMFoam-17A/B campaigns, only the ASBO (VISAR) diagnostic was used. The preliminary OHRV image (bottom right) shows a grid pattern consistent with the 3-D–printed foams' tiled pattern.

held both the sample and a pinhole to collimate the incoming x rays. A separate positioner held an image plate detector, and a shield attached to the backlighter prevented x rays from going straight through to the detector. The campaign tested several configurations for the backlighter shielding, pinhole, and detector filtering and also measured the background created by the sample drive. The campaign was successful in recording the first reflection diffraction signal, albeit a weak signal (as shown in Fig. 148.115). In future work shielding and collimation must be improved to in turn improve the diffraction resolution and signal-to-noise ratio.

Figure 148.115

Diffraction pattern from a Ta sample in reflection geometry. The two "Saturn ring" broad diffraction lines near the top are an indication that improvements in the x-ray collimation are needed.
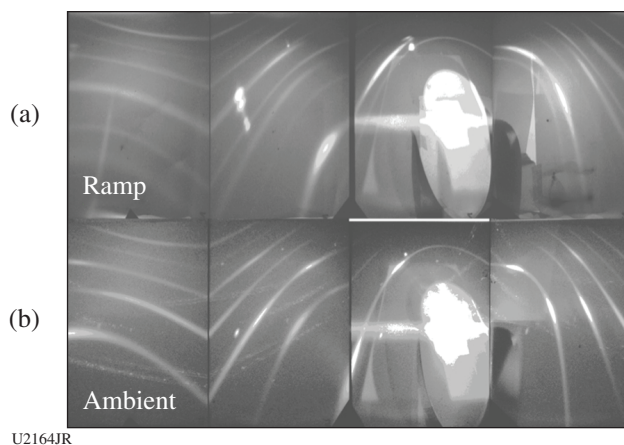

Figure 148.116

(a) Diffraction from (011) fiber-textured, ramp-compressed to 1.6 Mbar. (b) Diffraction from the same (011) fiber-textured sample under ambient conditions.

Understanding Plasticity Mechanisms in Ramp-Compressed Tantalum (OMEGA EP)

Principal Investigator: C. E. Wehrenberg

This campaign seeks to understand the mechanism for plasticity in ramp-compressed Ta, using x-ray diffraction (XRD) to track the texture change. The Ta samples initially had a sharp (011) fiber texture, which allowed one to easily detect subsequent texture changes that develop during compression. Since previous XRD campaigns studying Ta have encountered issues with the diffraction signal from the diamond pusher overlapping the expected Ta signal, this campaign developed a ramp drive using a Kapton ablator/pusher. This OMEGA EP campaign used two UV beams to drive a zinc backlighter and two more UV beams to drive a ramp wave through the Kapton ablator and into the Ta sample. Eight shots were performed, with the first four shots successfully demonstrating a ramp drive to 1.6 Mbar. Figure 148.116 compares the data from an ambient (static, undriven) sample and data from a 1.6-Mbar shot. The change in position of the azimuthal texture spots in the ramp-compressed pattern, when compared to the ambient one, will be used to determine the operative deformation mechanisms.

Understanding Plasticity Mechanisms in Shock-Compressed Tantalum (OMEGA)

Principal Investigator: C. E. Wehrenberg

This campaign seeks to understand the mechanism for plasticity in shock-compressed Ta, using XRD to track the texture change. Similar to the TaStrDiff-16A campaign on OMEGA EP,

which used ramp compression, in this campaign on OMEGA the Ta samples initially had a sharp (011) fiber texture, which allowed one to easily detect subsequent texture changes that develop during compression. This campaign used 16 beams to drive a zinc backlighter, and two beams to drive a steady shock through the Kapton ablator and into the Ta sample. A total of 13 shots were performed, scanning a pressure range from 30 to 160 GPa. Figure 148.117 shows example data for an
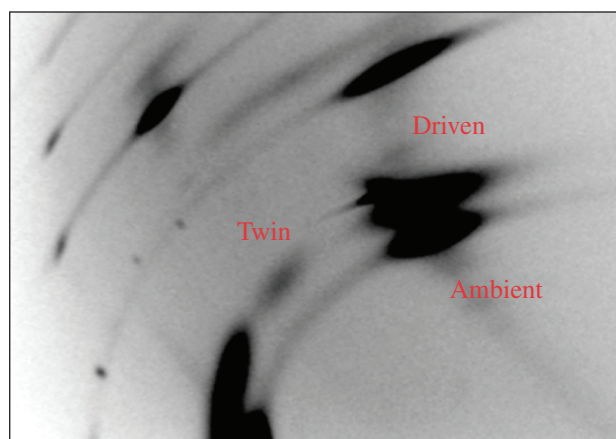

Figure 148.117

Diffraction data for (011) fiber-texture Ta, which has been shock compressed to ~80 GPa. The data were taken as the shock was in transit through the sample, so diffraction patterns from both ambient and compressed (driven) material are observed. A new texture component can be seen in the data from the compressed material, which corresponds to the twinning across the (112) plane.

~80-GPa shock. A new texture component is observed in the data that corresponds to twinning across the (112) plane, which produces a reorientation of the atomic lattice and therefore a change in the diffraction pattern. This type of driven data can now be used to determine the mechanism for plasticity during shock compression.

ACKNOWLEDGMENT

FY16 LANL Experimental Campaigns at the Omega Laser Facility

In FY16, Los Alamos National Laboratory (LANL) scientists carried out 22 shot days on the OMEGA and OMEGA EP Laser Systems in the areas of HED science and ICF. In HED we focused on the areas of radiation flow, hydrodynamic turbulent mix and burn, the equations of state of warm dense matter, and coupled Kelvin–Helmholtz (KH)/Richtmyer–Meshkov (RM) instability growth. Our ICF campaigns focused on the priority research directions (PRD's) of implosion phase mix and stagnation and burn, specifically as they pertain to laser direct drive (LDD). Several of our shot days also focused on transport properties in the kinetic regime. We continue to develop advanced diagnostics such as neutron imaging, gamma reaction history, and gas Cherenkov detectors. The following reports summarize our campaigns, their motivation, and the main results from this year.

Shear

The LANL Shear Campaign is examining instability growth and its transition to turbulence relevant to mix in ICF capsules using an experimental platform with counter-propagating flows about a shear interface to examine KH instability growth. The platform consists of a directly driven shock-tube target with an internal physics package. The physics package consists of two hemi-cylindrical foams separated by a layer of tracer material with gold plugs on opposing ends of the foams to limit shock propagation from the direct drive to only one end of the foam. This geometry collimates the shocks and sets a region of pressure-balanced shear flow at the center of the shock tube. Measurements of the tracer layer (shear interface) mixing dynamics are used to benchmark the LANL Besnard–Hazlow–Rauenzahn (BHR)[39] turbulence model. The mixing dynamics are characterized by measuring the mix width of the layer as well as examining multidimensional structure growth along the layer's surface.

The FY16 Shear Campaign continued an effort to examine instability and model initial condition parameter space by varying the characteristics of the target tracer layer. Both FY16 shot days were part of a three-shot-day study of instability mode growth caused by single-mode initial conditions, which employed sinusoidal tracer foils of various wavelengths as opposed to the previous flat and roughened foil campaigns. The sinusoids force instability growth by pre-seeding a coherent wavelength. In these experiments we observed (Fig. 148.118)
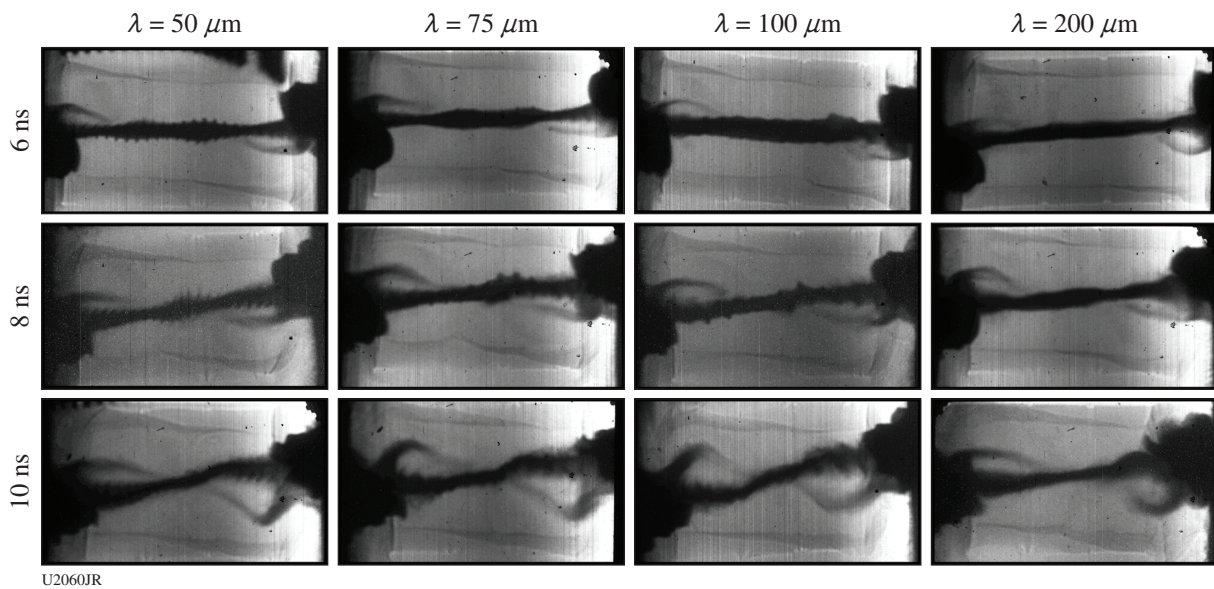

Figure 148.118
X-ray backlit images of a counter-flowing shear experiment showing the evolution of foil tracer layer at different perturbation wavelengths.

early-time (pre-shear) jets and "dust-up" structures, which are points of further study, as well as the persistence of the single-mode structures to late times in the experiment. The finished OMEGA mode growth study also confirms a most-unstable mode of $\lambda \approx 100$ to 150 μm, as predicted by observations of emergent rollers in our NIF experiment and a naïve application of the simple Rayleigh model.

Double-Shell Planar

The LANL Double-Shell Planar (DSPlanar) OMEGA Platform is part of the larger LANL Double-Shell Campaign. The DSPlanar experiments are intended to validate our ability to predict momentum transfer, hydrocoupling, and instability growth in a double-shell–relevant planar geometry. We choose to use a planar geometry since it is simpler to diagnose than full spherical implosions and can still give us an idea of how well the code simulates fundamental pieces of physics without the added complication of convergence. DSPlanar experiments serve a second purpose as a testing ground for the development of our target fabrication capability toward NIF double-shell capsules. DSPlanar target components will use similar materials as NIF double-shell targets but in a simpler-to-build geometry. We can use fabrication of these simpler parts as a first-pass test of our abilities and to identify where we require further R&D resources. The goals of this first DSPlanar shot day were to measure momentum transfer of an ablatively driven flyer into a mid-Z "inner shell" layer, as well as to test NIF-relevant ablator materials.

The DSPlanar target is an indirectly driven shock tube with a material stack approximating an unfolded double shell, with an ablator, a low-density foam cushion, an inner shell surrogate layer, and a final release foam. We varied on whether or not to include a tamper layer on the inner shell layer as part of our hydro-instability mitigation studies. The primary diagnostics

for the FY16 DSPlanar day were edge-on streaked and imaging radiography (Fig. 148.119). The streaked radiography was designed so that measurements of inner shell preheat expansion, ablator velocity pre-impact, and system velocity post-impact for momentum transfer studies could be obtained. On this shot day we identified modifications to the platform required for good streak data and good imaging data. We also obtained data that compared our standard sample Be ablator targets and AlBeMet (Al/Be alloy) targets required to inform FY17 decisions about our NIF platform.

Marble

In the Marble project, nuclear reactants of an ICF implosion are initially separated via a spherical low-density CD foam matrix infused with a T_2 gas fill. Through advanced target fabrication, voids can be selectively etched into the foam core to control the initial separation scale. These cores are encapsulated within a machined ablator and imploded in 60-beam direct-drive implosions with the key measurements being D–T and D–D yields. In the FY16 OMEGA experiments, targets were
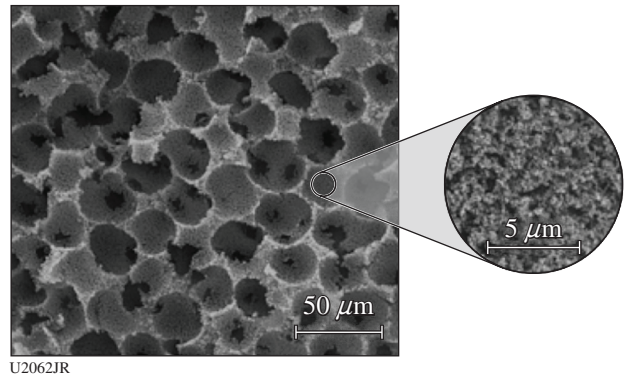

U2062JR

Figure 148.120
Marble CD foam with etched 30-μm voids.

AlBeMet ablator results

"Inner shell"

Ablator

0 to 4.5 ns

Al ablator synthetic image; no AlBeMet simulations for comparison

0 to 2 ns   Shot 81806

1.5 to 3.5 ns

Smaller preheat expansion than Be + Cu ablator
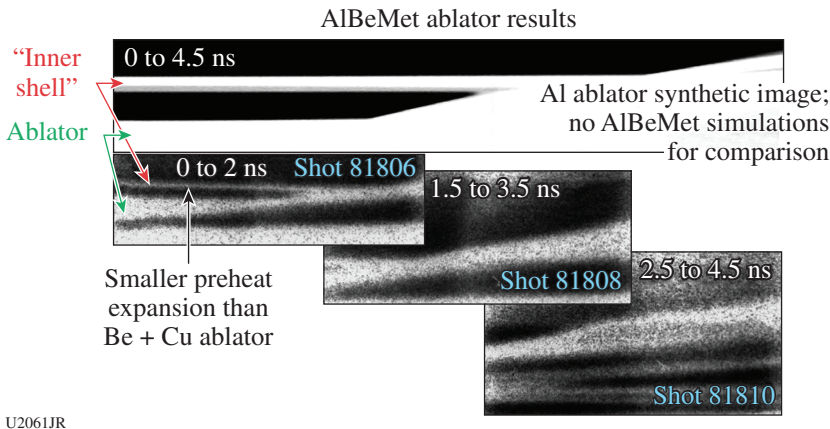
Shot 81808   2.5 to 4.5 ns

Shot 81810

U2061JR

Figure 148.119
Backlit streak data viewing edge-on of the planar double-shell experiment

imploded with an intrinsic foam structure as well as foam with engineered voids. Figure 148.120 shows an image of such engineered foam. Most recently, target improvements (full deuteration, advanced machining) resulted in an order-of-magnitude increase of D–T and D–D yields. We are currently awaiting an estimate of as-shot conditions, which we will then use to calculate a normalized ratio of the yield of the D–T reactions to D–D reactions—the key metric for comparison to theory.
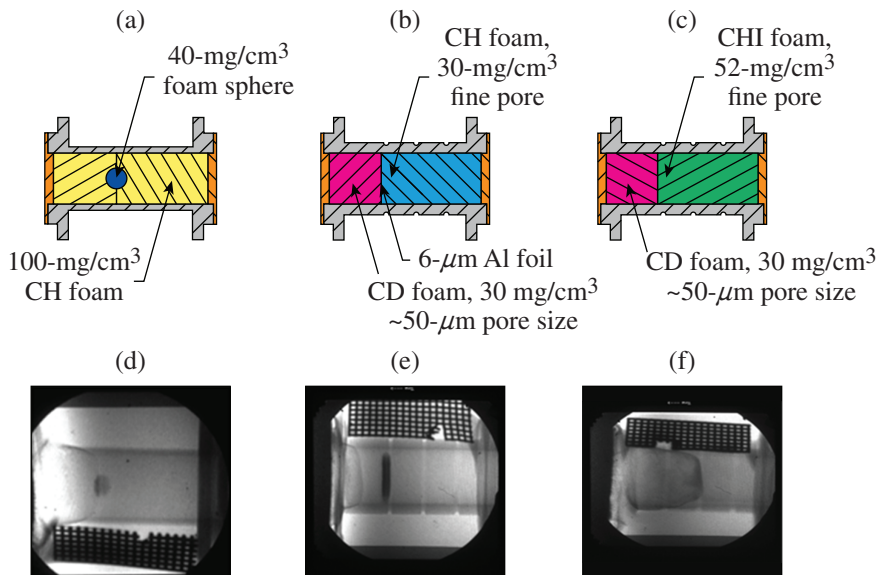
Marble Void Collapse

Marble is an experimental campaign intended to study the effects of heterogeneous mix on fusion burn. While designing the Marble implosion experiments, three questions emerged: First, how well do we understand the evolution of voids as the shock passes through? Is the evolution turbulent? Second, how well do we understand preheat inside our capsules? And finally, how accurate is the equation of state used for marble foams? To answer these questions, we designed an experimental campaign known as Marble Void Collapse. The idea was to take the well-understood shock-shear platform and modify it to answer these three questions. For the first type, a fine-cell 100-mg/cm^3 CH foam filled the Rexolite tube as shown in Fig. 148.121(a). Inside the foam, a sphere composed of iodine-doped CH foam (or tin-doped SiO$_2$ foam) was inserted. The density was chosen to be ~40 mg to give a similar Atwood number found in voids in the NIF foam capsules. The iodine (or tin) dopant provided a contrast with the vanadium and titanium backlighters. Figure 148.121(b) shows the second type, where a 6-μm-thick aluminum foil was embedded inside the shock tube to examine the expansion of the foil by preheat and measure the spread as the

perturbed shock passed through the foil. The last type [shown in Fig. 148.121(c)] was filled with a marble CD foam where the void size was 50 μm in diameter. Throughout these three experiments, high-quality radiographic data were acquired. The experimental result shown in Fig. 148.121(d) appears to confirm that the evolution of the void is not turbulent as the initial shock passes, seen in simulation. Also, the shock timing between simulation and experiment is well matched. This suggests an accurate understanding of the fine-pore foam's equation of state. As shown in Fig. 148.121(e), preheat effect was examined by the expansion of aluminum foil before a shock arrives. Figure 148.121(f) shows the shock speed measured through marble foam (50-μm-diam pore size), which can be used to determine the equation of state of the marble foam.

CoaxDiff

The COAX Experimental Campaign on OMEGA develops an advanced radiation flow diagnostic that can be used to characterize the subsonic and supersonic radiation front to provide constraining data for physics models. The intention is to eventually move these experiments to the NIF. In these experiments, a halfraum is used to launch a radiation front down a cylindrical foam target (contained by a Be sleeve) (Fig. 148.122). The subsonic radiation front is measured by imaging, while spectroscopy of a doped insert in the target is utilized to study the supersonic form of the radiation front by observing its impact on the ionization balance of the dopant. Originally Ti was used and was able to provide constraining data to the shape of the radiation front by comparison to *PrismSPECT* simulations. However, Ti K-shell absorption spectra were unable to probe

(a)

40-mg/cm^3 foam sphere

100-mg/cm^3 CH foam

(b)

CH foam, 30-mg/cm^3 fine pore

6-μm Al foil

CD foam, 30 mg/cm^3 ~50-μm pore size

(c)

CHI foam, 52-mg/cm^3 fine pore

CD foam, 30 mg/cm^3 ~50-μm pore size

(d)   (e)   (f)

U2063JR

Figure 148.121
The three Marble Void Collapse setups [types (a), (b), and (c)]. (d) Evolution of void was not turbulent; (e) preheat effect was examined by the expansion of aluminum foil; (f) shock speed measured through marble foam (50-μm-diam pore size) can be used to determine the equation of state of marble foam.

the shape of the front at temperatures below 100 eV. To probe the potentially non-Planckian character of the radiation front below 100 eV, we elected to shift to a Sc dopant. Because Sc has a lower Z than Ti, it requires less energy to exceed the ionization potential; therefore K-shell absorption spectra will occur at lower photon energies and lower temperatures than Ti. For both elements, absorption spectra are observed when photons generated by the laser-driven backlighter pass through the target and interact with electrons in auto-ionizing states in the L shell, which enables them to transition to a hole in the inner shell. At the current photon energy range of the NIF-5 spectrometer, Ti $1s$–$2p$ and Ti $1s$–$3p$ spectra are observable, but only Sc $1s$–$3p$ spectra are observable.

Three shot days were dedicated to COAX in FY16. In October 2015 imaging data and absorption spectra were observed

for Ti, and proof of principle was established for Sc by collecting Sc $1s$–$3p$ absorption spectra for the first time with the NIF-5 (Fig. 148.123). In April 2016 excellent image data of the doped aerogels were collected for both Ti- and Sc-doped foams, but issues with the spectroscopic backlighter resulted on only weak spectra being collected. In August a Kr-filled capsule backlighter design was successfully tested against a redesign of the previous wire backlighter, and a number of shots of strong Sc absorption spectra were collected using both backlighters. Initial data analysis suggests the T_e measured by the Sc was in the 75- to 90-eV range. No imaging data were collected in August, but we instead used the space to collect constraining information about the size, brightness, and symmetry of the capsule backlighter that would be used for the next set of experiments.
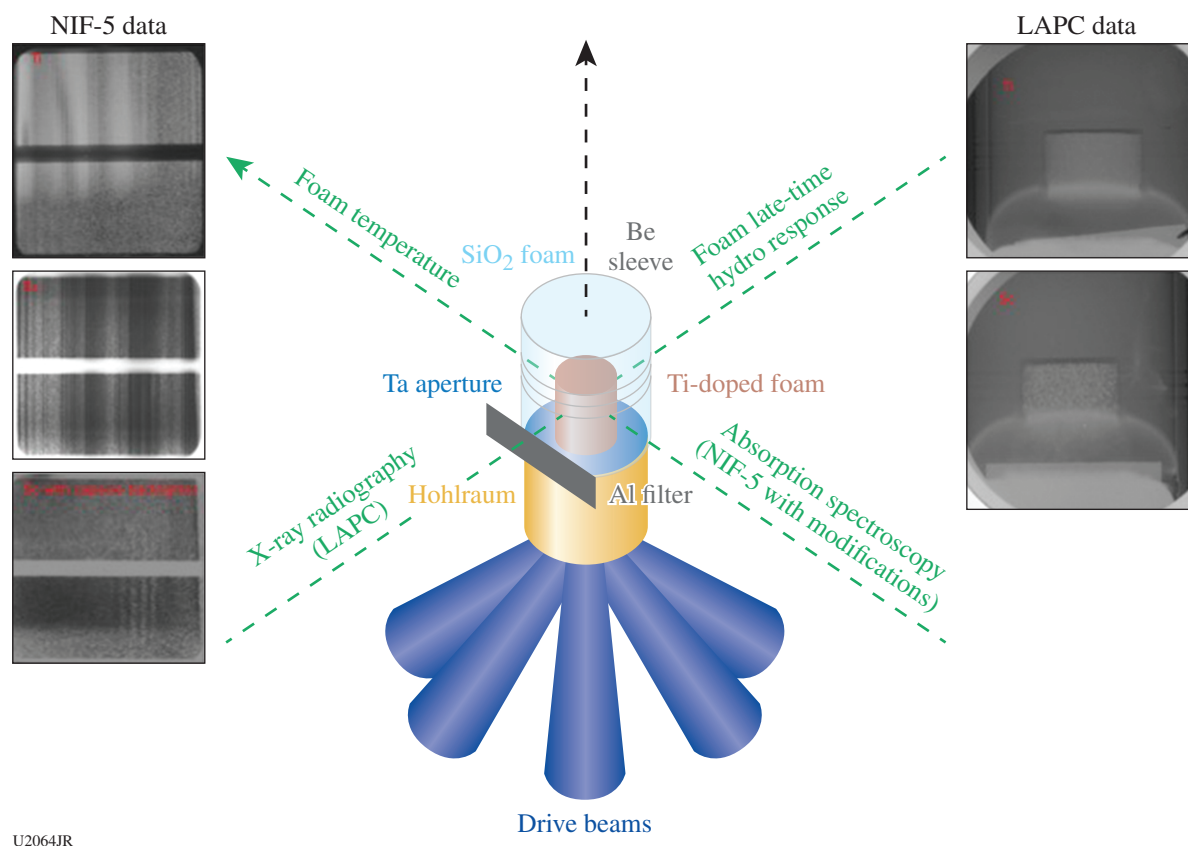
Figure 148.122

(a) Data collected for Ti from a prior year are compared to data from the latest shots with Sc in August. (b) Two radiographs from April with Sc- and Ti-doped aerogels. LAPC: LANL pinhole camera.
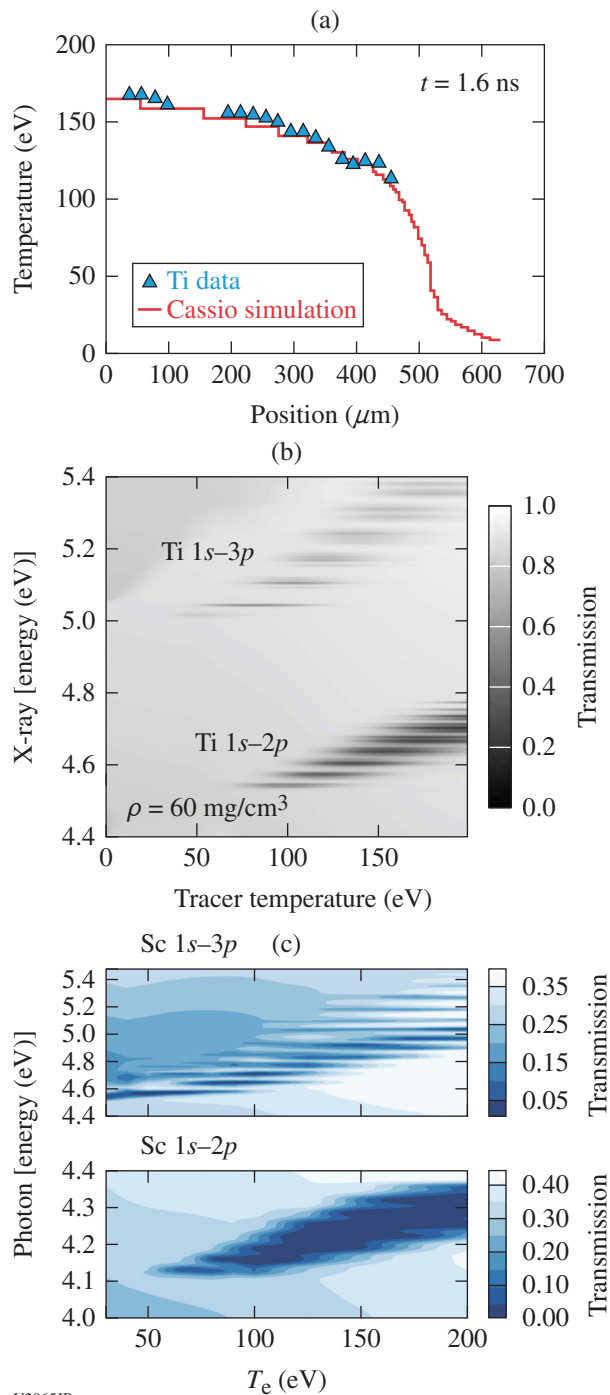
Figure 148.123

(a) The shape of the radiation front in simulation is compared to results from COAX experiments featuring Ti-doped aerogels. Simulated K-shell absorption spectra from *PrismSPECT* for (b) Ti and (c) Sc illustrate the change in temperature and photon energy distribution of lines for the same transitions in two different elements. These figures were presented at the 2016 High-Temperature Plasma Diagnostics Conference.

HEDmix

Anomalous low modes (particularly mode ~1) have been postulated as the cause of low hot-spot pressure of mid-adiabat implosions on OMEGA direct drive.[8,40] In the 2016 HED-MIX campaign, images captured emission signatures near stagnation, which are consistent with the presence of such hypothesized low-mode imbalance. The experiments used warm implosions with a Ti tracer at 1% by atom in the innermost 100 nm of the plastic shell. The Ti tracer emission was resolved spectrally using a unique imaging instrument termed the "multiple monochromatic imager" (MMI).[41] Figure 148.124(a) shows an image obtained from 5- to 6-keV Ti emission at time of peak neutron production. A mode-1 pattern appears in the emission and is quantified (~70% drop) in Fig. 148.124(b). Such a pattern appeared systematically within the day, although capsule mounting was excluded as the cause. Using 3-D modeling with LLE's *ASTER* code,[40] we found that such asymmetric emission results when such anomalous low modes are included in the drive. In the calculation, the emission drop results from reduced temperature on the overdriven side of the capsule where the tracer layer is compressed to a higher density. To quantifiably estimate this density imbalance from the data, first the measured spectrum is modeled [see Fig. 148.124(c)] to determine the tracer conditions from the emissive region ($n_e = 5.75 \times 10^{24}$ cm^{-3}, $T_e = 1350$ eV). Beginning with these conditions, Fig. 148.124(d) shows the reduction in observed emission as density increases and temperature is decreased under assumption of pressure balance. Similar to the type of density modulations observed in the simulation, the results suggest about 50% variation in density of the emissive layer across the observed mode-1 pattern.

HKMix

Mix is an important degradation mechanism for ICF and there is a programmatic need for strong benchmarks for mix models. A new experimental platform was developed, on this shot day and on THDGamma-16A, to study mix. Differentially thresholded gas Cherenkov detectors (GCD's) measure the γ-ray signal from a HT-fueled implosion with a deuterated shell, so that the HT burn comes from the core, while the D–T reactions occur from any mix of shell material into the hot spot. The detector with lower gas pressure (higher threshold) is more sensitive to the HT γ's. On this experiment, 860-μm-diam shells of 9- or 15-μm-thick plastic, with a 0.25-μm-thick inner deuterated layer, were filled with 9 atm of equimolar HT gas. A simultaneous forward fit to the two detectors was then used to infer both DT and HT burn histories. The data from shot 80348, which used a 15-μm-thick shell, are shown in Fig. 148.125. The difference in time between the core and mix burn will be used

to constrain time-dependent mix models. In this shot, the mix signal (DT) comes about 70 ps later than the core (HT) burn. This result is corroborated by a second analysis technique that uses a surrogate shot without the deuterated layer, clearly showing that the core (HT) signal comes early. The data from the 9-μm-thick shells show, in contrast, that the mix (DT) signal
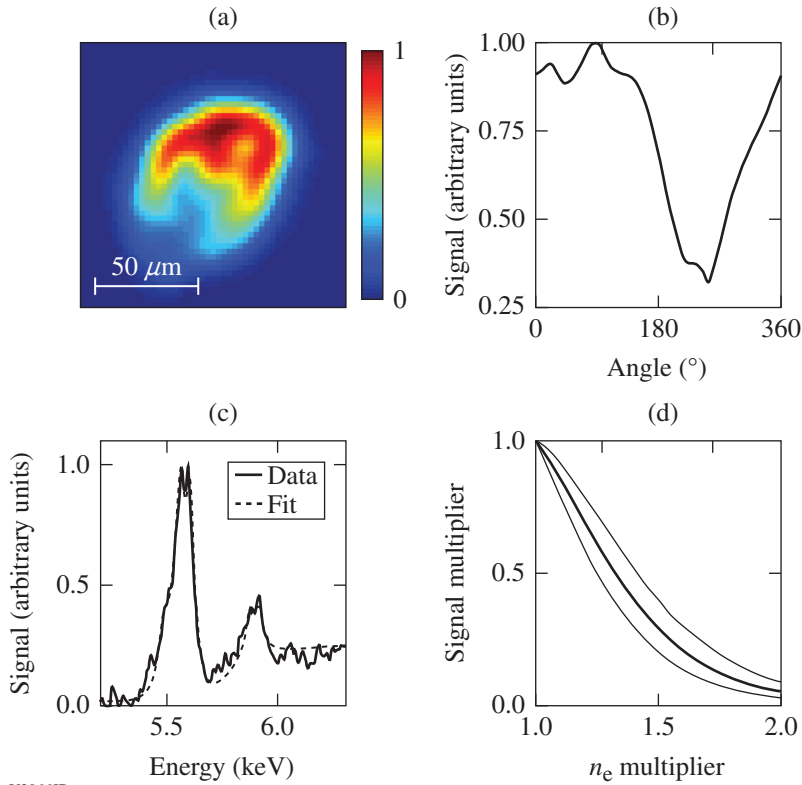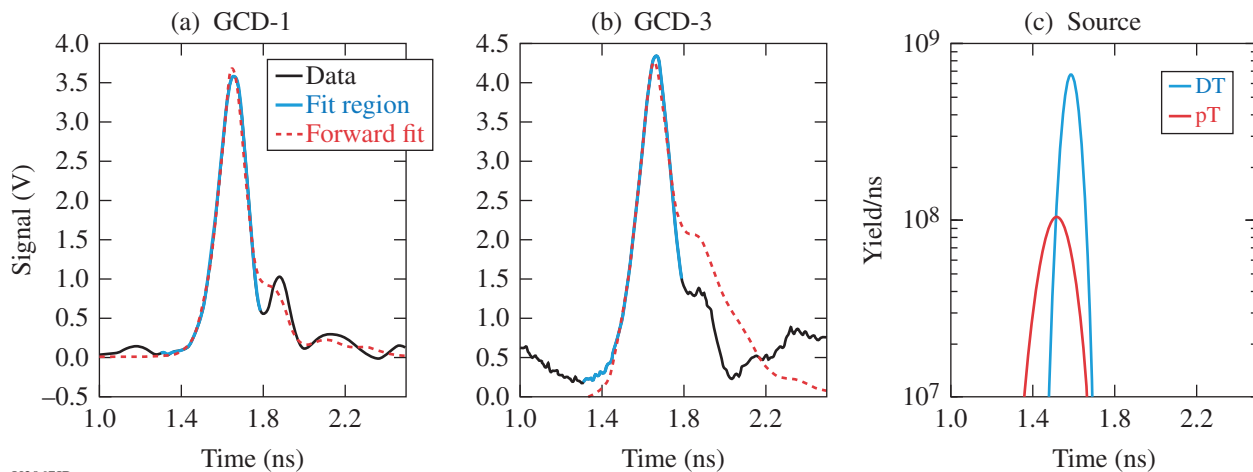

Figure 148.124
(a) Bang-time image of Ti emission from 5 to 6 keV; (b) peripheral signal versus angle; (c) measured multiple monochromatic imager (MMI) spectrum and fit; (d) modeled scaling of emission as density increases over nominal value from spectral fitting.

Figure 148.125
Cherenkov data from two detectors on shot 80348 using (a) 100 psi of CO_2 and (b) 30 psi of CO_2 on a mix shot. (c) The data are simultaneously forward fit using burn histories for pT and DT reactions to infer the difference in time between the core (pT) and mix (DT) burn.

comes earlier than the core burn, suggesting the importance of a nonhydrodynamic mix process. This technique will be used over future campaigns by varying implosion parameters to study mix under various conditions.

MSP

Measuring charged-particle stopping power (MSP) in dense plasmas relevant to ICF is challenging. The MSP-16A shot day tested a new technique based on measuring charged-particle downshift in the compressed shell of an implosion. The target design is shown in Fig. 148.126. A thick (25-μm) CH shell is imploded with a fuel mixture of D/T/^{3}He. The DT-n inelastically scatter on the C in the shell, producing 4.4-MeV γ rays that are detected with the GCD's, thereby measuring the areal density of the shell at peak burn. Simultaneously, the 15-MeV D^{3}He protons are emitted and slow down as they transit the

shell. The proton downshift gives a measurement of the average stopping power in the shell. A preliminary proton spectrum (Fig. 148.126) shows the proton downshift from its birth energy. X-ray spectroscopy [Fig. 148.126(c)] was also used to characterize the plasma conditions in the shell, analyzing absorption lines produced by a 2% atomic Ti dopant in the shell. Analysis of the proton, x-ray, and γ-ray data is continuing.

ZSP

The ZSP-16A Campaign studied charged-particle stopping power in warm dense plasma. The experimental concept was based on previous successful experiments in Be samples.[42] The experimental concept is shown in Fig. 148.127(a). The subject target is a 500-μm-thick graphite cylinder, doped with 1% atomic Pd, which is placed inside a Ti-coated tube. The tube is illuminated by 30 of the OMEGA laser beams, and the
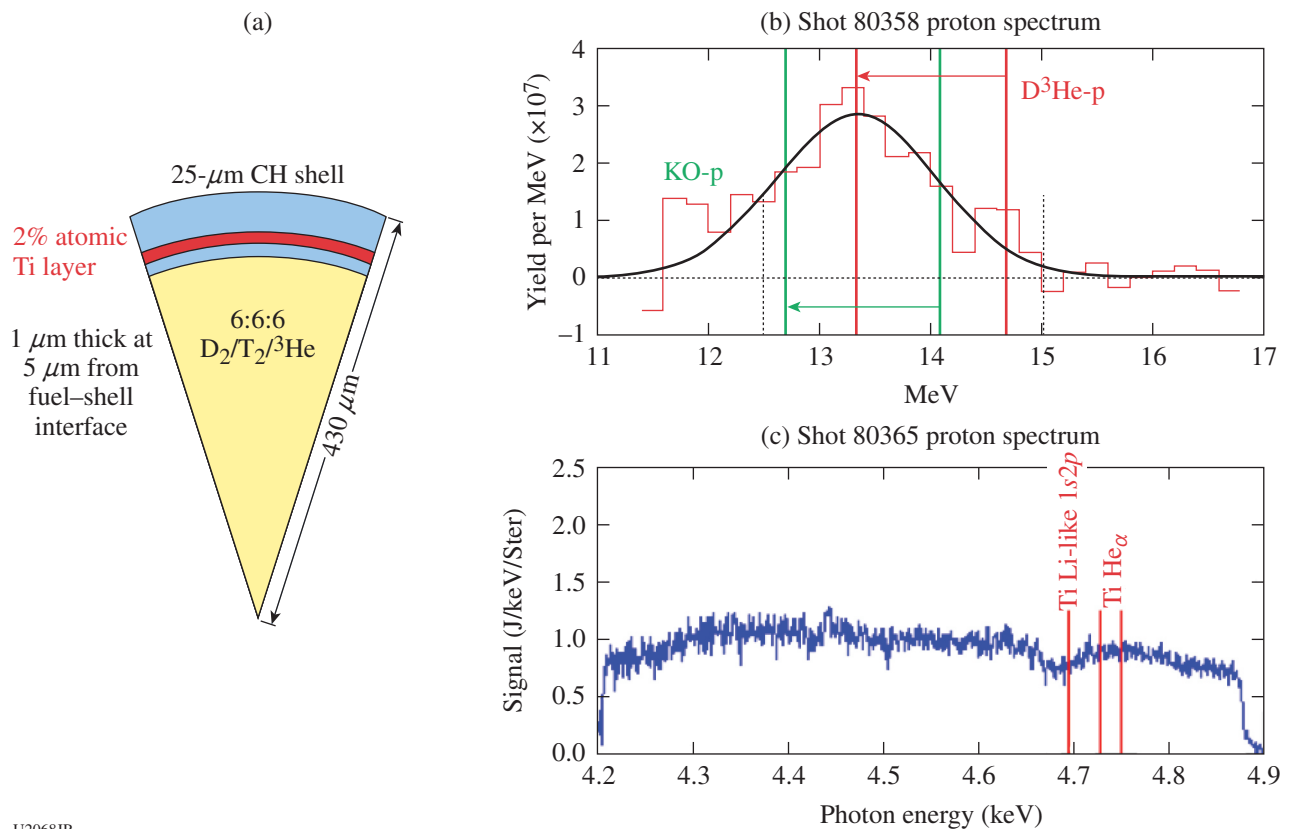
U2068JR

Figure 148.126
(a) Target pie diagram. (b) The D^{3}He proton spectrum measured on shot 80358, where the D^{3}He protons are downshifted from their birth energy by about 1.5 MeV. Knock-on (KO) protons are also observed, at lower energies, from elastic neutron scattering. (c) The Ti-doped layer in the shell is used for absorption spectroscopy to diagnose the shell's plasma conditions.
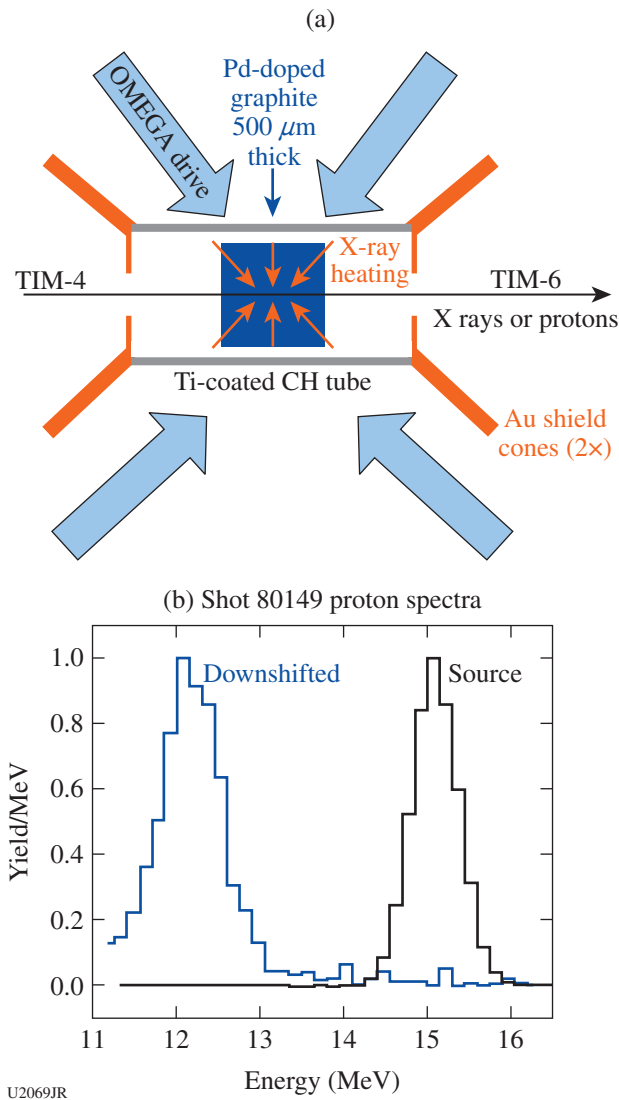
The proton downshift is a direct measurement of the average stopping power in the sample. Additional proton data are being analyzed. X-ray absorption data from the Pd dopant will be analyzed to infer the plasma conditions.

THDGamma

The HT fusion reaction produces a mono-energetic γ ray at 19.8 MeV. Thresholded Cherenkov detectors, like the GCD's,[43] are relatively more sensitive to higher-energy γ than the DT γ [see Fig. 148.128(a)]. The THDGamma-16A Campaign was conducted to demonstrate the detection of HT γ and study the signals observed under different implosion conditions. CH
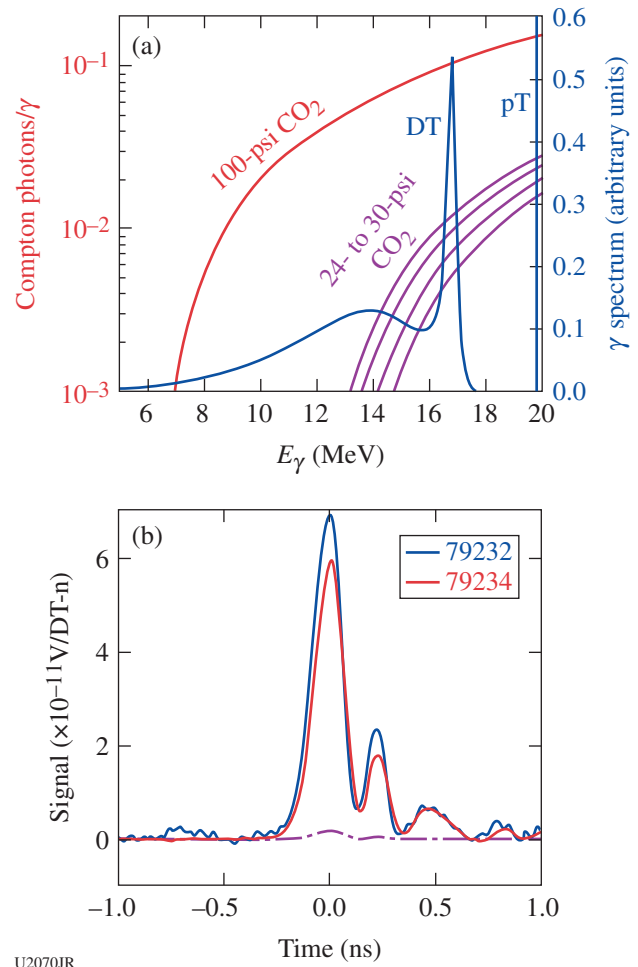

(a)

Figure 148.127
(a) ZSP-16A experimental schematic and (b) proton spectra. A cylindrical sample of Pd-doped graphite is heated isochorically by x rays generated at the outer surface of a Ti-coated tube. Probing protons or x rays sample the graphite along the axis. A sample proton spectrum from shot 80149 (peak normalized) is shown at right in (b).

Figure 148.128
(a) Cherenkov detector response for various pressures of CO_2 gas compared to the γ-ray spectrum from DT and HT fusion. The detector's relative sensitivity to HT γ increases for the lower gas pressures. (b) Signal from two $H_2 + T_2$ fueled implosions, normalized to the DT-n yield. The GCD was fielded at 100-psi CO_2. The dashed curves represent the signal contribution from DT-γ based on the measured DT-n yield, from a 0.1% D impurity. The signal is dominated by HT-γ, the first definitive detection of these γ rays in ICF implosions.

Ti x-ray emission isochorically heats the graphite sample. Au shield cones are placed on each end of the cylinder to shield the diagnostic line of sight from the laser spots. The sample is probed by protons or x rays along the TIM-4/TIM-6 axis.

Preliminary proton data from shot 80149 are shown in Fig. 148.127(b). The proton source is a directly driven exploding pusher, which creates an isotropic flux of 15-MeV D^3He protons. The source spectrum is measured directly. The proton spectrum after transiting the graphite sample is also measured.

shells (9 or 15 μm thick, 860 μm in diameter) were filled with an equimolar mixture of H and T, with either 0.1% or 2.0% D contamination. The shots with 0.1% D [Fig. 148.128(b)] show that the detector signal at 100 psi of CO_2 is dominated by the HT γ, as expected. This is the first definitive detection of these γ rays produced from an ICF implosion. As the D concentration is increased, in the initial gas fill or due to mix (e.g., from a CD shell), the relative importance of the DT γ contribution to the total signal increases. By using differentially thresholded detectors, both reactions may be measured simultaneously. This technique will be used in an upcoming LANL mix campaign. Preliminary shots with deuterated shells were also taken on this day and used to iterate the implosion design for the subsequent experiments (HKMix-16A).

WDFEOS

The WDFEOS experiment collects valuable information for understanding the equation of state of warm dense matter (WDM) under shocked conditions along the Hugoniot. The explored WDM conditions are relevant for ICF and the interiors of Jovian planets. On the WDFEOS shot date in February 2016, low-density CH foams under shock compression in the 1- to 4-Mbar range were studied using SOP and VISAR to measure shock velocity using shock breakout timing. After every VISAR/SOP shot there was an x-ray Thomson-scattering shot, with the imaging x-ray Thomson spectrometer (iXTS) looking at scattering from the Ni He$_\alpha$ line at 7.8 keV, timed based on the shock breakout of the prior shot. Note in Fig. 148.129 that the two types of targets have a different design to serve different purposes—the VISAR target includes a stepped foam to aid in the shock breakout measurement (Fig. 148.130), while the iXTS target includes a thin Ni foil used to probe the shocked foam with 7.8-keV x rays. The iXTS was used to primarily measure the temperature of the shocked foam.

An analysis of x-ray Thomson-scattering (XRTS) probe data (Fig. 148.131) so far demonstrates that as the shock progresses through the foam in time, there is a clear increase in T_e that appears as spectral broadening in the inelastic scattering feature. This also appears in time-integrated spectra within
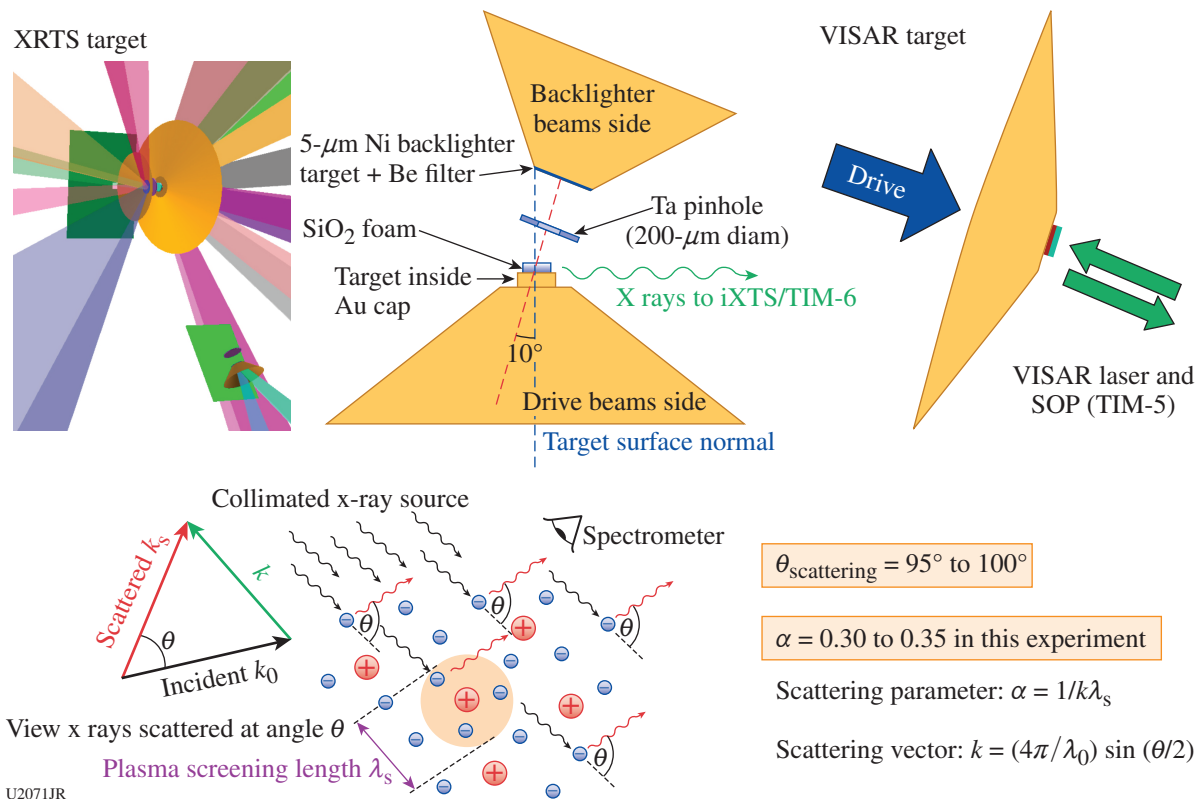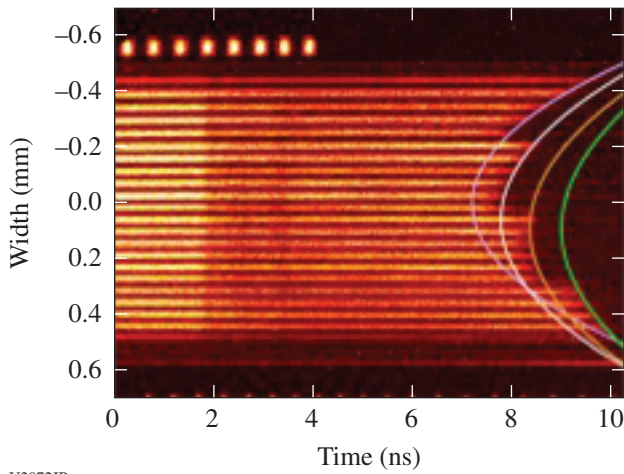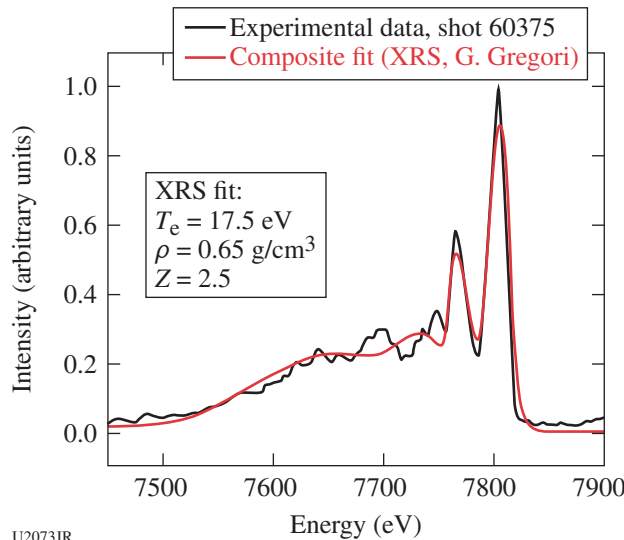

Figure 148.129
Schematics of the two types of targets used in WDFEOS experiments, as well as a simple explanation of the x-ray Thompson-scattering phenomenon. iXTS: imaging x-ray Thomson spectrometer.

Figure 148.130
Parabolic fits to VISAR data determine shock velocity based on shock breakout time. For shot 80371, shock velocity is 82 to 95 km/s at 5.5 ns, 75 to 87 km/s at 6.0 ns, and 67 to 81 km/s at 6.5 ns.

Figure 148.131
Temperature is determined by evaluating fits to the imaging x-ray Thomson spectrometer (iXTS) spectra after accounting for red-shift, contamination from blowoff plasma from the backlighter, and other corrections. XRS: x-ray scattering

the same shots (i.e., the shock propagates down, and upper profiles are wider and hotter). This increase of T_e with time is indicative of preheat. Simulations including up to 5 to 10 eV of preheat show little change to final temperature but expansion in the preheated foam reduces the initial density and results in higher shock speeds. This estimate is in agreement with SOP and VISAR analysis that shows higher shock speeds than previous experiments.

MixEOS-EP

Accurate simulations of fluid and plasma flows require accurate thermodynamic properties, which is typically represented by the EOS of the materials. For pure materials, the EOS may be represented by analytical models for idealized circumstances, or by tabular means, such as the *SESAME* tables. When a computational cell has a mixture of two or more fluids, however, the EOS is not well understood, particularly under the conditions of high-energy densities. For these mixed cells, mixture rules are typically used to provide the requisite information; however, the accuracy of these rules is uncertain. We have conducted experiments on OMEGA EP that provided EOS data, in the form of shock speed, of atomic mixtures of Ni and Al to study the mixed behavior and to validate various mixture rules used by our codes.

In our experiments we placed a quartz standard next to our test (NiAl) or reference (Al) metal specimen, all on top of a thick ablator material used to efficiently create high-pressure tens-of-Mbar shocks. The target geometry is shown in Fig. 148.132. With the ASBO, we measured the shock velocity inside the quartz standard as well as the shock transit time through our opaque metal test specimens. Since the EOS of quartz is well known, measuring the shock speed is sufficient to give us its shock pressure, which we also used to infer the shock pressure inside the ablator whose EOS we also assumed to be known (polystyrene and beryllium). Once the ablator shock pressure was known, along with any time-dependent variations as measured inside the quartz, we could apply that pressure in our simulations for each mixture rule and see which gave the closest prediction to the measured shock transit time through the test specimen. We repeated the experiments on Al reference specimens, whose EOS is assumed known, to verify the strategy was sound.

Figure 148.133 shows the as-built targets and raw ASBO streak-camera data for a CH ablator/NiAl target (OMEGA EP shot 22586) and a beryllium ablator/Al target (OMEGA EP shot 22587). The ASBO viewed at the center of the target across the quartz/specimen interface extending about 400 μm on either side. In these data we observed the time at which the shock front broke out of the ablator and entered the quartz witness, the subsequent shock velocity history in the quartz witness, the time the shock broke out of the specimen, and the subsequent shock velocity in the quartz after leaving the specimen. We measured shock velocities in our CH ablators of 43 km/s, which decreased to 35 km/s after entering the quartz due to differences in shock impedance at the interface. From measurements of shock transit time we found a shock velocity
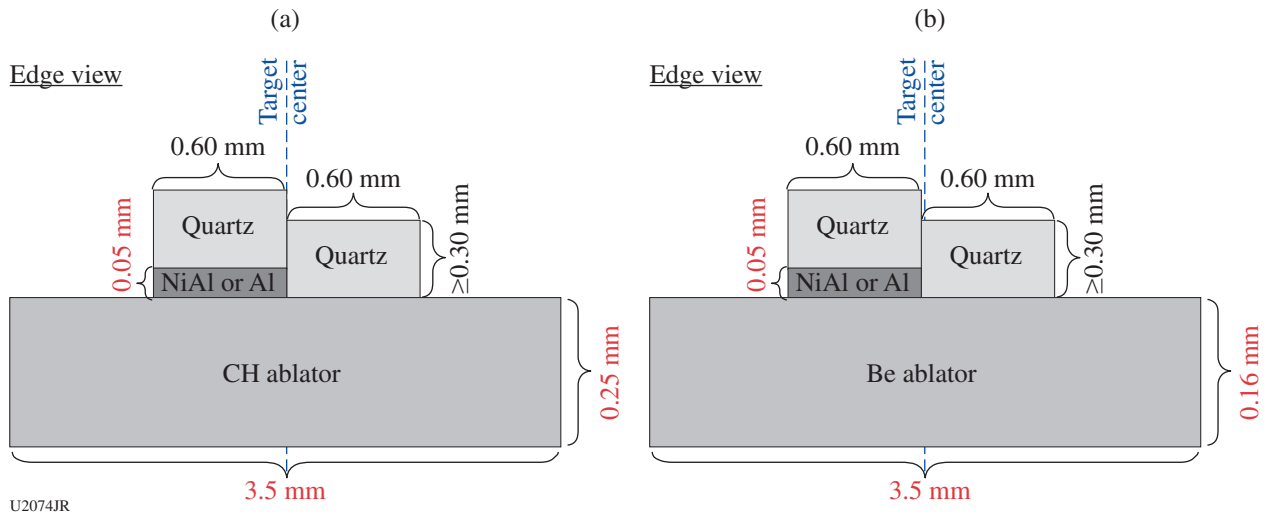
Figure 148.132
The two types of MixEOS targets used where specimens and quartz reference windows were placed on top of thick ablators designed to create steady shocks without wave reverberations.
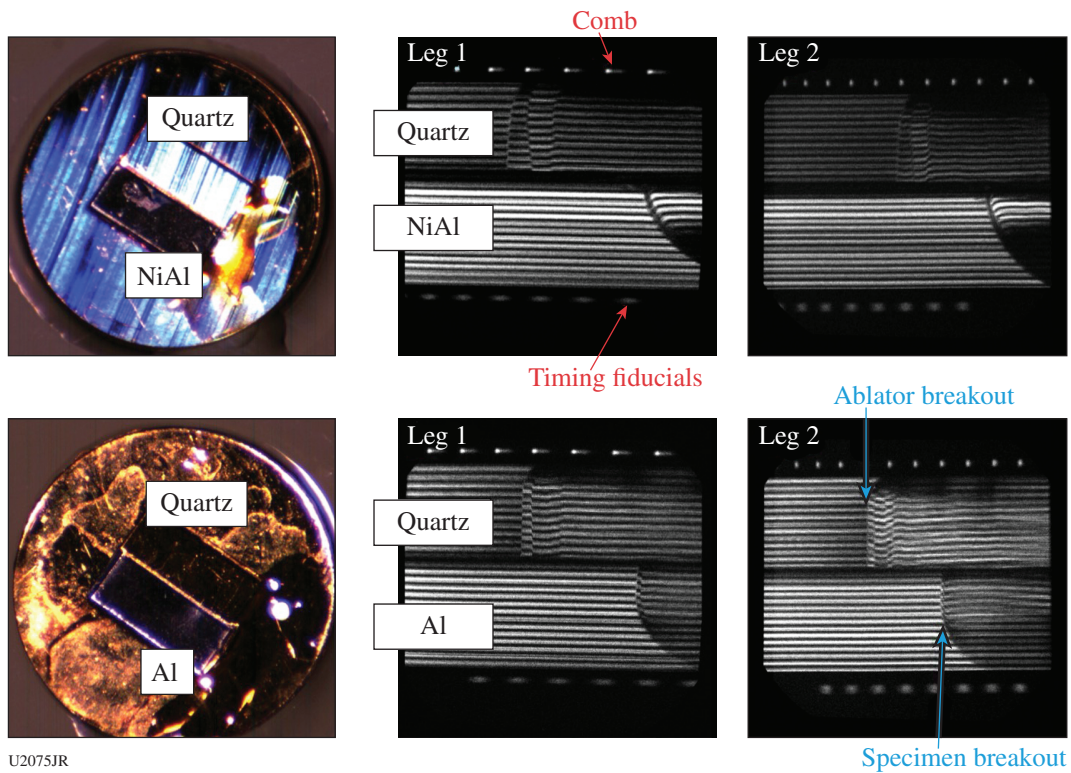

Figure 148.133
As-built targets and their ASBO streaked velocity data. Shock in the quartz is used to check steadiness and transit time through the specimen gives specimen shock velocity.

of about 36 km/s in Al specimens and 31 km/s in NiAl. This NiAl shock speed most closely matches the mixture rules of "additive volume" and ideal gas mixing.

ObliShock-EP

The mixing of modes between Rayleigh–Taylor (RT), Richtmeyer–Meshkov (RM), and Kelvin–Helmholtz (KH) instabilities occurs all across nature, from our terrestrial atmosphere and oceans[44] to astrophysical systems like accretion disks and supernovae.[45] The effects of shear on the growing spikes of the RT and RM processes is the reason for the production of the mushroom-like caps on these spikes[46] and can lead to a quicker onset and transition to turbulence.[47] Rarely is a flow interface purely shear or buoyancy driven; in the case of ICF, it is driven by a mix of passing shocks (RM), convergence (Bell–Plesset), and shearing shock flows

(KH). The Oblique Shock Platform developed by LANL in collaboration with the University of Michigan aims to understand the interplay between the various instabilities.

The platform shown in Fig. 148.134 is designed to allow one to control the amount of shear with respect to RM/RT growth. This is accomplished by a variable tilt interface. A steeper slope allows for more KH shear to enter the problem. Depicted is a 0° [Fig. 148.134(a)] and a 30° tilt [Fig. 148.134(b)] as seen by the diagnostic; the 30° case shows the field of view of the diagnostic (green dashed circle). The interface has an embedded strip of iodinated CH (CHI) as a tracer layer for better imaging and is density matched at ~1.45 g/cm^3 to the surrounding polyimidamide (PIA) substrate (top hat, light blue). When shocked using three of the OMEGA EP beams at full power (~5 kJ) for 10 ns, the interface is pushed into a
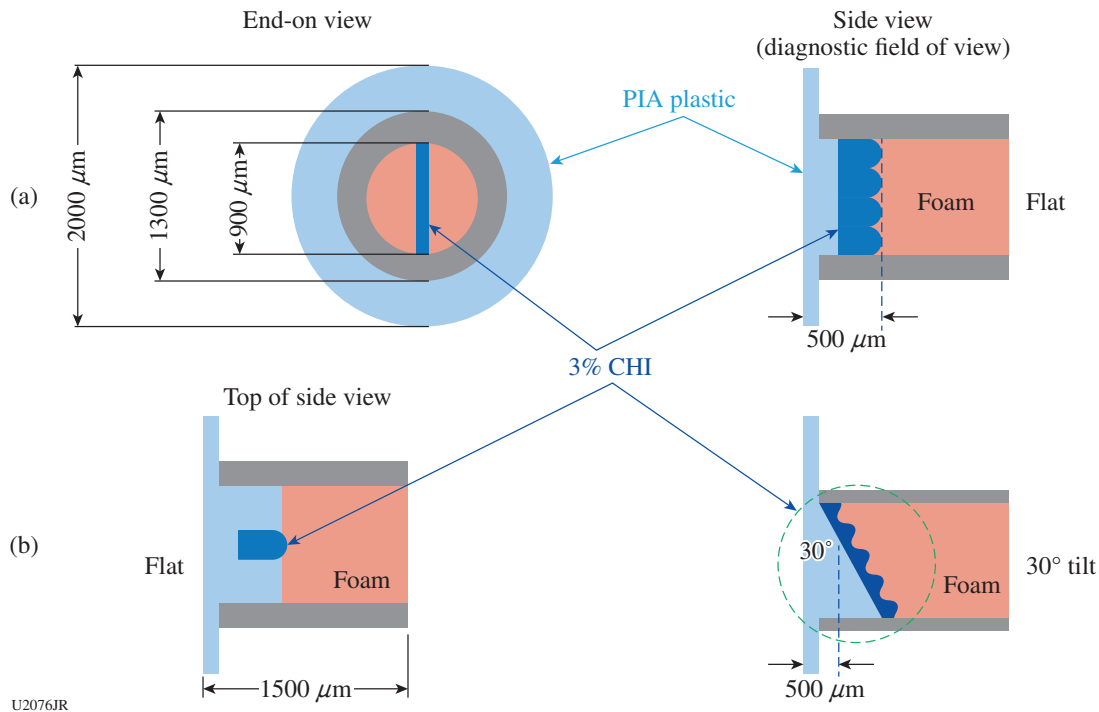
Figure 148.134
Setup of the OMEGA EP experiment. Three long-pulse 3ω beams of ~5 kJ each simultaneously irradiate the polyimidamide (PIA) ablator top-hat (light blue) and launch a shock into the experiment. A thin layer (100 μm) of density matched iodinated CH (CHI) (dark blue) is inserted into the PIA as a tracer layer for the perturbed interface inside a thin CH tube (gray). The tracer layer expands into a 100 mg/cm^3 foam (red). (a) A 0° tilt and (b) 30° tilt are illustrated. The interface evolution is then imaged at various times with the spherical crystal imager (SCI) using an 8-keV Cu K$_\alpha$ source driven by the fourth beam as a short-pulse (10-ps) backlighter. The area imaged by the SCI is indicated by the green dashed circle in the lower left 30° case. The field of view is shifted to follow the doped region as it transits the shock tube.

100-mg/cm^3 CH foam (Fig. 148.134, red) and is imaged using the OMEGA EP SCI from a short-pulse 10-ps Cu K$_\alpha$ back-lighter onto image plates. The tracer layer is subject to several forces: shock acceleration, deceleration into the foam, deceleration and decompression from the laser turn-off rarefaction, and shear flow across the layer, which cause a complex interplay of RM, RT, and KH in the growth of the spikes and bubbles seeded into the experiment. This is an important part of LANL's turbulent mix-modeling strategy, including the implementation of a new modal model[48] coupled to the LANL HR[49] mix model.

The first set of experiments was used to understand the shock velocity in the PAI/CHI and foam, to gauge our accuracy in modeling the platform in the multiphysics code *RAGE*. The data from campaigns in FY15 were used to benchmark the platform.[50] Figure 148.135 shows the shock position from 1-D *RAGE* simulations, next to one point in time from the experi-

ment, and the simulation. The FY16 campaigns have been focusing on the observing mode coupling from multimode sine waves and a band of modes to understand how the energy and growth are transferred from mode to mode.[51] The simulation shows similar growth of the layer and the characteristic turn-over of the spikes caused by the shear across the layer but shows significantly more small-scale rollup than the experiment. The experiment is not well enough resolved to make out such small structures but clearly exhibits the same rollup feature, which was expected because of the shear component in the system. The agreement is surprising considering the code used a simple mass source as a pusher for the hydrodynamics, which is unphysical at late time since the laser turns off at 10 ns and a rarefaction wave starts to enter the experiment, where in the code the source is on for the full simulation. This rarefaction catches up to the individual vortices at different times as a result of the varying ablator thickness, and vortex size can be seen to grow as the rarefaction catches up with each vortex. Work is currently ongoing to assess the growth rate of the spikes and bubbles using a new laser package for the *RAGE* calculations to simulate the full system end-to-end.[52] This is the first step before using this data to help verify the modal model in a pure RT/RM configuration, i.e., 0°.

FY16 NRL Experimental Campaigns at the Omega Laser Facility

During FY16, NRL/LLE collaboration on laser imprint led to three successful shot days on OMEGA EP. A new method was devised to allow smooth preheating of the coating without installing a dedicated laser for preheating. It utilized soft x rays generated by a low-energy laser pulse on an auxiliary gold foil to heat and expand the coating on the main target. Streaked x-ray radiography shows that the x rays successfully expanded the coating in front of the plastic foil prior to arrival of the main laser drive. Well-resolved measurements of RT-amplified laser imprint (Fig. 148.136) were obtained on OMEGA EP, showing significant reduction of the target perturbations with the gold overcoat. Initial analysis shows further reduction when the coating is pre-expanded by the prepulse (Fig. 148.137).
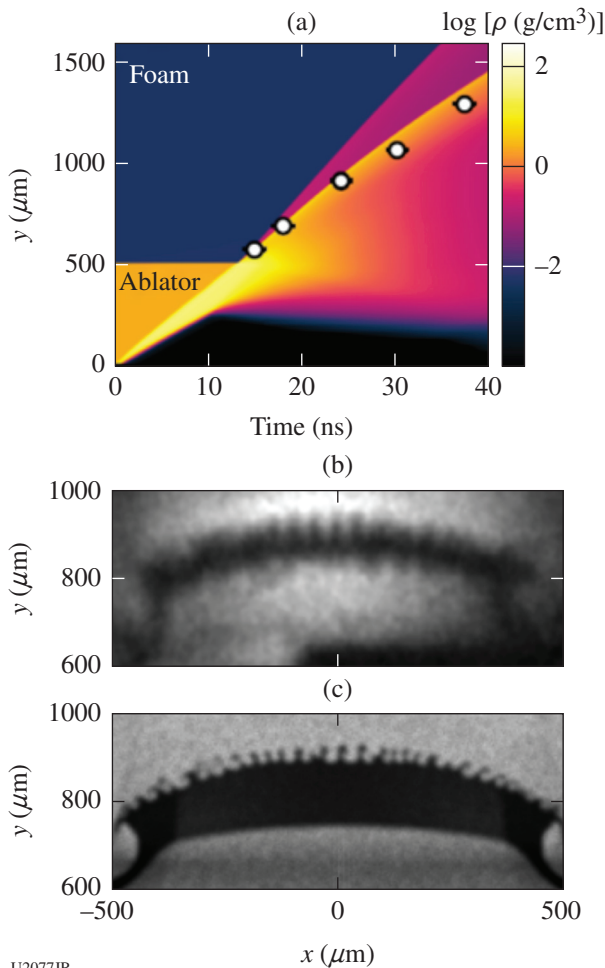

U2077JR

Figure 148.135
(a) Shock position/density jump as a function of time and images of the multimode band experiment (b) at 24 ns and (c) a 2-D *RAGE* simulation corresponding to the same time.
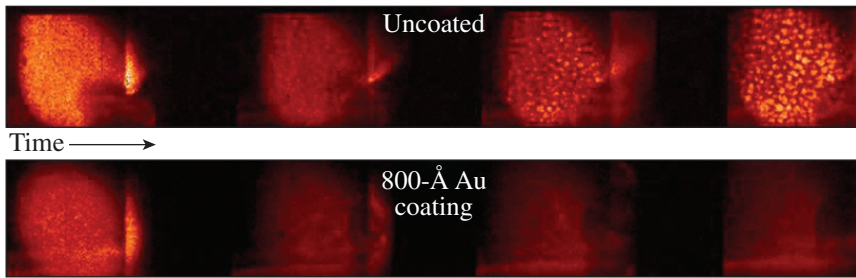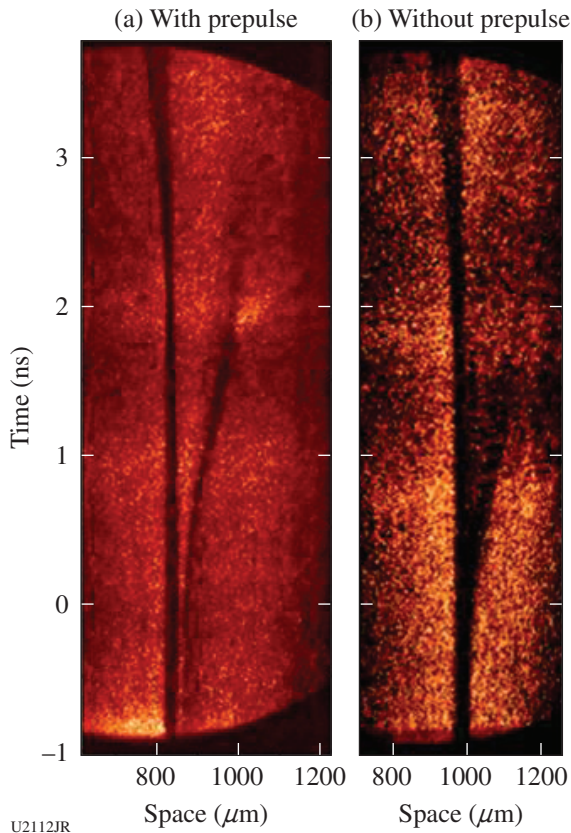
Figure 148.136
Measurements on OMEGA EP show laser imprint reduction with high-Z coating.

Figure 148.137
Gold coating is pre-expanded by an x-ray prepulse.

FY16 CEA Report on Omega Laser Facility Experiments

The Commissariat à l'énergie atomique et aux énergies (CEA) conducted 55 target shots on the OMEGA laser in FY16 for the campaigns discussed below.

Neutron-Induced Signals Generated on Coaxial Cables Exposed to OMEGA High-Yield Neutron Shots

Principal Investigators: J. L. Bourgade, J. L. Leray, B. Villette, O. Landoas, P. Leclerc, I. Lantuejoul-Thfoin, and J. E. Sauvestre (CEA-DAM-DIF)
Co-investigators: V. Yu. Glebov, T. C. Sangster, and G. Pien (LLE)

Since the first evidence of this effect in 2002 on OMEGA high-yield DT neutron shots,[53] it is now well demonstrated that high-pulsed, 14-MeV neutron irradiation can drive a transient current on various coaxial cables. Different geometries (based mainly on the same 0.141-in.-diam semi-rigid "SMA" coaxial cable with CF_4 dielectric) were used almost every year in the neutron "derby" on OMEGA since 2002 to better understand the current formation mechanisms.

In 2014 we selected a final experimental geometry that was able to induce a sufficient signal level with the neutron yield presently achievable on OMEGA direct-drive DT implosions ($Y_n \sim 10^{14}$). Since last year, the large effect of a weak magnetic field (~200 to 4000 Gauss) has been clearly demonstrated on this platform to generate a weaker current (by a factor of 12× less) at the same neutron irradiance than without it (see Ref. 54). These past results were obtained on coaxial cable embedded into a large amount of CHON, which was used to maintain the cable into its serpentine shape for inserting it into its protective cover tube.

In April 2016 the neutron derby shot day on OMEGA was used mainly to confirm results obtained in the past, which appear to show that the surrounding material of the coaxial cable under neutron irradiation induced a spurious signal that was larger than the internal signal generated only by the neutron interactions inside the coaxial cable.

According to our present hypothesis,[55] this current is mainly generated by traveling recoil nucleus into the coaxial cable, and we chose to switch the external support material from CHON to woven fiber glass and Macor ceramics. This change is driven by the fact that the heavier recoil nuclei ejected from these surrounding materials by the neutron knock-on processes is less energetic with a smaller range into matter than protons (CHON case) and therefore cannot penetrate the thin (~300-μm) Cu outside layer of our 0.141-in. coaxial cable (with CF_4 dielectric).

Figure 148.138(a) shows the FY15 coaxial cable embedded into the CHON epoxy glue as support material;

(a)

1st

CHON

2015 (with CHON)

(b)

1st   2nd   Neutro

B

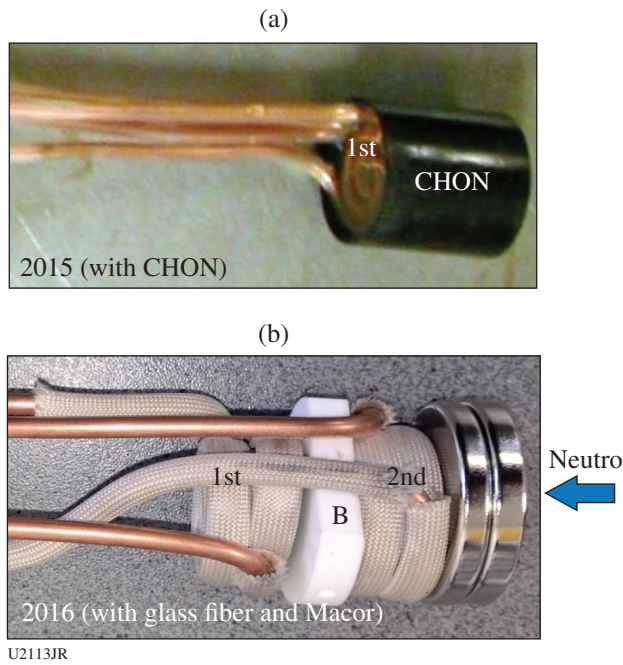2016 (with glass fiber and Macor)

U2113JR

Figure 148.138

(a) FY15 coaxial cable serpentines embedded into CHON epoxide glue (the first serpentine without permanent magnet B but invisible though the epoxide glue and the plastic black cylinder). (b) FY16 coaxial cable serpentines with a woven glass fiber sheath (surrounding the 0.141-in. coaxial cable), the white Macor ceramic to maintain a permanent magnet disk (not visible), and the Fe-Nd-B permanent magnets (two silver disks at the far right).

Fig. 148.138(b) shows the FY16 coaxial cable geometry with this fiber glass–woven fastener and the Macor ceramics used to carry the magnets. In Fig. 148.138(a) the three permanent magnets are invisible, hidden by the black plastic cylinder. In Fig. 148.138(b) only two permanent magnets disks are clearly visible (marked "B"), and the last magnet used to create a larger magnetic field into the gap between them is placed in the middle of the white Macor ceramic.

This year two identical devices were fabricated with the fiber glass–woven sheath and the permanent magnets. On one device the magnetic field was canceled by heating the magnets above their Curie point. We chose to keep the unmagnetized magnets in the same place in order to have similar mass for the neutron interactions. These two identical devices were exposed on the same day to neutron shots on OMEGA by exchanging them into our CEA cart load between consecutive shots in the middle of the shot day.

Figure 148.139 shows the spectacular decreasing of the signal levels on OMEGA measured between 2014, 2015, and 2016 devices exposed on almost the same neutron flux ($\sim 3 \times 10^{13}$ for 2014 and 2016 shots, and up to 7.5×10^{13} neutrons for 2015 shots —at the same distance of ~ 235 mm from the source).

If we compare the same scale (all the curves presented in Fig. 148.139 are normalized to the same value of 3×10^{13} neutrons/4π) the signals generated on a 50-Ω resistive charge— the largest current ever for this serpentine geometry—is generated by the one embedded into CHON without a magnetic field.

The signal differences of the two consecutives peaks (factor of ~ 2) are induced by a larger distance from the source (245 versus 239 mm, a factor of 1.05) for one of the serpentines (recorded here first in time by our choice) and also a larger neutron attenuation induced by the first serpentine (the CHON absorbing material used for fixing the serpentines in place and the permanent magnet and its plastic holder placed between the two serpentines as presented in Fig. 148.138). Nevertheless, Geant4 simulations performed to explain this difference were not sufficient to account for the signal level difference between the two serpentines and further calculations must be performed. For the glass fiber/Macor environment this measured difference is lower (by a factor of 1.2) because the neutron absorption is lower, resulting from less absorbing mass but still not accounted for in totality by the neutron absorption difference.

The glass fiber sheath/Macor without a magnetic-field device is the second in the row with a large reduction induced by replacing the outside material with fiber glass/Macor (factor of ~ 7.5 in our 2014/2015 shots comparison), confirming that surrounding CHON material generates a large part of the signal measured since first 2002 experiments.

A similar reduction factor has also been evaluated in the past on different coaxial cable geometries when CHON was replaced by a glass fiber sheath but have generated too weak signals even on the highest neutron yields achievable on OMEGA close to 10^{14} to be measured with enough accuracy. It is the first time since 2002 that such good data have been recorded and analyzed on different shots on OMEGA (three shots in 2016) on the same geometry with such accuracy for both magnetic field and higher atomic mass close materials. These clear measurements have also validated our choice of this new serpentine geometry used since 2013.

Finally the two devices with the magnetic field generate the lowest signals on this same neutron irradiation flux. For the *same* device without B field (2014) and magnetized again at Grenoble (Laboratoire National des Champs Magnétiques
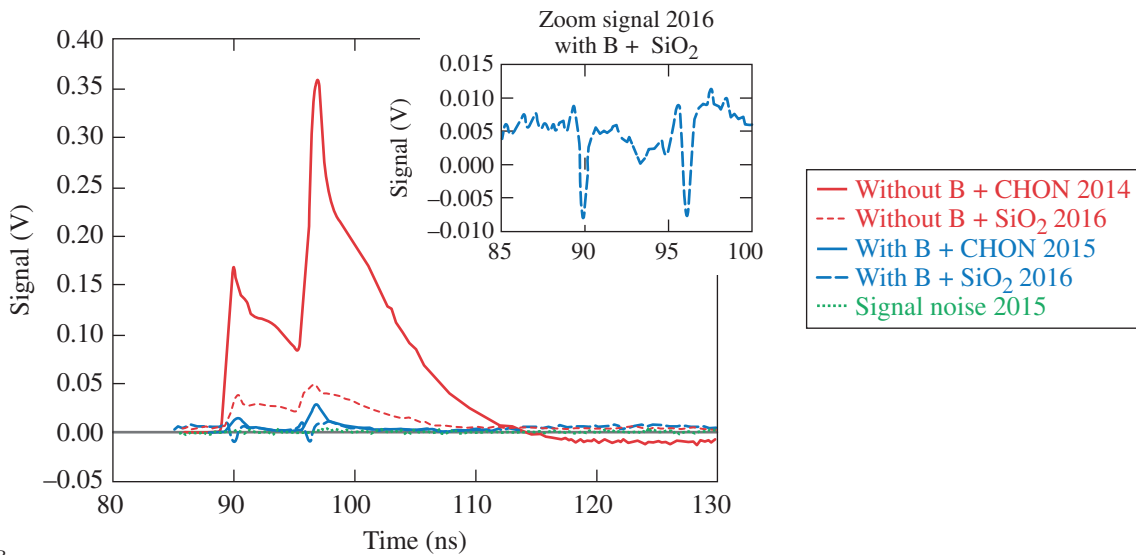
U2114JR

Figure 148.139

Summary of signal levels obtained since 2014 neutron derbies on the same geometry configuration "serpentine" on 0.141-in. coaxial cable with different configurations (with and without static magnetic field, with CHON and with glass fiber/Macor close environment). The lowest signal under neutron irradiation (normalized here for 3×10^{13} neutrons/4π) was obtained in the 2016 experiments by combining glass fiber/Macor close environment instead of CHON and by adding a static magnetic field. The two peaks are induced by two identical serpentines spaced electrically by a time delay coaxial cable of around 1.2 m (6 ns apart). The inset shows the weakest signal of 2016 around the 85- to 100-ns time window and the –10- to +15-mV range.

Intenses) in 2015, the reduction factor induced on both serpentines is even larger than for the outside material contribution (reduction factor of ~12).

The 2016 device (with glass fiber and Macor outside materials *and* with the magnetic field) shows the weakest current generation ever recorded. Fortunately it is just above the background level for these measurements (few mV peak to peak).

Moreover, the shape of this last signal is clearly different between the two identical devices. The one without a magnetic field always exhibits positive signals (as measured on all the geometries tested on OMEGA since 2002) while the magnetic field case exhibits more-complicated bipolar behaviors; therefore it is more difficult to derive a simple reduction factor from these two measurements. Nevertheless, if we try to crudely measure that value on the positive peaks only, this reduction factor is ~10.

Bipolar behaviors on the weakest signal obtained in 2016 (SiO_2 + B) can be analyzed as the following:

- The incoming neutrons interact with both the 3-mm-thick tungsten x-ray disc filter (added in front of the device to avoid any x rays below 200 keV generated by the laser–

plasma interaction on the microballoon, to reach the cable) and the two permanent magnets (two 5-mm-thick disks), create a strong pulsed γ-ray source (duration estimated to ~400 ps including the neutron source duration, its Doppler broadening during their time of flight and their travel into the converting disks) by the neutron-to-gamma conversion into these high-Z and massive materials.

- The gamma rays can generate only negative peaks on coaxial cables [as measured on a pulsed hard x-ray generator and calculated with standard system-generated electromagnetic-pulse (SGEMP) effects simulations].[56] The two negative peaks seen in this case in Fig. 148.139 (into the right zoom) are almost equal in durations (FWHM ~ 600 ps) and value in both serpentines because the source is a large one (38 to 35 mm in diameter with respect to the 35-mm-diam serpentine wrap) placed close to them (2 mm for the first one and 7 mm for the second).

- The remaining positive signal (associated with the neutron interaction within the coaxial cable itself) is very weak (a few millivolt, so just above the signal background) and can be seen only on the second peak (associated to the serpentine placed closer from the source).

Finally a careful analysis of the signals presented in Fig. 148.139 shows little time change for the peak positions that can be related to different implosion bang times as measured by other OMEGA neutrons diagnostics as the neutron time of flight (nTOF). Those small time changes clearly show that the current is generated only by the neutron irradiation and no other energy vectors emitted by the implosions as gammas or hard x rays.

Moreover, to confirm the neutron origin of the measured signal, any or very few peaks are generated when the neutron yield is low (in the range of few 10^{12}) as recorded for instance in Fig. 148.139 labeled as "signal noise 2015" (where the yield for this specific shot was as low as 2.2×10^{12}).

These past yearly "neutron derby" experiments on the current generated during the OMEGA neutron irradiation on the 0.141-in. semi-rigid coaxial cable [widely used on the NIF and/ or Laser Mégajoule (LMJ) to propagate fast electrical signals with their very large bandwidth up to few ten of GHz] are now well measured and their origin characterized. Some mitigation techniques were found to greatly reduce (by a factor of nearly 100) this spurious current:

- Avoid placing any CHON material in close proximity of the coaxial cable and replace any of these plastic materials by woven glass fiber and Macor–type ceramics as fixtures and holders if necessary.

- Add some permanent magnets (as Fe-Nd-B) along the coaxial cable able to maintain a few-hundred-Gauss magnetic field along the cable.

- With these precautions these coaxial cables widely used on our diagnostics signal transport can continue to be used even on the highest neutron flux perhaps achievable on the NIF and LMJ up to the ignition level (10^{17} to 10^{18} neutron yield at their 5-m-radius target chamber surface).

Progress in the Diamond Anvil Cell Target Setup for OMEGA

Principal Investigators: S. Brygoo and P. Loubeyre (CEA) Co-investigators: R. Jeanloz (University of California, Berkeley); M. Millot, P. M. Celliers, and J H. Eggert (LLNL); and G. W. Collins, J. R. Rygg, and T. R. Boehly (LLE)

Measuring the properties of H and He and other simple molecular systems under deep planetary conditions has generated a great deal of interest.[58–59] The thermodynamic states there are qualified as warm dense matter, i.e., those of a plasma strongly correlated and with partly degenerated electrons. If the temperature is low enough, specifically in hydrogen, intriguing properties could be disclosed, like the possible existence of a plasma phase transition. To probe those states, pressures up to the TPa range must be generated but associated to temperatures below 1 eV. This range is well outside the principal Hugoniot of deuterium for which only pressures less than 0.1 TPa are associated to temperature below 1 eV.

The most-common technique for reaching off-Hugoniot states is to generate a multishock compression, through either reverberation between two anvils or a succession of small shocks. These two techniques make it possible to reach final pressures of several Mbar associated with temperatures close to an isentropic compression, but the thermodynamic state of the system is inferred indirectly using a hydro-simulation of the experiment. To keep the advantage of the single Hugoniot compression that provides a direct measurement of the final thermodynamic state by relating P, V, E values to the shock and particle velocities through the Rankine–Hugoniot equations, the CEA/UC Berkeley/LLNL/LLE team has developed a novel approach over the past ten years under the NLUF program. It is based on the concept of the diamond anvil cell (DAC) target, i.e., the sample is initially under an initial pressure of a few GPa. The Hugoniot curves generated from these precompressed initial states are therefore much cooler than the principal Hugoniot, which is illustrated in Fig. 148.140 for hydrogen, where different Hugoniot corresponding to different initial pressures are plotted.

The concept of the precompressed target is explained in Fig. 148.141. The figure of merit of this concept is the initial pressure that can be achieved using a thin-enough diamond window so that a strong shock can propagate to the sample. Since our first measurements on OMEGA, the initial pressure has been multiplied by a factor of 100, increasing from 0.16 GPa to 16 GPa. This increase has been made possible thanks to the evolution of the shape of the drive diamond going from a flat to a conical shape, which makes it possible to drastically increase the initial pressure for the same thickness. Also, to reduce the force on the diamond window, the culet size of the diamond anvil has been reduced. Increase of the initial pressure is consequently made at the expense of the diameter of the sample available. The evolution of the sample diameter is shown in Fig. 148.141. It should be stressed that even for a 100-μm-diam sample, the dimension of the sample for the 16-GPa initial pressure, the quality of the VISAR image remains good enough for an accurate analysis, made possible by OMEGA's constant
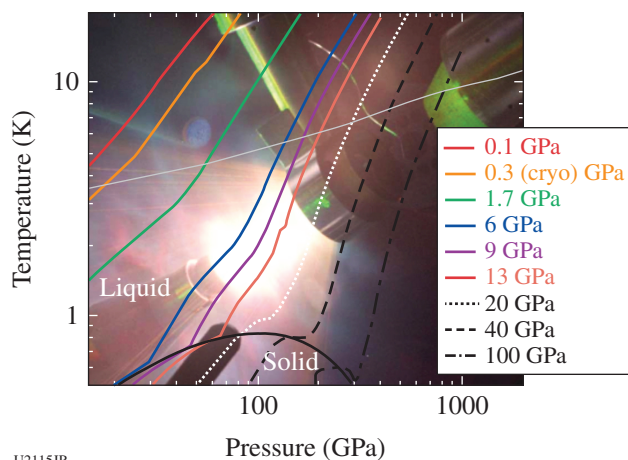
U2115JR

Figure 148.140
Precompressed H_2 Hugoniot curves associated with different initial pressures. By changing the initial pressure, a bundle of Hugoniot can be generated and consequently the equation of state can be measured over a large pressure–temperature phase domain. The colored Hugoniot are those that have been investigated on OMEGA up to now.
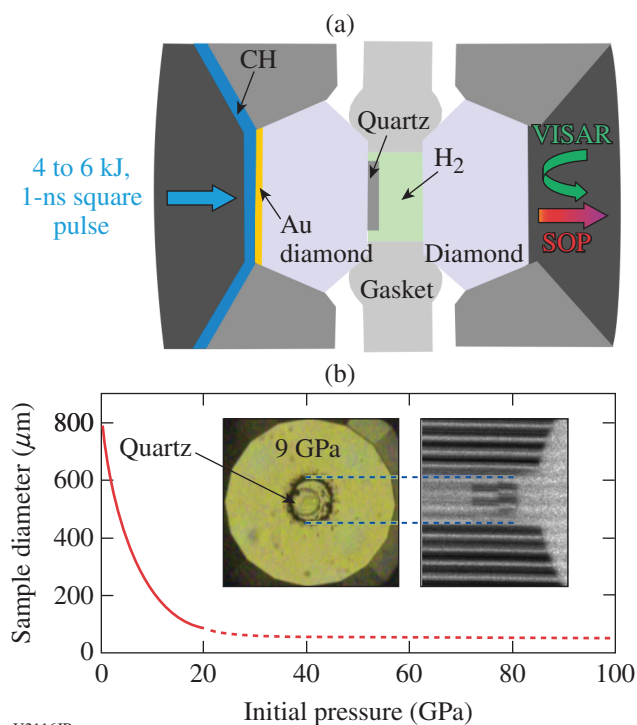
U2116JR

Figure 148.141
Evolution of the target over the years. (a) A typical target. (b) The diameter of the inside of a target as a function of the initial pressure. The inset represents the target before the shot and its associated VISAR image obtained for a 9-GPa precompression, respectively.

upgrade of the VISAR/SOP diagnostic. Finally, the laser-shock experiment on precompressed samples is analyzed using a quartz reference; this analysis framework has recently been improved. The roadmap of our effort on OMEGA is to continue the increase of the precompression and to extend the use of the precompressed target for simple molecular systems. Over the next two years, precompression of 40 GPa should be feasible.

Wall Motion Experiment on OMEGA
Principal Investigators: C. Courtois, L. Lecherbourg, and F. Girard

The objective of the experiment performed 15 September 2016 was to characterize the interaction between laser beams and expanded plasma from walls that occur in a halfraum. The expansion of the gold plasma wall produced by the external laser cone can indeed modify the propagation of laser beams of the internal cone and then directly affect the cavity energetics.

This OMEGA experiment is the second of this type (the first campaign was in June 2014). The cavity uses a double-wall design (one wall tilted by 30° relative to the second one) (see Fig. 148.142). At t_0, laser beams from the 21° and 59° cones (heating beams) are focused inside the cavity. The 59° cone is at the origin of the plasma bubbles of interest. At $t_0 + \delta t$, laser beams from the 42° cone (interaction beams) are focused inside the halfraum and propagate through the plasma bubbles that are more or less expanded, depending on the time delay δt and the methane gas filling pressure P. During the 2014 experiment, delays up to 1 ns were tested as a "3-D" pointing of the 59° cone beams. This 3-D pointing was chosen to maximize the size of the expanding plasma and, consequently, the interaction strength. The 2016 experiment tested longer delays (up to 2.2 ns) and also a 2-D pointing aimed at producing a more-cylindrical, expanding plasma wall.

On the opposite side of the laser entrance hole (LEH), the halfraum exhibits a window that gives direct access to the plasma bubbles (the interaction area). In the configuration called "P8" represented in Fig. 148.142, the interaction area is studied using an x-ray imager positioned in TIM-5. In the P5 configuration, the target is turned by 180° and the plasma bubbles are studied using the broadband x-ray spectrometers DMX and Dante.

In the P8 configuration, the hard x-ray imager in the TIM-5 provides access to the heating laser beam (59° cones) as it

impacts on the halfraum walls. Hard x-ray emission is observed through an oblong observation window. Figure 148.143 shows experimental results obtained for $\delta t = 1.4$ ns and $P = 1$ bar. The maximum emission of the heating laser beams (59° cone) can be seen in Fig. 148.143(b). Persistence of the signal and features at $t_0 + 3.3$ ns [Fig. 148.143(c)] suggest 42° cone laser beam energy deposition inside the expanding plasma, producing hard x-ray emission.

The hard x-ray emission produced by the plasma bubbles (created by the heating beam from the 59° cone and the interaction beam during its propagation through this bubble) can be absolutely measured using the broadband x-ray spectrometers DMX and Dante [Fig. 148.144(b)]. The amplitude of the second peak associated with the interaction beam–deposited energy increases with the delay δt and decreases with the methane gas filling pressure P.
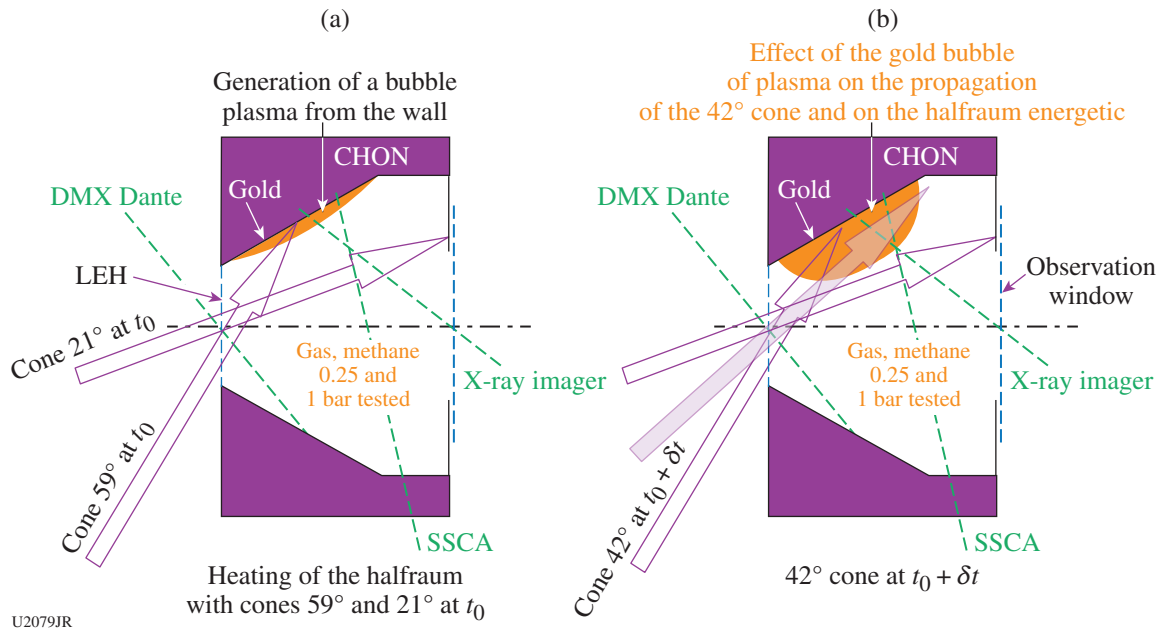
Figure 148.142
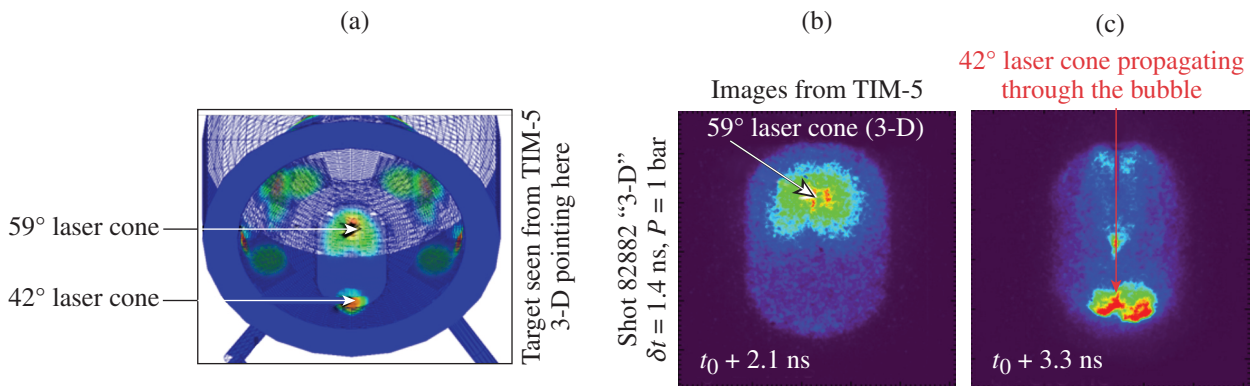Principle of the experiment (P8 configuration). LEH: laser entrance hole.

Figure 148.143
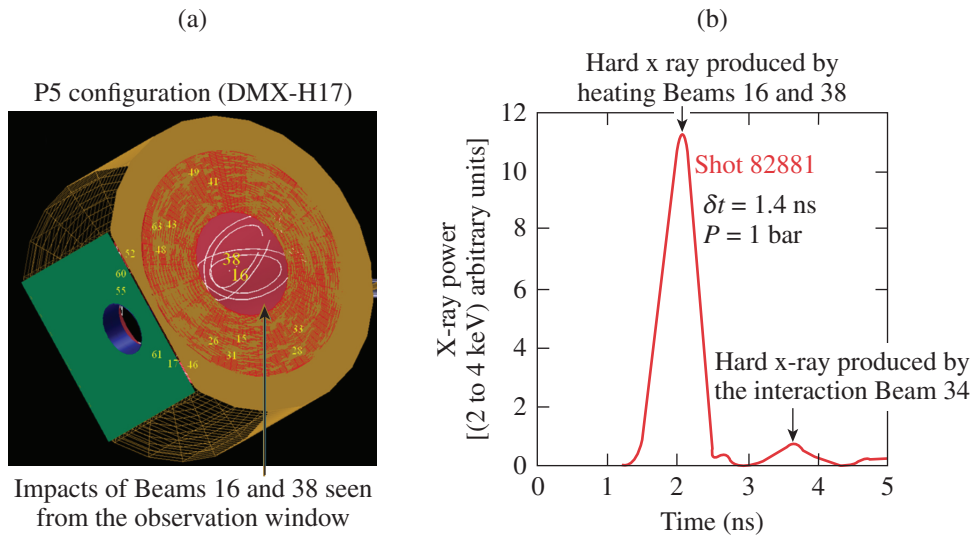Images obtained with the hard x-ray imager in TIM-5 (P8 configuration).

(a)

P5 configuration (DMX-H17)

Impacts of Beams 16 and 38 seen from the observation window

U2081JR

(b)

Figure 148.144

(a) Visrad image showing the target seen from DMX; (b) hard x-ray power (2 to 4 keV) measured by DMX.

REFERENCES

1. R. A. Fischer *et al*., Earth Planet. Sci. Lett. **373**, 54 (2013).

2. G. Fiksel, W. Fox, A. Bhattacharjee, D. H. Barnak, P.-Y. Chang, K. Germaschewski, S. X. Hu, and P. M. Nilson, Phys. Rev. Lett. **113**, 105003 (2014).

3. C. K. Li, P. Tzeferacos, D. Lamb, G. Gregori, P. A. Norreys, M. J. Rosenberg, R. K. Follett, D. H. Froula, M. Koenig, F. H. Séguin, J. A. Frenje, H. G. Rinderknecht, H. Sio, A. B. Zylstra, R. D. Petrasso, P. A. Amendt, H. S. Park, B. A. Remington, D. D. Ryutov, S. C. Wilks, R. Betti, A. Frank, S. X. Hu, T. C. Sangster, P. Hartigan, R. P. Drake, C. C. Kuranz, S. V. Lebedev, and N. C. Woolsey, Nat. Commun. **7**, 13081 (2016).

4. H. Sio, J. A. Frenje, J. Katz, C. Stoeckl, D. Weiner, M. Bedzyk, V. Glebov, C. Sorce, M. Gatu Johnson, H. G. Rinderknecht, A. B. Zylstra, T. C. Sangster, S. P. Regan, T. Kwan, A. Le, A. N. Simakov, W. T. Taitano, L. Chacòn, B. Keenan, R. Shah, G. Sutcliffe, and R. D. Petrasso, Rev. Sci. Instrum. **87**, 11D701 (2016).

5. N. V. Kabadi, H. Sio, V. Glebov, M. Gatu Johnson, A. MacPhee, J. A. Frenje, C. K. Li, F. Séguin, R. Petrasso, C. Forrest, J. Knauer, and H. G. Rinderknecht, Rev. Sci. Instrum. **87**, 11D817 (2016).

6. G. D. Sutcliffe, L. M. Milanese, D. Orozco, B. Lahmann, M. Gatu Johnson, F. H. Séguin, H. Sio, J. A. Frenje, C. K. Li, R. D. Petrasso, H.-S. Park, J. R. Rygg, D. T. Casey, R. Bionta, D. P. Turnbull, C. M. Huntington, J. S. Ross, A. B. Zylstra, M. J. Rosenberg, and V. Yu. Glebov, Rev. Sci. Instrum. **87**, 11D812 (2016).

7. B. Lahmann *et al*., Rev. Sci. Instrum. **87**, 11D801 (2016).

8. S. P. Regan, V. N. Goncharov, I. V. Igumenshchev, T. C. Sangster, R. Betti, A. Bose, T. R. Boehly, M. J. Bonino, E. M. Campbell, D. Cao, T. J. B. Collins, R. S. Craxton, A. K. Davis, J. A. Delettrez, D. H. Edgell, R. Epstein, C. J. Forrest, J. A. Frenje, D. H. Froula, M. Gatu Johnson, V. Yu. Glebov, D. R. Harding, M. Hohenberger, S. X. Hu, D. Jacobs-Perkins, R. T. Janezic, M. Karasik, R. L. Keck, J. H. Kelly, T. J. Kessler, J. P. Knauer, T. Z. Kosc, S. J. Loucks, J. A. Marozas, F. J. Marshall, R. L. McCrory, P. W. McKenty, D. D. Meyerhofer, D. T. Michel, J. F. Myatt, S. P. Obenschain, R. D. Petrasso, R. B. Radha, B. Rice, M. Rosenberg, A. J. Schmitt, M. J. Schmitt, W. Seka, W. T. Shmayda, M. J. Shoup, III, A. Shvydky, S. Skupsky, S. Solodov, C. Stoeckl, W. Theobald, J. Ulreich, M. D. Wittman, K. M. Woo, B. Yaakobi, and J. D. Zuegel, Phys. Rev. Lett. **117**, 025001 (2016); **117**, 059903(E) (2016).

9. A. B. Zylstra, H. W. Herrmann, M. Gatu Johnson, Y. H. Kim, J. A. Frenje, G. Hale, C. K. Li, M. Rubery, M. Paris, A. Bacher, C.R. Brune, C. Forrest, V. Yu. Glebov, R. Janezic, D. McNabb, A. Nikroo, J. Pino, T. C. Sangster, F. H. Séguin, W. Seka, H. Sio, C. Stoeckl, and R. D. Petrasso, Phys. Rev. Lett. **117**, 035002 (2016).

10. A. Bose, K. M. Woo, R. Betti, E. M. Campbell, D. Mangino, A. R. Christopherson, R. L. McCrory, R. Nora, S. P. Regan, V. N. Goncharov, T. C. Sangster, C. J. Forrest, J. Frenje, M. Gatu Johnson, V. Yu. Glebov, J. P. Knauer, F. J. Marshall, C. Stoeckl, and W. Theobald, Phys. Rev. E **94**, 011201(R) (2016).

11. A. B. Zylstra, J. A. Frenje, P. E. Grabowski, C. K. Li, G. W. Collins, P. Fitzsimmons, S. Glenzer, F. Graziani, S. B. Hansen, S. X. Hu, M. Gatu Johnson, P. Keiter, H. Reynolds, J. R. Rygg, F. H. Séguin, and R. D. Petrasso, J. Phys.: Conf. Ser. **717**, 012118 (2016).

12. Y. Kim, H. W. Herrmann, N. M. Hoffman, M. J. Schmitt, P. A. Bradley, S. Gales, C. J. Horsfield, M. Rubery, A. Leatherland, M. Gatu Johnson, J. Frenje, and V. Yu. Glebov, J. Phys.: Conf. Ser. **717**, 012030 (2016).

13. G. Kagan, H. W. Herrmann, Y.-H. Kim, M. J. Schmitt, P. Hakel, S. C. Hsu, N. M. Hoffman, D. Svyatsky, S. D. Baalrud, J. O. Daligault, H. Sio, A. B. Zylstra, M. J. Rosenberg, H. G. Rinderknecht, M. Gatu Johnson, J. A. Frenje, F. H. Séguin, C. K. Li, R. D. Petrasso, B. J. Albright, W. Taitano, G. A. Kyrala, P. A. Bradley, C.-K. Huang, C. J. McDevitt, L. Chacon, B. Srinivasan, A. M. McEvoy, T. R. Joshi, and C. S. Adams, J. Phys.: Conf. Ser. **717**, 012027 (2015).

14. P. B. Radha, V. N. Goncharov, M. Hohenberger, T. C. Sangster, R. Betti, R. S. Craxton, D. H. Edgell, R. Epstein, D. H. Froula, J. A. Marozas, F. J. Marshall, R. L. McCrory, P. W. McKenty, D. D. Meyerhofer,

D. T. Michel, S. X. Hu, W. Seka, A. Shvydky, S. Skupsky, J. A. Frenje, M. Gatu-Johnson, P. D. Petrasso, T. Ma, S. Le Pape, and A. J. Mackinnon, J. Phys.: Conf. Ser. **688**, 012006 (2016).

15. F. H. Séguin, C. K. Li, J. L. DeCiantis, J. A. Frenje, J. R. Rygg, R. D. Petrasso, F. J. Marshall, V. Smalyuk, V. Yu. Glebov, J. P. Knauer, T. C. Sangster, J. D. Kilkenny, and A. Nikroo, Phys. Plasmas **23**, 032705 (2016).

16. F. J. Marshall, P. B. Radha, M. J. Bonino, J. A. Delettrez, R. Epstein, V. Yu. Glebov, D. R. Harding, C. Stoeckl, J. A. Frenje, M. Gatu Johnson, F. H. Séguin, H. Sio, A. Zylstra, and E. Giraldez, Phys. Plasmas **23**, 012711 (2016).

17. S. Laffite, J. L. Bourgade, T. Caillaud, J. A. Delettrez, J. A. Frenje, F. Girard, V. Yu. Glebov, T. Joshi, O. Landoas, G. Legay, S. Lemaire, R. C. Mancini, F. J. Marshall, L. Masse, P. E. Masson-Laborde, D. T. Michel, F. Philippe, C. Reverdin, W. Seka, and V. Tassin, Phys. Plasmas **23**, 012706 (2016).

18. H. G. Rinderknecht, J. Rojas-Herrera, A. B. Zylstra, J. A. Frenje, M. Gatu Johnson, H. Sio, N. Sinenian, M. J. Rosenberg, C. K. Li, F. H. Séguin, R. D. Petrasso, T. Filkins, J. A. [Jeffrey] Steidle, J. A. [Jessica] Steidle, N. Traynor, and C. Freeman, Rev. Sci. Instrum. **86**, 123511 (2015).

19. J. A. Frenje, P. E. Grabowski, C. K. Li, F. H. Séguin, A. B. Zylstra, M. Gatu Johnson, R. D. Petrasso, V. Yu. Glebov, and T. C. Sangster, Phys. Rev. Lett. **115**, 205001 (2015).

20. M. Rosenberg, "Studies of Ion Kinetic Effects in Shock-Driven Inertial Confinement Fusion Implosions at OMEGA and the NIF and Magnetic Reconnection Using Laser-Produced Plasmas at OMEGA," Ph.D. thesis, Massachusetts Institute of Technology, 2014.

21. R. Nora, W. Theobald, R. Betti, F. J. Marshall, D. T. Michel, W. Seka, B. Yaakobi, M. Lafon, C. Stoeckl, J. A. Delettrez, A. A. Solodov, A. Casner, C. Reverdin, X. Ribeyre, A. Vallet, J. Peebles, F. N. Beg, and M. S. Wei, Phys. Rev. Lett. **114**, 045001 (2015).

22. W. Theobald, R. Nora, W. Seka, M. Lafon, K. S. Anderson, M. Hohenberger, F. J. Marshall, D. T. Michel, A. A. Solodov, C. Stoeckl, D. H. Edgell, B. Yaakobi, A. Casner, C. Reverdin, X. Ribeyre, A. Shvydky, A. Vallet, J. Peebles, F. N. Beg, M. S. Wei, and R. Betti, Phys. Plasmas **22**, 056310 (2015).

23. A. Deltuva, Institute of Theoretical Physics and Astronomy, Vilinus University, Vilinus, Lithuania, private communication (2015).

24. G. Hale, Los Alamos National Laboratory, private communication (2015).

25. T. R. Boehly, D. L. Brown, R. S. Craxton, R. L. Keck, J. P. Knauer, J. H. Kelly, T. J. Kessler, S. A. Kumpan, S. J. Loucks, S. A. Letzring, F. J. Marshall, R. L. McCrory, S. F. B. Morse, W. Seka, J. M. Soures, and C. P. Verdon, Opt. Commun. **133**, 495 (1997).

26. J. B. Neaton and N. W. Ashcroft, Nature **400**, 141 (1999).

27. Q. Liu, C. Fan, and R. Zhang, J. Appl. Phys. **105**, 123505 (2009).

28. C. J. Pickard and R. J. Needs, Nat. Mater. **9**, 624 (2010).

29. G. I. Kerley, Sandia National Laboratory, Albuquerque, NM, Report SAND2003-3613 (2003).

30. M. D. Knudson and M. P. Desjarlais, Phys. Rev. Lett. **103**, 225501 (2009).

31. H. Sio *et al.*, "A Broadband Proton Backlighting Platform to Probe Shock Propagation in Low-Density Systems," submitted to Review of Scientific Instruments.

32. D. E. Fratanduono, T. R. Boehly, M. A. Barrios, D. D. Meyerhofer, J. H. Eggert, R. F. Smith, D. G. Hicks, P. M. Celliers, D. G. Braun, and G. W. Collins, J. Appl. Phys. **109**, 123521 (2011).

33. A. M. Saunders *et al.*, Rev. Sci. Instrum. **87**, 11E724 (2016).

34. A. V. Bushman *et al.*, *Intense Dynamic Loading of Condensed Matter* (Taylor & Francis, Washington, DC, 1993).

35. D. C. Swift and C. R. Ruiz, AIP Conf. Proc. **845**, 1297 (2006).

36. R. F. Heeter, S. B. Hansen, K. B. Fournier, M. E. Foord, D. H. Froula, A. J. Mackinnon, M. J. May, M. B. Schneider, and B. K. F. Young, Phys. Rev. Lett. **99**, 195001 (2007).

37. R. F. Smith, S. M. Pollaine, S. J. Moon, K. T. Lorenz, P. M. Celliers, J. H. Eggert, H.-S. Park, and G. W. Collins, Phys. Plasmas **14**, 057105 (2007).

38. R. F. Smith, C. A. Bolme, D. J. Erskine, P. M. Celliers, S. Ali, J. H. Eggert, S. L. Brygoo, B. D. Hammel, J. Wang, and G. W. Collins, J. Appl. Phys. **114**, 133504 (2013).

39. D. Besnard *et al.*, Los Alamos National Laboratory, Los Alamos, NM, Report LA-12303-MS (1992).

40. I. V. Igumenshchev, V. N. Goncharov, F. J. Marshall, J. P. Knauer, E. M. Campbell, C. J. Forrest, D. H. Froula, V. Yu. Glebov, R. L. McCrory, S. P. Regan, T. C. Sangster, S. Skupsky, and C. Stoeckl, Phys. Plasmas **23**, 052702 (2016).

41. R. Tommasini, J. A. Koch, N. Izumi, L. A. Welser, R. C. Mancini, J. Delettrez, S. P. Regan, and V. Smalyuk, Proc. SPIE **6317**, 631716 (2006).

42. A. B. Zylstra, J. A. Frenje, P. E. Grabowski, C. K. Li, G. W. Collins, P. Fitzsimmons, S. Glenzer, F. Graziani, S. B. Hansen, S. X. Hu, M. Gatu Johnson, P. Keiter, H. Reynolds, J. R. Rygg, F. H. Séguin, and R. D. Petrasso, Phys. Rev. Lett. **114**, 215002 (2015).

43. H. W. Herrmann, Y. H. Kim, C. S. Young, V. E. Fatherley, F. E. Lopez, J. A. Oertel, R. M. Malone, M. S. Rubery, C. J. Horsfield, W. Stoeffl, A. B. Zylstra, W. T. Shmayda, and S. H. Batha, Rev. Sci. Instrum. **85**, 11E124 (2014).

44. W. R. Peltier and C. P. Caulfield, Annu. Rev. Fluid Mech. **35**, 135 (2003); J. D. Woods, J. Fluid Mech. **32**, 791 (1968).

45. D. P. Lathrop and C. B. Forest, Phys. Today **64**, 40 (2011); H. Xu *et al.*, Astrophys. J. Lett. **698**, L14 (2009); S. A. Balbus and J. F. Hawley, Rev. Mod. Phys. **70**, 1 (1998); A. R. Bell, Mon. Not. R. Astron. Soc. **353**, 550 (2004); T. Ebisuzaki, T. Shigeyama, and K. Nomoto, Astrophys. J. Lett. **344**, L65 (1989); I. Hachisu *et al.*, Astrophys. J. Lett. **358**, L57 (1990).

46. T. Yabe, H. Hoshino, and T. Tsuchiya, Phys. Rev. A **44**, 2756 (1991); N. J. Zabusky, Annu. Rev. Fluid Mech. **31**, 495 (1999).

47. Y. Zhou, H. F. Robey, and A. C. Buckingham, Phys. Rev. E **67**, 056305 (2003); Y. Zhou, Phys. Plasmas **14**, 082701 (2007).

48. B. Rollin and M. J. Andrews, J. Turbul. **14**, 77 (2013).

49. D. Besnard, F. H. Harlow, and R. Rauenzahn, Los Alamos National Laboratory, Los Alamos, NM, Report LA-10911-MS (1987).

50. G. Malamud *et al.*, High Energy Density Phys. **9**, 122 (2013).

51. C. A. Di Stefano *et al.*, submitted to Applied Physics Letters.

52. A. M. Rasmus *et al.*, to be submitted to Physical Review Letters.

53. *LLE Review Quarterly Report* **96**, 284, Laboratory for Laser Energetics, University of Rochester, Rochester, NY, LLE Document No. DOE/SF/19460-509, NTIS Order No. PB2006-106668 (2003).

54. *LLE Review Quarterly Report* **144**, 280, Laboratory for Laser Energetics, University of Rochester, Rochester, NY, LLE Document No. DOE/NA/1944-1242 (2015).

55. J. L. Leray *et al.*, IEEE Trans. Nucl. Sci. **59**, 1289 (2012).

56. J. L. Leray, S. Bazzoli, J. E. Sauvestre, and V. Yu. Glebov, IEEE Trans. Nucl. Sci. **55**, 3060 (2008).

57. R. Jeanloz, P. M. Celliers, G. W. Collins, J. H. Eggert, K. K. M. Lee, R. S. McWilliams, S. Brygoo, and P. Loubeyre, Proc. Natl. Acad. Sci. USA **104**, 9172 (2007).

58. P. Loubeyre, S. Brygoo, J. Eggert, P. M. Celliers, D. K. Spaulding, J. R. Rygg, T. R. Boehly, G. W. Collins, and R. Jeanloz, Phys. Rev. B **86**, 144115 (2012).

59. S. Brygoo, M. Millot, P. Loubeyre, A. E. Lazicki, S. Hamel, T. Qi, P. M. Celliers, F. Coppari, J. H. Eggert, D. E. Fratanduono, D. G. Hicks, J. R. Rygg, R. F. Smith, D. C. Swift, G. W. Collins, and R. Jeanloz, J. Appl. Phys. **118**, 195901 (2015).

Publications and Conference Presentations

Publications

M. Anthamatten, J. J. Ou, J. A. Weinfeld, and S. H. Chen, "Enthalpy Versus Entropy: What Drives Hard-Particle Ordering in Condensed Phases?" Chem. Phys. Lett. **660**, 18 (2016).

P. X. Belancourt, W. Theobald, P. A. Keiter, T. J. B. Collins, M. J. Bonino, P. M. Kozlowski, S. P. Regan, and R. P. Drake, "Demonstration of Imaging X-Ray Thomson Scattering on OMEGA EP," Rev. Sci. Instrum. **87**, 11E550 (2016).

A. Bose, K. M. Woo, R. Betti, E. M. Campbell, D. Mangino, A. R. Christopherson, R. L. McCrory, R. Nora, S. P. Regan, V. N. Goncharov, T. C. Sangster, C. J. Forrest, J. Frenje, M. Gatu Johnson, V. Yu. Glebov, J. P. Knauer, F. J. Marshall, C. Stoeckl, and W. Theobald, "Core Conditions for Alpha Heating Attained in Direct-Drive Inertial Confinement Fusion," Phys. Rev. E **94**, 011201(R) (2016).

B. P. Chock, T. B. Jones, and D. R. Harding, "Effect of a Surfactant on the Electric-Field Assembly of Oil-Water Emulsions for Making Foam Targets," Fusion Sci. Technol. **70**, 206 (2016).

P. S. Datte, J. S. Ross, D. H. Froula, K. D. Daub, J. Galbraith, S. Glenzer, B. Hatch, J. Katz, J. Kilkenny, O. Landen, D. Manha, A. M. Manuel, W. Molander, D. Montgomery, J. Moody, G. F. Swadling, and J. Weaver, "The Design of the Optical Thomson Scattering Diagnostic for the National Ignition Facility," Rev. Sci. Instrum. **87**, 11E549 (2016).

P. Datte, J. S. Ross, D. Froula, J. Galbraith, S. Glenzer, B. Hatch, J. Kilkenny, O. Landen, A. M. Manuel, W. Molander, D. Montgomery, J. Moody, G. Swadling, J. Weaver, G. Vergel de Dios, and M. Vitalich, "The Preliminary Design of the Optical Thomson Scattering Diagnostic for the National Ignition Facility," J. Phys.: Conf. Ser. **717**, 012089 (2016).

A. K. Davis, D. T. Michel, R. S. Craxton, R. Epstein, M. Hohenberger, T. Mo, and D. H. Froula, "X-Ray Self-Emission Imaging Used to Diagnose 3-D Nonuniformities in Direct-Drive ICF Implosions," Rev. Sci. Instrum. **87**, 11E340 (2016).

W. R. Donaldson, J. Katz, T. Z. Kosc, J. H. Kelly, E. M. Hill, and R. E. Bahr, "Enhancements to the Timing of the OMEGA Laser System to Improve Illumination Uniformity," Proc. SPIE **9966**, 996607 (2016).

R. K. Follett, J. A. Delettrez, D. H. Edgell, R. J. Henchen, J. Katz, J. F. Myatt, and D. H. Froula, "Plasma Characterization Using Ultraviolet Thomson Scattering from Ion-Acoustic and Electron Plasma Waves," Rev. Sci. Instrum. **87**, 11E401 (2016) (invited).

C. J. Forrest, V. Yu. Glebov, V. N. Goncharov, J. P. Knauer, P. B. Radha, S. P. Regan, M. H. Romanofsky, T. C. Sangster, M. J. Shoup III, and C. Stoeckl, "High-Dynamic-Range Neutron Time-of-Flight Detector Used to Infer the D(t,n)^{4}He and D(d,n)^{3}He Reaction Yield and Ion Temperature on OMEGA," Rev. Sci. Instrum. **87**, 11D814 (2016).

D. R. Harding, D. C. Whitaker, and C. Fella, "Growth of a Solid DT Crystal from the Liquid Inside Inertial Confinement Fusion Targets," Fusion Sci. Technol. **70**, 173 (2016).

M. Hohenberger, A. Shvydky, J. A. Marozas, G. Fiksel, M. J. Bonino, D. Canning, T. J. B. Collins, C. Dorrer, T. J. Kessler, B. E. Kruschwitz, P. W. McKenty, D. D. Meyerhofer, S. P. Regan, T. C. Sangster, and J. D. Zuegel, "Optical Smoothing of Laser Imprinting in Planar-Target Experiments on OMEGA EP Using Multi-FM 1-D Smoothing by Spectral Dispersion," Phys. Plasmas **23**, 092702 (2016).

S. X. Hu, B. Militzer, L. A. Collins, K. P. Driver, and J. D. Kress, "First-Principles Prediction of the Softening of the Silicon Shock Hugoniot Curve," Phys. Rev. B **94**, 094109 (2016).

O. A. Hurricane, D. A. Callahan, D. T. Casey, E. L. Dewald, T. R. Dittrich, T. Döppner, S. Haan, D. E. Hinkel, L. F. Berzak Hopkins, O. Jones, A. L. Kritcher, S. Le Pape, T. Ma, A. G. MacPhee, J. L. Milovich, J. Moody, A. Pak, H.-S. Park, P. K. Patel, J. E. Ralph, H. F. Robey, J. S. Ross, J. D. Salmonson,

B. K. Spears, P. T. Springer, R. Tommasini, F. Albert, L. R. Benedetti, R. Bionta, E. Bond, D. K. Bradley, J. Caggiano, P. M. Celliers, C. Cerjan, J. A. Church, R. Dylla-Spears, D. Edgell, M. J. Edwards, D. Fittinghoff, M. A. Barrios Garcia, A. Hamza, R. Hatarik, H. Herrmann, M. Hohenberger, D. Hoover, J. L. Kline, G. Kyrala, B. Kozioziemski, G. Grim, J. E. Field, J. Frenje, N. Izumi, M. Gatu Johnson, S. F. Khan, J. Knauer, T. Kohut, O. Landen, F. Merrill, P. Michel, A. Moore, S. R. Nagel, A. Nikroo, T. Parham, R. R. Rygg, D. Sayre, M. Schneider, D. Shaughnessy, D. Strozzi, R. P. J. Town, D. Turnbull, P. Volegov, A. Wan, K. Widmann, C. Wilde, and C. Yeamans, "Inertially Confined Fusion Plasmas Dominated by Alpha-Particle Self-Heating," Nat. Physics **12**, 800 (2016).

S. T. Ivancic, C. R. Stillman, D. Nelson, I. A. Begishev, C. Mileham, P. M. Nilson, and D. H. Froula, "Design of an Extreme Ultraviolet Spectrometer Suite to Characterize Rapidly Heated Solid Matter," Rev. Sci. Instrum. **87**, 11E538 (2016).

J. Katz, R. Boni, R. Rivlis, C. Muir, and D. H. Froula, "A Pulse-Front-Tilt–Compensated Streaked Optical Spectrometer with High Throughput and Picosecond Time Resolution," Rev. Sci. Instrum. **87**, 11E535 (2016).

A. S. Moore, J. Benstead, M. F. Ahmed, J. Morton, T. M. Guymer, R. Soufli, T. Pardini, R. L. Hibbard, C. G. Bailey, P. M. Bell, S. Hau-Riege, M. Bedzyk, M. J. Shoup III, S. P. Regan, T. Agliata, R. Jungquist, D. W. Schmidt, L. B. Kot, W. J. Garbett, M. S. Rubery, J. W. Skidmore, E. Gullikson, and F. Salmassi, "Two-Color Spatial and Temporal Temperature Measurements Using a Streaked Soft X-Ray Imager," Rev. Sci. Instrum. **87**, 11E313 (2016).

P. M. Nilson, F. Ehrne, C. Mileham, D. Mastrosimone, R. K. Jungquist, C. Taylor, C. R. Stillman, S. T. Ivancic, R. Boni, J. Hassett, D. J. Lonobile, R. W. Kidder, M. J. Shoup III, A. A. Solodov, C. Stoeckl, W. Theobald, D. H. Froula, K. W. Hill, L. Gao, M. Bitter, P. Efthimion, and D. D. Meyerhofer, "High-Resolving-Power X-Ray Spectrometer for the OMEGA EP Laser," Rev. Sci. Instrum. **87**, 11D504 (2016) (invited).

S. P. Regan, V. N. Goncharov, I. V. Igumenshchev, T. C. Sangster, R. Betti, A. Bose, T. R. Boehly, M. J. Bonino, E. M. Campbell, D. Cao, T. J. B. Collins, R. S. Craxton, A. K. Davis, J. A. Delettrez, D. H. Edgell, R. Epstein, C. J. Forrest, J. A. Frenje, D. H. Froula, M. Gatu Johnson, V. Yu. Glebov,

D. R. Harding, M. Hohenberger, S. X. Hu, D. Jacobs-Perkins, R. Janezic, M. Karasik, R. L. Keck, J. H. Kelly, T. J. Kessler, J. P. Knauer, T. Z. Kosc, S. J. Loucks, J. A. Marozas, F. J. Marshall, R. L. McCrory, P. W. McKenty, D. D. Meyerhofer, D. T. Michel, J. F. Myatt, S. P. Obenschain, R. D. Petrasso, P. B. Radha, B. Rice, M. J. Rosenberg, A. J. Schmitt, M. J. Schmitt, W. Seka, W. T. Shmayda, M. J. Shoup III, A. Shvydky, S. Skupsky, A. A. Solodov, C. Stoeckl, W. Theobald, J. Ulreich, M. D. Wittman, K. M. Woo, B. Yaakobi, and J. D. Zuegel, "Demonstration of Fuel Hot-Spot Pressure in Excess of 50 Gbar for Direct-Drive, Layered Deuterium-Tritium Implosions on OMEGA," Phys. Rev. Lett. **117**, 025001 (2016).

J. S. Ross, P. Datte, L. Divol, J. Galbraith, D. H. Froula, S. H. Glenzer, B. Hatch, J. Katz, J. Kilkenny, O. Landen, A. M. Manuel, W. Molander, D. S. Montgomery, J. D. Moody, G. Swadling, and J. Weaver, "Simulated Performance of the Optical Thomson Scattering Diagnostic Designed for the National Ignition Facility," Rev. Sci. Instrum. **87**, 11E510 (2016).

M. Sharpe, W. T. Shmayda, and W. U. Schröder, "Tritium Migration to the Surfaces of Type 316 Stainless Steel; Aluminum 6061; and Oxygen-Free, High-Conductivity Copper," Fusion Sci. Technol. **70**, 97 (2016).

W. T. Shmayda, M. D. Wittman, R. F. Earley, J. L. Reid, and N. P. Redden, "The Laboratory for Laser Energetics' Hydrogen Isotope Separation System," Fusion Eng. Des. **109**, 128 (2016) (invited).

C. R. Stillman, P. M. Nilson, S. T. Ivancic, C. Mileham, I. A. Begishev, R. K. Junquist, D. J. Nelson, and D. H. Froula, "A Streaked X-Ray Spectroscopy Platform for Rapidly Heated, Near-Solid Density Plasmas," Rev. Sci. Instrum. **87**, 11E312 (2016) (invited).

C. Stoeckl, W. Theobald, S. P. Regan, and M. H. Romanofsky, "Calibration of a Time-Resolved Hard-X-Ray Detector Using Radioactive Sources," Rev. Sci. Instrum. **87**, 11E323 (2016).

M. P. Valdivia, D. Stutman, C. Stoeckl, C. S. Mileham, I. A. Begishev, J. Bromage, and S. P. Regan, "A Talbot–Lau X-Ray Deflectometer as a High-Energy Density Plasma Diagnostic," IEEE Trans. Plasma Sci. **44**, 1592 (2016).

N. D. Viza, M. H. Romanofsky, M. J. Moynihan, and D. R. Harding, "The Effects of a Surfactant on the Operation of

T-Junctions for Mass-Producing Foam Targets," Fusion Sci. Technol. **70**, 219 (2016).

H. Wen, A. V. Maximov, R. W. Short, J. F. Myatt, R. Yan, and C. Ren, "Two-Plasmon Decay Instability in Inhomogeneous Plasmas at Oblique Laser Incidence," Phys. Plasmas **23**, 092713 (2016).

A. B. Zylstra, H. W. Herrmann, M. Gatu Johnson, Y. H. Kim, J. A. Frenje, G. Hale, C. K. Li, M. Rubery, M. Paris, A. Bacher, C. R. Brune, C. Forrest, V. Yu. Glebov, R. Janezic, D. McNabb, A. Nikroo, J. Pino, T. C. Sangster, F. H. Séguin, W. Seka, H. Sio, C. Stoeckl, and R. D. Petrasso, "Using Inertial Fusion Implosions to Measure the T + ^{3}He Fusion Cross Section at Nucleosynthesis-Relevant Energies," Phys. Rev. Lett. **117**, 035002 (2016).

Forthcoming Publications

S. G. Demos and R. A. Negres, "Morphology of Ejected Particles and Impact Sites on Intercepting Substrates Following Exit-Surface Laser Damage with Nanosecond Pulses in Silica," to be published in Optical Engineering.

C. Dorrer, W. A. Bittle, R. Cuffney, M. Spilatro, E. M. Hill, T. Z. Kosc, J. H. Kelly, and J. D. Zuegel, "Time-Multiplexed Pulse Shaping," to be published in the Journal of Lightwave Technology.

C. Dorrer and J. Hassett, "Model-Based Optimization of Near-Field Binary Pixelated-Beam Shapers," to be published in Applied Optics.

R. Epstein, S. P. Regan, B. A. Hammel, L. J. Suter, H. A. Scott, M. A. Barrios, D. K. Bradley, D. A. Callahan, C. Cerjan, G. W. Collins, S. N. Dixit, T. Döppner, M. J. Edwards, D. R. Farley, K. B. Fournier, S. Glenn, S. H. Glenzer, I. E. Golovkin, A. Hamza, D. G. Hicks, N. Izumi, O. S. Jones, M. H. Key, J. D. Kilkenny, J. L. Kline, G. A. Kyrala, O. L. Landen, T. Ma, J. J. MacFarlane, A. J. Mackinnon, R. C. Mancini, R. L. McCrory, D. D. Meyerhofer, N. B. Meezan, A. Nikroo, H.-S. Park, P. K. Patel, J. E. Ralph, B. A. Remington, T. C. Sangster, V. A. Smalyuk, P. T. Springer, R. P. J. Town, and J. L. Tucker, "Applications and Results of X-Ray Spectroscopy in Implosion Experiments on the National Ignition Facility," to be published in Proceedings of Atomic Processes in Plasmas (invited).

C. Fagan, M. Sharpe, W. T. Shmayda, and W. U. Schröder, "The Impact of Acid Treatments and Electropolishing Stainless-Steel Surfaces on Tritium Inventories," to be published in Fusion Science and Technology.

M. C. Gregor, R. Boni, A. Sorce, J. Kendrick, C. A. McCoy, D. N. Polsin, and T. R. Boehly, "Absolute Calibration of the OMEGA Streaked Optical Pyrometer for Temperature Measurements of Compressed Materials," to be published in Review of Scientific Instruments.

S. X. Hu, D. T. Michel, A. K. Davis, R. Betti, P. B. Radha, E. M. Campbell, D. H. Froula, and C. Stoeckl, "Understanding the Effects of Laser Imprint on Plastic-Target Implosions on OMEGA," to be published in Physics of Plasmas.

C. K. Li, P. Tzeferacos, D. Lamb, G. Gregori, P. A. Norreys, M. J. Rosenberg, R. K. Follett, D. H. Froula, M. Koenig, F. H. Séguin, J. A. Frenje, H. G. Rinderknecht, H. Sio, A. B. Zylstra, R. D. Petrasso, P. A. Amendt, H. S. Park, B. A. Remington, D. D. Ryutov, S. C. Wilks, R. Betti, A. Frank, S. X. Hu, T. C. Sangster, P. Hartigan, R. P. Drake, C. C. Kuranz, S. V. Lebedev, and N. C. Woolsey, "Scaled Laboratory Experiments Explain the Kink Behaviour of the Crab Nebula Jet," to be published in Nature Communications.

J. B. Oliver, "Analysis of a Planetary Rotation System for Evaporated Optical Coatings," to be published in Applied Optics.

J. B. Oliver, "Impact of Deposition-Rate Fluctuations on Thin-Film Thickness and Uniformity," to be published in Optics Letters.

S. Papernov, A. A. Kozlov, J. B. Oliver, C. Smith, L. Jensen, S. Günster, H. Mädebach, and D. Ristau, "Role of HfO_2 / SiO_2 Thin-Film Interfaces in Near-Ultraviolet Absorption and Pulsed Laser Damage," to be published in Optical Engineering.

B. W. Plansinis, W. R. Donaldson, and G. P. Agrawal, "Spectral Splitting of Optical Pulses Inside a Dispersive Medium at a Temporal Boundary," to be published in IEEE Journal of Quantum Electronics.

S. Salzman, H. J. Romanofsky, G. West, K. L. Marshall, S. D. Jacobs, and J. C. Lambropoulos, "Acidic Magneteorhological Finishing of Infrared Polycrystalline Materials," to be published in Applied Optics.

A. A. Solodov, B. Yaakobi, D. H. Edgell, R. K. Follett, J. F. Myatt, C. Sorce, and D. H. Froula, "Measurements of Hot-Electron Temperature in Laser-Irradiated Plasmas," to be published in Physics of Plasmas.

Conference Presentations

V. N. Goncharov, S. P. Regan, E. M. Campbell, T. C. Sangster, P. B. Radha, J. F. Myatt, D. H. Froula, R. Betti, T. R. Boehly, J. A. Delettrez, D. H. Edgell, R. Epstein, C. J. Forrest, V. Yu. Glebov, D. R. Harding, S. X. Hu, I. V. Igumenshchev, F. J. Marshall, R. L. McCrory, D. T. Michel, W. Seka, A. Shvydky, C. Stoeckl, W. Theobald, and M. Gatu-Johnson, "National Direct-Drive Program on OMEGA and the National Ignition Facility," 43rd European Physical Society Conference on Plasma Physics, Leuven, Belgium, 4–8 July 2016 (invited).

D. Polsin, T. R. Boehly, J. A. Delettrez, M. C. Gregor, C. A. McCoy, B. Henderson, D. E. Fratanduono, R. Smith, R. Kraus, J. H. Eggert, R. Collins, F. Coppari, and P. M. Celliers, "Observation of Solid-Solid Phase Transitions in Pump-Compressed Aluminum," High-Pressure Research, Holderness, NH, 17–22 July 2016.

J. B. Oliver, C. Smith, B. Taylor, J. Spaulding, S. MacNally, and T. Shea, "Characterization of Glancing-Angle–Deposited Magnesium Oxide Films," Novel Optical Materials and Applications, Vancouver, British Columbia, Canada, 18–20 July 2016.

D. H. Froula, P. M. Nilson, S. T. Ivancic, C. R. Stillman, C. Mileham, I. A. Begishev, A. A. Solodov, R. K. Jungquist, R. Boni, D. Hassett, C. Stoeckl, W. Theobald, F. Ehrne, D. Mastrosimone, D. Nelson, C. Taylor, D. J. Lonobile, R. W. Kidder, M. J. Shoup III, K. W. Hill, L. Gao, M. Bitter, and P. C. Efthimion, "Understanding the Material Response to Powerful Energy Fluxes Driven by Picosecond Lasers at the Laboratory for Laser Energetics," JOWOG37, Aldermaston, UK, 18–22 July 2016.

J. D. Zuegel, J. Bromage, E. M. Campbell, W. Krupke, T. Y. Fan, D. H. Martz, P. Reeves-Hall, and W. Leemans, "High-Average-Power, Ultra-Intense Laser Technology for Laser-Plasma Acceleration," 17th Advanced Accelerator Concepts Workshop, National Harbor, MD, 31 July–5 August 2016.

W. T. Shmayda, J. Ulreich, R. Earley, and M. D. Wittman, "Filling Inertial Confinement Fusion Targets with DT Using Palladium Tritide," The 22nd Topical Meeting on the Technology of Fusion Energy (TOFE 2016), Philadelphia, PA, 22–25 August 2016.

W. R. Donaldson, J. Katz, T. Z. Kosc, J. H. Kelly, E. M. Hill, and R. E. Bahr, "Enhancements to the Timing of the OMEGA Laser System to Improve Illumination Uniformity," 2016 Optical Engineering and Applications, San Diego, CA, 28 August–1 September 2016.

E. M. Campbell, "Symmetric Illumination and Direct Drive at the National Ignition Facility," Symmetric Direct-Drive Study, Livermore, CA, 7–8 September 2016.

The following presentations were made at the 7th International Conference on Ultrahigh Intensity Lasers, Montebello, Quebec, Canada, 11–16 September 2016:

S.-W. Bahk, J. B. Oliver, R. K. Jungquist, J. Bromage, E. M. Schiesser, and J. P. Rolland "Beam-Transport Systems for Ultra-Broadband Lasers."

I. A. Begishev, S.-W. Bahk, R. Cuffney, C. Dorrer, D. Haberberger, D. H. Froula, C. Mileham, P. M. Nilson, C. Stoeckl, J. D. Zuegel, and J. Bromage, "Extensions to the Multi-Terawatt Laser for Laser Development and Plasma Physics Studies."

S. Bucht, D. Haberberger, J. Bromage, and D. H. Froula, "Transforming the Idler-to-Seed Raman Amplification."

C. Dorrer, L. J. Waxer, A. Kalb, E. M. Hill, and J. Bromage, "Temporal Characterization of Optical Pulses by Spectral Phase Diversity."

D. Haberberger, A. Davies, S. Bucht, J. Bromage, J. D. Zuegel, D. H. Froula, R. Trines, R. Bingham, and P. A. Norreys, "Plans for a Tunable Raman Amplifier at The Laboratory for Laser Energetics."

R. Betti, "Status and Prospects for Demonstrating Ignition via Laser Fusion," The 3rd International Conference on High Energy Density Physics (ICHEDP-3), Shenzhen, China, 23–26 September 2016.

The following presentations were made at the XLVIII Annual Symposium on Optical Materials for High-Power Lasers, Boulder, CO, 25–28 September 2016:

S. G. Demos, C. W. Carr, and D. A. Cross, "Electrostatic Effects Following Irradiation of Fused Silica Surfaces with Nanosecond Laser Pulses."

A. A. Kozlov, S. Papernov, J. B. Oliver, A. L. Rigatti, B. Taylor, B. Charles, and C. Smith, "Study of the Picosecond Laser Damage in HfO_2/SiO_2-Based Thin-Film Coatings in Vacuum."